NUMERICAL MODELING OF CROSS-SHORE SEDIMENT TRANSPORT AND SANDBAR MIGRATION

A Thesis
Presented to
The Academic Faculty

by

Mustafa Kemal Cambazoğlu

In Partial Fulfillment
of the Requirements for the Degree
Doctor of Philosophy in the
School of Civil and Environmental Engineering

Georgia Institute of Technology
December 2009

NUMERICAL MODELING OF CROSS-SHORE SEDIMENT TRANSPORT AND SANDBAR MIGRATION

Approved by:

Dr. Kevin A. Haas, Advisor
School of Civil and Environmental Engineering
Georgia Institute of Technology

Dr. Hermann M. Fritz
School of Civil and Environmental Engineering
Georgia Institute of Technology

Dr. Paul A. Work
School of Civil and Environmental Engineering
Georgia Institute of Technology

Dr. Emanuele Di Lorenzo
School of Earth and Atmospheric Sciences
Georgia Institute of Technology

Dr. Terry W. Sturm
School of Civil and Environmental Engineering
Georgia Institute of Technology

Date Approved: 28 July 2009

To my love and happiness, Özlem Kurt

and

To my family, İpek, Gencer and Selim Cambazoğlu

ACKNOWLEDGEMENTS

My deepest thanks go to Dr. Kevin A. Haas. From the first day till the last, he has been a great advisor and a great friend. His patience, guidance and ideas made this dissertation happen.

I would like to thank Dr. Paul Work for his valuable comments and for all the field trip experiences. I also would like to thank Dr. Hermann Fritz, Dr. Emanuele Di Lorenzo and Dr. Terry Sturm for serving on my committee and their comments.

This dissertation has been completed succesfully because you complete me Özlem Kurt. Your love gives me hope, your support gives me strength, your existence gives me happiness. My parents Gencer and İpek Cambazoğlu and my brother Selim were always with me. Even if thousands of miles separate us, your love and trust have always been with me in my heart giving me courage. I thank you all for always believing in me.

A classmate, a colleague, an officemate, a roommate, a great friend, Zafer Defne; Thank you very much for all the laughs and memories shared. Many thanks to Yavuz Özeren for his endless friendship and support. I thank Hüseyin Demir for welcoming me to US, sharing his home with me and his great friendship. Great thanks to Ayşe Erdölen and Servet Karasu who brought joy to our homes in Savannah.

Thanks to my fellow graduate student friends and colleagues at Georgia Tech Savannah, Elza Bystrom, Mesut Türel, Brian Sapp, Jeseon Yoo, Fahad Mohammed, Chris Blount, Heidi Hammerstein, Adam Sapp among the others. Thanks to Dr. Cheryl Ann Blain, my supervisor at Naval Research Laboratory for her understanding during the time that I finished my thesis and to Dr. Daniel M. Hanes, the PI of my funding project from USGS, for all his encouragement throughout my studies.

TABLE OF CONTENTS

LIST OF TABLES

LIST OF FIGURES

LIST OF SYMBOLS

A	complex amplitude of the free surface (m)
A_w	amplitude of nearbed orbital trajectory (m)
A'	roller area (m^2)
B	breaking wave coefficient representing intensity of breaking (-)
B_o	surface shape parameter (-)
C	wave celerity (m/s)
C_g	wave group velocity (m/s)
C_p	persistence length calibration constant (-)
C_r	roller lag length calibration coefficient (-)
C_ν	coefficient for eddy viscosity due to bottom friction (-)
C_1	calibration coefficient for Haas and Hanes (2004) sediment transport formula (-)
C_2	calibration coefficient for slope term of Haas and Hanes (2004) sediment transport formula (-)
C^+	phase speed of bedform propagating in the positive x-direction (m/s)
C^-	phase speed of bedform propagating in the negative x-direction (m/s)
d	model skill by Willmott (1981) (-)
d_{50}	medium grain size (m)
D	wave energy dissipation (N/m)
E	energy density of the organized wave motion (N/m)
E_r	roller energy density (N/m)
f	wave frequency (Hz)
f_w	friction factor (-)

$\overline{f}$	mean frequency of the energy spectrum (1/s)
f_α	short wave forcing, local contribution to the radiation stress (m/s^2)
f_{cw}	combined wave-current related bottom friction coefficient (-)
f_v	calibration factor for breaking wave induced depth averaged eddy viscosity (-)
f_x^r	roller contribution to the short wave forcing in x-direction
$F_\alpha^{(0)}$	leading order total forcing for depth-varying currents
$F_\alpha^{(1)}$	first order total forcing for depth-varying currents
g	gravitational acceleration (m/s^2)
h	local water depth (m)
h_o	still water depth (m)
H	wave height (m)
H_m	maximum possible wave height before breaking (m)
H_{mo}	energy-based significant wave height (m)
H_o	deep water wave height (m)
H_{rms}	root-mean-square wave height (m)
H_s	significant wave height (m)
$ilag$	roller lag length in terms of grid spacing (-)
k	local wave number (1/m)
L	wave length (m)
L_b	persistence length (m)
L_o	deep water wave length (m)
L_r	roller lag length (m)
M	coefficient for eddy viscosity due to wave breaking (-)
n	ratio of group velocity to wave celerity (-)
n_p	bed porosity (-)

nr	coefficient denoting depth variation of the roller contribution to the short wave forcing (-)
p	pressure (N/m)
$P(H)$	probability distribution of waves (-)
$P_b(H)$	probability distribution of breaking waves (-)
q_{HH}	total volumetric sediment transport rate estimated by *HH* (Haas and Hanes, 2004) sediment transport formula (m^2/s)
q_{BBB}	total volumetric sediment transport rate estimated by *BBB* (Bagnold, 1966; Bowen, 1980; Bailard, 1981) sediment transport formula (m^2/s)
q_{slope}	volumetric sediment transport rate due to bed slope (m^2/s)
q_w	volumetric sediment transport rate due to waves (m^2/s)
q_V	volumetric sediment transport rate due to currents (m^2/s)
q^+	sediment transport rate associated with the bedform propagation in the positive x-direction (m^2/s)
q^-	sediment transport rate associated with the bedform propagation in the negative x-direction (m^2/s)
$\hat{q}$	WENO reconstructed sediment transport rate (m^2/s)
Q_a	transformation/wave-current interaction term in mild slope equation
Q_b	fraction of breaking waves (-)
$Q_{b,lag}$	fraction of breaking waves due to roller lag (-)
$Q_{b,new}$	fraction of newly breaking waves (-)
$Q_{b,tot}$	total fraction of breaking waves (-)
$Q_{b,tot}^{mod}$	modified total fraction of breaking waves due to roller lag (-)
$Q_{b,TG83}$	fraction of breaking waves estimated by *TG83* (-)
$Q_{b,per}$	fraction of persistent breakers (-)
$Q_{w\alpha}$	wave induced volume flux in α direction (m^2/s)

$Q_{w\alpha r}$	roller component of wave volume flux in α direction (m^2/s)
$Q_{w\alpha o}$	non-broken wave component of wave volume flux in α direction (m^2/s)
Q_α	total volume flux in α direction (m^2/s)
r	bed roughness (m)
R_a	transformation/wave-current interaction term in mild slope equation
S	near-bed orbital wave velocity skewness (-)
S_a	transformation/wave-current interaction term in mild slope equation
$S_{\alpha\alpha}$	radiation stress in α-α direction (N/m)
$S_{\alpha\alpha r}$	roller component of radiation stress in α-α direction (N/m)
$S_{\alpha\alpha o}$	non-broken wave component of radiation stress in α-α direction (N/m)
SG	specific gravity (-)
t	time (s)
$tan\beta$	bottom slope (-)
$\tan\phi$	angle of internal friction (-)
T	wave period (s)
$T_{\alpha\beta}$	the Reynolds stresses (N/m^2)
T_a	transformation/wave-current interaction term in mild slope equation
T_c	phase of wave crest (s)
T_t	phase of wave trough (s)
T_z	zero down crossing wave period (s)
T_1	normalized phase of wave crest (-)
T_2	normalized phase of wave trough (-)
T_0	normalized phase of zero down crossing (-)
u	near-bed horizontal orbital velocity (m/s)
u_{rms}	root mean square value of the orbital velocity (m/s)

u_α	instantaneous total fluid velocity in α direction (m/s)
u'_α	turbulent fluid velocity in α direction (m/s)
$u_{w\alpha}$	short wave velocity in α direction (m/s)
U_c	maximal orbital velocity under wave crest (m/s)
U_t	maximal orbital velocity under wave trough (m/s)
$\hat{U}_{Airy}$	orbital velocity amplitude according to Airy wave theory (m/s)
$\overline{U}$	depth-averaged cross-shore current velocity (m/s)
U_1	normalized maximal orbital velocity (-)
U_2	velocity asymmetry parameter (-)
U^*	sum of orbital velocity amplitudes under wave crest and trough (m/s)
V_α	wave averaged current velocity in α direction (m/s)
$V_{d\alpha}(z)$	depth varying current velocity in α direction (m/s)
$V_{d\alpha}^{(0)}$	leading order solution for the depth-varying current velocity (m/s)
$V_{d\alpha}^{(1)}$	first order solution for the depth-varying current velocity (m/s)
$V_{m\alpha}$	depth-averaged current velocity in α direction (m/s)
w	vertical short wave velocity (m/s)
w_{BL}	dissipation for the turbulent bottom boundary layer
W	vertical current velocity (m/s)
$W(H)$	weighting function for probability distribution of waves (-)
W_o	fall velocity of the bed material (m/s)
x	horizontal coordinate (m)
$x(j)$	measured data used in model skill calculations
$y(j)$	modeled data used in model skill calculations
$\overline{x}$	mean of measured data used in model skill calculations
Y	combined breaking wave coefficient (-)
z	vertical coordinate (m)

α_{BJ}	a constant representing intensity of breaking in *BJ78* dissipation formula (-)
α_d	dissipation term in mild slope equation
ϵ_s	efficiency factor for suspended-load (-)
ϵ_b	efficiency factor for bed load (-)
η	surface displacement (m)
γ	breaking wave coefficient (-)
κ	the von Karman constant (-)
μ	sediment packing factor (-)
∇	horizontal gradient operator (1/m)
ν_s	smagorinsky eddy viscosity (m^2/s)
ν_t	eddy viscosity representing the turbulence created by bottom friction and wave breaking (m^2/s)
$\nu_{t,0}$	background eddy viscosity (m^2/s)
$\overline{\nu}_{t,wave}$	breaking wave induced depth averaged eddy viscosity (m^2/s)
ν_{tb}	constant eddy viscosity in the bottom boundary layer (m^2/s)
φ	angle of repose for the bed material
ρ	fluid density (m^3/s)
σ	angular frequency of waves (1/s)
σ_r	angle of the roller front slope (°)
τ_α^B	bottom shear stress in α direction (N/m^2)
τ_{cr}	critical shear stress found according to Shield's incipient motion criteria (N/m^2)
τ_{eff}	effective bottom shear stress (N/m^2)
τ_α^S	surface shear stress in α direction (N/m^2)
τ^{SB}	steady streaming stress (N/m^2)
θ	wave direction

ξ	vertical coordinate after transformation (m)
$\overline{\zeta}$	mean water level (m)
Δx	grid spacing (m)

SUMMARY

Nearshore processes on barred beaches are studied with a process-based numerical model. The two major goals of the study are to expand the body of knowledge about nearshore processes on barred beaches gaining a better understanding of the physical mechanisms affecting bar migration events and to enhance the numerical model in order to accomplish realistic simulations of bar migration events. The numerical model is used to study the effect of physical processes on the hydrodynamics and morphodynamics in the nearshore environment.

The hydrodynamics on barred beaches and mechanics of sediment transport related to bar migration are studied on storm time scales. The numerical model system consists of a linear spectral refraction-diffraction model, REF/DIF S, a quasi-3D nearshore circulation model, SHORECIRC, energetics-based sediment transport models, and a morphological evolution model. A laboratory experiment conducted in the Delta Flume, Netherlands which had an erosive test stage with offshore bar migration followed by an accretive test stage with onshore bar migration is used for modeling purposes and verifications.

The sediment transport is driven by the near-bed wave orbital velocities and the undertow current at the bottom. For that reason, accurate predictions of nearshore hydrodynamics are important for predictions of morphodynamics and successful simulations of bar migration events. A number of enhancements are made to the wave and circulation modules of the numerical model system specifically for simulations on barred beaches. The model modifications and enhancements are:

- a combined breaking wave parameter with a spatial variation in the wave model;
- a method accounting for breaking wave persistence in the wave model;

- a method accounting for the new breaker roller lag in the wave model;
- the dynamic pressure component in the radiation stress forcing;
- a roller contribution with different depth variation options for the short wave forcing in the circulation model;
- wave height instead of water depth as the turbulent length scale in the eddy viscosity calculations in the circulation model;
- a slope term for the default sediment transport formula.

The depth-integrated cross-shore momentum balance in the surf zone shows the strong dependence of the mean water level on radiation stresses. The effect of surface shape parameter and the roller face angle on radiation stress and mean water level predictions are investigated. In reality, the organized wave energy is transferred to roller development over a transition distance and the roller does not immediately contribute to the radiation stresses; therefore, showing the importance of the roller lag mechanism for mean water level predictions.

The cross-shore variation of the vertical momentum balance is studied to observe the variation of forcing agents of the undertow current. The cross-shore pressure gradient is the most dominant forcing term affecting the depth structure of the undertow current. The effect of different depth variations of the roller contribution to the short wave forcing on the undertow current is investigated. The mechanism accounting for breaking wave persistence and the mechanism accounting for the roller lag are shown to be important for predictions of the undertow currents on barred beaches.

The performance of the model in predicting offshore bar migration and onshore bar migration events on storm time-scales is investigated. The skewed wave orbital velocities are introduced to the linear wave model by an empirical parametrization method and are found to contribute strongly to the onshore bar migration. The

enhancements made to the wave dissipation and roller are found to significantly affect the predicted migration of the bar as well as the maintainance of the trough.

CHAPTER I

INTRODUCTION

The nearshore environment is very dynamic and complex with wave action, circulation due to currents, movements of sediment on the ocean bottom and the interaction between all of them. The continuous action of waves and currents drives sediment transport, leading to the formation of morphological features. Researchers have been working hard to fully understand the physics of this complex environment. Our knowledge of the physics of nearshore hydrodynamics is more complete than our knowledge of the physics of sediment transport. Sediment transport on beaches is an active research field with many unknowns and uncertainties that await answers from the scientific community. Even with the most sophisticated sediment transport models, many empirical relations or coefficients are used to predict or simulate field or laboratory observations.

As deep water waves approach the shore, they enter shallower water and shoal with an increase in their wave height. During this shoaling process the waves become skewed with a higher wave crest, which also pitches forward. After the wave height reaches a certain limit, the waves start to break. This causes a decrease in their height and a decrease in their mass and momentum fluxes in the surf zone. The momentum flux due to waves, or the radiation stress, decreases during breaking, resulting in an increase of the mean water level as a counteracting pressure gradient. The pressure gradient also drives an offshore directed current, or the undertow. Once the waves break, a roller is also formed at the surface that contributes to the mass and momentum of the waves.

Some of the most common morphological features in the nearshore region are

longshore sandbars. The cross-shore sediment transport is not only a mechanism causing the sandbars to form on the ocean floor but also a mechanism for modifying the bar location, height and alignment. These changes in bathymetry influence the wave and circulation patterns in the nearshore which has a corresponding effect on the sediment transport and morphological evolution. Because of this important feedback between the morphology and hydrodynamics, the mechanisms causing the formation and migration of nearshore sandbars are of significant interest.

The generation and evolution of nearshore sandbars have been under investigation for several decades. Field and laboratory studies have been conducted in order to observe bar formation and migration events. Lately, numerical simulations accompany the measurements to investigate the effect of different mechanisms in more detail. Measurements and observations show that during high-energy winter seasons and storm events, longshore bars form and migrate offshore whereas during less energetic spring-summer conditions and post-storm events, the bar migrates onshore and gets destroyed during beach recovery. In order to be able to accurately model the bar formation and onshore-offshore migration events, the mechanisms causing the cross-shore sediment transport that leads to sandbar formation and migration have to be understood.

In order to make accurate morphological simulations, it is required to predict the hydrodynamics as accurately as possible. The existence of a sandbar introduces many complications for numerical modelers compared to simpler monotonic beach profiles. For this reason, it is important to understand the capabilities of a numerical model, the processes that are simulated by a model in addition to the processes that are excluded. Most of the model systems use a wave model to simulate the waves in conjunction with a circulation model to simulate the currents. After the hydrodynamic predictions are made, the sediment transport and morphological evolution may be estimated.

This chapter introduces the mechanisms that are suggested to be responsible for bar formation and migration in the nearshore region. The sediment transport models used in predicting the morphological evolution and bathymetric changes are listed as well. Section 1 discusses the formation of a bar. The mechanisms causing sandbar migration are introduced in Section 2. The sediment transport models described in the literature are listed in Section 3. Section 4 summarizes parametric dissipation models used for simulation of the waves. Section 5 describes the models used to predict the undertow current. Section 6 lists some of the studies in the literature on numerical modeling of cross-shore sediment transport and bar migration events. The last section outlines the scope of this study.

1.1 Bar Formation

The generation of sandbars has been studied in both field and experimental conditions and also simulated with numerical models in order to understand the mechanisms causing the formation of a bar. These studies introduce two main hypotheses that lead to the formation of a bar: the breakpoint hypothesis and the long wave hypothesis. Although both of them prove to have a role in bar formation, other mechanisms such as the harmonic decomposition of surface waves have also been suggested as responsible for bar formation.

1.1.1 Breakpoint Hypothesis

While water waves approach the shore, entering shallower water, the wave height starts to increase. During this so-called shoaling process, the increase in wave height is accompanied by a decrease in the mean water level. Outside the surf zone, there is a weak seaward directed current stronger at the surface than at the bottom (Putrevu and Svendsen, 1993). After breaking, the wave height starts to decrease accompanied with an increase in the mean water level. The mass flux of waves above the trough level is balanced by a return current, i.e. undertow, which flows offshore stronger near

the bottom in the surf zone. This results in a convergence of bottom flow beneath the breakpoint.

The sediment motion associated with these flows results in a convergence of sediment transport at the breaker line, leading to the formation of a longshore bar. The accumulation of the sediment grains on the bar stops either when the slope gets so steep that the bottom current cannot carry the particles up to the crest of the bar or when the amount carried up by the current balances the amount returned in suspension (Dyhr-Nielsen and Sørensen, 1970; Sunamura and Maruyama, 1987; Thornton *et al.*, 1996).

After the formation of the bar, the waves begin to break further offshore. This offshore movement of the breakpoint results in either the growth or the offshore migration of the bar. For a monochromatic wave there is a narrow breaking region, however for random waves there is no definitive breakpoint and the wave breaking takes place over a broad region. For random waves, measurements and numerical model studies supporting bar formation under the breakpoint are unable to explain the formation of multiple bars, but are able to describe the formation of the seaward-most bar. The bar formation inside the inner surf zone, away from the initial breakpoint, could not be explained with the breakpoint hypothesis (Sallenger *et al.*, 1989; Houston and Dean, 1991). This suggests processes other than the breakpoint mechanism such as infragravity waves for bar formation. From laboratory experiments and field measurements, it is hypothesized that those bars in the surf zone shoreward of the breakpoint might be formed under the action of a return current which delivers the sediments from the shore and deposits them when equilibrium is reached (Dally, 1987; Sallenger *et al.*, 1989). Although earlier studies suggested that the breakpoint hypothesis is valid for plunging breakers only, it has been shown that it may also be valid for spilling type breakers (Dally, 1987).

The breakpoint hypothesis is a reasonable physical explanation of bar formation

and is supported by not only measurements but also model predictions. However, there is not a definitive breakpoint in nature when there are random waves. Moreover, it is apparent that it may not be solely responsible for bar formation due to the fact that bar formation is observed under non-breaking wave conditions and multiple bar formations are observed away from the breakpoint for some situations. These observations led scientists to the investigation of other possible mechanisms associated with bar formation.

1.1.2 Infragravity Wave Field

Another mechanism proposed for bar formation is the presence of long infragravity waves in the nearshore field. The formation of a bar close to the shoreline which could not be explained by the breakpoint hypothesis is suggested to be associated with the long wave hypothesis (Sallenger and Holman, 1987; Stive, 1987). When there are groupy waves approaching the shoreline, a bound long wave travels with the group velocity. The breaking of the short waves causes the release of the long wave, i.e. a free long wave and the reflection of this long wave from the shore leads to the generation of a standing long wave field.

Due to the existence of standing long waves, such as edge waves or leaky waves, the undisturbed bed follows the behavior of the waves and a series of bars is formed at the bottom either at the nodes (minima) or antinodes (maxima) of the wave field. Whether the sediment converges under the nodes or the antinodes is observed to depend on the dominant sediment transport mechanism depending on the grain type, that is, bed load vs. suspended load. Field measurements show strong correlation between the predicted positions of the antinodes and the nodes of the standing infragravity waves, and the positions of longshore sandbar crests (Short, 1975).

Investigations of the effect of standing infragravity edge waves on bar formation

suggest that the location of bars after major storm events are probably not associated with the breakpoint hypothesis and the edge waves are the likely cause of bar formation. The strong correlation between the bar dimensions and the structure of edge waves strengthens this hypothesis (Aagaard, 1988).

If the waves are not propagating obliquely while approaching the shore, the shore-normal incidence of waves will not result in edge wave formation but a partially standing wave field due to the reflection of long waves from the shore. The coupling between the groupy short waves and the long waves may result in bar formation at the bottom (Stive, 1987; Roelvink and Stive, 1989). It is hypothesized that the sediment is mobilized by short waves and then transported by long waves. Model tests with this proposed mechanism predict the formation of multiple bar systems. As described earlier, bar locations are associated with the nodes of the envelope of the partially standing long wave field. Further studies of the same model with varying incoming wave group period and magnitude of the incoming bound long wave show that the formation of multiple bars is probable if the breakpoint-forced, free long wave is larger than the bound long wave (O'Hare and Huntley, 1994).

Similarly, laboratory studies and model simulations with monochromatic non-breaking waves reflecting off the beach to generate the partially-standing wave field show similar characteristics to those demonstrated by the standing long waves. Bars over a flat erodible bed are observed to follow the surface wave motion and form with spacings of half the surface wavelength. Crests of bars are observed to be beneath the antinodes for dominant suspended sediment transport and closer to the nodes when bed load is dominant and coarser grains at the crests stabilize the bar formation. The formation of bars at the bottom increases the reflection of incident waves resulting in a stronger standing wave field and further growth of the bars (O'Hare and Davies, 1990, 1993).

This hypothesis helps to explain the formation of bars outside the surf zone where

no wave breaking is observed but is not proven to be the only mechanism responsible for bar formation outside the surf zone. It was found that experiments especially designed to favor the long wave hypothesis showed very little support for the long wave hypothesis of bar formation. In those experiments, almost no correlation was found between the surf beat envelope and bar formation. The results suggested that a breakpoint/undertow mechanism is more likely responsible for bar formation and a bar is formed in the vicinity of the outer-most breakpoint in the domain (Dally, 1987).

1.1.3 Nonlinear Wave Interactions

Studies with a partially standing wave field simply suggest that the modulations in the erodible bed are a replica of those on the surface. In other words, the envelope of the first harmonic of the wave controls the sediment transport and bedforms.

Early mathematical models were able to explain bar formation when there is a nonbreaking wave condition, in which case offshore flows are weak, and also when there is no reflection of waves, when there is no partially-standing wave field. The bed surface development into a system of crest and troughs is influenced by the wave regime and the spacing of sandbars is shown to be connected with the distance between two successive minima of the second harmonic amplitude. The wave-bottom interaction governs the modulations on the erodible bed. The model predictions are compared with field measurements and bar numbers and spacings correlate well with those observed in the nearshore (Boczar-Karakiewicz and Davidson-Arnott, 1987).

Further investigations and laboratory studies on the effect of nonlinear wave interactions on bar formation support the continuous adaptation between the wave and the bottom for nonbreaking wave conditions. Experiments show that the bed fits the wave motion in the early development stages of erosion. Then, the changes in the bottom force the waves to fit the bed. The continuous interaction between the wave

and the bottom leads to the formation and growth of sand bars at the bottom. This coupling is shown to be the strongest when the waves are partially standing. As the number and size of bars increase, the reflection of incident waves from the bottom also grows causing the formation of a stronger standing wave field. Experiments show that for both a pure regular wave and a bimodal wave, the bed profile is a replica of the envelope of the first harmonic of the wave (Dulou *et al.*, 2000).

Laboratory studies under breaking wave conditions suggest that increased nonlinear wave-wave interactions also have a role in bar formation. The nonbreaking wave experiments of Dulou *et al.* (2000) are extended to include both nonbreaking and breaking wave conditions and a bar is formed associated with the envelope of the second harmonic for both conditions. It is observed that nonlinearities cause the formation of a bar for breaking wave conditions even under the action of weak undertow which reduces the possibility of bar formation due to the breakpoint hypothesis. Again, there is a dependence on the mode of sediment transport, i.e. bed load vs. suspended load, for the bar formation (Dulou *et al.*, 2002).

There have been many studies searching for the answer to the question: "What causes the formation of a sandbar?"Many mechanisms were proposed to be the answer of this question. However, it may easily be said that none have been proven to be solely responsible for the bar formation yet it is still unclear if a combination of several mechanisms might cause the formation of sandbars at the bottom of nearshore regions.

1.2 Sandbar Migration

So far, the formation of bar systems and the mechanisms causing those formations have been discussed. However, the bar also evolves after formation, in other words, migrates, grows or possibly gets destroyed. The processes responsible for the evolution of the bar have also been investigated in order to make predictions of beach evolution.

Several processes related to erosion-accretion patterns and bar migration are the

skewed/asymmetric oscillatory flow of short waves, breaking wave induced undertow current and the long wave field. All of these processes cause the sediment particles resting on the ocean bottom to be mobilized and move in the cross-shore direction thus, changing the morphology.

Experimental and numerical studies show that some of these mechanisms contribute to the shoreward sediment transport and onshore bar migration events while others contribute to the seaward sediment transport and offshore bar migration events. Therefore, it is useful to classify bar migration as offshore and onshore bar migration events and discuss the effect of transport mechanisms accordingly.

1.2.1 Offshore Sandbar Migration

Studies have shown that offshore sandbar migration may occur due to wave breaking induced undertow or the interaction of infragravity waves with either the longshore current or short waves. During high-energy conditions, the strong undertow current at the bottom becomes the main driving force for offshore sediment transport and bar migration.

1.2.1.1 Wave Breaking Induced Undertow

The strong breaking of waves under storm conditions induces a strong return current, known as the undertow current which dominates the sediment transport and causes offshore directed sediment transport and seaward migration of nearshore sandbars. Stive and Battjes (1985) developed a model that incorporates this mechanism exclusively for sediment transport and bathymetric evolution calculations. The model results are compared with laboratory observations of bar generation, dune erosion and the offshore movement of a step. The satisfactory level of their predictions show that the breaking-induced return flow is a dominant mechanism in cross-shore sediment transport.

Laboratory studies including the effect of undertow showed that it is one of the

main mechanisms causing offshore sediment transport and sandbar migration (Stive, 1987; Roelvink and Stive, 1989). Field measurements support this hypothesis in the nearshore regions of natural beaches (Trowbridge and Young, 1989; Thornton *et al.*, 1996; Gallagher *et al.*, 1998; Elgar *et al.*, 2001). Numerical model predictions investigating the contribution of undertow to the sandbar migration show that offshore bar migration is observed when the undertow is strong after breaking (Stive and Battjes, 1985; Stive, 1987; Thornton *et al.*, 1996; Elgar *et al.*, 2001; Hoefel and Elgar, 2003; Henderson *et al.*, 2004; Hsu *et al.*, 2006).

1.2.1.2 Infragravity Waves

The undertow current at the bottom is not the only mechanism associated with the offshore bar migration. It is hypothesized that edge waves in the presence of a strong longshore current are responsible for the formation and evolution of bars (Howd *et al.*, 1991, 1992; Shand *et al.*, 1999). Observations of 2-D evolution of a beach profile with the presence of strong longshore currents and unidirectional edge waves in the nearshore shows offshore migration of a sandbar. The maximum longshore current was always located in the bar trough. An analytical study accompanying this field survey showed that a hypothetical effective beach profile depending on the true profile, current velocity and the edge wave celerity might be introduced under the presence of strong longshore currents and a dominant direction of edge wave progression. The wave-current interaction leads to the modification of edge waves such that the nodes of infragravity waves coincide with the bar crest of the effective beach profile. As a result, the true profile moves towards the effective beach profile (Howd *et al.*, 1991).

The coupling between the groupy short waves and the long waves may result in not only bar formation but also bar migration (Stive, 1987; Roelvink and Stive, 1989). If the bound long wave dominates, short wave - long wave coupling causes the offshore movement of the sediment, therefore offshore migration of existing sandbars in the

nearshore region (O'Hare and Huntley, 1994).

1.2.2 Onshore Sandbar Migration

The undertow current is stronger inside the surf zone and is the main mechanism transporting the moving sediment particles offshore resulting in offshore bar movement. However, both outside and inside the surf zone during low-energetic conditions, the undertow current is much weaker and other mechanisms dominate the transport of sediment and thus onshore bar migration is observed under these circumstances.

1.2.2.1 Asymmetry of Short Waves

An important mechanism in the generation and development of a bar is the asymmetry of the wave field. As waves enter the shallow water region and shoal, they become nonlinear and their shape starts to change and become skewed such that the wave crest becomes narrower and higher while the wave trough becomes broader and flatter. The orbital velocities associated with the crest and trough also is skewed and it has been hypothesized that the onshore-directed sediment transport associated with the wave crest becomes greater than the offshore-directed sediment transport associated with the wave trough.

It is important here to describe the differences between horizontal and vertical asymmetry. The horizontal asymmetry is also defined (in this study) as the wave skewness. It is the asymmetry with respect to the mean water level. As the waves approach breaking, the crest becomes higher but narrower and the trough becomes lower and broader. The vertical asymmetry, on the other hand, is commonly termed as the wave asymmetry. The waves not only become skewed as they approach breaking but the crest start to pitch forward and the wave becomes asymmetric with respect to the vertical plane through the crest. As a result of this definition, it may be said that a skewed wave does not have to be asymmetric; similarly an asymmetric wave does not have to be skewed.

Velocity Skewness

The sediment transport rate is a function of the third moment of near-bed orbital velocities. From a mathematical standpoint, the velocity skewness is defined as the third moment of the velocity such that:

$$S = \frac{\overline{u^3}}{{u_{rms}}^3} \tag{1}$$

where u is the near-bed horizontal orbital velocity. The overbar represents an average over the wave period and u_{rms} is the root mean square value of the orbital velocity. It is the near-bed orbital velocity which is important for the cross-shore sediment transport. That is why near-bed velocities are used in the analysis for velocity skewness predictions.

Cornish (1898) was the first to realize the important effect of the near-bed velocity on cross-shore sediment transport. He noticed that the onshore velocity associated with the wave crest was more effective transporting the coarse sediment than the offshore velocity associated with the trough. Nonlinear wave theories support these observations by predicting horizontal orbital velocities with higher crests of shorter duration and shallower troughs with longer durations.

The sinusoidal wave theory is widely used for modeling the hydrodynamics inside the surf zone. Also known as the linear wave theory, it gives acceptable results considering the waves and currents. However, it has a major drawback for predicting the wave-induced cross-shore sediment transport as the orbital velocities under the crest and trough are going to be equal. This causes no net transport due to near-bed wave motion. For this reason, in order to have better cross-shore sediment transport predictions, the skewed near-bed orbital velocities and therefore, the velocity skewness has to be accounted for and modeled properly.

Stive (1987) extended the model developed by Stive and Battjes (1985) with transport due to skewness of the wave motion, in order to include a mechanism for onshore

transport. Accounting for the effects of wave skewness, it is assumed that the instantaneous sediment transport rate is proportional to a power of the local relative velocity at the bottom (Stive, 1987, Equation (1)). For this reason, the energetics-based transport formulation of Bailard (1981) is reduced for application in the cross-shore direction and utilized (Stive, 1987, Equation (2)). This sediment transport formulation uses vertically integrated equations and the transport is assumed to respond to the near bottom total water velocity in an instantaneous, quasi-steady manner which might be considered valid for sheet-flow conditions (Bailard, 1981).

After the sediment transport rate is calculated from Bailard's formulation, the bottom changes are estimated through the application of mass balance for the sediment. A field data set of observations of the formation and deformation of a bar system in an estuary region and laboratory measurements of profile deformation of an initially plane beach are used for comparisons. The model gave satisfactory results for the field scale comparisons. For the laboratory scale, the model is only able to predict the onset of the bar formation outside the surf zone but failed to predict the subsequent bar growth and the development of the shoreside of the bar. The bar growth is believed to be associated with a third mechanism which is the resonance of particular long wave modes forced by the wave grouping effects (Stive, 1987).

After Stive (1987) showed the importance of including wave asymmetry as velocity skewness in near bottom orbital velocities to explain shoreward transport, other studies followed incorporating the same mechanism in order to predict the onshore directed bar migration during less energetic conditions. Most of these studies correctly predict the growth and offshore migration events of larger storm waves. However, some of these studies either underpredict or fail to predict the observed onshore migration events of low-energy wave conditions (Roelvink and Stive, 1989; Thornton *et al.*, 1996; Gallagher *et al.*, 1998).

Hsu *et al.* (2006) extended the energetic-type sediment transport model by separating the transport associated only with the orbital velocities from the transport associated with the undertow and used different friction coefficients for both. After this modification, the energetics-based model that depends on the velocity skewness instead of the acceleration skewness is observed to have predictive skill similar to the boundary layer model (Henderson *et al.*, 2004) and the energetics-based model including the vertical velocity asymmetry, i.e. acceleration skewness (Hoefel and Elgar, 2003). A direct comparison is made between the predictive skills of the previously developed wave-resolving eddy-diffusive model by Henderson *et al.* (2004), an energetics-based model including acceleration skewness by Hoefel and Elgar (2003), with the newly developed models of an energetics-based model with modified friction factors and a new wave-resolving boundary layer model which calculates the sediment transport rate from a Meyer-Peter and Mueller power law suggested for sheet-flow. The results show similar and accurate predictions of onshore sandbar migration by all models and further studies are recommended in order to understand which mechanisms are dominant for cross-shore sediment transport and onshore sandbar migration.

Recently, Cambazoglu *et al.* (2006) studied the effect of velocity skewness on sandbar migration. An energetics-based sediment transport formula is used to isolate the effect of velocity skewness. The results show that the non-existence of wave nonlinearities and velocity skewness leads to offshore bar migration, while the inclusion of wave nonlinearities and velocity skewness leads to onshore bar migration in the field for low-energy wave conditions.

While the waves shoal, the symmetric shape of deep water waves starts to become asymmetric. The self interaction of a wave causes energy transfer between the wave with its higher harmonics and this causes the wave shape to be skewed as well as the orbital velocities.

Nonlinear wave theories, on the other hand, are capable of producing more realistic wave shapes. Consequently, there will be more accurate orbital velocity predictions leading to more accurate cross-shore sediment transport calculations. Some of these are Stokes wave theory, Stream Function Theory, Nonlinear Shallow water equations, Cnoidal wave theory, and Boussinesq wave theory. All these theories may be used to solve for the wave properties such as the surface water elevation, orbital velocities, pressure, trajectories, energy, etc. However, for some of them the range of applicability of the equations is a limitation.

Mathematical models based on higher order Boussinesq equations have recently been developed and demonstrated accurate predictions for both the velocity skewness and wave orbital velocities. However, these models are computationally expensive and may not be appropriate for all applications. Parametrization studies for both velocity skewness and wave orbital velocities have been done recently in which empirical formulations are developed.

Doering *et al.* (2000) developed an expression for velocity skewness using an evolutionary genetic algorithm analyzing more than 55,000 samples collected in the field. Their expression resulted in relatively accurate predictions for the velocity skewness considering the large amount of data used. The inclusion of skewness in a sediment transport model demonstrated its importance in predicting the shoreward sediment transport during periods of beach recovery.

Elfrink *et al.* (2006) parametrized the near-bed orbital velocities under irregular waves in shallow water in terms of important wave properties. They utilized an evolutionary genetic algorithm to derive an expression for the wave orbital velocities. The velocity skewness is then calculated using the predicted near-bed orbital velocities.

Doering and Bowen (1995) used bispectral analysis to parametrize horizontal and vertical asymmetry of waves in terms of the Ursell number. They suggested that the evolution of orbital velocities is not strongly dependent on the beach slope.

Isobe and Horikawa (1982) analyzed the wave shoaling using the fifth-order Stokes and third-order Cnoidal wave theories simultaneously. A semi-empirical theory is used to estimate the asymmetry of the velocity profile using two empirically driven parameters.

Swart and Loubster (1978) introduced the vocoidal wave theory for nonbreaking waves for application in all water depths. After an extensive analysis, the performance of 13 different wave theories is tested and it is shown that only the Vocoidal theory and Dean's stream function theory consistently yield good results in all water depths under consideration.

Kennedy *et al.* (2000) used a higher-order Boussinesq model to estimate wave properties. Their predictions for the asymmetry, a measure of left-right differences in a wave, and skewness, a measure of crest-trough shape, showed good agreement with the measurements. Their model reasonably simulated the increase in skewness during shoaling and breaking and the decrease in skewness as the waves approach the shore after breaking.

Elfrink *et al.* (1999) studied the effect of near-bed velocity skewness on cross-shore sediment transport. It was shown that a phase resolving method based on Boussinesq equations is able to produce both the velocity skewness and the sediment transport. The phase-averaged model based on Cnoidal, Vocoidal wave theories and the empirical formulation of Isobe and Horikawa are unable to reproduce the skewness and transport inside the surf zone.

Acceleration skewness

Because of the inconsistent predictions made by including the wave skewness as the only mechanism contributing to the onshore sediment transport, other mechanisms contributing to the onshore sediment transport and shoreward bar migration have been investigated. The most frequently investigated mechanism is the acceleration skewness (Elgar *et al.*, 2001; Hoefel and Elgar, 2003; Henderson *et al.*, 2004).

Asymmetrical wave orbital velocities result in skewed fluid accelerations with larger accelerations under the steep front face of the wave than under the gently sloping rear face. It is observed that the temporal variation of the location of bar crest closely follows the locations of near bottom orbital acceleration skewness maxima but not the velocity skewness maxima (Elgar *et al.*, 2001). The failed simulations of onshore bar migration events by the models incorporating the velocity skewness were simulated successfully by models incorporating the acceleration skewness instead (Hoefel and Elgar, 2003).

1.2.2.2 Wave-induced Momentum Flux and Stokes Drift

Henderson *et al.* (2004) investigated the effect of wave-induced momentum fluxes and the Stokes drift on onshore bar migration. A wave-resolving eddy-diffusive model of water and sediment motion in the bottom boundary layer is used, including the nonlinear advection by assuming no change in wave form. Their model predictions showed that asymmetry dependent transport alone does not lead to successful predictions of observed shoreward bar migration and, momentum fluxes and the Stokes drift are also required. Model runs with the nonlinear advective terms switched off showed that removal of advective terms from the momentum equation accounted for almost the half of the advectively induced flux. Therefore, a wave-generated flux of shoreward momentum is shown to encourage shoreward bar migration as previously suggested by Trowbridge and Young (1989). A further shoreward flux, most of which was due to the nonlinear advection of sediment by Stokes drift is also shown to contribute to shoreward bar migration.

1.3 Sediment Transport Models

The transport of sediment in the marine environment is hypothesized to take place in two modes. The first mode is the bed load transport which is the sliding, rolling or saltation of the material in the flow direction. This mode of transport occurs in a thin

layer over the stationary boundary at the bottom and the driving force is the grain-to-grain interaction. The second mode is the suspended load which is the transport of individual particles by the fluid flow away from the bottom. The driving force is the stress of the streaming fluid in which the particles are suspended. Field data and experimental studies show that sometimes one mode or the other is dominant, but both modes appear together in both nature and experimental conditions (Bagnold, 1966).

Many sediment transport models have been developed. Each model gives predictions of sediment transport rates. However, the assumptions undertaken during the development stages of a model restrict the applicability of that model to a range of conditions. For this reason, there is no consensus over a single sediment transport model which is applicable for all conditions. It is critical to review the range of models and decide on utilizing the most appropriate ones regarding the flow, geometry and physical conditions.

The earlier sediment transport models developed by hydraulic engineers are for river or open channel flow. Those models predict the sediment transport rates under the action of stream flow and tests about their accuracy show agreement with measurements under certain conditions. The nearshore region, on the other hand, contains much more complex flow conditions under the combined action of waves and currents which continuously changes the morphology. Coastal engineers found it useful to apply those models developed for open channel flow to the coastal regions with necessary modifications. Although those predictions give reasonable results for certain conditions, the complexity related with the flow makes it necessary to develop more sophisticated models describing the flow and sediment transport.

In order to make accurate predictions of the sediment transport rates for a variety of conditions, physics of sediment transport needs to be considered as much as possible. Many different types of models have been developed for the nearshore region.

These models might be classified according to the ideas that they have been developed upon. Here, some of those models that have been used in cross-shore sediment transport predictions are listed.

1.3.1 Energetics-Type Sediment Transport Models

Process-based energetics-type sediment transport models are used extensively in cross-shore sediment transport analyses and sandbar migration predictions. Bagnold (1966) derived a formula depending on the general physics and related the sediment transport to the water velocity for steady, two-dimensional stream flow in open channels. According to this model, the total transport rate is divided into bed and suspended load and both parts are related to the available stream power of the flowing fluid, a function of flow velocity, which causes the motion of sediment particles. The fluid flow is imitated as a mechanical device such that not all the available power can be consumed for the transport of sediment and efficiencies are defined to find that part of the power used for sediment transport. The model is tested extensively with field data and experimental findings. It is concluded that the model gives reasonable predictions for high stages of flow.

Bagnold's equations are shown to give reasonable results for river flows and flume experiments. In order to apply Bagnold's model in the nearshore environment, it is necessary to replace the stream flow velocity with the total velocity of nearshore flow that consists of the orbital velocity of progressive waves and the velocity of the mean currents. Other parameters in the equation, i.e. the efficiencies of bed load and suspended load, fall velocity and angle of repose of sediment particles, density of fluid, and the slope of bed are again provided according to the experimental or field conditions. Once the nearshore flow velocity is used, Bagnold's equation takes into account the waves and currents as the driving force of sediment transport. However, sediment particles tend to slide down a slope until equilibrium is reached, even in

the absence of the action of waves and currents. For that reason, it is recommended that a sediment transport model should include the gravitational effect of the bed slope (Bowen, 1980). Bagnold's equation is applied to the problem of onshore-offshore sediment transport on beaches. The oscillatory velocity of water waves is substituted to the velocity in the equation. It is shown that with necessary modifications and improvements, Bagnold's model is applicable to the marine environment. The wave reflection is also taken into consideration and it is shown that the bar formation is associated with the reflected or standing waves (Bowen, 1980).

Bailard and Inman (1981) developed a bed load sediment transport model for oscillatory flow based on Bagnold's equations. Their model consisted of two contributions to the transport of the bed material, one associated with the velocity of the fluid flow above the mobile bed and the other one associated with the gravitation pull. The velocity of fluid flow is constructed to include both the steady current and the oscillatory flow components. They predicted onshore-offshore sediment transport rate and showed that Bagnold's model is applicable to the sediment transport in the surf zone only for weak longshore currents and near-normal incidence of progressive waves.

Bailard (1981) extended Bailard and Inman (1981) to present a total load sediment transport model for time-varying flow over a plane sloping beach. A gravity induced component directed downslope is added to both bed load and suspended load transport rates of Bagnold's equation. Similar to the studies of Bailard and Inman (1981) and Bowen (1980), oscillatory flow velocity is introduced into the transport rate equations.

Ribberink (1998) developed a bed load transport formula based on the bed-shear concept of Meyer-Peter and Mueller (1948). The fundamental idea is to relate the sediment transport rate to the shear stress exerted by the fluid on the mobile bed. The developed formula was tested for steady, unidirectional flows observed in rivers

and oscillatory flow interacting with currents mostly observed in the nearshore environment. The idea is to develop a model that will predict the bed-load transport rates for both steady and unsteady flow regimes. However, it has limitations due to the existence of empirical parameters in the formula. For that reason, the application of the formula is limited to the conditions that are similar to those experimental conditions used for the development of the equation and the determination of empirical coefficients.

Watanabe (1993) developed a model that relates the sediment transport rate to the maximum instantaneous bottom shear stress for the combined waves and currents. The sediment transport is not divided into bed load and suspended load components but the total load is predicted. The main driving mechanisms that initiate and maintain the sediment transport are the waves and currents. It is assumed that the total shear stress applied on the bottom forces the sediment particles in motion and the total flow velocity advects these particles. Once the stress is described as a function of velocity, the transport rate becomes a function of the wave-averaged total flow velocity as in applications using Bagnold's equations.

Haas and Hanes (2004) developed a generic sediment transport formula based on the general principles of physics of the nearshore environment. The model is very similar to Watanabe's model. The main difference is the use of wave-averaged effective bed shear stress instead of the maximum shear stress. As a result, the sediment transport rate becomes a function of the third power of instantaneous flow velocity.

It is assumed in the vertical integration method of energetics-type sediment transport models that the instantaneous sediment transport rate is a function of the instantaneous near-bed velocities. The failure of these models is associated with the noninstantaneous response or strong vertical variations in sediment transport rate near the bottom. A transport formulation which uses a near bottom flow property

such as the asymmetry of accelerations is suggested to introduce the noninstantaneous response and results in improved results (Roelvink and Stive, 1989; Elgar *et al.*, 2001). Field observations of Elgar *et al.* (2001) supported this idea by showing that the spatial variation and corresponding cross-shore gradients of acceleration skewness are consistent with erosion offshore and accretion onshore of the bar crest. It is also shown that the location of the maximum of near-bottom cross-shore orbital velocity skewness usually was between the location of the sandbar and the shoreline, and was not correlated with the location of the bar crest. Inclusion of the effects of skewed accelerations in the energetics-based sediment transport model results in improved predictive skill, both for high-energy and low-energy conditions.

In order to study various transport mechanisms, the oscillatory velocity terms in these transport equations are further partitioned into low-frequency and high frequency components (Roelvink and Stive, 1989; Thornton *et al.*, 1996). According to those studies, the long-wave associated transport is generally smaller and directed offshore. The largest contribution by long waves is observed offshore over the bar due to the phase coupling with the short wave variance.

1.3.2 Concentration-Based Suspended Sediment Transport Models

The energetics-type sediment transport models predict the instantaneous response of sediment particles to the flow and estimates the sediment transport in an average sense in the vertical. However, in reality, both the sediment concentration and the flow velocity vary in the vertical. In order to take into account these variations, more sophisticated models are used.

A method to quantify the sediment transport rate when the suspended sediment transport is dominating is to use the concentration profile and the flow velocity along the water column. The concentration profile might be evaluated depending on the sediment characteristics through the fall velocity and flow characteristics through the

shear stress. Predictions of bar formation and migration using this method help to explain the summer and winter profiles with the variations in wave height, but due to the complexity of flow around the breakpoint, poor modeling of the flow velocity results in inaccurate transport rate predictions and bathymetric evolution modeling (Dally and Dean, 1984). A more sophisticated approach is to model the vertical distribution of suspended sediment concentration using the diffusion equation (Rouse, 1937).

Bakker (1974) extended Rouse's study for open channel flow to oscillatory flows and solved the diffusion equation for velocities and sediment concentrations inside and outside the wave boundary layer. Later studies (Nielsen, 1992) solving the diffusion equation utilized different bottom boundary conditions and reference concentrations and also introduced a pick-up function to define a rate of sediment pickup from the bottom instead of using a reference concentration. Nielsen (1992) added a convection mechanism to the diffusion models to develop a combined diffusion-convection model.

The velocity distribution in the water column needs to be modeled by a quasi-3D or 3D nearshore circulation model for the current flow and by a refraction-diffraction model for the wave flow simultaneously. The sediment flux along the water column is found by multiplying the concentration with the velocity and then integrating across the water column in order to calculate the sediment transport rate. This transport rate corresponds to that of the suspended sediment particles only. However, in most cases, there is a bed load at the bottom and especially most of the sediment transport takes place in a thin layer called the sheet flow layer. Moreover, the suggested transport model does not work for high concentrations which are generally found near the bed. Therefore, it is necessary to couple this model with another model which resolves the sediment transport in the thin layer on top of the stationary boundary. Most of the bed load is believed to happen in the boundary layer. A boundary layer model may be used to solve for the flow in the boundary layer and then coupled with

a separate sheet-flow model (Demir, 2007).

1.3.3 Two-Phase Models

Energetics-based and concentration-based sediment transport models do not account for fluid-particle and particle-particle interactions. More sophisticated techniques for estimating the sediment transport in the nearshore environment accounting for those interactions are two-phase flow models.

In recent years, several two-phase flow modeling techniques have been developed. Asano (1991) proposed a partial two-phase flow model in which the vertical velocity of particles was approximated by an empirical expression. Li and Sawamoto (1995) formulated a complete set of two-phase flow equations. Gotoh and Sakai (1997) presented a numerical simulation of the sediment transport and flow kinematics with a closure for particle-particle interactions in the sheet flow regime. Dong and Zhang (1999) proposed a complete two-phase flow model that simulates the fluid and sediment motions in the sheet flow regime under oscillatory flow conditions. All major forcing terms such as the fluid-particle and particle-particle interactions and the turbulent stresses are included in their model.

Hsu *et al.* (2003) introduced a two-phase model to calculate the sediment concentration and velocity profiles. Boundary layer approximations were adopted in a semianalytical approach and concentration profiles that improve upon the single-phase Rouse formula were obtained. Hsu *et al.* (2004) used the same two-phase flow model with a collisional theory to study sheet-flow over a mobile bed. The flow in the region of high concentration over the stationary bed and several features of sheet flow are studied. Amoudry *et al.* (2008) uses the model to provide information in the near-bed region where the transition from the solid-like to the fluid-like behavior of sediment particles is resolved to evaluate both the bed load layer thickness and bed load transport rate.

1.3.4 Stochastic Sediment Transport Models

In certain cases, it is necessary to get predictions of morphological changes on a decadal time-scale for coastal zone management. The sediment transport calculations are driven with stochastic hydrology models for such simulations. Using such an approach, the sediment transport rate estimates are based on the natural variability of characteristics in the study area. Singer and Dunne (2004) made decadal simulations of sediment fluxes at the Sacramento River channel network. Many studies have been done on long term simulations and the inaccuracies involved in them. Wilcock (1992) focused on the effect of bed shear stress and Paola and Seal (1995) investigated the sensitivity of models to grain size distributions.

1.4 Wave Dissipation Models

Waves and currents generate the main driving forces causing morphological changes and beach deformation. Waves not only drive the currents in the nearshore environment but also transport sediment. Radiation stresses, volume fluxes and energy dissipation are some of the major wave properties which are proportional to the square of wave height in the surf zone. Those parameters and their gradients affect the set-up/set-down variation, current estimations and ultimately the sediment transport and morphological changes. For this reason, an accurate prediction of the wave field is important in numerical models.

Many numerical models have been developed to predict the transformation of waves inside the surf zone. Most of these models solve the energy flux balance equation (Battjes and Janssen, 1978; Thornton and Guza, 1983). In this equation, the cross-shore gradient of the cross-shore wave energy flux is assumed equal to the local mean rate of energy dissipation. As the waves propagate towards the shore, they become steeper and eventually break. Wave breaking dominates the dissipation of wave energy and the wave height decreases mainly due to breaking rather than due to bottom

friction (Thornton and Guza, 1983). The description of energy dissipation is very important for accurate predictions of the wave field, especially on non-monotonic beaches with alongshore sandbars.

The first class of models for wave energy dissipation due to breaking is parametric models. In this class of models, the dissipation of a broken wave is estimated as a propagating bore of corresponding height. It is required to specify which waves are breaking in order to calculate the dissipation. The breaker height is assumed to be proportional to the water depth at any location. But, a specific breakpoint may not be defined for random wave fields and only a fraction of waves break at a given location. The higher waves break earlier than the lower waves and eventually all waves break close to the shoreline. A Rayleigh-type wave height distribution is used and the fraction of breaking waves is estimated by using the corresponding probability distribution function. The dissipation is then calculated by multiplying dissipation estimated from the bore dissipation by the fraction of breaking waves. The way this type of models handles the probability distribution of wave heights and the fraction of breaking wave calculations varies. While some of the models use a truncated Rayleigh distribution and estimate the fraction of breaking waves accordingly (Battjes and Janssen, 1978; Battjes and Stive, 1985), other models use the full Rayleigh distribution of surf zone wave heights. The breaking wave distributions are written as a weighting of the Rayleigh distribution for all waves. The average rate of energy dissipation is then calculated by multiplying the dissipation for a single broken wave by the probability of breaking and then integrating for all waves (Thornton and Guza, 1983; Baldock *et al.*, 1998; Ruessink *et al.*, 2003; Janssen and Battjes, 2007).

Another class of energy dissipation models is the representative wave approach. In this approach the energy dissipation model for a regular wave is applied to irregular waves by using representative regular waves with equivalent wave height. The energy dissipation of a regular wave is estimated either by the bore concept, which is also

used in parametric approaches, or a stable energy concept in which the energy dissipation rate is considered proportional to the difference between the local energy flux and a stable energy flux (Dally *et al.*, 1985). In the representative wave approach, dissipation of energy is turned on when wave height reaches a breaker wave height and turned off when the local energy flux reaches a stable energy flux (Rattanapitikon *et al.*, 2003).

Spectral wave models simulate the transformation of a wave spectrum using multiple frequency and directional components. Generally, a parametric approach is incorporated for the energy dissipation due to breaking waves in phase-averaged spectral models. This imposes the same amount of dissipation for each spectral component and the shape of the wave spectrum is retained for the entire domain for linear approaches. Nonlinear approaches describe the dissipation as a function of frequencies and the transfer of energy between different wave harmonics may be captured (Mase and Kirby, 1993; Kaihatu and Kirby, 1995; Kirby and Kaihatu, 1997). Another method of incorporating the dissipation in spectral models is to formulate it in a spectral form and distribute the random-wave energy dissipation over the frequency spectrum (Eldeberky and Battjes, 1996).

1.5 Undertow Models

The undertow current is one of the main forcing agents for the sediment transport in the nearshore environment. As mentioned in the earlier sections, it plays an important role in the formation and the offshore migration of a bar. Dyhr-Nielsen and Sørensen (1970), Wright *et al.* (1982), Guza and Thornton (1985) and Greenwood and Osborne (1990) measured the undertow current in the field. Svendsen (1984a), Dally and Dean (1984), Svendsen *et al.* (1987), Svendsen and Hansen (1988), Okayasu *et al.* (1988) and Putrevu and Svendsen (1993) are some of the studies analysing it theoretically while Faria *et al.* (2000) and Rattanapitikon and Shibayama (2000) analysed it numerically.

Svendsen (1984a) studied the mechanisms responsible for the undertow. In his paper, Svendsen argued that the mass of water carried shoreward by the breaking waves in the surf zone will be compensated by a seaward return flow, the undertow. Considering the mass balance, it is shown that the mean return current in the cross-shore direction is related to the Stokes drift. The depth-integrated, wave-averaged horizontal momentum equation in the cross-shore direction gives the relationship between the radiation stress gradient, the wave set-up pressure gradient and the turbulent stresses. It is through the turbulent stresses that the depth variation of the undertow velocity is introduced. Therefore, the imbalance between the wave setup pressure gradient and the depth-varying radiation stress gradient is the driving mechanism of the undertow.

The turbulent front of a continuously breaking wave in which water is tumbling down towards the trough, as the wave propagates, is called the roller. Svendsen (1984a) used a uniform velocity distribution inside the roller with a magnitude equal to the wave celerity, and outside the roller, with a magnitude equal to the horizontal particle velocity. Earlier, Svendsen (1984b) showed that the roller has a significant contribution to the radiation stresses. Svendsen (1984a) showed that it causes a significant increase in wave volume fluxes as well, eventually influencing the undertow.

Faria *et al.* (2000) modeled the undertow profile over a barred beach and made comparisons with field measurements. The vertical structure of the undertow is modeled using a turbulent eddy-viscosity closure model. In this study, the cross-shore and vertical variation of the eddy viscosity and the corresponding change in the undertow profile are investigated. It is observed that the maximum undertow is on top of or on the shoreward slope of the bar. Due to the strong undertow, they observed an offshore migration of the bar during their 2-day field experiment period. The cross-shore momentum is discussed and the contributions from the radiation stress gradient, setup gradient and mean momentum flux gradient to the undertow forcing

were investigated. Initially a constant eddy viscosity, and then a depth varying eddy viscosity formulation was used in their eddy viscosity model. It is concluded that a depth-dependent eddy viscosity model does not substantially improve the description of the vertical structure of the undertow. They relate the largest errors in the vertical profile of mean undertow to the failure of existing models to predict correctly the surface mass flux in breaking waves.

Kuriyama and Nakatsukasa (2000) developed a one-dimensional model for undertow. A different roller model was used in which the velocity linearly varies in the roller and the roller area not only depends on the square of wave height but is also limited by the maximum energy available to be transferred from the wave motion. The undertow velocity is calculated on a wave-by-wave basis from the volume flux due to the organized wave motion and due to the surface roller. The study investigates the effect of different roller and roller velocity descriptions on the undertow and compare the findings with laboratory and field experiments as well as other results from De Vriend and Stive (1987) and Reniers and Battjes (1997). An empirical coefficient was used to relate the roller area to the square of wave height and this coefficient is calibrated using measurements. A constant value was used as a first approximation and a formula depending on the surf similarity parameter is used. It is shown for some cases the rectangular-shaped distribution of the time averaged velocity above the wave-trough level is inappropriate, while for other cases it gives good approximations. For that reason further and more detailed investigations on the roller structure and development were proposed.

Rattanapitikon and Shibayama (2000) developed a simple model for the undertow profile by using an eddy viscosity approach based on a re-analysis of the existing undertow models and experimental results. In their model, the eddy viscosity coefficient and the shear stress depend on the rate of energy dissipation due to wave breaking. The surf zone is divided into a transition zone and an inner zone and the undertow in

these two zones is discussed separately. The mean velocity components due to waves and the roller are calculated separately and used in the calculation of the undertow current velocity as a boundary condition. The performance of various formulas for computing the mean velocity due to wave motion and due to roller is investigated and the appropriate one comparing with the collected experimental results is developed.

As discussed by Putrevu and Svendsen (1993), the undertow profiles inside and outside the surf zone are quite different because the forcing is different. There is an onshore flow due to waves inside the boundary layer which is called the steady streaming. It was found that the steady streaming plays an important role outside the surf zone.

1.6 Process-based Profile Models

Process-based models incorporate important physical mechanisms affecting fluid flow and sediment transport in the nearshore environment while profile models are used to simulate the cross-shore sediment transport when alongshore nonuniformities are negligible.

Southgate and Nairn (1993) and Nairn and Southgate (1993) introduced a full numerical model system to simulate the waves, currents, sediment transport and beach profile development. The model used an energetics-based sediment transport formula and introduced refinements to the efficiency factors and to the friction factor by enhancing it for sheet-flow conditions. The model was used to simulate onshore and offshore sediment transport over a beach with only one bar as well as a multi-barred beach. The model was observed to perform well for the test cases with reasonable errors.

Thornton *et al.* (1996) studied the bar/trough generation over a natural beach using an energetics-based sediment transport formula. The sediment eroded by the strong longshore current was predicted to be carried offshore by the undertow current

in the cross-shore. Outside the surf zone, the onshore transport by the skewed waves was estimated to overcome the weaker undertow current, resulting in net onshore transport. The model was observed to perform well for the offshore bar migration case but gave inconsistent results for the onshore bar migration cases under mild conditions. Gallagher *et al.* (1998) followed Thornton *et al.* (1996) and used a similar model for modeling sandbar evolution. The model performed well for an offshore bar migration case but could not predict the observed onshore bar migration in the field. The reason for the failure to predict the onshore bar migration cases was predicted to be either not including the fluid accelerations or neglecting the phase lag between the fluid and sediment flow.

Van Rijn *et al.* (2003) compared five process-based morphodynamic models for their ability to predict profile changes at storm and seasonal scales. The performance of UNIBEST-TC (Bosboom *et al.*, 1997), COSMOS (Nairn and Southgate, 1993), CROSMOR2000 (Van Rijn, 2000), BEACH 1/3D (O'Connor *et al.*, 1998) and CIIRC (Sierra *et al.*, 1997) in predicting the waves and currents as well as sediment transport and bed evolution was tested by comparing with hydrodynamics and morphodynamics data from laboratory and field studies on storm and seasonal time scales. The models were observed to perform well for wave height predictions after proper calibration; however, none of the models were observed to predict the relatively large reduction in wave height in the inner bar zone. The current predictions of the models were also reasonable, except an underprediction of the peak current values in the surf zone. All the models were observed to predict the offshore bar movement events quite well except for discrepancies in the beach zone. Those models using non-linear wave theories were observed to predict the near-bed orbital velocities and asymmetry in a sufficiently accurate way leading to successful simulations of onshore bar migration on seasonal time scales.

Van Rijn (1998) studied the effect of sand decomposition for accretive events using the CROSMOR model and showed the effect of fine and coarse sands on sediment transport and profile evolution. Van Rijn *et al.* (2007) studied nearshore bar migration with sediment transport formulas of using the CROSMOR model. The latter was observed to produce reasonable results with the waves-alone case only, ignoring the undertow current while the former was capable of reasonably predicting the offshore bar migration case. However, none of them predicted the onshore bar migration case accurately due to a lack of accurate predictions of near-bed orbital velocities.

1.7 Scope of this study

The purpose of this study is to expand the body of knowledge about physical processes on barred beaches and to enhance an existing numerical model to enable it to perform accurate bar migration simulations. Both the hydrodynamics and morphodynamics on barred beaches are studied by means of a process-based numerical model system. The two major goals of the study are to investigate the effect of physical processes on bar migration events and to enhance the numerical model in order to accomplish realistic simulations of bar migration events.

The first step in understanding the physics of cross-shore sediment transport on barred beaches is to understand the hydrodynamics in the nearshore environment. The sediment transport is initiated by the mobilization of sediment particles resting on the bottom. The force generated by the waves and currents is the major physical agent affecting this initiation and also the continuation of sediment transport. The mechanisms associated with the waves and currents such as near-bottom orbital wave velocities, and undertow currents also have an effect on cross-shore sediment transport and bar migration.

An existing state of the art numerical model system is used in this study. The model system has not been developed specifically for studying dynamics on barred

beaches or cross-shore sediment transport with bar migration. Therefore, necessary changes are done in the model to incorporate all the relevant processes for barred beaches. Both the hydrodynamics and the morphodynamics parts of the model are studied and modified in order to improve the representation of the physics. The existing numerical model system and the modifications and enhancements made in this study are presented in Chapter 2.

The numerical model system is used as a tool for understanding the hydrodynamics of the nearshore environment. The main parameters under consideration are the cross-shore variations of wave height, mean water level, near-bottom orbital velocity skewness and depth-varying undertow current. As the hydrodynamics of the nearshore environment are studied, the effects of different hydrodynamics parameters are investigated. Some of these parameters are the surface shape parameter, the breaking wave parameters, the eddy viscosity, the roller component, the near-bed orbital velocity skewness and the depth structure of currents. The model predictions are compared to results from laboratory experiments conducted in Delta Flume within the framework of the European Large Installation Plan, LIP, and the results are presented in Chapter 3.

Chapter 4 presents the numerical simulations for the bar migration events observed during the Delta Flume experiments focusing on bar movements on storm time scales. It is important to make accurate sediment transport estimations in order to be able to make accurate morphological simulations. The performance of sediment transport formulas are studied compared to measurements. The transport due to waves is compared to the transport due to the currents using an energetics-based sediment transport formula. The effect of the enhancements made for the hydrodynamic predictions of the model on sediment transport and morphodynamics are investigated. The role of the introduced physical mechanisms, i.e. persistence length and roller lag methods as well as the roller itself, during offshore and onshore bar

migration events is studied to better understand the physics involved in nearshore bar migration events.

The final chapter makes a conclusion of the study summarizing the findings. Suggestions as to the directions for continued development are offered.

CHAPTER II

MODEL DESCRIPTION

This chapter describes the numerical model system and outlines the governing equations. The first section gives an overview of the numerical model and describes the interactions between different modules.

The second section describes the governing equations for the wave module. The energy decay mechanism and the roller model are explained in detail. A new method accounting for the persistence of breaking waves is introduced. The parameterization method used for near-bed orbital wave velocity calculations is described.

The third section describes the governing equations for the circulation module. The time-averaged and depth-integrated mass and momentum equations are outlined. The governing equations for the vertical variations of the currents are given in detail. This method follows Haas and Svendsen (2000) but utilizes a modified description of the wave forcing for the currents. The sediment transport formulas that are utilized are listed and explained in detail.

The final section outlines the equations for the morphology module. The numerical scheme solving the sediment conservation equation is explained in detail.

2.1 Numerical Model

The numerical model used in this study is part of the Nearshore Community Model (NearCoM), developed as part of the National Oceanographic Partnership Program, (NOPP). The model consists of three modules computing the waves, circulation and morphodynamics simultaneously. The wave module and the circulation module are coupled together in order to solve the hydrodynamics. The sediment transport fluxes are calculated in the circulation module and are fed into the morphology module

which solves for the morphological changes.

A master program controls time stepping of the model system, the application of individual modules as well as the flow of information between the modules. The user defines total time for the model run, the time stepping interval, the repetition intervals of each module and the controls for the interactions between modules in an input file for the master program. During the time stepping, the three main modules of the model work consecutively according to the repetition intervals defined in the input file of the master program.

Although the three modules of the model work consecutively, the coupling of the modules enables them to act seamlessly as a single model. The modules of the numerical model are coupled together through wave-current interaction, wave-bed interaction and current-bed interaction. The interactions allow each module to use variables computed in the other modules.

2.2 Wave Module

REF/DIF-S (Kirby *et al.*, 2004) is used as the wave module of the numerical model. It is the spectral extension of the combined refraction and diffraction model, REF/DIF-1, for the case where a directional spectral sea is simulated. It accounts for the refraction, shoaling, energy dissipation and diffraction processes to predict the wave field. The wave module solves for the short wave component of the flow.

REF/DIF-S is a parabolic model based on the mild-slope equation of Berkhoff (1972), given as

$$\nabla_h \cdot (CC_g \nabla_h \eta) + \sigma^2 \frac{C_g}{C} \eta = 0 \tag{2}$$

in which η is the surface displacement, σ is the angular frequency of waves found from the linear wave theory dispersion relationship given as

$$\sigma = \sqrt{gk \tanh kh}, \tag{3}$$

k is the local wave number, h is the local water depth, g is the gravitational acceleration, C is the wave celerity (angular frequency over the wave number) and C_g is the group velocity,

$$C_g = \frac{C}{2}\left(1 + \frac{2kh}{sinhkh}\right). \tag{4}$$

The model REF/DIF-S computes the shoreward evolution of a directional wave spectrum using a number of frequency and direction components representing a random sea. The initial wave conditions at the offshore boundary of the domain are required and the model marches forward in space solving the mild slope equation for each possible frequency and direction combination until the shoreward end of the grid. The model can be written in terms of the complex amplitude of the free surface, A_n, as

$$C_{gn}A_{n,x} + QA_n + RA_{n,yy} + SA_{n,xy} + TA_{n,yyx} + \alpha_d A_n = 0 \tag{5}$$

where Q_a, R_a, S_a and T_a includes all transformation and wave-current interaction terms. The subscript n denotes a component with specific frequency and direction, subscripts x and y refer to partial differentiation and α_d is the dissipation term. Equation 5 is solved for all frequency and directional component combinations at each forward step. The parabolic model is solved with the finite difference method and an implicit Crank-Nicholson scheme is used to get accurate results. The nonlinear terms are treated with a two-pass iterative technique.

A periodic boundary condition is used for lateral boundaries. The energy dissipation may be calculated differently for laminar bottom boundary layers, turbulent bottom boundary layers, porous bottom and wave breaking. The details for the energy dissipation due to wave breaking are given in the next subsection. The bottom boundary layer is generally turbulent under field conditions and the dissipation for the turbulent bottom boundary layer is included in model computations. The dissipation term is then written as

$$w_{BL} = \frac{2\sigma k f_w |A|}{3\pi \sinh 2kh \sinh kh} \tag{6}$$

where A, k, σ and h were defined above and f_w is the friction factor. The friction factor may be calculated by using different formulas most of which depend on the roughness of the bed. The main formula used in this analysis for friction factor predictions is Swart's formula

$$f_w = exp(5.213(\frac{r}{A_w})^{0.194} - 5.977) \tag{7}$$

where r is the bed roughness and A_w is the amplitude of the nearbed orbital trajectory. The r value is described as $2.5d_{50}$ for steady flows but a value between $100d_{50}$ and $1000d_{50}$ is recommended for oscillatory flows (Nielsen, 1992).

Sandy seafloors are porous and the wave flow may penetrate the bottom resulting in wave damping. Therefore, the dissipation due to a porous bottom is also included in model computations. Further details of the wave module may be found in Kirby *et al.* (2004).

2.2.1 Energy Decay Mechanism

In the standard version of REF/DIF-S, an energy decay mechanism is used and the energy balance is defined as

$$\frac{dEC_g}{dx} = -D \tag{8}$$

where E is the energy density of the organized wave motion, C_g is the group velocity and D is the dissipation.

A choice between two formulations for the energy dissipation due to breaking is offered in the wave module. The first one by Battjes and Janssen (1978), denoted hereafter as *BJ78*, estimates the energy dissipation rate in a broken wave from that in a bore of corresponding height. The dissipation per unit area, D, for periodic waves with frequency, f, may then be written as

$$D = \frac{1}{4} f \rho g \frac{H^3}{h} \tag{9}$$

where g is gravitational acceleration, H is wave height, h is water depth and ρ is the fluid density.

In a random wave field, only a fraction of the waves break and the dissipation has to be calculated accordingly. *BJ78* assumed that all the breaking waves have a height equal to maximum possible wave height, H_m, attained right before breaking and use a probability of occurrence of those waves, Q_b, which is also called the fraction of breaking waves, to obtain the overall mean dissipation rate per area as

$$D = \frac{\alpha_{BJ}}{4}\overline{f}\rho g\frac{H_m^3}{h}Q_b \tag{10}$$

where $\overline{f}$ is the mean frequency of the energy spectrum used as a representative value of f. The value of α is a constant representing the intensity of breaking and relating the dissipation due to breaking to the dissipation in a bore. The ratio H_m/h is considered to be on the order of one in the region where most of the dissipation occurs and the equation reduces to

$$D = \frac{\alpha_{BJ}}{4}\overline{f}\rho g H_m^2 Q_b. \tag{11}$$

The Miche's breaking criterion is adopted to estimate the maximum wave height of periodic waves of constant form (Miche, 1944), as

$$H_m = \frac{0.88}{k}\tanh(\frac{\gamma\, k\, h}{0.88}) \tag{12}$$

where γ is an adjustable coefficient which reduces to the wave height to water depth ratio at breaking, H_m/h in shallow water.

Earlier studies showed that non-breaking, deep water waves may be well approximated by a Rayleigh wave height distribution assuming that the random wave motion is a narrow-banded, linear Gaussian process (Longuet-Higgins, 1952; Goda, 2000). *BJ78* assumed the probability distribution of wave heights, $Pr(H)$ to be of Rayleigh-type throughout the surf zone, with a truncation at $H = H_m$. The truncation implies that all the breaking or broken waves have the same maximum possible wave height,

H_m. The fraction of breaking waves is calculated by using the probability of a given wave to be associated with breaking or broken waves. $Q_b = Pr(H = H_m)$ is found as a function of H_{rms}/H_m from

$$\frac{1 - Q_b}{\ln Q_b} = -\left(\frac{H_{rms}}{H_m}\right)^2. \tag{13}$$

The second energy dissipation mechanism by Thornton and Guza (1983), denoted hereafter as *TG83*, models the energy dissipation in a breaking wave after a periodic bore similar to *BJ78*. The energy dissipation per unit area of a breaking or broken wave, D, is written as

$$D = \frac{\overline{f}}{4}\rho g \frac{(BH)^3}{h} \tag{14}$$

where B is a breaking wave coefficient representing the intensity of breaking. A value of 1 for B indicates that the dissipation of a breaking wave is equivalent to the dissipation of a periodic bore. One of the major differences between the *BJ78* and *TG83* approaches is the formulation of energy dissipation. *TG83* retains the original form of the dissipation equation [Equation 10] following the bore approach and the energy dissipation is proportional to H^3/h as given in Equation 14. On the other hand, *BJ78* assumes that H_m/h is equal to 1 in the surfzone and the energy dissipation reduces to be a function of H^2 as given in Equation 12.

According to *TG83*, the average rate of energy dissipation is then calculated by taking the ensemble average of the product of the dissipation of each broken wave with the probability of wave breaking at that given wave height, $P_b(H)$, written as

$$D = \frac{B^3}{4}\rho g \frac{\overline{f}}{h} \int_0^\infty \left(H^3\right) P_b(H) dH. \tag{15}$$

The observations of *TG83* show that the Rayleigh distribution can be used as a reasonable description of waves even in the surf zone. The Rayleigh probability distribution function is defined as (Thornton and Guza, 1983, Equation (11))

$$P(H) = \frac{2H}{H_{rms}^2} \exp\left[-\left(\frac{H}{H_{rms}}\right)^2\right]. \tag{16}$$

Then, the probability distribution of breaking waves is found by weighting of the Rayleigh distribution for all waves

$$P_b(H) = W(H)P(H). \tag{17}$$

The weighting function $W(H)$ is initially defined as

$$W(H) = \left(\frac{H_{rms}}{\gamma\, h}\right)^n \tag{18}$$

where H_{rms} is the root-mean-square wave height and n is a constant determined as 4 from observations. Another definition which more heavily weights the larger waves is

$$W(H) = \left(\frac{H_{rms}}{\gamma\, h}\right)^n \left[1 - \exp\left(-\left(\frac{H}{\gamma\, h}\right)^2\right)\right]. \tag{19}$$

After substituting weighting functions, Equation 18 or Equation 19, into $P_b(H)$ [Equation 17] and inserting results into D [Equation 15] yields

$$D = \frac{3\sqrt{\pi}}{16}\rho g \frac{B^3\overline{f}}{\gamma^4 h^5} H_{rms}^7 \tag{20}$$

or

$$D = \frac{3\sqrt{\pi}}{16}\rho g B^3 \overline{f} \frac{H_{rms}^5}{\gamma^2 h^3}\left[1 - \frac{1}{\left(1 + (H_{rms}/\gamma\, h)^2\right)^{5/2}}\right] \tag{21}$$

respectively.

Both parametric wave models described above introduce two free parameters in the dissipation calculations. The coefficient B in *TG83* [Equation 15] and, the coefficient α in *BJ*78 [Equation 10] account for the different breaker types and represent the intensity of breaking. The coefficient γ in Equation 20 and Equation 21 is the wave height to water depth ratio inside the surf zone. These earlier models use constant values for both coefficients (Thornton and Guza, 1983; Battjes and Janssen, 1978). Later studies showed that they are in fact interdependent on each other (Battjes and Stive, 1985; Lippmann *et al.*, 1996). The dependence of γ on beach slope, surf similarity parameter, deep-water wave steepness, relative water depth, and incident

wave steepness are investigated (Battjes and Stive, 1985; Sallenger and Holman, 1987; Baldock *et al.*, 1998; Ruessink *et al.*, 2003; Rattanapitikon, 2007; Alsina and Baldock, 2007; Janssen and Battjes, 2007; Apotsos *et al.*, 2008). A slight but systematic dependence on the deep water steepness was observed and a formula was developed after a calibration effort and used in different models. Since the model is stationary in time, deep-water wave steepness is a constant value for all points on a cross-shore transect, that is why this varying gamma function does not introduce a spatial variability but only a temporal variability. A strong correlation of γ with relative water depth was also observed. A least-square linear fit by Ruessink *et al.* (2003) yields a formulation of γ written as

$$\gamma = 0.76kh + 0.29 \tag{22}$$

in terms of relative water depth, kh, which varies in the cross-shore.

The free parameters used in the models vary for different wave conditions. Extensive data sets were collected to evaluate and improve the values and formulations of the free parameters used in the dissipation models. The purpose of these efforts is to increase the model-data agreement by calibrating the constant coefficients to their optimal values minimizing the errors in wave height predictions (Rattanapitikon, 2007; Apotsos *et al.*, 2008).

In the standard version of REF/DIF-S, the *TG83* wave model of Equation 21 is used and both γ and B are described as constants. Since Equation 21 introduces an empirical formulation to account for the effect of larger waves, it has been decided to use Equation 20 in this study which leads to an analytical solution. It is shown that γ and B may be reduced into a single constant, Y, given as

$$Y = \frac{B^3}{\gamma^4}. \tag{23}$$

The need for a spatially varying Y is shown and the variability is introduced by Equation 22 for γ while B is kept constant.

2.2.2 The Persistence Length Method

Wave breaking over non-monotonic beach profiles, such as barred beaches, frequently occurs offshore of the bar crest, followed by secondary breaking at the onshore end of the trough. Both the *BJ78* and *TG83* methods estimate the energy dissipation due to wave breaking in terms of local values of wave height and water depth. For this reason, as the water depth increases from the bar crest into the trough, their formulation results in an immediate decrease of the fraction of breaking waves and the energy dissipation. This results in a reduction of the rate of decrease of important wave properties, i.e. wave height, radiation stress, volume flux, etc.

In reality, the dissipation does not cease immediately as the broken waves propagate towards the shore and measurements show that wave height continues to decrease well into the trough zone (S.-Arcilla *et al.*, 1994; Rivero *et al.*, 1994). This shows a weakness of parametric models of the *BJ78* and *TG83* type. The discrepancies in wave amplitude/height variations, especially in the vicinity of the bar-trough zone, may lead to erroneous estimations of the values and gradients of radiation stresses, volume fluxes, currents, and sediment transport which controls the morphological changes and bar migration calculations. For these reasons, it is crucial to make necessary improvements in the default *TG83* model in order to enhance the model performance. A method to include the breaking wave persistence has been developed based on the model of Southgate and Wallace (1994) to improve the energy dissipation description as well as wave field predictions of the model.

Southgate and Wallace (1994), hereafter referred as *SW94*, proposed a method to improve the predictions for the fraction of breaking waves in dissipation models by introducing the persistence of breaking waves over a distance. According to their method, broken waves are assumed to persist and contribute to the fraction of breaking waves at those points shoreward of their initial breaking within a given persistence length proportional to the wave height of broken waves. Therefore, the fraction of

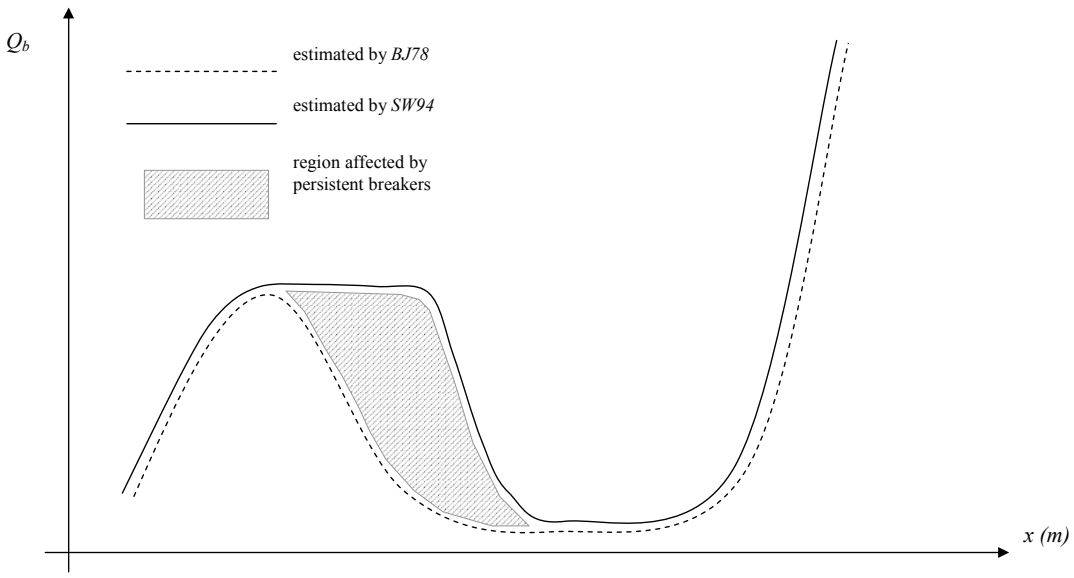

Figure 1: Schematic variation of fraction of breaking waves on a barred beach and the effect of breaking wave persistence.

persisting breaking waves at any point of interest, x_i, on a cross-shore profile is calculated as the sum of the fraction of newly breaking waves at points seaward of x_i, within the persistence length. The fraction of newly breaking waves at the point of interest, x_i, is calculated as the difference between the fraction of breaking waves estimated by the *BJ78* formulation, and the fraction of persisting breaking waves. However, if the fraction of persisting breaking waves exceeds the amount estimated by the *BJ78* formulation, the fraction of newly breaking waves is considered as none. Finally, the total fraction of breaking waves is defined as the sum of newly breaking waves and persisting breaking waves. Figure 1 shows an example variation of the fraction of breaking waves on a barred beach and the effect of the *SW94* method.

Even if the *SW94* method improves the dissipation description by improving the fraction of breaking wave estimations, the way that the newly breaking waves are described may lead to errors. The fraction of newly breaking waves may be overestimated resulting in erroneous estimations of the fraction of persisting breaking waves as well as the total fraction of breaking waves. Furthermore, *SW94* leads to a

sharp reduction in the total fraction of breaking waves once the persistence shuts off. Therefore, a new model is developed in this study to improve the estimations of the fraction of breaking waves and eventually enhancing the predictions for the energy dissipation over non-monotonic beach profiles.

The fraction of breaking waves is calculated by integrating the probability distribution of breaking waves over all possible wave heights:

$$Q_b = \int_0^\infty P_b(H) dH \tag{24}$$

$Q_{b,TG83}$ is found after $P_b(H)$ [Equation 17] is substituted in Equation 24 as

$$Q_{b,TG83} = \frac{H_{rms}^4}{\gamma^4 h^4}. \tag{25}$$

The dissipation may then be re-written in terms of the fraction of breaking waves as

$$D = \frac{3\sqrt{\pi}}{16} \rho g B^3 \overline{f} \frac{H_{rms}^3}{h} Q_{b,TG83}. \tag{26}$$

The assumption is that Equation 25 predicts the percent of waves that are breaking purely due to local effects disregarding any previously breaking waves. Therefore, at any point of interest, i, in a cross-shore transect, the fraction of newly breaking waves, $Q_{b,new}^i$ is estimated by using

$$Q_{b,new}^i = \frac{1}{2} \left[\left(Q_{b,TG83}^i - Q_{b,tot}^{i-1} \right) + \left| Q_{b,TG83}^i - Q_{b,tot}^{i-1} \right| \right] \tag{27}$$

where $Q_{b,TG83}^i$ is the fraction of breaking waves estimated by *TG83* at point i, and $Q_{b,tot}^{i-1}$ is the total fraction of breaking waves, at the previous point, $i-1$. According to this formulation, if the *TG83* predicted fraction is larger than the previous total fraction, then the new fraction is simply the difference of the two and represents the increase in total fraction of breaking waves. If the *TG83* predicted fraction is smaller than the previous total fraction, the new fraction is zero.

It is assumed that any newly breaking wave will persist for a certain length and contribute to the dissipation in shoreward locations while continuing to break. Therefore, the percent of persistent breakers, $Q^i_{b,per}$, is calculated as the sum of the fraction of newly breaking waves at all those earlier points, j, within the persistence length, L^j_b, such that $x_j - x_i < L^j_b$, using

$$Q^i_{b,per} = \sum_j Q^j_{b,new}. \tag{28}$$

SW94 defines the persistence length as a factor of wave height. However, the persistence of breakers is expected to be not just a function of wave height but more likely a function of the intensity of breaking. Therefore, the persistence length, here, is initially defined as a function of deep water wave steepness and significant wave height.

$$L^j_b = C_p(H_o/L_o)H_o \tag{29}$$

where C_p is the persistence length calibration constant and $L_o = gT^2/2\pi$ with T as the wave period.

Finally, Equation 29 is converted to a function of local parameters using the shoaling coefficient equation to write deep water wave height as

$$H_{so} = H^j_s\sqrt{\frac{C_g}{C_{go}}} \tag{30}$$

where

$$C_g = \frac{1}{2}c(1+G) \tag{31}$$

with $c = 2\pi/kT$ and $G = 2kh/sinh2kh$. As a result, the persistence length, L^j_b is written as

$$L^j_b = C_p\frac{8\pi^4(1+G)(H^j_s)^2}{g^2kT^4} \tag{32}$$

where, n is the ratio of group velocity to wave celerity, and H^j_s is the significant wave height at point j. The total fraction of breaking waves is then calculated as

$$Q^i_{b,tot} = \min\left\{\left(Q^i_{b,TG83} + Q^i_{b,per}\right), \left(Q^{i-1}_{b,tot} + Q^i_{b,new}\right)\right\}. \tag{33}$$

The minimization prevents the total fraction of breaking waves at any grid point x_i from exceeding the total fraction of breaking waves at a grid point offshore of x_i due to persistence alone, and prevents the total fraction of breaking waves at a given point to exceed the value of 1 due to the persisting breakers alone. It also provides a gradual decrease of the local maximum of energy dissipation rate in contrast to sharper cutoff observed in the method of *SW94*.

After the fraction of breaking waves is modified using this persistence length method, the energy dissipation is described in terms of the newly defined total fraction of breaking waves including the breaking wave persistence as

$$D = \frac{3\sqrt{\pi}}{16}\rho g B^3 \overline{f}\frac{H_{rms}^3}{h}Q_{b,tot}. \tag{34}$$

The main difference between the method developed here and the *SW94* method are the definitions of newly breaking waves by Equation 27 and total fraction of breaking waves by Equation 33 used in the dissipation equation. Besides, *SW94* uses the fraction of breaking waves defined by *BJ78* in Equation 13 as an initial total fraction of breaking waves while Equation 25 is used in this method as the estimation. The persistence length in *SW94* is only a function of wave height while it is defined here as a function of both wave height and the wave length.

2.2.3 Roller Model

The radiation stresses are calculated in the model as the sum of a non-broken wave component, $S_{\alpha\beta o}$, and a roller component, $S_{\alpha\beta r}$, as

$$S_{xx} = S_{xxo} + S_{xxr} \tag{35}$$

$$S_{yy} = S_{yyo} + S_{yyr} \tag{36}$$

$$S_{xy} = S_{xyo} + S_{xyr} \tag{37}$$

The non-broken radiation stress components S_{xxo}, S_{yyo}, and S_{xyo} are defined as

$$S_{xxo} = \frac{1}{2}\rho g \sum_{n=1}^{ndir}\sum_{m=1}^{nfreq} |A_{n,m}|^2 \left[\frac{(C_g)_{n,m}}{C_{n,m}}(1+\cos^2\theta_n) - \frac{1}{2}\right] \tag{38}$$

$$S_{yyo} = \frac{1}{2}\rho g \sum_{n=1}^{ndir} \sum_{m=1}^{nfreq} |A_{n,m}|^2 \left[\frac{(C_g)_{n,m}}{C_{n,m}} (1 + \sin^2\theta_n) - \frac{1}{2} \right] \tag{39}$$

$$S_{xyo} = \frac{1}{4}\rho g \sum_{n=1}^{ndir} \sum_{m=1}^{nfreq} \frac{(C_g)_{n,m}}{C_{n,m}} |A_{n,m}|^2 \sin 2\theta_n. \tag{40}$$

The subscript o denotes non-broken wave conditions, ρ is the fluid density, $\theta_{n,m}$ is the direction, $A_{n,m}$ is the complex amplitude, $C_{n,m}$ and $(C_g)_{n,m}$ are the phase speed and the group velocity of the component with the frequency, m, and direction, n. $nfreq$ and $ndir$ are the total number of frequency and directional components, respectively.

Similarly, the mass fluxes are defined as

$$Q_{wx} = Q_{wxo} + Q_{wxr} \tag{41}$$

$$Q_{wy} = Q_{wyo} + Q_{wyr} \tag{42}$$

where the wave-induced mass fluxes for non-broken wave conditions, Q_{wxo} and Q_{wyo} are defined as

$$Q_{wxo} = \frac{1}{2} \sum_{n=1}^{ndir} \sum_{m=1}^{nfreq} \frac{g k_{n,m}}{\omega_m} |A_{n,m}|^2 \cos\theta_n \tag{43}$$

$$Q_{wyo} = \frac{1}{2} \sum_{n=1}^{ndir} \sum_{m=1}^{nfreq} \frac{g k_{n,m}}{\omega_m} |A_{n,m}|^2 \sin\theta_n \tag{44}$$

where $k_{n,m}$ is the wave number of the component with the frequency, m, and direction, n and ω_m is the wave frequency of the m^{th} frequency component.

As waves break, turbulence is generated in a detached, aerated volume of water at the surface, which is defined as the surface wave roller. The existence of rollers during the breaking process increases the radiation stresses and short-wave mass fluxes. The roller formulation of Lippmann *et al.* (1996) is used in the model. It is tied in with the dissipation mechanism of Thornton and Guza (1983) described earlier. One key element of REF/DIF-S is the inclusion of rollers on a component by component basis. Lippmann *et al.* (1996) describes the roller area, A' , as

$$A'_{n,m} = \frac{D_{n,m}}{f_n \tan\sigma_r} \tag{45}$$

where n and m denotes a directional and a frequency component respectively. D is the dissipation described by Equation 26, f_n is the frequency of the n^{th} component of the random wave spectrum and $\tan\sigma_r$ is the slope of the roller front. Roller energy density, E_r , is calculated from the roller area (Svendsen, 1984a) of each component separately as

$$(E_r)_{n,m} = \frac{\rho {A'}_{n,m} {C_{n,m}}^2}{2L_{n,m}}. \tag{46}$$

The roller contributions to the radiation stresses, S_{xxr}, S_{yyr}, and S_{xyr} are defined as

$$S_{xxr} = \sum_{n=1}^{ndir} \sum_{m=1}^{nfreq} 2(E_r)_{n,m} \cos^2\theta_n \tag{47}$$

$$S_{yyr} = \sum_{n=1}^{ndir} \sum_{m=1}^{nfreq} 2(E_r)_{n,m} \sin^2\theta \tag{48}$$

$$S_{xyr} = \sum_{n=1}^{ndir} \sum_{m=1}^{nfreq} 2(E_r)_{n,m} \cos\theta_m \sin\theta_m. \tag{49}$$

The volume flux addition due to the roller, Q_{xr} , Q_{yr} is

$$Q_{xr} = \sum_{n=1}^{ndir} \sum_{m=1}^{nfreq} \frac{{A'}_{n,m}}{T_m} \cos\theta_n \tag{50}$$

$$Q_{yr} = \sum_{n=1}^{ndir} \sum_{m=1}^{nfreq} \frac{{A'}_{n,m}}{T_m} \sin\theta_n. \tag{51}$$

As an additional option for the roller model in REF/DIF-S, the roller model by Okayasu *et al.* (1986), is added to the numerical model. The difference between Lippman's and Okayasu's roller models is the description of the roller area. Okayasu *et al.* (1986) defines the roller area as;

$$A' = 0.06HL \tag{52}$$

where H is the wave height and L is the wave length. The roller contributions to the volume fluxes are then calculated by Equation 50 and Equation 51 multiplied by the total fraction of breaking waves and the roller contributions to the radiation stresses are found by Equation 47 to Equation 49 multiplied by the total fraction of breaking waves.

2.2.3.1 Roller lag method

Southgate and Nairn (1993) and Nairn *et al.* (1990) discuss a transition zone in which a wave transforms from a non-breaking state to a fully developed bore. It is in this zone that the organized wave energy and momentum is transferred to the surface roller development before turbulence dissipation. Therefore, the roller does not immediately contribute to the radiation stresses and wave volume fluxes. For this reason, when the waves break, the corresponding radiation stress gradients are found to begin at a distance beyond the breakpoint (Svendsen, 2005).

Both Nairn *et al.* (1990) and O'Shea *et al.* (1991) determine the transition zone length as a function of local parameters such as bed slope, wave height at the breakpoint and water depth. This approach is applicable for monochromatic waves, but when the waves are random there is no definitive breakpoint. Therefore, a roller lag length is defined here in terms of local parameters not restricted to the breakpoint but applied at any location in the cross-shore. The roller lag length, L_r, is defined as a function of water depth, h, and wave steepness, H_{rms}/L as follows:

$$L_r = C_r h \left(\frac{H_{rms}}{L} \right)^3 . \tag{53}$$

According to Equation 53, the roller lag length strongly depends on the wave steepness. This is similar to Nairn *et al.* (1990) and O'Shea *et al.* (1991) using the surf similarity parameter to find the transition zone length as a function of wave breaking intensity. The roller lag length is also a function of water depth similar to the 'depth method' followed by Southgate and Nairn (1993). C_r is a calibration coefficient for the roller lag length determined by analyzing the model results for the roller component of the radiation stress.

Once the roller lag length is determined, the dissipation used in the roller calculations is modified by changing the total fraction of breaking waves. Since the aim of applying the roller lag is to delay an immediate response of the roller to breaking,

the fraction of newly breaking waves is subtracted from the total fraction of breaking waves within the roller lag length in order to do this. The modified total fraction of breaking waves to be used in roller calculations at any point in the cross-shore in the model domain is defined as

$$Q_{b,tot}^{mod}(i,j) = Q_{b,tot}(i,j) + Q_{b,lag}(i,j) \tag{54}$$

where $Q_{b,tot}$ is the total fraction of breaking waves found by the persistence length method using Equation 33. $Q_{b,lag}$ is calculated using a linear transition of the newly breaking waves over the roller lag length

$$Q_{b,lag}(i,j) = -\sum_{m=ir}^{m=ir+ilag} Q_{b,new}(ir,j) * (1 - \frac{(m-ir)}{ilag}) \tag{55}$$

with $ilag = L_r(ir)/$ is an integer defined at ir. $Q_{b,lag}$ varies between 0 and $Q_{b,new}$ removing new breaking, $Q_{b,new}(ir,j)$, from the total breaking, $Q_{b,tot}(i,j)$.

2.2.4 Near-bed Orbital Velocity Calculations

One of the major enhancements affecting the hydrodynamics in the model simulations is the inclusion of skewed wave orbital velocities. Since the wave module of the numerical model is a linear wave model, the effect of wave nonlinearities are introduced in the near-bed orbital velocities by a parameterization method developed by Elfrink *et al.* (2006) from extensive analysis of field data using evolutionary algorithms. A set of empirical equations that describes characteristic velocity parameters as functions of wave height, wave period, local water depth and local bed slope introduces skewed orbital velocities and therefore nonzero velocity skewness. Figure 2 shows some of the important velocity parameters, such as the velocities under the crest and trough, the zero upcrossing location, etc., used to find the characteristic velocity parameters used in nearbed orbital velocity calculations.

The five characteristic velocity parameters used in the parameterized equation to

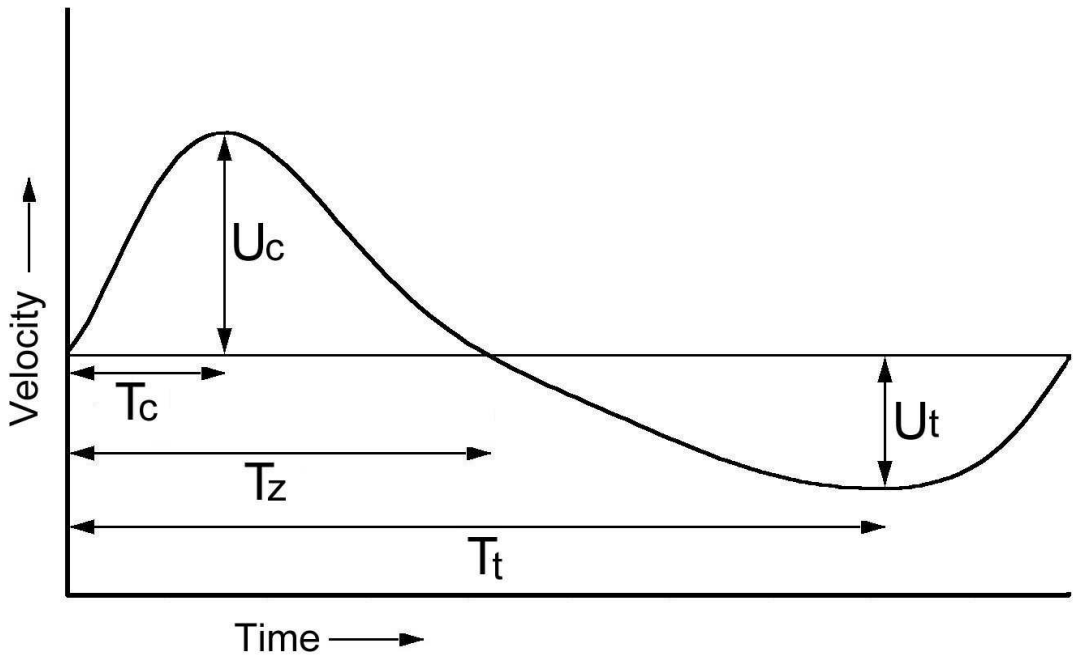

Figure 2: A definition sketch of normalized near-bed orbital velocities (Elfrink *et al.*, 2006)

find nearbed orbital wave velocities are originally defined as

$$U_1 = U_C/(U_C + U_T) \tag{56}$$

$$U_2 = \tfrac{1}{2}(U_C + U_T)\Big/\hat{U}_{Airy} \tag{57}$$

$$T_1 = T_C/T \tag{58}$$

$$T_0 = T_Z/T \tag{59}$$

$$T_2 = T_T/T. \tag{60}$$

Elfrink *et al.* (2006) derived expressions for these five characteristic velocity parameters in terms of the local wave flow properties such as wave height, wave length, wave period, water depth and bed slope. The derived expressions for U_1, U_2, T_0, T_1 and T_2 along with other empirical expressions are given in Elfrink *et al.* (2006). According to this description, the expression for time-varying orbital velocity is

$$U(t) = U_C \sin\left[\tfrac{1}{2}\pi\, t/T_1\right] \qquad 0 < t < T_1 \tag{61}$$

$$U(t) = U_C \cos\left[1/2\pi\,(t - T_1)/(T_0 - T_1)\right]$$
$$- U_0 \sin\left[\pi(t - T_1)/(T_0 - T_1)\right] \qquad T_1 < t < T_0 \tag{62}$$

$$U(t) = -U_T \sin\left[1/2\pi\,(t - T_0)/(T_2 - T_0)\right] \qquad T_0 < t < T_2 \tag{63}$$

$$U(t) = -U_T \cos\left[1/2\pi(t - T_2)/(1 - T_2)\right] \qquad T_2 < t < 1 \tag{64}$$

where $t = t'/T$ with t' = time (s) and T = wave period (s).

The velocity amplitudes U_C, U_T and U_0 are calculated as:

$$U_C = U_1\, U^* \tag{65}$$

$$U_T = U^* - U_C \tag{66}$$

$$U_0 = \left[U_C\, T_0 - U_T\,(1 - T_0)\right]/(T_0 - T_1) \tag{67}$$

where $U^* = 2U_2\hat{U}_{Airy}$ in which $\hat{U}_{Airy}$ is the wave orbital velocity calculated from Airy wave theory. It is important to emphasize here that Elfrink's model introduces the velocity skewness in near-bottom orbital wave velocities which is one of the major mechanisms responsible for onshore sandbar migration.

The model output from the wave module consists of the complex wave amplitude, significant wave height, mean wave direction over the domain, radiation stresses, short wave forcing term, wave-induced mass flux, and near-bed orbital velocities. These output variables are used as input for the circulation module. For more information about the wave model, the reader may refer to Kirby *et al.* (2004).

2.3 Circulation Module

SHORECIRC is used as the circulation module of the numerical model system, solving for the mean water level and nearshore currents as well as sediment transport rates. SHORECIRC is a quasi-3D nearshore circulation model which solves the short wave-averaged nearshore flow equations. It combines the numerical solution for depth-integrated 2-D horizontal equations with an analytical solution for depth-varying currents (Svendsen *et al.*, 2002).

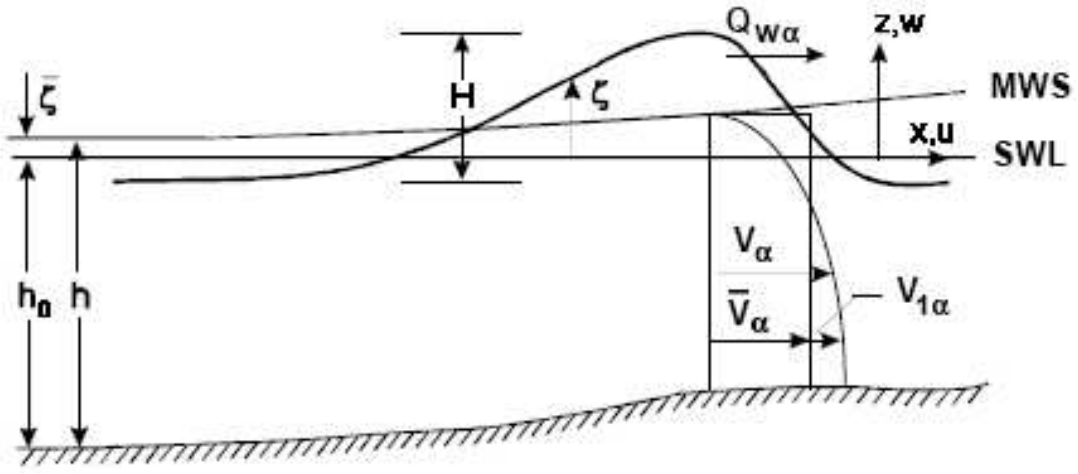

Figure 3: A definition sketch for circulation module variables (Svendsen *et al.*, 2002)

In SHORECIRC, the instantaneous total fluid velocity, u_α, is written as:

$$u_\alpha = u'_\alpha + u_{w\alpha} + V_\alpha \tag{68}$$

where u'_α is the turbulent fluid velocity, $u_{w\alpha}$ is the short wave velocity, V_α is the current velocity and α denotes both directions x and y.

The local water depth, h , is defined as

$$h = h_o + \overline{\zeta} \tag{69}$$

where h_o is the still water depth and $\overline{\zeta}$ is the mean water level as indicated in Figure 3.

SHORECIRC solves the depth-integrated wave-averaged shallow water wave equations. The final form of the continuity equation is given by

$$\frac{\partial \overline{\zeta}}{\partial t} + \frac{\partial \overline{Q_\alpha}}{\partial x_\alpha} = 0 \tag{70}$$

where the overbar is defined as

$$\overline{\cdots} = \frac{1}{T} \int_0^T \cdots \, dt \tag{71}$$

where T is the short wave period.

The total volume flux, Q_α , is defined as

$$Q_\alpha = \int_{-h_o}^{\overline{\zeta}} V_\alpha dz + Q_{w\alpha} \tag{72}$$

and the short wave volume flux, $Q_{w\alpha}$, defined between the wave trough level and the mean surface elevation is as follows

$$Q_{w\alpha} = \overline{\int_{-h_o}^{\zeta} u_{w\alpha} dz} = \overline{\int_{\zeta_t}^{\zeta} u_{w\alpha} dz} \tag{73}$$

where ζ_t indicates the trough level.

The horizontal momentum equation is written as

$$\begin{aligned} &\frac{\partial \overline{Q_\alpha}}{\partial t} + \frac{\partial}{\partial x_\beta} \overline{\int_{-h_o}^{\zeta} V_\alpha V_\beta dz} + \frac{\partial}{\partial x_\beta} \overline{\int_{\zeta_t}^{\zeta} u_{w\alpha} V_\beta + u_{w\beta} V_\alpha dz} = \\ &-gh\frac{\partial \overline{\zeta}}{\partial x_\alpha} - \frac{1}{\rho}\frac{\partial}{\partial x_\beta}\left[S_{\alpha\beta} - \overline{\int_{-h_o}^{\zeta} T_{\alpha\beta} dz} \right] + \frac{\tau_\alpha^S}{\rho} - \frac{\tau_\alpha^B}{\rho} \end{aligned} \tag{74}$$

where, $T_{\alpha\beta}$ is the Reynolds stress, τ_α^B is the bottom shear stress and τ_α^S is the surface shear stress.

2.3.1 Depth-Varying Currents

The wave-averaged current velocity, V_α , is defined as the total of a depth-averaged part and a depth-varying part as follows

$$V_\alpha(z) = V_{m\alpha} + V_{d\alpha}(z) \tag{75}$$

where the depth-averaged part, $V_{m\alpha}$, is defined in terms of the volume fluxes as

$$V_{m\alpha} = \frac{\overline{Q_\alpha} - Q_{w\alpha}}{h}. \tag{76}$$

The depth-varying currents are computed by solving the local (non-depth-integrated) wave-averaged horizontal momentum equations assuming quasi-steady flow for the

mean currents (Putrevu and Svendsen, 1999). The local momentum balance is written as

$$\frac{\partial u_\alpha}{\partial t}+\frac{\partial u_\alpha u_\beta}{\partial x_\beta}+\frac{\partial u_\alpha w}{\partial z}=-\frac{1}{\rho}\frac{\partial p}{\partial x_\alpha}+\frac{1}{\rho}\left(\frac{\partial T_{\alpha\beta}}{\partial x_\alpha}+\frac{\partial T_{\alpha z}}{\partial z}\right). \tag{77}$$

The total velocity is split into short wave velocity and the current velocity as

$$u_\alpha = u_{w\alpha}+V_\alpha. \tag{78}$$

First this split is introduced into Equation 77, then the equation is time-averaged and the pressure is written as

$$\overline{p}=\rho g(\overline{\zeta}-z)-\rho\overline{w^2} \tag{79}$$

In the previous version of SHORECIRC, the pressure was assumed hydrostatic and the dynamic pressure component, $-\rho\overline{w^2}$, was not included. The dynamic pressure component is not ignored in this study. By using the local continuity for the current

$$\frac{\partial V_\alpha}{\partial x_\alpha}+\frac{\partial W}{\partial z}=0 \tag{80}$$

where W is the mean vertical current. Equation 77 may be rewritten as

$$\frac{\partial\overline{V_\alpha}}{\partial t}+V_\beta\frac{\partial V_\alpha}{\partial x_\beta}+W\frac{\partial V_\alpha}{\partial z}+\frac{\partial\overline{u_{w\alpha}u_{w\beta}}}{\partial x_\beta}+\frac{\partial\overline{u_{w\alpha}w_w}}{\partial z}-\frac{\partial\overline{w^2}}{\partial x_\beta}=$$
$$-g\frac{\partial\overline{\zeta}}{\partial x_\alpha}+\frac{1}{\rho}\left(\frac{\partial\overline{T_{\alpha\beta}}}{\partial x_\alpha}+\frac{\partial\overline{T_{\alpha z}}}{\partial z}\right). \tag{81}$$

f_α is defined as the short-wave forcing, which is the local contribution to the radiation stress, as

$$f_\alpha=\frac{\partial\overline{u_{w\alpha}u_{w\beta}}}{\partial x_\beta}+\frac{\partial\overline{u_{w\alpha}w_w}}{\partial z}-\frac{\partial\overline{w^2}}{\partial x_\beta}. \tag{82}$$

In the previous version of SHORECIRC, the third term was not included since the pressure was assumed hydrostatic only. Therefore, Equation 81 may be re-written as

$$\frac{\partial V_\alpha}{\partial t}+V_\beta\frac{\partial V_\alpha}{\partial x_\beta}+W\frac{\partial V_\alpha}{\partial z}+f_\alpha=-g\frac{\partial\overline{\zeta}}{\partial x_\alpha}+\frac{1}{\rho}\left(\frac{\partial\overline{T_{\alpha\beta}}}{\partial x_\alpha}+\frac{\partial\overline{T_{\alpha z}}}{\partial z}\right) \tag{83}$$

where the turbulent stresses are expressed using an eddy viscosity formulation as

$$\overline{T_{\alpha\beta}}=\rho(\nu_t+\nu_s)\left(\frac{\partial V_\beta}{\partial x_\alpha}+\frac{\partial V_\alpha}{\partial x_\beta}\right) \tag{84}$$

$$\overline{T_{\alpha z}} = \rho(\nu_t + \nu_s)\left(\frac{\partial V_\alpha}{\partial z} + \frac{\partial W}{\partial x_\alpha}\right) \tag{85}$$

where ν_t and ν_s are the components of eddy viscosity representing the turbulence created by bottom friction and wave breaking, and the turbulence created by the horizontal shear in the flow, respectively.

Once the velocity split as in Equation 75 is introduced, Equation 83 becomes

$$\begin{aligned}
&\frac{\partial V_{d\alpha}}{\partial t} - \frac{\partial}{\partial z}\left((\nu_t + \nu_s)\frac{\partial V_{d\alpha}}{\partial z}\right) = -\left(\frac{\partial V_{m\alpha}}{\partial t} + V_{m\beta}\frac{\partial V_{m\alpha}}{\partial x_\beta} + g\frac{\partial \overline{\zeta}}{\partial x_\alpha} + f_\alpha\right) \\
&-\left(V_{m\beta}\frac{\partial V_{d\alpha}}{\partial x_\beta} + V_{d\beta}\frac{\partial V_{m\alpha}}{\partial x_\beta} + V_{d\beta}\frac{\partial V_{d\alpha}}{\partial x_\beta} + W\frac{\partial V_{d\alpha}}{\partial z}\right) \\
&+\frac{\partial}{\partial x_\alpha}\left((\nu_t + \nu_s)\left(\frac{\partial V_\alpha}{\partial x_\beta} + \frac{\partial V_\beta}{\partial x_\alpha}\right)\right) + \frac{\partial}{\partial z}\left((\nu_t + \nu_s)\frac{\partial W}{\partial x_\alpha}\right).
\end{aligned} \tag{86}$$

After the mean current component is written in terms of volume fluxes as in Equation 76 and using the depth-integrated momentum balance, Equation 86 may be rewritten as

$$\begin{aligned}
&\frac{\partial V_{d\alpha}}{\partial t} - \frac{\partial}{\partial z}\left((\nu_t + \nu_s)\frac{\partial V_{d\alpha}}{\partial z}\right) = \left(\frac{1}{\rho h}\frac{\partial S'_{\alpha\beta}}{\partial x_\beta} - \frac{\tau^S_\alpha}{\rho h} + \frac{\tau^B_\alpha}{\rho h} - f_\alpha\right) \\
&-\left\{\left(\frac{\overline{Q_\beta}}{h}\frac{\partial V_{d\alpha}}{\partial x_\beta} + V_{d\beta}\frac{\partial \frac{\overline{Q_\beta}}{h}}{\partial x_\beta} + V_{d\beta}\frac{\partial V_{d\alpha}}{\partial x_\beta} + W\frac{\partial V_{d\alpha}}{\partial z}\right)\right. \\
&-\left(\frac{\partial \frac{Q_{w\alpha}}{h}}{\partial t} + \frac{\overline{Q_\beta}}{h}\frac{\partial \frac{Q_{w\alpha}}{h}}{x_\beta} + \frac{Q_{w\beta}}{h}\frac{\partial \frac{\overline{Q_\alpha}}{h}}{\partial x_\beta} - \frac{Q_{w\beta}}{h}\frac{\partial \frac{Q_{w\alpha}}{h}}{\partial x_\beta} + \frac{Q_{w\beta}}{h}\frac{\partial V_{d\alpha}}{x_\beta} + V_{d\beta}\frac{\partial \frac{Q_{w\alpha}}{h}}{\partial x_\beta}\right) \\
&\left.-\frac{1}{h}\frac{\partial}{\partial x_\beta}\overline{\int_{-h_o}^{\zeta} V_{d\alpha}V_{d\beta}dz} - \frac{1}{h}\frac{\partial}{\partial x_\beta}\overline{\int_{\zeta_t}^{\zeta} u_{w\alpha}V_{d\beta} + u_{w\beta}V_{d\alpha}dz}\right\} \\
&+\left\{\frac{\partial}{\partial x_\beta}\left((\nu_t + \nu_s)\left(\frac{\partial V_\alpha}{\partial x_\beta} + \frac{\partial V_\beta}{\partial x_\alpha}\right)\right) + \frac{\partial}{\partial z}\left((\nu_t + \nu_s)\frac{\partial W}{\partial x_\alpha}\right)\right\}.
\end{aligned} \tag{87}$$

Equation 87 may be considered as the governing equation for the depth-varying currents, $V_{d\alpha}$. Since quasi-steady flow is considered, the time variations of the current flow field are assumed to be slow enough and the unsteady term may be neglected. As a result, only one term remains on the left hand side. In order to be able to solve for $V_{d\alpha}$, it is necessary to integrate the equation twice. Therefore, two boundary conditions are required to solve the equation. First, the shear stress at the bottom is

matched as the first boundary condition

$$(\nu_t + \nu_s)\frac{\partial V_{d\alpha}}{\partial z}|_{z=-h_o} = \frac{\tau_\alpha^B}{\rho} \tag{88}$$

Then, using Equation 72 and Equation 76 together, the second boundary condition becomes

$$\int_{-h_o}^{\overline{\zeta}} V_{d\alpha} = 0. \tag{89}$$

Now, equation Equation 87 may be solved for considering the right hand side as the forcing for the depth-varying current. A scaling analysis of these forcing terms is made by Putrevu and Svendsen (1999). Following their analysis, both the forcing and the velocity are broken down into several orders and solve Equation 87 using a perturbation method. As a result, the velocity is written as

$$V_{d\alpha} = V_{d\alpha}^{(0)} + V_{d\alpha}^{(1)} + \dots \tag{90}$$

and the velocities may be solved by integrating their corresponding governing equations:

$$-\frac{\partial}{\partial z}\left((\nu_t + \nu_s)\frac{\partial V_{d\alpha}^{(0)}}{\partial z}\right) = F_\alpha^{(0)} \tag{91}$$

$$-\frac{\partial}{\partial z}\left((\nu_t + \nu_s)\frac{\partial V_{d\alpha}^{(1)}}{\partial z}\right) = F_\alpha^{(1)} \tag{92}$$

with

$$F_\alpha^{(0)} = \left(\frac{1}{\rho h}\frac{\partial S'_{\alpha\beta}}{\partial x_\beta} - \frac{\tau_\alpha^S}{\rho h} + \frac{\tau_\alpha^B}{\rho h} - f_\alpha\right) \tag{93}$$

and

$$\begin{aligned} F_\alpha^{(1)} = -\Bigg\{ & \left(\frac{\overline{Q_\beta}}{h}\frac{\partial V_{d\alpha}}{\partial x_\beta} + V_{d\beta}\frac{\partial \frac{\overline{Q_\beta}}{h}}{\partial x_\beta} + V_{d\beta}\frac{\partial V_{d\alpha}}{\partial x_\beta} + W\frac{\partial V_{d\alpha}}{\partial z}\right) \\ & - \left(\frac{\overline{Q_\beta}}{h}\frac{\partial \frac{Q_{w\alpha}}{h}}{x_\beta} + \frac{Q_{w\beta}}{h}\frac{\partial \frac{\overline{Q_\alpha}}{h}}{\partial x_\beta} - \frac{Q_{w\beta}}{h}\frac{\partial \frac{Q_{w\alpha}}{h}}{\partial x_\beta} + \frac{Q_{w\beta}}{h}\frac{\partial V_{d\alpha}}{x_\beta} + V_{d\beta}\frac{\partial \frac{Q_{w\alpha}}{h}}{\partial x_\beta}\right) \\ & - \frac{1}{h}\frac{\partial}{\partial x_\beta}\overline{\int_{-h_o}^{\zeta} V_{d\alpha}V_{d\beta}dz} - \frac{1}{h}\frac{\partial}{\partial x_\beta}\overline{\int_{\zeta_t}^{\zeta} u_{w\alpha}V_{d\beta} + u_{w\beta}V_{d\alpha}dz}\Bigg\} \end{aligned} \tag{94}$$

The reader may refer to Haas and Svendsen (2000) for a more complete derivation of the depth-varying currents.

2.3.2 Closure Models

The local radiation stress in Equation 82 is calculated using long wave theory in the numerical model. This representation of the short wave forcing does not include the effect of rollers on the forcing. However, it is expected to have a roller forcing created at the surface due to wave breaking which is reduced towards the bottom. In this study, another modeling option is presented with the roller contribution to the radiation stress forcing included in the short wave forcing as an additional term.

Svendsen (1984a) introduced a simple model to include the effect of surface roller on wave motion as a volume of water equal to the volume of the roller, carried by the wave celerity at a certain thickness below the water surface. Therefore, the particle velocities were considered equal to the wave celerity within that thickness. Since the wave roller is a formation at the surface, the roller contribution to the momentum as well as wave forcing is expected to be dominant closer to the surface. However, considering the dissipation of turbulent energy created by breaker, the effect of the roller is expected to decrease moving away from the surface in the water column until it becomes minimum at the bottom or at a specific depth above the bottom. In light of this argument, the roller contribution to the short wave forcing is introduced by using the depth variation of the roller generalized with the constant nr in the equation

$$f_x^r = -\frac{\partial S_{xx}^r}{\partial x}\frac{nr+1}{h^{nr+1}}\xi^{nr} \tag{95}$$

where S_{xx}^r is the roller component of the radiation stress, h is water depth and ξ is the vertical coordinate after transformation, i.e. $\xi = z + h_o$, as described in Van Dongeren and Svendsen (1997) and Haas and Svendsen (2000).

According to Equation 95, the roller contribution to short wave forcing is constant over depth if $nr = 0$, it is linearly varying over depth if $nr = 1$ and it quadratically

varies over depth if $nr = 2$. As nr gets larger, the effect of the roller is more contained to a region just below the surface. Therefore, a value of nr greater than or equal to 3 is suggested in this study. The previous version of SHORECIRC did not include the roller contribution to short wave forcing.

The eddy viscosity due to bottom friction and wave breaking used in solving for the depth-varying currents is defined as;

$$\nu_t = C_{/nu}\kappa\sqrt{\frac{f_{cw}}{2}}u_0 h + Mh(\frac{D}{\rho})^{1/3} + \nu_{t,0} \tag{96}$$

where, κ is the von Karman constant, f_{cw} is the combined wave-current related bottom friction coefficient, D is the energy dissipation in the breaking waves per unit area defined by Equation 34, $\nu_{t,0}$ is an empirical measure of background eddy viscosity, C_{1v} and M are constant coefficients. The first term represents the turbulence created by the bottom friction based on the works by Zai-Jin (1994) and Coffey and Nielsen (1985).

The second term on the right hand side of Equation 96 represents the turbulence generated by the breaking wave dissipation based on a modified Battjes (1975) model and it is the dominant term inside the surf zone. The water depth inside that term represents the turbulent length scale. But, barred beaches are non-monotonic and using water depth as the turbulent length scale might cause local increases in the eddy viscosity following increases in water depth as in the bar trough. Battjes (1975) assumes a length scale equal to H_{rms} and describes the breaking wave-induced depth-averaged eddy viscosity as

$$\overline{\nu}_{t,wave} = f_v H_{rms}(\frac{D}{\rho})^{1/3} \tag{97}$$

where f_v is a calibration factor. Therefore, it has been decided to follow a similar description and rewrite the total eddy viscosity in the version of SHORECIRC used in this study, using H_{rms} rather than depth and this requires a change in the coefficient

M.

$$\nu_t = C_{/nu}\kappa\sqrt{\frac{f_w}{2}}u_0 h + MH_{rms}(\frac{D}{\rho})^{1/3} + \nu_{t,0}. \tag{98}$$

As a result, the definition of eddy viscosity in SHORECIRC is modified in this study. The previous version of SHORECIRC uses h as the turbulent length scale, the version used in this study uses H_{rms} instead.

The eddy viscosity ν_s in the governing equations is the Smagorinsky eddy viscosity which models the turbulence generated by the shear in the flow and accounts for the eddies that are too small to be resolved by the grid resolution;

$$\nu_s = (C_s\Delta)^2\sqrt{2e_{\alpha\beta}e_{\alpha\beta}} \tag{99}$$

where

$$\Delta = \sqrt{\Delta x \Delta y}. \tag{100}$$

$$e_{\alpha\beta} = \frac{1}{2}\left(\frac{\partial V_\alpha}{\partial x_\beta} + \frac{\partial V_\beta}{\partial x_\beta}\right). \tag{101}$$

The wave-averaged bottom shear stress, $\overline{\tau_\alpha^B}$, is evaluated as;

$$\overline{\tau_\alpha^B} = \frac{1}{2}\rho f_{cw} u_0(\beta_1 V_{b\alpha} + \beta_2 u_{0\alpha}) \tag{102}$$

where

$$\beta_1 = \overline{[(\frac{V_b}{u_0})^2 + 2\frac{V_b}{u_0}\cos\theta\cos\mu + \cos^2\theta]^{1/2}} \tag{103}$$

$$\beta_2 = \overline{\cos\theta[(\frac{V_b}{u_0})^2 + 2\frac{V_b}{u_0}\cos\theta\cos\mu + \cos^2\theta]^{1/2}} \tag{104}$$

$$|u_{0,\alpha}| = u_0 cos\theta \tag{105}$$

and f_{cw} is a combined friction factor for the waves and currents which is defined as constant in the model by default.

The steady streaming induced by the oscillatory nature of the bottom boundary layer is important, particularly outside the surfzone (Putrevu and Svendsen, 1993).

In SHORECIRC, the bottom shear stress is applied at the top of the bottom boundary layer neglecting the effect of the bottom boundary layer. Therefore, the steady streaming stress τ^{SB} is included by using the formulation of Longuet-Higgins (1956)

$$\tau_{\alpha}^{SB}{}_{\alpha} = \rho \frac{u_0 u_{0\alpha}}{c} \sqrt{\frac{\omega \nu_{tb}}{8}} \tag{106}$$

where ν_{tb} is the constant eddy viscosity in the boundary layer given by Svendsen *et al.* (1987) as follows

$$\nu_{tb} \cong 0.08 f_{cw}^2 \left(\frac{H}{h}\right)^2 \frac{c}{k}. \tag{107}$$

Once the steady streaming is included, the bottom boundary condition is modified as follows

$$(\nu_t + \nu_s) \frac{\partial V_{d\alpha}}{\partial z}|_{z=-h_o} = \frac{\tau_{\alpha}^{B} - \tau_{\alpha}^{SB}}{\rho}. \tag{108}$$

The system of governing equations is solved using a Predictor-Corrector scheme. This is a central finite difference scheme on a fixed spatial grid which is implemented with an explicit, third-order, Adams-Bashforth predictor and a third-order Adams-Moulton corrector time-stepping scheme. The difference scheme is fourth-order in the grid size in space, except for diffusion terms which are second-order in space. For details of the numerical scheme, see Sancho and Svendsen (2000).

2.3.3 Sediment Transport Formulations

The sediment transport calculations are incorporated in the circulation module. The sediment transport fluxes calculated in the circulation module are passed by the master program to the morphology module to be used in the calculations to find the morphological changes. There are several different sediment transport formulas incorporated in the model. The first one is a generic local sediment transport formula developed by Haas and Hanes (2004) denoted hereafter as the *HH* formula.

According to the *HH* formula, the time-averaged local sediment transport rate is related to the product of a sediment load, characterized by the time-averaged bottom

shear stress magnitude, and an advective velocity, characterized by the total velocity. This wave-averaged, cross-shore transport is given as:

$$q_{HH} = \frac{2C_1}{\rho g}\overline{u(t)\tau_{eff}} \tag{109}$$

where ρ is the water density, g is gravitational acceleration, u is the total velocity, τ_{eff} is the effective shear stress and C_1 is a constant calibration coefficient. The total flow velocity might be separated into a wave component and a current component such that

$$u = u_w + V \tag{110}$$

where u_w is the near-bed wave orbital velocity and V is the near-bed current velocity in the cross-shore direction. The effective bottom shear stress is

$$\tau_{eff} = |\tau| - \tau_{cr} \tag{111}$$

where τ is the bottom shear stress and τ_{cr} is the critical shear stress found according to Shield's incipient motion criterion. The bottom shear stress is calculated as a function of the flow velocity as follows

$$\tau = \frac{1}{2}\rho f_{cw} \left|u(t)\right| u(t). \tag{112}$$

After Equation 111 and Equation 112 are substituted into Equation 109, the sediment transport rate becomes a function of the total flow velocity. Finally, the velocity split as in Equation 110 is introduced into the equation and the result is rearranged in order to write the sediment transport rate in terms of wave and current velocities. The resultant sediment transport rate is broken down into a wave component and a current component as follows:

$$q_{HH} = q_V + q_w \tag{113}$$

with

$$q_V = \frac{C_1 f_{cw}}{g}\left(\overline{u_w^2} + V^2\right) V \tag{114}$$

and

$$q_w = \frac{C_1 f_{cw}}{g}\left(\overline{u_w^3} + 2\overline{u_w^2}V\right) \tag{115}$$

where q_V represents the sediment transported by the current and q_w represents the sediment transported by the waves.

The first term in Equation 114 represents the sediment mobilized by the waves and advected by the current while the second term in Equation 114 represents the sediment mobilized by the current and advected by the current. The first term in Equation 115 represents the sediment mobilized by the waves and advected by the waves while the second term in Equation 115 represents the sediment mobilized by the combined wave-current interaction and advected by the waves.

The default *HH* formula was developed aiming to predict longshore sediment transport and it does not contain a diffusion-type slope term. However, during cross-shore sediment transport and especially over barred beaches and steep beaches, the sediment transport may also be affected by the slope of the bed. The sediment transport may be enhanced if the transport direction is downslope and may be reduced if the transport direction is upslope. The lack of such a term leads to the growth of unrealistic features over the bed in the model simulations. Therefore, an effort is made to develop a slope term in this study.

Other energetics-based sediment transport formulas including the effect of slope on sediment transport components is reviewed (Bailard and Inman, 1981; Bowen, 1980). The effect of slope on the total load is included through the use of two terms;

$$\left(\frac{\tan\beta}{\tan\varphi}\right)$$

and

$$\left(\frac{1}{W_o/\left|u\right|}\right)$$

with the former representing the effect on the bed load and the latter on the suspended load, where $tan\beta$ is the bottom slope and φ is the angle of repose for the bed material.

HH formula does not separate bed load and suspended load. Therefore, a combined effect is introduced by combining those two terms

$$q_{HH} = \frac{2C_1}{\rho g}\overline{u(t)\tau_{eff}} - \frac{2C_1}{\rho g}\overline{u(t)\tau_{eff}}\left(\frac{\tan\beta}{\tan\varphi}\right)C_2\left(\frac{1}{w/|u|}\right). \tag{116}$$

The sediment transport rate is calibrated by changing C_2 term, considering stability issues and the magnitude of the slope term. Here it should be noted that *HH* formula assumes an instantaneous response of sediment transport. However, in reality there is about a 45 degree lag between the flow and the sediment transport.

The second sediment transport formula used in this study is another energetics-based sediment transport formula attributed to Bailard (1981); Bagnold (1966) and Bowen (1980), denoted hereafter as the *BBB* formula. According to the *BBB* formula, the total sediment transport, q_{BBB}, is written as

$$\begin{aligned} q_{BBB} = {} & \frac{\epsilon_s f_w}{(SG-1)g(1-p)W_o}\overline{|u^2|^{3/2}u} + \frac{\epsilon_b f_w}{(SG-1)g(1-p)tan\phi}\overline{|u^2|u} \\ & + \frac{f_w}{(SG-1)g(1-p)}\left[\left(\frac{\epsilon_s}{W_o}\right)^2\overline{|u^2|^{5/2}} + \frac{\epsilon_b}{\tan^2\phi}\overline{|u^2|^{3/2}}\right] \end{aligned} \tag{117}$$

where ϵ_s is the efficiency factor for suspended-load, ϵ_b is the efficiency factor for the bed load, W_o is the fall velocity, SG is the specific gravity, n_p is the porosity, $\tan\phi$ is the angle of internal friction and u is the total flow velocity at the bottom.

2.4 Morphology Module

After the sediment transport rates are determined by the chosen sediment transport formula, the bathymetric evolution is calculated by the conservation of sediment mass equation as;

$$\frac{dq_U}{dx} + \frac{dq_V}{dy} = \mu\frac{dh}{dt} \tag{118}$$

where $\frac{dq_U}{dx}$ and $\frac{dq_V}{dy}$ are the gradients of sediment transport rate, h is the bed elevation, and dh/dt is the change in bed elevation with time and μ is the sediment packing

factor, which is $1/(1-p)$ with p as the bed porosity. The morphological evolution is then computed by using Equation 118. Positive (negative) transport gradients which mean increase (decrease) of the transport rate in cross-shore direction indicate erosion (accretion) regions. The direction of bar migration depends on the location of these accretive/erosive regions.

Equation 118 is solved using a fifth-order, Euler-WENO(Weighted Essentially Non-Oscillatory) numerical scheme. This scheme is introduced to sediment transport calculations by Long *et al.* (2006). The Euler-WENO scheme was shown to have significant advantages for phase-resolving sediment transport models.

According to the Euler-WENO scheme, the sediment transport rate, q, is split into parts associated with the bedform propagation in the positive and negative x-directions as:

$$q^+ = (1-n_p)\int_0^{z_b} C^+(z)dz \tag{119}$$

$$q^- = (1-n_p)\int_0^{z_b} C^-(z)dz \tag{120}$$

where C^+ and C^- are phase speeds of bedform propagating in the positive and negative x-direction respectively. In the end, $C = C^+ + C^-$ and therefore, $q = q^+ + q^-$. The WENO scheme approximates the dq/dx term as;

$$\frac{dq}{dx} = \frac{\hat{q}_{i+1/2} - \hat{q}_{i-1/2}}{\Delta x} \tag{121}$$

where $\hat{q}_{i+1/2}$ is an approximation for the sediment transport rate at grid point $x = i+1/2$ and similarly $\hat{q}_{i-1/2}$ is an approximation at $x = i-1/2$. These approximations are also split into a left-biased and a right-biased flux such that;

$$\hat{q}_{i+1/2} = \hat{q}^-_{i+1/2} + \hat{q}^+_{i+1/2} \tag{122}$$

Here the left-biased flux is calculated as:

$$\hat{q}^-_{i+1/2} = w_1 q^1_{i+1/2} + w_2 q^2_{i+1/2} + w_3 q^3_{i+1/2}, C_{i+1/2} \geq 0 \tag{123}$$

$$\hat{q}^{-}_{i+1/2} = 0, C_{i+1/2} < 0$$

where

$$q^{1}_{i+1/2} = \frac{1}{3}q_{i-2} - \frac{7}{6}q_{i-1} + \frac{11}{6}q_i \tag{124}$$

$$q^{2}_{i+1/2} = -\frac{1}{6}q_{i-1} + \frac{5}{6}q_i + \frac{1}{3}q_{i+1} \tag{125}$$

$$q^{3}_{i+1/2} = \frac{1}{3}q_i + \frac{5}{6}q_{i+1} - \frac{1}{6}q_{i+2} \tag{126}$$

are three stencils for estimating q at point $i + 1/2$ with third-order accuracy. As can be seen, three points are used to the left of $i + 1/2$ while two points are used to the right of it. For that reason, this term is called left-biased. The weights in the above equation are carefully chosen such that the left-biased flux becomes a fifth-order approximation of q at grid location $i + 1/2$. The scheme is nonlinear since the weights are calculated in terms of the sediment transport rates.

Similarly, the right-biased flux is calculated as:

$$\hat{q}^{+}_{i+1/2} = w_1\tilde{q}^{1}_{i+1/2} + w_2\tilde{q}^{2}_{i+1/2} + w_3\tilde{q}^{3}_{i+1/2}, C_{i+1/2} < 0 \tag{127}$$

$$\hat{q}^{+}_{i+1/2} = 0, C_{i+1/2} \geq 0$$

where

$$\tilde{q}^{1}_{i+1/2} = -\frac{1}{6}q_{i-1} + \frac{5}{6}q_i + \frac{1}{3}q_{i+1} \tag{128}$$

$$\tilde{q}^{2}_{i+1/2} = \frac{1}{3}q_i + \frac{5}{6}q_{i+1} - \frac{1}{6}q_{i+2} \tag{129}$$

$$\tilde{q}^{3}_{i+1/2} = \frac{11}{6}q_{i+1} - \frac{7}{6}q_{i+2} + \frac{1}{3}q_{i+3} \tag{130}$$

The reader may refer to Long *et al.* (2006) for further information.

Finally, a simple, Euler-explicit scheme is used to solve for the conservation of sediment mass as follows:

$$\frac{z^{n+1}_{bi} - z^{n}_{bi}}{\Delta t} + \frac{1}{1 - n_p}\frac{\hat{q}_{i+1/2} - \hat{q}_{i-1/2}}{\Delta x} = O(\Delta t, \Delta x^5) \tag{131}$$

Here z^{n+1}_{bi} is the updated bed elevation at time $n+1$ found from the sediment transport rate and the bed elevation at time n, z^{n}_{bi}.

The Euler-WENO scheme was shown to have significant advantages for phase-resolving, advection-type sediment transport models. However, the diffusion-type terms in the transport equation are needed to be handled with a different type of scheme. Although Euler-WENO is intended to reduce the stability problems introduced in widely used Lax-Wendroff schemes, whenever the bulk sediment transport rate is used in Euler-WENO including the slope term, additional stability problems occur. The Euler-WENO scheme solves for dq/dx considering the advection of the bedform in positive and negative x-direction. However, the slope term has a diffusive nature which contradicts the solution technique. In order to overcome this problem, the slope term is split into two parts.

$$q_{slope} = q_2 \frac{dh}{dx} \tag{132}$$

where the first part is the slope itself, dh/dx and the second part is

$$q_2 = \frac{2C_1}{\rho g} \overline{u(t)\tau_{eff}} \left(\frac{1}{\tan\varphi} \right) C_2 \left(\frac{1}{w/|u|} \right). \tag{133}$$

Since dq/dx is used in order to find dh/dt as in Equation 118;

$$\frac{dq_{slope}}{dx} = \frac{dq_2}{dx}\frac{dh}{dx} + q_2 \frac{d^2h}{dx^2}. \tag{134}$$

Clearly, the second term on the right hand side is a diffusion-type term. Therefore only q_2 goes into the Euler-WENO scheme in order to find $\frac{dq_2}{dx}$. Then the result is multiplied by $\frac{dh}{dx}$ and the first term on the right hand side is found. In order to find the second term, central differencing is used on $\frac{d^2h}{dx^2}$ and the result is multiplied by q_2. In the end, the results are found to be more stable.

CHAPTER III

NUMERICAL MODELING OF NEARSHORE HYDRODYNAMICS ON A BARRED BEACH

The first goal of a scientist who studies nearshore processes on barred beaches must be to understand the physics involved. A process-based model, described in Chapter 2, is used to simulate the hydrodynamics on barred beaches in order to replicate bar movements occurring in nature. It is imperative for accurate numerical modeling to develop a comprehensive understanding of both the hydrodynamics and the morphodynamics of the nearshore environment. By comparing the numerical results with experimental measurements, we can evaluate whether the model contains proper mechanisms for accurate simulations of hydrodynamics on barred beaches and incorporates additional processes where necessary.

This chapter presents the numerical modeling results for the hydrodynamics on a barred beach simulated in a laboratory flume. The experiments were conducted in a large-scale flume at Delft Hydraulics, Netherlands in 1994 (Roelvink and Reniers, 1995). Model simulations are done for bar migration events under highly erosive and strongly accretive wave conditions for short time scales (order 10 hours).

The first section briefly outlines the experiments conducted in the large-scale flume. The next section presents the results of the numerical model for the hydrodynamics over barred beaches. The wave height, radiation stresses, mean water level and depth-varying current predictions are compared with the experimental measurements. The effects of the model enhancements described in Chapter 2 are investigated and presented along with the calibrations made to improve model performance. The flow dynamics on barred beaches are explored in order to gain a better understanding

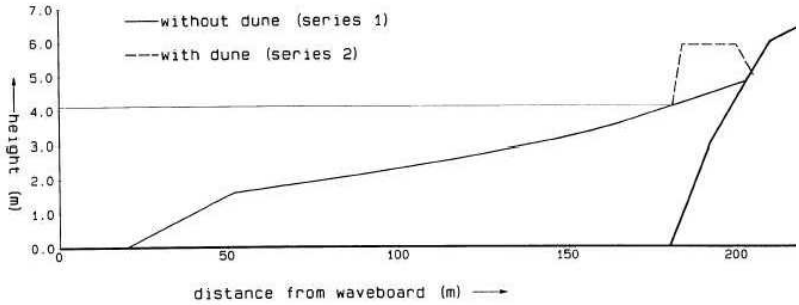

Figure 4: Profile view of the Delta Flume during LIP experiments with the initial bottom profile (Roelvink and Reniers, 1995).

of the relationship between all the relevant processes.

3.1 Delta Flume Data

A set of laboratory experiments were carried out at Delft Hydraulics, Netherlands in 1994 in order to observe the response of a 2DV beach under equilibrium, erosive and accretive conditions. Measurements of hydrodynamics and sediment transport in the surf zone were conducted within the framework of the European Large Installation Plan (LIP) (Arcilla et al., 1994; Roelvink and Reniers, 1995).

The LIP experiments were carried out in a 2D large-scale wave flume, called the Delta Flume, which is 233 m long, 5 m wide and 7 m deep. Figure 4 shows the general cross-sectional view of the experimental setup. The flume had a concrete bottom at z=0 m and was filled with sand, with a grain diameter of 0.22 mm, as shown. The test stages were designed so that they may represent a sequence of events observed in the development of a natural beach with different sea states. Narrow-banded random waves were generated by a wave paddle with its middle position located at x=0. Table 1 shows the wave conditions generated at the wave paddle for the test stages, 1A, 1B and 1C, which mimic slightly erosive, highly erosive and strongly accretive wave conditions, respectively. All experiments were repeated for those test stages over a beach with and without a dune, respectively.

Since the beach response is more pronounced and because of the availability of

Table 1: The wave parameters generated by the wave paddle for the Delta Flume experiments

Test Case	$H_{mo}(m)$	T_p (s)
1A	0.95	4.85
1B	1.21	5.02
1C	0.58	7.97

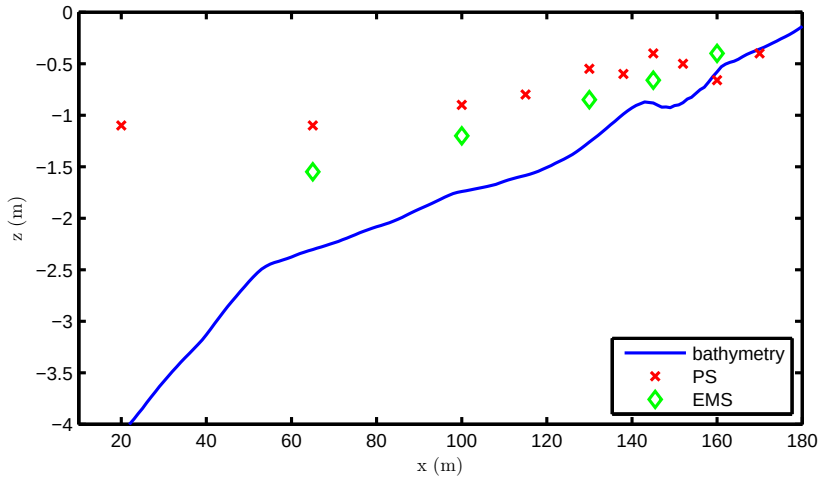

Figure 5: Location of fixed instruments, electro-magnetic current meters (EMS) and pressure sensors (PS), at the Delta Flume (adapted from Roelvink and Reniers (1995).

data, the last two of stages of the LIP experiments are used in this study. Test stage 1B is an 18-hour simulation of an offshore bar migration event followed by test stage 1C which is a 13-hour simulation of an onshore bar migration event. The still water level and wave conditions were kept constant during each test stage.

The measurements were conducted separately for each hour, called the wave hour, of a test stage. The water surface elevation was gathered from stationary pressure sensors attached to the flume wall. The current velocities were gathered from electro-magnetic current meters attached to the flume. The location of the fixed instruments are shown in Figure 5. A movable carriage was also used in order to get the depth-varying structure of the currents. The location of the carriage was changed once

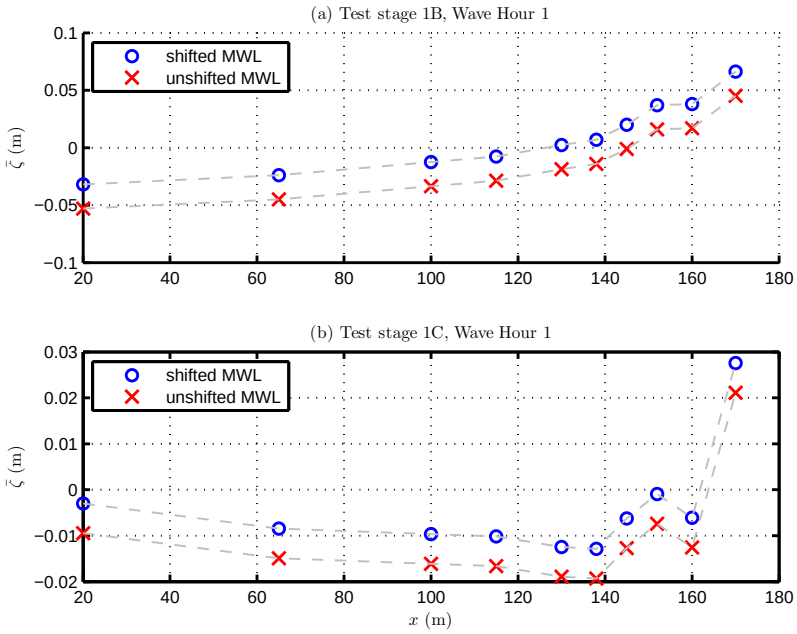

Figure 6: Cross-shore variation of the mean water level ($\overline{\zeta}$) for raw measurements (crosses) and corrected measurements (circles) during (a) wave hour 1 of test stage 1B; (b) wave hour 1 of test stage 1C.

every hour of a test and only one measurement set was collected at one location each hour. Five current meters were mounted on the carriage and the vertical location of the current meters on the carriage is adjusted so that the lowest instrument is always 0.10 m above the bed. A profile follower (PROVO) was mounted on the carriage to measure the bottom profile using an automated sounding system which combines an echo sounder with rod measurements to get accurate underwater profile measurements. All instruments were sampled at 10 Hz.

The time series of the raw measurements of the water surface elevation were used to extract the mean water levels at each instrument location by simply taking the mean of the measured time series. The cross-shore variation of the mean water level , showing the set-up and the set-down inside the surf zone, may then be constructed for all wave hours of both test stages. It was observed from the initial mean water level variations that water mass was not conserved. Several reasons may be that the water

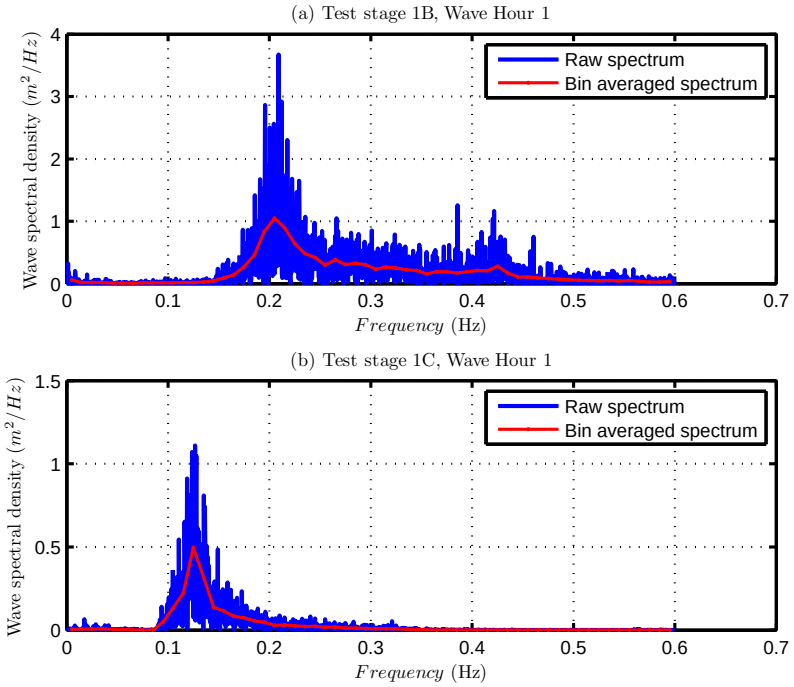

Figure 7: Raw power spectrum (blue) and the 0.01 Hz bin averaged power spectrum (red) of waves at the most offshore gage at wave hour 1 for (a) test stage 1B; (b) test stage 1C.

is trapped behind the wave paddle, or the water is penetrating into the sand bed, or an error in the datum of the water level. However, the mass must be conserved since the experiments were conducted in a closed wave flume. Therefore, the mean water level variations are corrected for mass conservation in our analysis.

Since the measurements are discrete in space, a spline is fitted to the mean water level values extracted from measurements to calculate the area underneath. The result is then subtracted uniformly from the measured mean water level variation to shift it up, for 0.021 m for test stage 1B and 0.0065 m for test stage 1C, so that the mass will be conserved in the flume. Figure 6 shows the mean water level variations of test stages 1B and 1C extracted from pressure sensor measurements from the first wave hour of test runs before and after the shift. Since the wave field was kept constant throughout both test stages, the mean water level variations from other wave hours

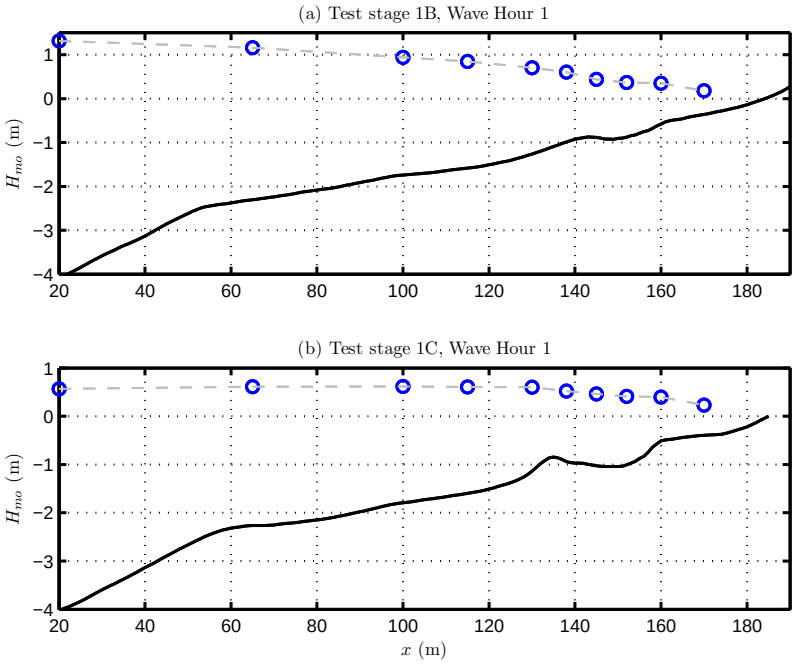

Figure 8: Cross-shore variation of wave height, (H_{mo}), from the measurements over the bathymetry (black solid line) during (a) wave hour 1 of test stage 1B; (b) wave hour 1 of test stage 1C.

only slightly deviated from those shown in Figure 6.

The wave height variation is also extracted from the water surface elevation time series using spectral analysis. The time series over the interval of 10 min to 60 min of each wave hour are transformed to a frequency spectrum by Fast Fourier Transform (FFT) for each instrument. The power spectra are then computed using a pressure response factor, derived from linear wave theory, to convert the pressure data to wave height data. Moreover, the spectra are averaged over 0.01 Hz bins as a means of averaging in order to reduce the noise. Figure 7 shows the power spectrum of both test stages generated for the most offshore gage during the first wave hour. The significant wave height, H_s, is then computed as 4.01 times the area underneath the power spectrum.

It has already been discussed in Chapter 1 that the bar movements are not only dominated by the short waves and the currents generated by the short wave motion

but also affected by the long waves and the low-frequency wave motion. The numerical model in our study does not resolve the low-frequency wave motion. Thus, we restrict the focus of our study to analyze the effects of short waves. For that reason, the low-frequency motion observed at both test stages is filtered before the wave height is calculated from the power spectrum. It is also observed that the wave energy becomes insignificant above 0.6 Hz in both test stages. Therefore a band-pass filter of 0.145-0.595 Hz is used for test stage 1B and a band-pass filter of 0.085-0.595 Hz is used for test stage 1C in order to isolate the short wave motion effects.

Once the analysis is repeated for each instrument, the cross-shore variation of wave height is constructed as shown in Figure 8. It is observed from Figure 8(a) that the waves are larger for test stage 1B and the breaking starts even at the offshore boundary of the domain. On the other hand, the waves are smaller for test stage 1C with the waves shoaling first as indicated by an increase in wave height as shown in Figure 8(b). The increase in wave height in the shoaling area causes a decrease in the mean water level , i.e. set-down, followed by set-up after breaking is initiated, shown in Figure 6(b).

The depth-varying currents are measured by five electromagnetic current meters mounted on the moving carriage. The layout of current meters on the measurement carriage remained fixed but the vertical position of the carriage was changed so that the current meter closest to the bottom was always 10 cm above the bed. At some measurement locations, some of the instruments were above the wave trough level and those measurements are discarded from our analysis. Figure 9 shows the measured currents over the bed for both test stages. As can be seen from the figure, the currents are stronger for test stage 1B and the strongest current is around 0.3 m/s, in-shore of the bar crest in the trough where major wave breaking is expected to occur. Since breaking was initiated earlier for stage 1B, the currents have a depth-varying structure even at locations farther offshore from the bar. In test stage 1C,

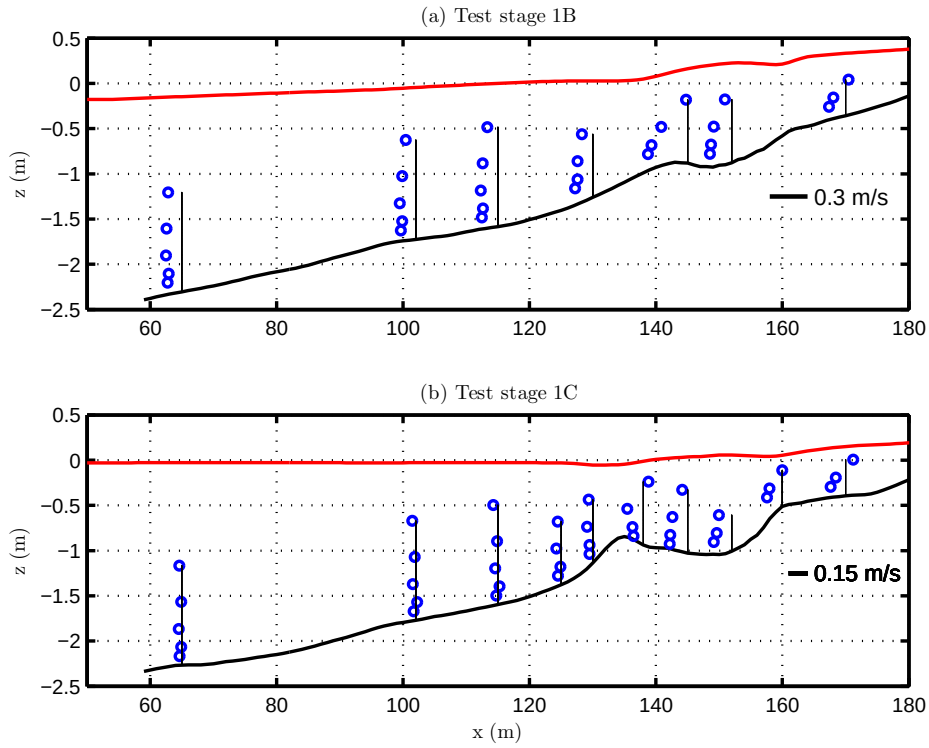

Figure 9: Measured depth-varying current profiles over the bed (black solid line) for (a) test stage 1B; (b) test stage 1C below the mean water level (red line). Black vertical lines indicate the zero velocity reference point for each measurement location.

the current has almost no depth variation for the offshore measurement locations.

The bathymetry was measured at the end of each wave hour at every 1 cm across the domain to record the morphological evolution of the sand bed . The experiments were started with the bottom profile as shown in Figure 4. During slightly erosive test stage 1A, an alongshore bar was formed at the bottom and the final profile for test stage 1A was the initial profile for test stage 1B. In the more energetic and highly erosive test stage 1B, the sandbar was observed to move offshore for 12 wave hours while the bar height was also increasing. The initial and the final measured profiles of test stage 1B are shown in Figure 10(a). Test stage 1C starts with the final profile of test stage 1B and the onshore migration of the sandbar for 18 wave hours may be observed in Figure 10(b) under strongly accretive wave conditions.

As has been shown so far, the LIP test stages 1B and 1C are highly appropriate

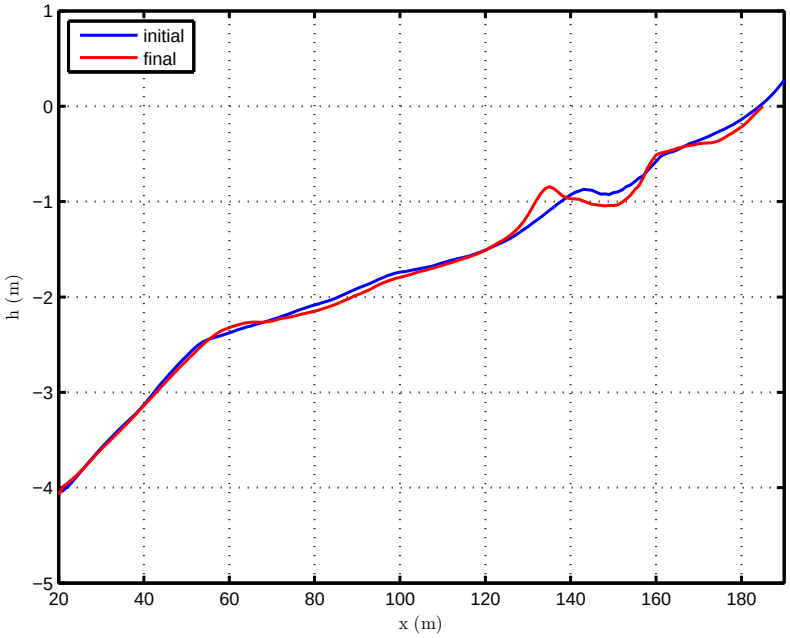

(a)

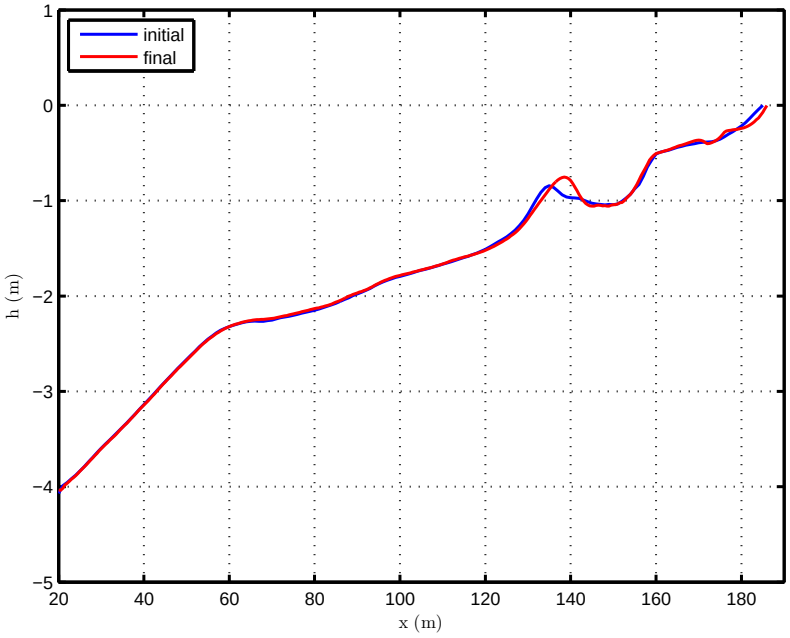

(b)

Figure 10: Measured profiles and morphological evolution (a) for 18 hours during test stage 1B; (b) for 13 hours during test stage 1C.

for studying numerical modeling of barred beaches. The following section will present the results of the numerical model and comparison with these measurements for test stages 1B and 1C.

3.2 Model Results for LIP Test Stages

As mentioned in the previous chapter, the numerical model contains three main modules, wave, circulation and morphology, working consecutively. In this section, as the numerical model results are presented, analyzed and compared with the measurements, the effect of the enhancements to the numerical model on the results will be evaluated. In each section, the results for test stages 1B and 1C will be presented consecutively.

The spectral wave module, REF/DIF-S, may work with measured frequency and directional spectra input. Since the power spectrum may be extracted from pressure sensor measurements as discussed in the previous section, it is preferred to input a measured spectrum to the wave module. The most offshore pressure sensor is located at x=20 m and the first 20 meters of the flume was flat concrete. So, it is appropriate to start the numerical domain at x=20 m and consider the measured band-pass filtered spectrum input at the most offshore gage as our offshore boundary condition. The wave paddle generated unidirectional waves perpendicular to the shoreline during the experiments. For that reason, only one directional component is used for the numerical model and the number of frequency components is determined by the number of 0.01 Hz bins used during the averaging process to eliminate the noise from the raw spectrum.

A minimum depth criterion of 10 cm is used to determine the last wet point for numerical computations and a moving shoreline boundary is utilized to track the location of the shoreline. Hence, the length of the numerical domain is chosen to

include even some portions of the dry beach inside the numerical domain. The numerical grid has 1 m spacing in both x and y directions and the number of grid points in the x-direction is 184 points for test stage 1B and 166 points for test stage 1C while it is 11 grid points in the y-direction for both test stages. Since the Delta Flume experiments were intended for the study of cross-shore sediment transport and alongshore uniformity was desired, $\partial/\partial y$ terms are excluded from the governing equations and calculations. A no-flux boundary condition is used at the shoreline position while a wall boundary condition is used at the offshore boundary. As described in the previous chapter, a periodic boundary condition is used at the cross-shore lateral boundaries.

3.2.1 Dissipation and Wave Height

The wave module, REF/DIF-S, uses spectral components in order to calculate wave parameters such as wave height, volume fluxes, radiation stresses as well as wave forcing which drives the currents. The dissipation mechanism, which controls the evolution of amplitudes of spectral components in the cross-shore direction, may then be considered as the backbone of the spectral wave module. For that reason, the discussion on hydromechanics begins with the dissipation immediately followed by the wave height variation.

It may be seen in Equation 20 that there are two free parameters, γ and B, in the parametric dissipation model of Thornton and Guza (1983), *TG83*, which controls the magnitude of dissipation. *TG83* calibrated these parameters as 0.42 and 1.54, respectively. It was observed that different combinations of these two constants may result in the same dissipation. Hence, instead of trying to calibrate these parameters separately to manage more accurate simulations, they may be combined into a single breaking wave parameter, Y, as given by Equation 23 in the previous chapter.

Test Stage 1B

In Figure 11, the measured spectrum for LIP test stage 1B and 3 different modeled spectra results are shown. The linear wave model computes the dissipation in an ensemble fashion as mentioned in the previous chapter and applies a constant dissipation rate for all the frequency and directional components. The shape of the given input spectrum at the offshore boundary is maintained as the solution is found for other cross-shore grid points by marching forward in space from the offshore boundary to the shoreline. Therefore, energy can only be dissipated over each frequency and not redistributed across frequencies.

By comparing the measured spectrum with the modeled spectrum and looking at the magnitude and variation of the wave amplitude, we may qualitatively compare the amount of dissipation modeled with the actual amount of dissipation of the experiment. All model results are initially identical to the measured spectrum at the offshore boundary.

The results are presented for 3 different combined breaking wave parameter, Y, values. $Y = 117$ is the case for default *TG83* parameters with $B = 1.54$ and $\gamma = 0.42$, $Y = 39$ is an intermediate value for comparative purposes and $Y = 12$ will be shown to be the value giving the best correlation to the wave height measurements. It is observed that when the default *TG83* parameters are used, the dissipation is overestimated throughout the domain. The wave energy densities are smaller than measured values. For $Y = 12$, the model predicted spectrum is closer to the measured spectrum for the first 6 gages offshore of x=140 m. After that point, the model starts to overestimate the spectral densities. This is an indication that the dissipation in the model is underpredicted compared to the dissipation of the measurements. An underprediction of dissipation leads to the overprediction of the complex amplitudes and consequently the wave heights.

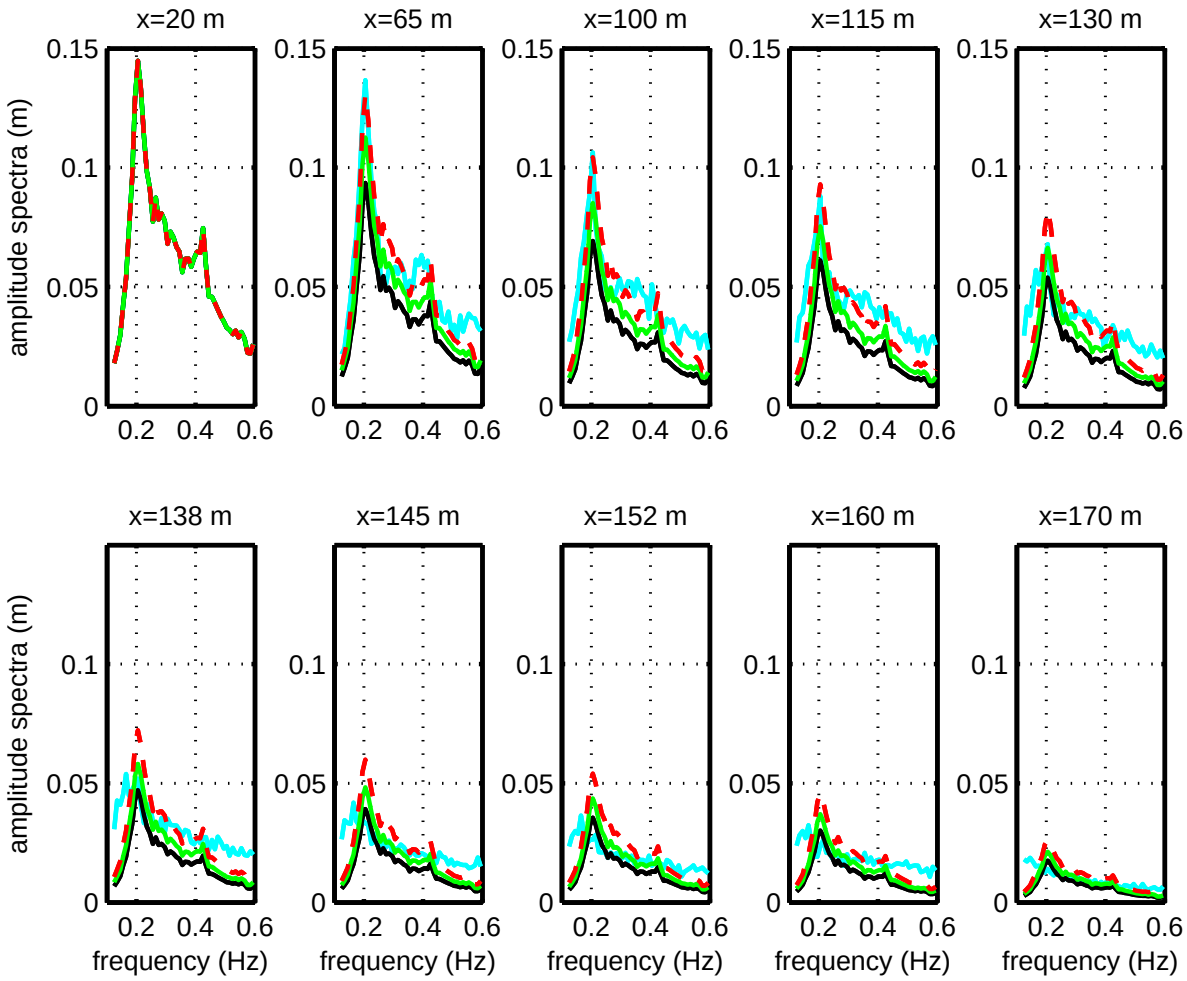

Figure 11: The evolution of power spectrum in the cross-shore direction at gage locations for test stage 1B: Measured spectra (cyan solid line), modeled spectra with the combined breaking wave parameter, Y=117 (black solid line), Y=39.2 (green solid line), Y=11.8 (red dash line).

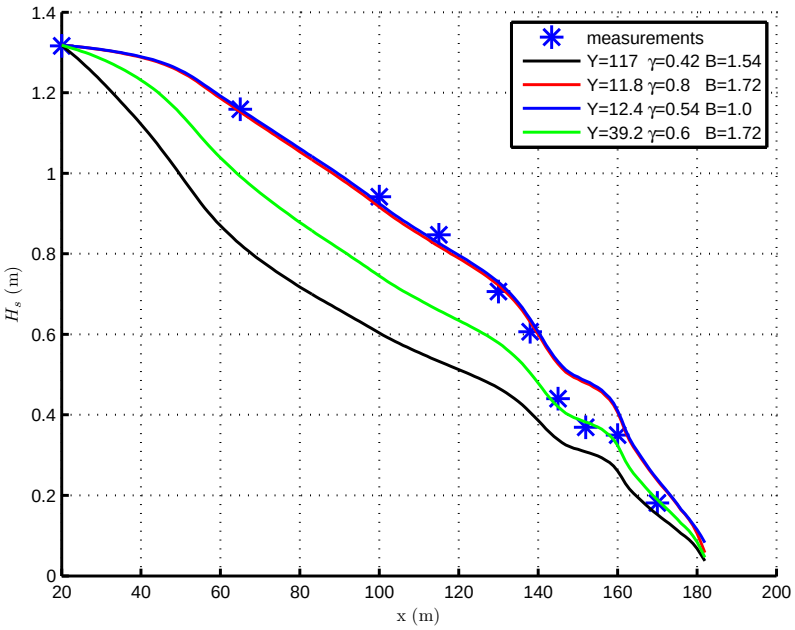

Figure 12: The cross-shore variation of significant wave height, H_s, for the measurements during test stage 1B (blue stars); for the model results with different combined breaking wave parameter, Y, values used (solid lines).

Figure 12 shows the wave height predictions for different Y values with the corresponding γ and B values used in the model. Since the default γ and B values result in a large Y value causing dissipation higher than the observations, the model underpredicts the wave height variation.

As can be seen from the figure, the wave height variations are almost the same for those cases with almost equal combined breaking wave parameter, Y, values even if the breaking wave parameters of Thornton and Guza (1983), γ-B, values are different, i.e. 0.8-1.72 and 0.54-1. The γ value of the first γ-B couple was chosen specifically since the value of 0.8 is close the maximum wave height to water depth ratios reported since the late 19th century (Svendsen, 2005). The B value of the second γ-B couple was chosen specifically since the value of 1 corresponds to fully developed bores. The resulting wave height variations for these two couples with the Y values of around 12

are very close to the measurements up to x=138 m but are larger than the measurements shoreward of that location. A final couple with an Y value of around 39.2 is also shown in the figure as an intermediate case. The wave height variation for this Y value matches the measurements after x=145 m but underpredicts offshore of that location due to higher dissipation.

Therefore, it is not possible to match the measurements both offshore and onshore of x=140 m where the sandbar is located if a constant combined breaking wave parameter, Y, value is used. It was mentioned in the previous chapter that a spatially varying γ value is incorporated in the wave model as a model enhancement in order to overcome this problem. The value of B is still kept constant so that Y gets its variation only from the varying γ. The formula by Ruessink et al. (2003) [Equation 22] is used to calculate γ in terms of relative depth kh, i.e. h/L. It is expected to have larger values offshore for deep water waves with larger water depth and smaller wave length. The maximum possible value of γ is restricted with a cap at 0.8 so that unrealistic values may not be used in the numerical model.

The wave height variation and the variation of combined breaking wave parameter, Y, are shown in Figure 13. It is observed in Figure 13(a) that allowing γ to vary does not make any difference offshore or where the values match the constant value of 0.8 due to the cap. The wave height predictions are improved starting from around the bar crest towards the shoreline due to the fact that varying γ values are smaller than the constant value of 0.8 leading to a larger Y as shown in Figure 13(b) and hence more dissipation.

Although the wave height predictions are significantly improved compared to the predictions with the default values of the breaking wave model, the model results in the bar trough still overpredict measurements at locations x=145 and x=152 m. It is observed from Figure 13(a) that the modeled wave height does not decrease as much as seen in the measurements between x=145 m, right onshore of the bar crest,

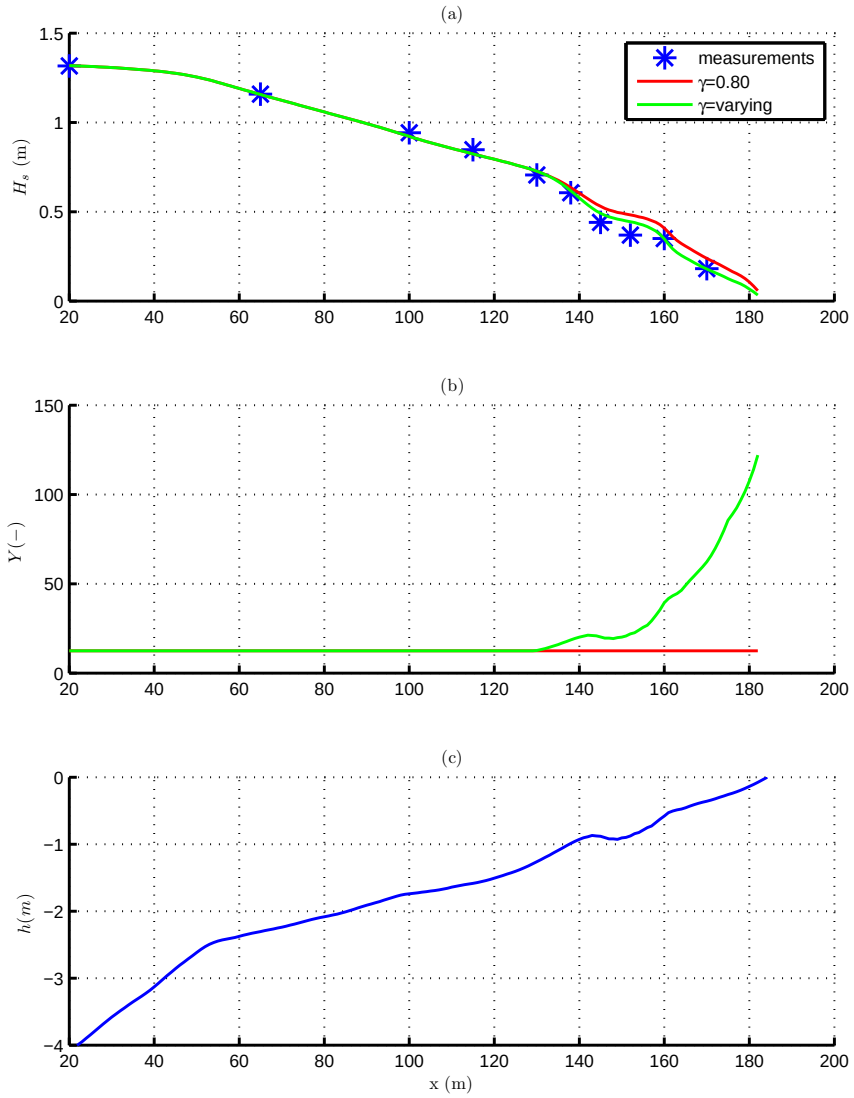

Figure 13: The cross-shore variation of (a) significant wave height, H_s, for the measurements (blue stars) during test stage 1B, the model results (solid lines) with constant combined breaking wave parameter, Y, and with varying Y; (b) constant Y vs. varying Y values; (c) bathymetry at the beginning of test stage 1B.

and x=152 m. This is a result of the model dissipation being defined in terms of local parameters, such that it immediately starts decreasing as the water depth starts increasing onshore of the bar crest into the bar trough.

The final enhancement to the model regarding the energy dissipation and the wave height predictions is the implementation of the persistence length method. The simplest method is to define the persistence length as a constant. However, instead of using a constant value throughout the domain it was found more appropriate to define it as a function of wave parameters as described by Equation 32. This equation contains a calibration constant, C_p, and the results were found to be sensitive to this constant.

The persistence length method affects the wave height variation by changing the total fraction of breaking waves, $Q_{b,tot}$, and therefore the energy dissipation, D, by accounting for the breaking wave persistence into deeper water. For this reason, it is useful to understand the effect of persistence length method on those parameters. The cross-shore variation of the total fraction of breaking waves in the entire domain for cases with different C_p values is shown in Figure 14(a). As the waves travel towards the shore, the fraction of breaking waves increases as the water depth decreases. In fact, the fraction of breaking waves is close to 0% offshore and increases towards the shore. However, because the depth is not monotonically decreasing, the total fraction of breaking waves decreases immediately after the bar, as observed in Figure 14(a) for the case with no persistence.

Figure 15 shows the same variation focusing on the bar-trough zone in subplot (a), along with the bathymetry in the same zone in subplot (b). It may be seen that the total fraction of breaking waves, $Q_{b,tot}$ reaches a local maxima at x=140 m. That is the location where major breaking occurs right offshore of the bar crest. For the case with no breaking wave persistence, $Q_{b,tot}$ starts decreasing right after that point until it hits a local minima at x=148 m. This decrease in $Q_{b,tot}$ is first initiated by

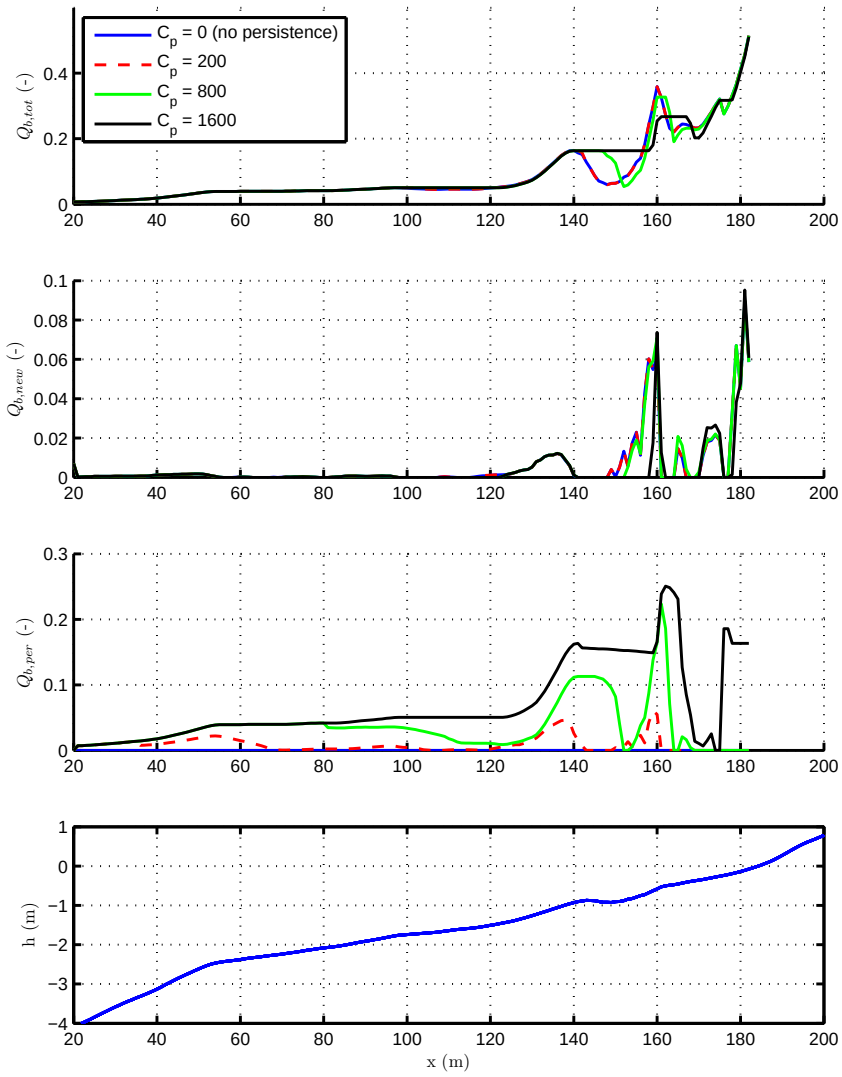

Figure 14: The cross-shore variation of the fraction of breaking waves for test stage 1B with different persistence length calibration constant, C_p, values. (a) total fraction of breaking waves, $Q_{b,tot}$, (b) fraction of newly breaking waves, $Q_{b,new}$, (c) fraction of persisting breakers, $Q_{b,per}$, (d) the bathymetry.

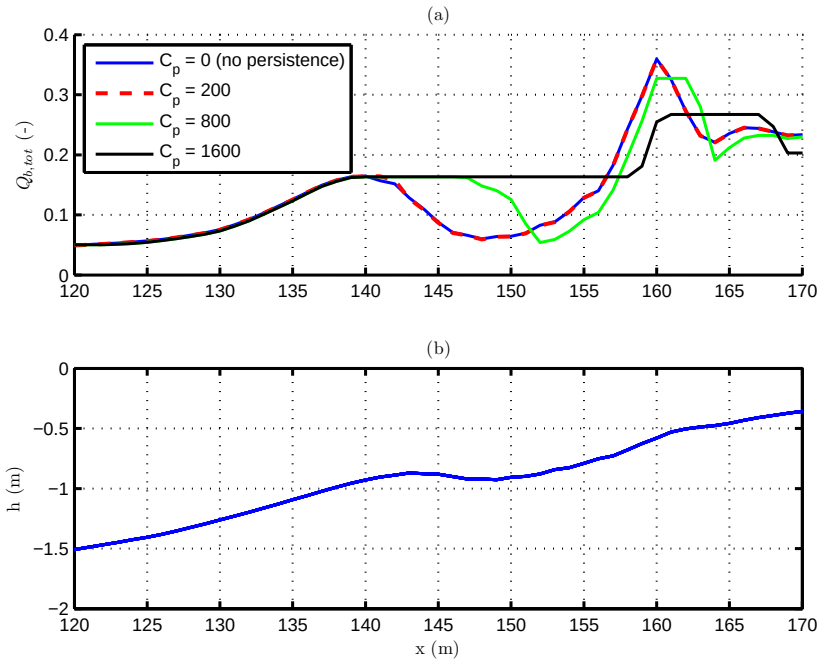

Figure 15: (a) The cross-shore variation of the total fraction of breaking waves, $Q_{b,tot}$, in the bar-trough zone with varying combined breaking wave parameter, Y, and for different persistence length calibration constant, C_p, values (b) The bathymetry in the bar-trough zone.

the decrease in wave height and then enhanced by the increase in water depth. $Q_{b,tot}$ begins to increase where the water depth starts decreasing in the second half of the trough. The effect of the persistence length method is shown by the continuation of the local maxima of $Q_{b,tot}$ for a distance. It may be observed that this distance is very small for a persistence length calibration constant, C_p, value of 200 and large for a C_p value of 1600 such that the local maxima persists throughout the bar trough. The $Q_{b,tot}$ variation with the C_p value of 800 shows the effect of $Q_{b,tot}$ remaining constant between x=140 and x=147 and then decreasing until x=152 m.

Figure 14 shows the variation of total fraction of breaking waves over depth along with the other components used in the persistence length method, i.e. the fraction of newly breaking waves and the fraction of persisting broken waves. As the persistence length constant gets larger, a larger fraction of breaking waves contributes to the

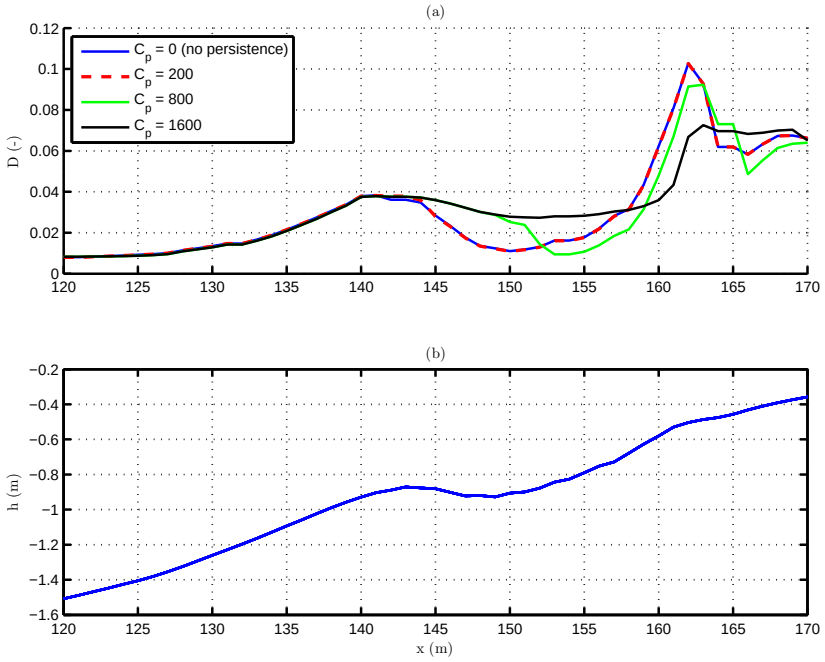

Figure 16: (a) The cross-shore variation of energy dissipation, D given by Equation 34, during test stage 1B in the bar-trough zone with varying combined breaking wave parameter, Y, and for different persistence length constant, C_p, values (b) The bathymetry in the bar-trough zone.

fraction of persisting breakers. For the larger C_p value of 1600, this results in a higher fraction of breaking waves persisting across the bar trough. In consequence, there is no new breaking until the end of trough at x=160 m and all of the secondary breaking occurs almost at the same location at x=160 m. The fractions of newly breaking waves for the other two cases are very close to each other. However, the fraction of persisting breakers for $C_p = 200$ is not large enough to make a considerable impact on the total fraction of breaking waves. On the other hand, the fraction of persisting waves for the case of $C_p = 800$ covers almost half of the trough and makes an impact on the total fraction of breaking waves.

The effect of breaking wave persistence and the use of persistence length method on the cross-shore variation of dissipation is shown in Figure 16. It may be observed that the variation of dissipation is similar to but not the same as the variation of

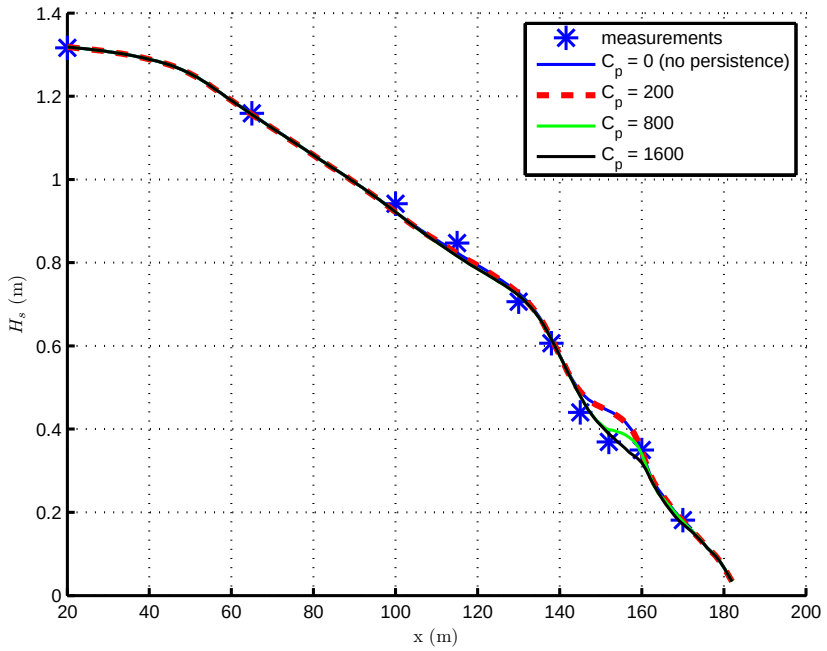

Figure 17: The cross-shore variation of significant wave height, H_s, for the measurements during test stage 1B (blue stars); for the model results with different persistence lengths (solid lines) with varying Y

the total fraction of breaking waves. The dissipation peaks at x=140 m as a higher percentage of waves start breaking right offshore of the bar crest. In the case with no persistence, the dissipation is observed to start decreasing slightly at this point due to the decrease in wave height. In fact, the rate of the decrease steepens starting from x=143 m where the water depth starts increasing onshore of the bar crest. Once the persistence length method is used, the waves breaking offshore of x=140 m but persisting even after this point contributes to the dissipation which is observed to decrease at a more gradual rate.

The wave height variations for cases with different persistence lengths are shown in Figure 17. It is observed that for $C_p = 1600$ the wave height decreases almost with a constant slope after the primary breaking offshore of the bar crest. However, the rate of decrease in the measured wave height is smaller in the second half of the trough between x=152 and 160 m indicating an intermediate shoaling of the waves offshore

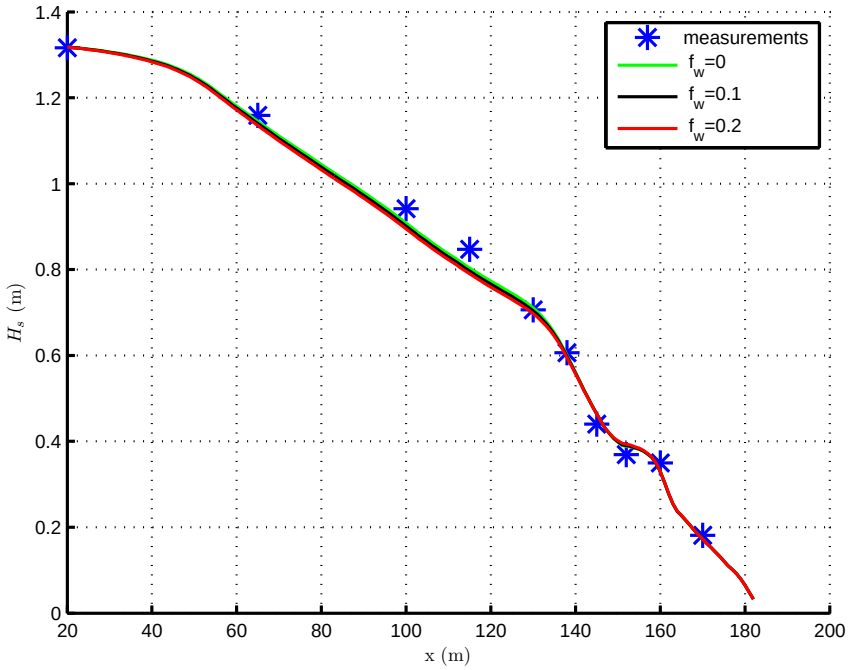

Figure 18: The cross-shore variation of significant wave height, H_s, for the measurements during test stage 1B (blue stars); for the model results with different friction factor, f_w, used in the wave module (solid lines).

of secondary breaking at the end of the trough. Therefore, the dissipation needs to start decreasing as the effect of persisting breakers decrease after the midpoint of the trough. A more realistic wave height variation is acquired by using a C_p value of 800 as the persistence length constant.

It has been demonstrated so far that the energy dissipation due to breaking and the wave height variation is strongly affected by the value of Y and the persistence length constant, C_p. Another parameter which affects the energy dissipation is the wave friction factor which is used in the calculation of the dissipation due to bottom friction. Although dissipation due to breaking is expected to be dominant over the dissipation due to turbulent bottom boundary layer, the latter may be comparably large in those locations where breaking is not intense. Consequently, a range for the friction factor is determined as a function of bed roughness by looking at estimates using different friction factor formulas such as Nielsen's equation, the Swart formula

and the Kamphuis formula. Although the friction factor is estimated to be in the range of 0.03-0.05 by these formulas, Nielsen suggested that the roughness value under oscillatory flow may actually be considered much larger than under steady flow (Nielsen, 1992). Considering that, the friction factor is estimated to be on the order of 0.05-0.2 for test stage 1B. Figure 18 shows wave height for the different wave friction factors. Since energy dissipation due to wave breaking is dominant during test stage 1B, it may be observed that the friction factor in the wave module does not have a significant effect throughout the domain.

For a comprehensive calibration, the wave height predictions are compared to the measurements and the model skill is calculated while determining the parameter values giving the most accurate results. The accuracy of the modeled wave height is quantified using the index of agreement between model and measurements data as proposed by Willmott (1981). The model skill, d, is computed as

$$d = 1 - \frac{\sum_{j=1}^{n} [y(j) - x(j)]^2}{\sum_{j=1}^{n} [|y(j) - \overline{x}| + |x(j) - \overline{x}|]^2} \tag{135}$$

where $x(j)$ are the measured data, $y(j)$ are the modeled data, and $\overline{x}$ is the mean of measured data. A value of $d = 1$ indicates perfect agreement, and a value of $d = 0$ indicates total disagreement.

Table 2 shows the variation of model skill for wave height predictions for a set of model runs with different model parameter values. Although many more combinations have been studied, these are chosen to be presented here showing the increase in model skill as the model is enhanced. Run number 1 is with the default *TG83* parameters. Runs 1 through 4 are those for different values of the constant Y presented in Figure 12. Runs 5 and 6 are those before and after the varying Y implementation presented in Figure 13. Runs 7 through 9 are those after the persistence length method is implemented for the evaluation of persistence length constant C_p shown

Table 2: The model skill calculated by Equation 135 for all instrument locations, d_H, and only trough locations, $d_{Htrough}$, for wave height predictions of test stage 1B with different values of the model parameters, combined breaking wave parameter, Y, the breaking wave parameters γ and B of Thornton and Guza (1983), persistence length constant, C_p, and wave friction factor, f_w.

Run number	Y	γ	B	C_p	f_w	d_H	$d_{Htrough}$
1	117.4	0.42	1.54	0	0.2	0.9090	0.5192
2	39.3	0.6	1.72	0	0.2	0.9717	0.9303
3	12.4	0.8	1.72	0	0.2	0.9938	0.5707
4	11.8	0.54	1	0	0.2	0.9931	0.5531
5	12	0.8	1.7	0	0.2	0.9934	0.5595
6	varying	varying	1.7	0	0.2	0.9980	0.7736
7	varying	varying	1.7	200	0.2	0.9980	0.7766
8	varying	varying	1.7	1600	0.2	0.9990	0.9113
9	varying	varying	1.7	800	0.2	0.9991	0.9129
10	varying	varying	1.7	800	0.1	0.9987	0.9456
11	varying	varying	1.7	800	0	0.9990	0.9475

in Figure 17. It is seen in Table 2 that the model skill considering all measurement locations, d_H, increases from 0.909 for the default *TG83* parameters to an almost perfect 0.999. Table 2 also shows the model skill only for the measurement locations within the bar trough, $d_{Htrough}$, i.e. x=145, 152 and 160 m. It is observed that the model skill for wave height in the bar trough increases from 0.519 to 0.91 which more clearly shows the effect of the model improvements and enhancements. Consequently, an f_w value of 0.2, a B value of 1.7 and a C_p value of 800 are chosen to be used in the wave model for LIP test stage 1B model runs.

Test Stage 1C

Test Stage 1C was initialized with the final bathymetric profile of test stage 1B and was conducted to simulate a less energetic case. The instrument locations for the pressure gages were not changed. The power spectra generated from the gage measurements are shown in Figure 19 along with the modeled spectra at the instrument locations. Once again, the initial model spectrum is matched with the measured

spectrum at the most offshore pressure gage. The power spectrum at the most offshore gage in test stage 1B not only had an energy peak at 0.2 Hz, i.e. mean period of 5 seconds, but also had significant energy at higher frequencies and even had a secondary peak at 0.4 Hz. On the other hand, the most offshore gage in test stage 1C has most of the energy contained close to the peak frequency of 0.125 Hz, i.e. mean period of 8 sec, and only very little energy is observed for frequencies over 0.4 Hz. The measurements show that considerable amount of energy is contained in frequencies higher than 0.2 Hz at other instrument locations, even with a secondary peak at 0.25 Hz at locations offshore of the bar crest. This indicates a nonlinear shift of energy to the higher harmonics in the shoaling region. However, the linear model maintains the shape of the initial spectrum which inherently results in higher than normal dissipation and causes an underprediction of the energy under higher frequencies throughout the domain no matter what the Y value is. The large Y value of 117 is observed to give reasonable estimates of the magnitude of spectral density at the peak frequency and the smaller values are observed to overestimate it; however, the total area underneath the spectrum which is the total amount of wave energy is more important.

The constant combined breaking wave parameter, Y, value giving the best results offshore of the bar crest tended to be smaller than the best value of 12 for test stage 1B. This can be explained with a smaller B value of 1.00 compared to the 1.72 used for test stage 1B. Since the B value is related to the intensity of breaking, the breaking is expected to be less intense for test stage 1C, because test stage 1C was designed to mimic a low-energetic case.

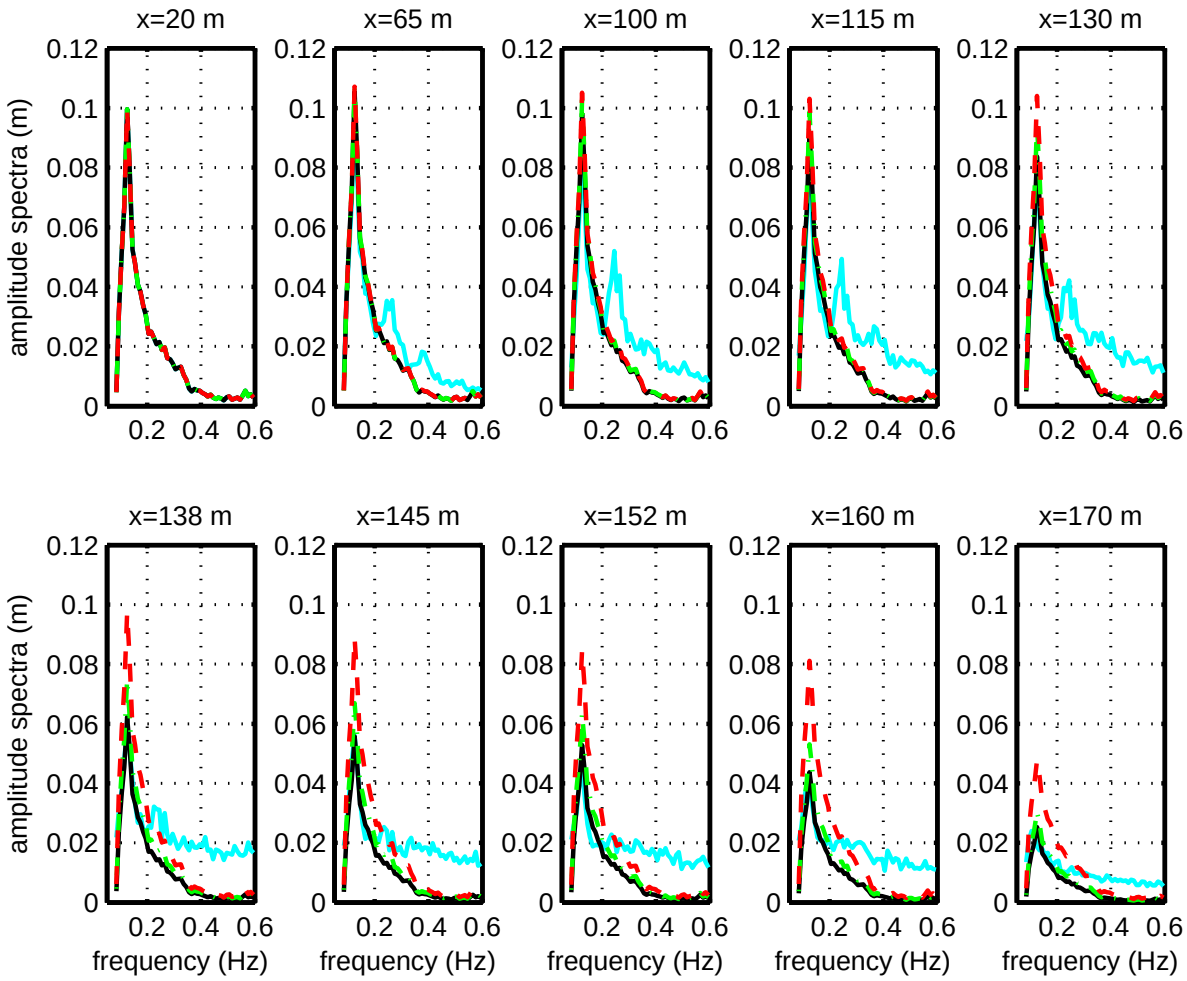

Figure 19: The evolution of power spectrum in the cross-shore direction at gage locations for test stage 1C: Measured spectra (cyan solid line), modeled spectra with the combined breaking wave parameter, Y=117 (black solid line), Y=39.2 (green dot-dash line), Y=2.4 (red dash line).

Figure 20(a) shows the wave height variation for cases with different combined breaking wave parameter, Y, values. It may be seen that with $Y = 117$ which corresponds to the default value of *TG83*, the wave height is underpredicted throughout the domain similar to the test stage 1B result because of an overestimated wave energy dissipation. With the constant Y value of 2.4, the wave height predictions are close to the measurements up to x=132 just offshore of the bar crest shown in Figure 20(c), but overpredicts in the surf zone due to the reduced dissipation. As with test stage 1B, a varying value of γ is used to introduce the spatial cross-shore variability in Y and hence in dissipation. Figure 20(b) shows the varying Y along the constant value of 2.4 and as in test stage 1B, the varying Y value matches the constant value at the offshore boundary. As before, using a varying value of Y enhances the model predictions which are in good agreement with the measurements throughout the domain except the bar - trough zone where the model still overpredicts the wave height. As in test stage 1B, the rate of decrease in wave height reduces in the bar trough in the model because of the reduced dissipation due to the increase in depth within the bar trough.

Figure 21 shows the cross-shore variation of the total fraction of breaking waves along with the fractions for the new and persisting breakers in the entire domain for cases with different persistence length constants, i.e. C_p values. Even if a C_p value of 800 was chosen for test stage 1B, the same value does not have much of an effect for test stage 1C. As the C_p value and consequently the persistence length increases, the effect of persistence length method is extended into the bar - trough zone by having a larger percentage of persisting breakers. It is observed that the C_p value of 6000 results in a very large amount of persisting breakers such that the persisting breakers cover the entire bar trough and there is almost no new breaking occurring at the end of the trough at x=160 m. The results using the intermediate C_p values of 2400 and 4800 are similar in characteristics such that the persistence is effective up to a certain

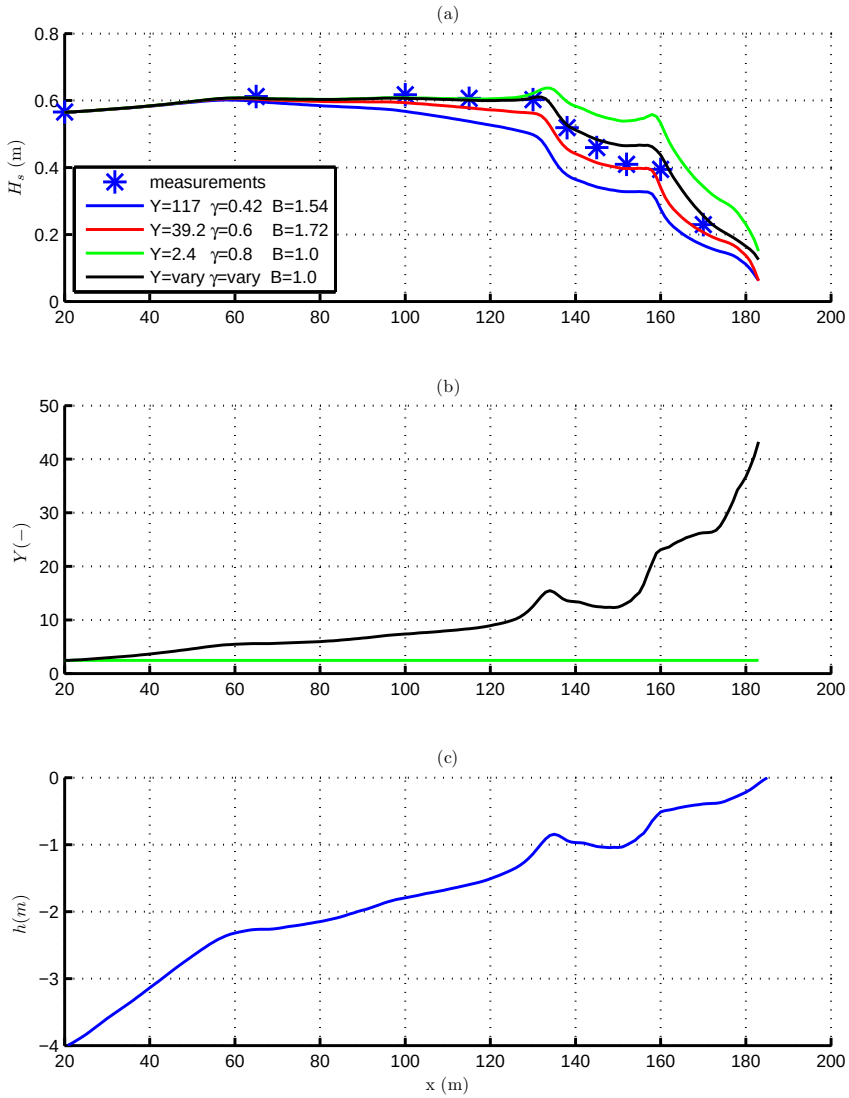

Figure 20: The cross-shore variation of (a) significant wave height, H_s, for the measurements during test stage 1C (blue stars); the model results (solid lines) with constant combined breaking wave paramater, Y, values and with varying Y; without the persistence length method, (b) constant Y vs. varying Y values, (c) bathymetry at the beginning of test stage 1C.

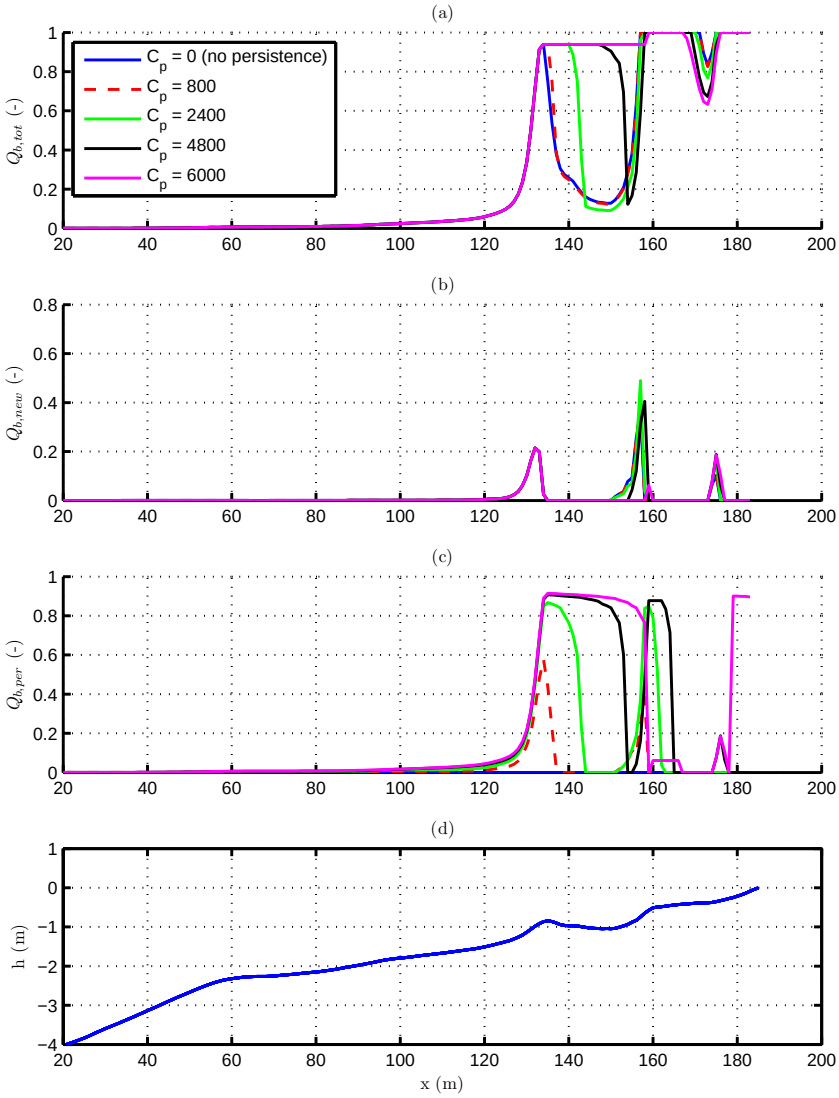

Figure 21: The cross-shore variation of the fraction of breaking waves for test stage 1C with different persistence length calibration constant, C_p, values. (a) total fraction of breaking waves, $Q_{b,tot}$, (b) fraction of new breakers, $Q_{b,new}$, (c) fraction of persisting breakers, $Q_{b,per}$, (d) the bathymetry.

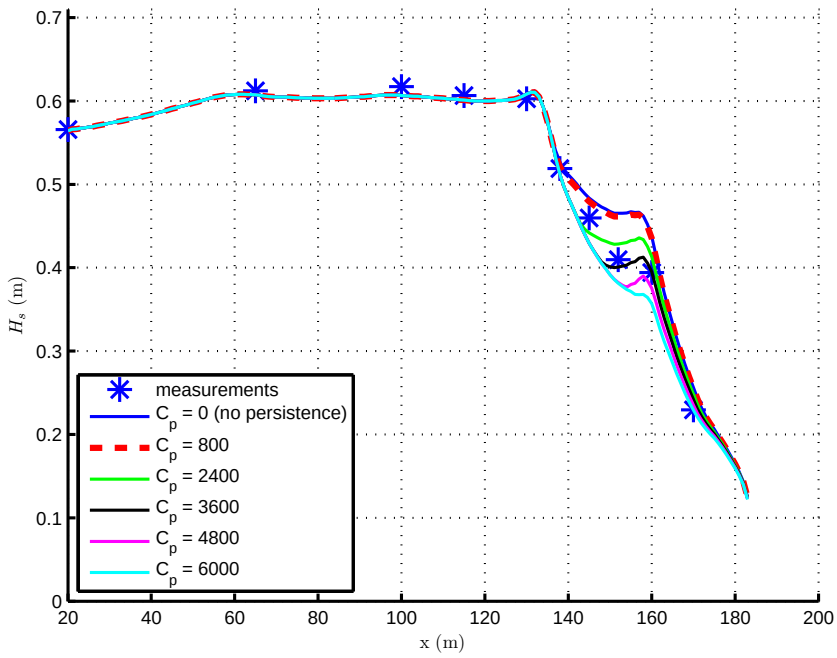

Figure 22: The cross-shore variation of significant wave height for the measurements during test stage 1C (blue stars); for the model results with different persistence lengths (solid lines) with varying γ, a B value of 1.00.

point in the bar trough and up to 40% of the waves break again at the end of the trough.

Figure 22 shows the wave height variation for those cases with different C_p values. It is clearly seen that the case with $C_p = 800$ has an insignificant effect on the wave height variation. The case with $C_p = 6000$ causes the wave height to decrease to a level lower than the measurements at all trough locations including x=160 m. The cases with C_p values of 3600 and 4800 gives better agreement to the measured wave height at the end of the trough. Even though $C_p = 2400$ is also close to the measurements for the trough locations, the rate of decrease in wave height stops earlier than it is observed in the measurements indicating that the dissipation is underpredicted in the latter half of the bar trough. Larger C_p values of 3600 and 4800 are close to the measurements and they are both used in further analysis of the hydrodynamics.

It needs to be mentioned here that for test stage 1C a wave friction factor value of

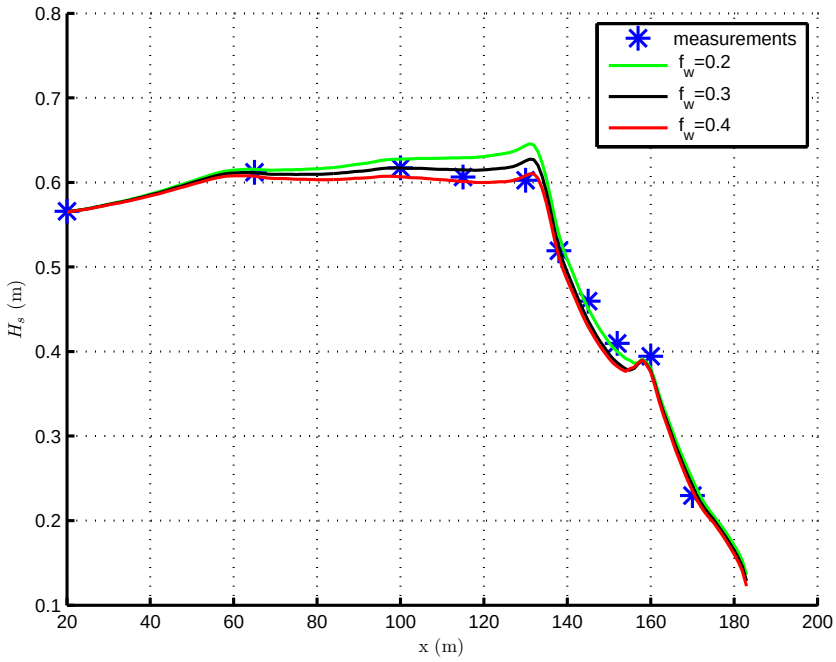

Figure 23: The cross-shore variation of significant wave height for the measurements during test stage 1C (blue stars); for the model results with different friction factor, f_w, used in the wave module (solid lines).

0.4 is preferred instead of 0.2. Although the Wilmott skill of the model is better for the smaller value of 0.2, the reason for this change is to acquire a better estimation of dissipation in the shoaling zone before breaking. It may be seen in Figure 23 that the wave height predictions are better before breaking when a friction factor value of 0.4 is used instead of 0.2. As described in chapter 2, the wave friction factor, f_w is used during the calculations of dissipation due to the turbulence bottom boundary layer, the effect of which will be more pronounced for the less energetic test stage 1C compared to the high energetic test stage 1B where the dissipation due to breaking dominates. Since the orbital excursion for test stage 1C is going to be smaller, a larger friction factor value is reasonable according to Equation 7.

Table 3 shows the variation of model skill for wave height predictions during test stage 1C along with model parameter values. An increase in model skill is observed as the model is enhanced. Run 1 is with the default *TG83* parameters. Runs 1 through

Table 3: The model skill calculated by Equation 135 for all instrument locations, d_H, and only trough locations, $d_{Htrough}$, for wave height predictions of test stage 1C with different values of the model parameters, combined breaking wave parameter, Y, the breaking wave parameters γ and B of Thornton and Guza (1983), persistence length constant, C_p, and wave friction factor, f_w.

Run number	Y	γ	B	C_p	f_w	d_H	$d_{Htrough}$
1	117.4	0.42	1.54	0	0.4	0.8951	0.3660
2	39.3	0.6	1.72	0	0.4	0.9794	0.6577
3	2.4	0.8	1	0	0.4	0.8551	0.3143
4	varying	varying	1	0	0.4	0.9873	0.6333
5	varying	varying	1	800	0.4	0.9891	0.6523
6	varying	varying	1	6000	0.4	0.9946	0.7637
7	varying	varying	1	2400	0.4	0.9962	0.7991
8	varying	varying	1	4800	0.4	0.9970	0.7947
9	varying	varying	1	4800	0.3	0.9866	0.8654
10	varying	varying	1	4800	0.2	0.9744	0.9944

3 are with constant Y and Run 4 is with the varying Y presented in Figure 20. Runs 5 through 8 are after the persistence length method is implemented and with C_p values of 800, 6000, 2400 and 4800 respectively, also shown in Figure 17. It is seen in Table 3 that the model skill considering all measurement locations, d_H, increases from 0.895 using the default parameters of *TG83* to an almost perfect 0.997 after varying Y is used and the persistence length method is implemented and calibrated. Table 3 also shows the model skill only for the measurement locations within the bar trough, $d_{Htrough}$, i.e. x=145, 152 and 160 m. It is observed that the model skill for wave height in the bar trough with the default parameters of *TG83* is only 0.366. The model skill increases to 0.8 showing the effect of the model improvements and enhancements. As expected the persistence length method has a significant effect in the bar-trough as may be seen in Table 3 while the model skill considering all measurement locations is not much different for the Runs 5 through 8. Therefore, an f_w value of 0.4, a B value of 1.7 and a C_p value of 4800 are selected as parameter values to be used in the wave model for LIP test stage 1C model runs.

3.2.2 Radiation Stresses

The radiation stresses are computed from the complex amplitudes in the wave module and passed to the circulation module by means of the master program. The mean water level is then computed in the circulation module by solving the cross-shore momentum balance. The dominant cross-shore momentum balance may be written as:

$$\frac{\partial S_{\alpha\beta}}{\partial x_\beta} = -\rho g h \frac{\partial \overline{\zeta}}{\partial x_\alpha} - \tau_\alpha^B. \tag{136}$$

As the momentum balance indicates, the pressure gradient, $\rho g h \frac{\partial \overline{\zeta}}{\partial x_\alpha}$, is a function of the radiation stress gradient, $\frac{\partial S_{\alpha\beta}}{\partial x_\beta}$, and the bottom shear stress, τ_α^B. The surface shear stress is not included in Equation 136 since winds are neglected in this study. In the surf zone, the radiation stress gradient is dominant over the bottom stress term (Svendsen, 2005). The cross-shore variation of the dominant cross-shore momentum balance is shown in Figure 24. It is observed that the variations in the pressure gradient is driven by the variations in radiation stress gradient. So, accurate predictions of the radiation stresses are important for accurate predictions of the mean water level variation.

As described in Chapter 2, the radiation stresses are calculated as the sum of a non-broken wave component and a roller contribution (Equation 35). The non-broken wave component is a function of the complex amplitudes and is directly proportional to the surface shape parameter, B_o (Equation 38). Once the other free parameter values affecting dissipation are set as described in the previous section, only Bo may change the magnitude and variation of non-broken wave component of radiation stresses. The default value (from linear wave theory) of B_o in the model is 1/8. Another free parameter to be calibrated is introduced in the roller contribution to the radiation stresses as the front slope angle of the roller at the surface, σ_r (Equation 47). The default value of σ_r is defined as 10 degrees which is also used by Madsen *et al.* (1997) based on the analogy to the hydraulic jump. Madsen *et al.* (1997) also

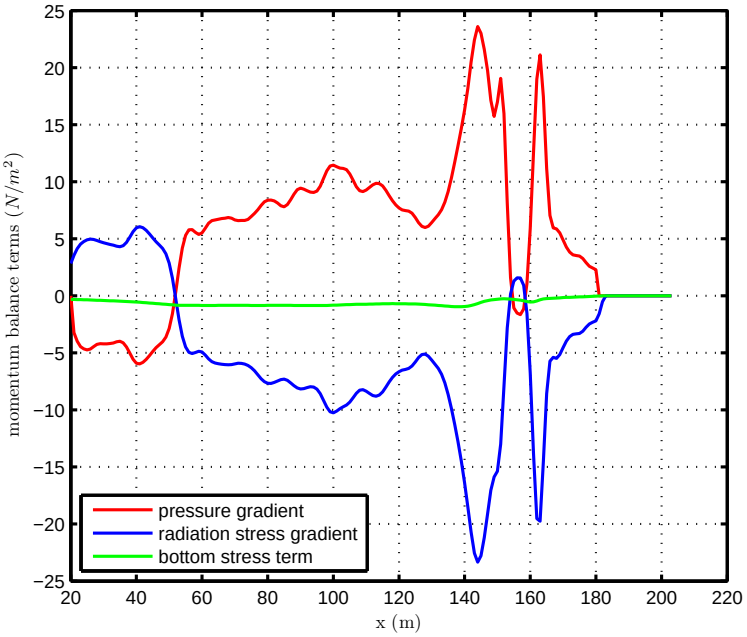

Figure 24: Cross-shore variation of depth integrated momentum balance from the model for test stage 1B.

suggests that a smaller value of 7 degrees be used as a special case of breaking over the horizontal part of a submerged bar.

Test Stage 1B

Figure 25 shows the modeled cross-shore variation of total radiation stress, S_{xx} using a B_o value of 0.125 and a σ_r value of 10. The roller component of the radiation stress is inversely proportional to the front slope, such that as σ_r increases, the roller contribution decreases. The effect of the roller is an enhancement to the radiation stress shifting the momentum shoreward by increasing the magnitude of S_{xx} at locations where breaking occurs. The peaks of the roller contribution are right offshore of the bar crest at x=140 m and at the end of the bar trough at x=160 m. At these locations, as the roller contribution increases, the gradient of radiation stresses increases which changes the mean water level variation. Therefore, it is important to choose appropriate values of parameters for accuracy. Since there are no direct

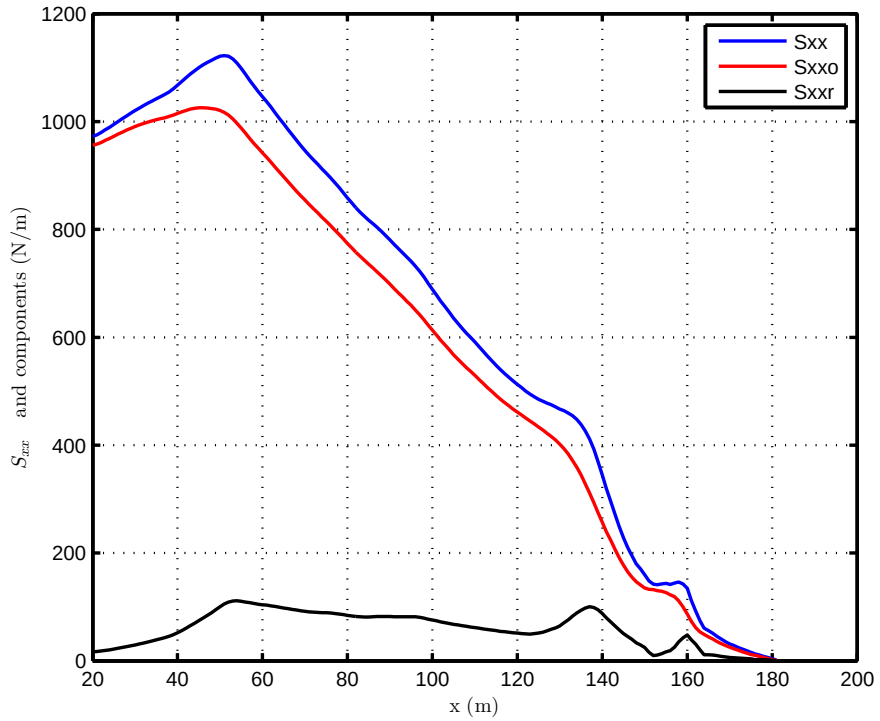

Figure 25: The modeled cross-shore variation of total radiation stress S_{xx} and its components; non-broken wave component, S_{xxo} and roller component, S_{xxr} for test stage 1B.

radiation stress measurements, it is necessary to use the mean water level variations as a proxy for estimating radiation stresses from the measurements.

The cross-shore momentum balance as given by Equation 136, and neglecting the bottom stress term, is used to find the total radiation stress $S_{xx,m}$, calculated from the measured mean water level. The non-broken wave component of the radiation stress $S_{xxo,m}$ is calculated as a function of measured wave height variation (Svendsen, 2005) using

$$S_{xxo,m} = H_{meas}^2 \left(\frac{c^2}{\sqrt{gh}} + \frac{1}{2} \right) B_o \tag{137}$$

where the subscript m denotes that it is calculated by using measured values, H_{meas} is a spline to the root-mean-squared wave height values extracted from the measurements, c is the wave speed evaluated via linear wave theory and h is the water depth. Finally, the roller component of the radiation stress from the measurements is found

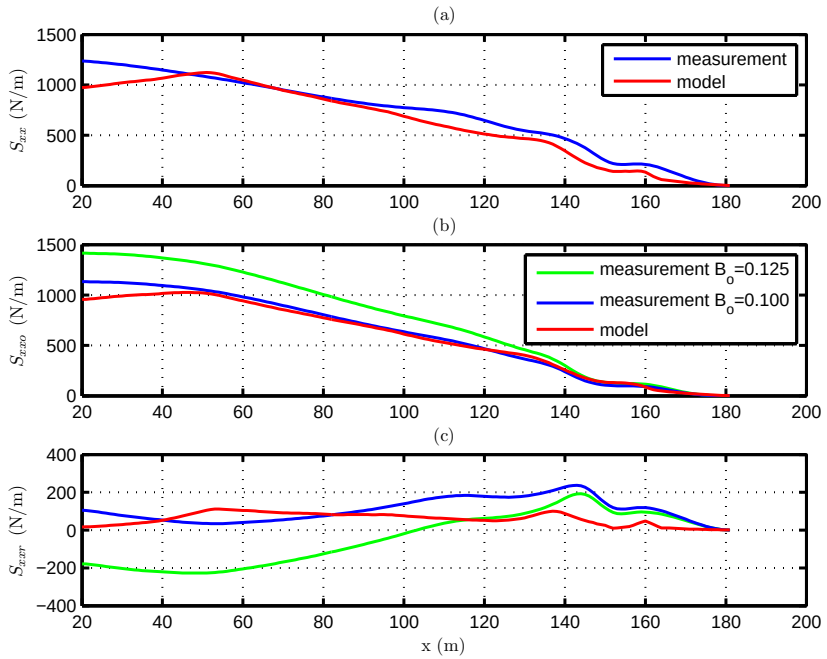

Figure 26: Model results with B_o=0.125 of the cross-shore variation of (a) total radiation stress S_{xx}, (b) non-broken wave component, S_{xxo}, (c) roller component, S_{xxr} for test stage 1B vs. estimations from measurements with Equation 137.

by the difference between $S_{xx,m}$ and $S_{xxo,m}$.

Figure 26(a) shows the total radiation stress for test stage 1B. The model results using the default surface shape parameter, B_o, value of 0.125 and the default roller front slope angle, σ_r, value of 10 are observed to underpredict the total radiation stress across much of the domain. Figure 26(b) and (c) shows the non-broken wave component of the radiation stress, S_{xxo}, and the roller component of the radiation stress, S_{xxr} respectively. The model underpredicts S_{xxo} compared to the measurements when B_o value of 0.125 is used for both as shown in Figure 26(b). The estimate of the non-broken wave component of the radiation stress extracted from the measurements, $S_{xxo,m}$ depends on the value of B_o used in Equation 137. It may be observed that when the default B_o value of 0.125 is used while calculating $S_{xxo,m}$, the roller component of the radiation stress, $S_{xxr,m}$, from the measurements goes negative offshore of x=100 m. This indicates that the default B_o value leads to unrealistically high $S_{xxo,m}$

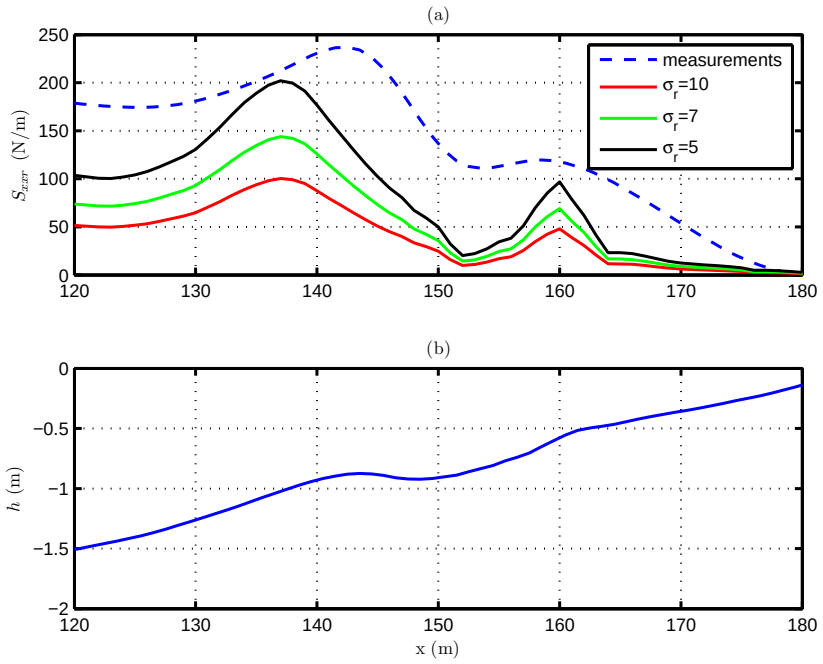

Figure 27: (a) Model results of the cross-shore variation of the roller component of radiation stress, S_{xxr}, with different roller front slope angle, σ_r values vs. the estimation from measurements with Equation 137 for test stage 1B using B_o=0.125, (b) bathymetry in the bar - trough zone.

values leading to erroneous $S_{xxr,m}$ estimations. When a lower B_o value of 0.100 is used while extracting the radiation stresses from measurements, the results for $S_{xxr,m}$ are realistic and the $S_{xxr,m}$ values are now positive in the offshore section as shown in Figure 26(c). On the other hand, the roller component of radiation stress, S_{xxr} is also observed to be underpredicted by the model using the default σ_r value of 10. This causes the total radiation stress to be underpredicted by the model. It needs to be mentioned here that the model results only for the default B_o value of 0.125 are shown for both test stages in this section since there are no direct measurements for S_{xx} and the calibration for B_o will be made during the mean water level analysis.

Figure 27(a) shows the cross-shore variation of the roller component of the radiation stress, S_{xxr}, in the bar - trough zone along with the bathymetry in Figure 27(b). The effect of using different roller front slope, σ_r, values is shown. As the σ_r value

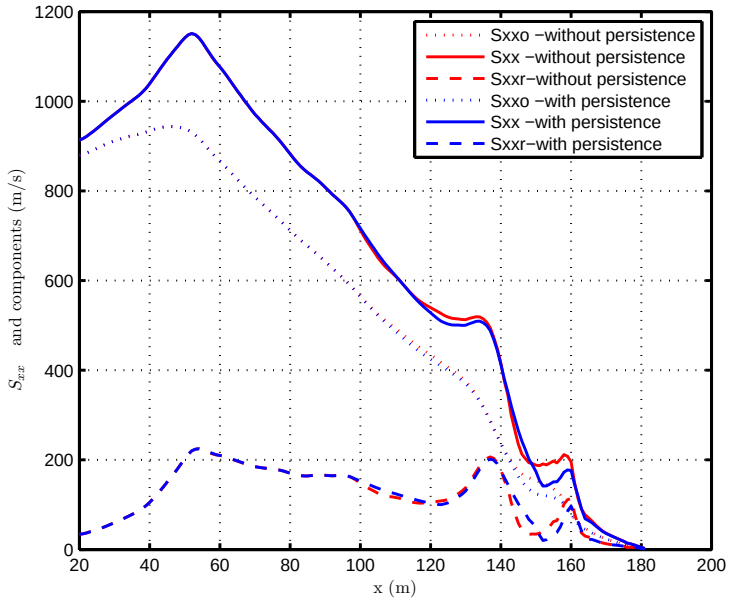

Figure 28: Model results of the cross-shore variation of total radiation stress S_{xx} (solid lines), non-broken wave component, S_{xxo} (dotted lines), roller component, S_{xxr} (dash lines) for test stage 1B with (blue lines) and without (red lines) the persistence length method implementation (with B_o=0.115 and $\sigma_r = 5$)

gets smaller than the default value of 10, the results are observed to be closer to the estimated S_{xxr} in magnitude. The values of $S_{xxr,m}$ extracted from measurements show that S_{xxr} peaks after major breaking occurs, i.e. first at the bar crest, x=142 m, and then at the end of trough, x=160 m. It may be seen from the wave height plots in Figure 18 in the previous section that the decrease in wave height starts earlier than those peak locations. On the other hand, the model predicts the first peak of S_{xxr} earlier than the measurements, because the model predicts S_{xxr} as a function of dissipation so that S_{xxr} starts decreasing as soon as dissipation starts decreasing as shown in Figure 16. This means the wave roller associated with wave breaking in the model has an immediate contribution earlier than the estimated $S_{xxr,m}$ from the measurements. This difference in the momentum of waves leads to a shift in the mean water level predictions as will be shown later.

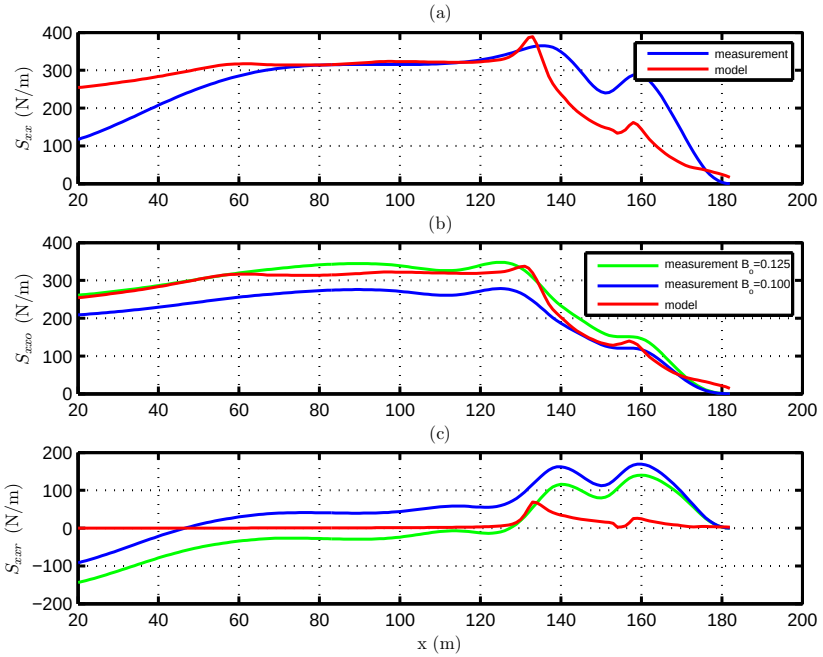

Figure 29: Model results with B_o=0.125 of the cross-shore variation of (a) total radiation stress S_{xx}, (b) non-broken wave component, S_{xxo}, (c) roller component, S_{xxr} for test stage 1C vs. estimations from measurements with Equation 137.

Figure 28 shows the cross-shore variation of the total radiation stress and the roller component of it before and after the persistence length method is implemented. The increase in dissipation due to persistence in the seaward half of the trough, as shown in Figure 16, causes an increase in the roller component of the radiation stress, which is proportional to the dissipation as given in Equation 47. In contrast, the increase in dissipation causes a decrease in the non-breaking wave component of the radiation stress associated with the decrease in wave height. Overall, the total radiation stress slightly increases between x=140 and 148 m. In the second half of the trough, the radiation stress is smaller after the persistence length method is implemented.

Test Stage 1C

The total radiation stress for test stage 1C is shown in Figure 29(a). The model results using the default surface shape parameter, B_o, value of 0.125 are observed to underpredict the total radiation stress after breaking occurs on the bar crest.

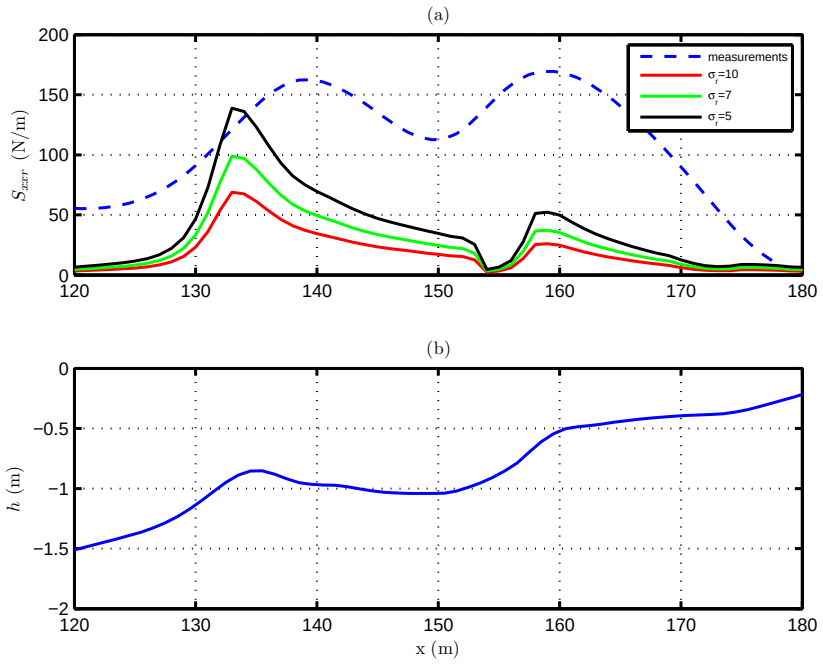

Figure 30: (a) Model results of the cross-shore variation of the roller component of radiation stress, S_{xxr}, with different roller front slope angle, σ_r values vs. the estimation from measurements with Equation 137 for test stage 1C using a surface shape parameter, $B_o = 0.125$, (b) bathymetry in the bar - trough zone.

Figure 29(b) shows the non-broken wave component of the radiation stress, S_{xxo}, and Figure 29(c) shows the roller component of the radiation stress, S_{xxr}. Unlike test stage 1B, the model predictions for S_{xxo} using the default B_o value of 0.125 are already close to the measured values calculated from the wave height measurements using the same B_o value.

Similar to test stage 1B, it is observed that when the default surface sape parameter, B_o, value of 0.125 is used while calculating the non-broken wave component of the radiation stress extracted from the measurements, $S_{xxo,m}$, the roller component $S_{xxr,m}$ from the measurements goes negative offshore of x=130 m. For this reason, as done in test stage 1B analysis, a smaller B_o value of 0.100 is used while extracting the radiation stresses from measurements. The $S_{xxr,m}$ values are still negative in part of the domain and then above zero in the offshore section immediately preceding the

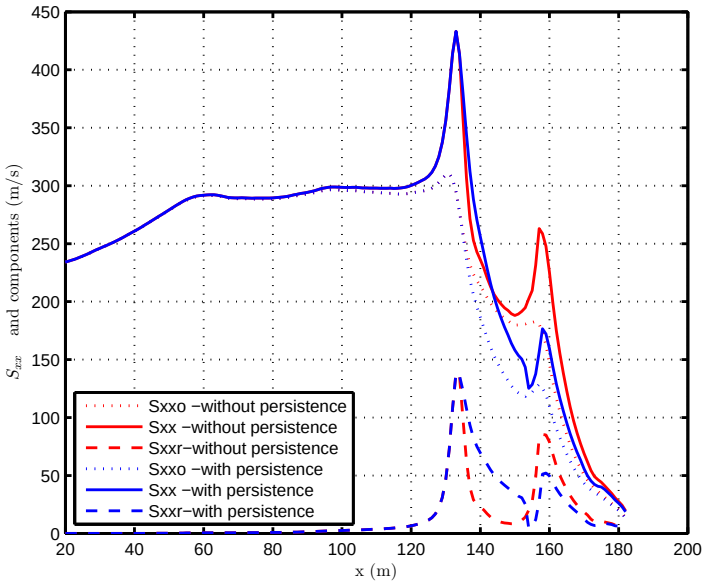

Figure 31: Model results of the cross-shore variation of total radiation stress S_{xx} (solid lines), (b) non-broken wave component, S_{xxo} (dotted lines), (c) roller component, S_{xxr} (dash lines) for test stage 1C with (blue lines) and without (red lines) the persistence length method implementation (with B_o=0.115 and $\sigma_r = 5$).

breaking on the bar crest at x=138 m as shown in Figure 29(c). However, since shoaling occurs offshore of the bar crest and there is almost no breaking offshore of the bar crest which would lead to roller formation at the surface, the roller contribution should be minimal prior to the bar crest. The calibration of B_o will later be discussed in the mean water level analysis. Finally, the roller component S_{xxr} is observed to be underpredicted in the bar/trough region by the model using the default roller front slope angle, σ_r, value of 10 as in test stage 1B.

Figure 30(a) and (b) show the cross-shore variation of the roller component of the radiation stress, S_{xxr}, and the bathymetry in the bar - trough zone respectively. Similar to case 1B, as the roller front slope angle, σ_r, value gets smaller than the default value of 10, the S_{xxr} predictions get larger and closer to the measured $S_{xxr,m}$ in magnitude. Similar to test stage 1B, the model predicts the first peak in S_{xxr} earlier than the measurements. It may be seen in Figure 22 that the wave height

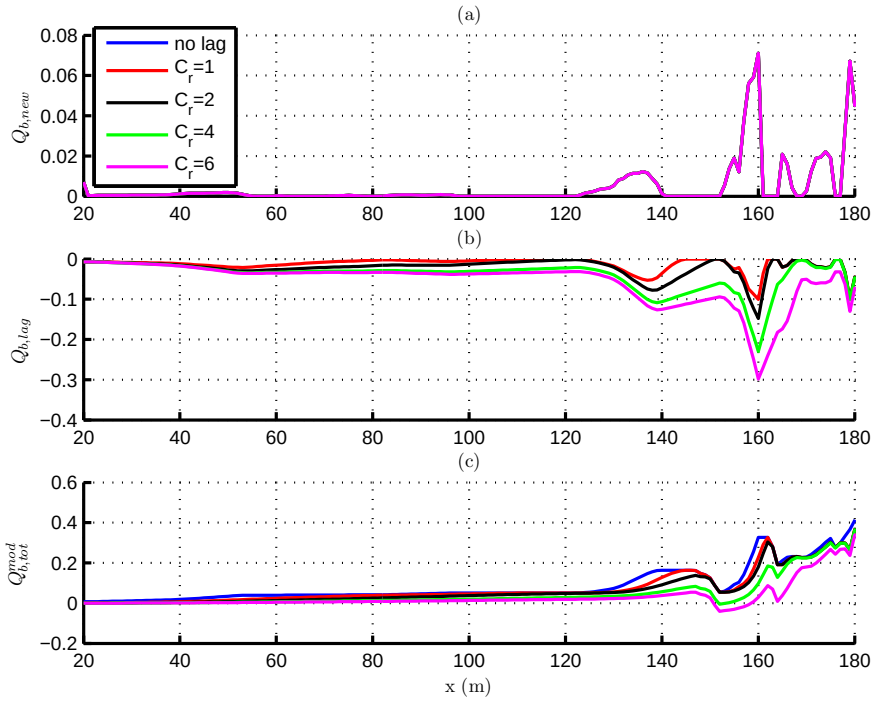

Figure 32: Fraction of breaking waves for test stage 1B and the effect of roller lag length. (a) fraction of newly breaking waves, $Q_{b,new}$, (b) fraction of breaking waves causing roller lag, $Q_{b,lag}$, (c) modified total fraction of breaking waves, $Q_{b,tot}^{mod}$ using a roller front slope, σ_r, value of 5 and a surface shape parameter, B_o, value of 0.1 .

starts decreasing at x=132 m. But, the $S_{xxr,m}$ values extracted from measurements show that it initially peaks after this point where major breaking occurs and then where breaking occurs at the end of trough, at x=160 m. Moreover, $S_{xxr,m}$ shows the second peak at the end of the trough to be similar or slightly larger than the first one at the bar crest while the model predicts the second peak to be much smaller than the first peak.

Figure 31 shows the cross-shore variation of the total radiation stress and the roller component of it before and after the persistence length method is implemented. Similar to the result for test stage 1B, the increase in dissipation due to persistence in the seaward half of the trough, as shown in Figure 21(a), causes an increase in the roller component of the radiation stress. Meanwhile, the increase in dissipation causes a decrease in the non-breaking wave component of the radiation stress associated with

the decrease in wave height. In the seaward section of the trough the former effect described above overcomes the latter and the total radiation stress slightly increases between x=134 and 143 m. After x=143 up to the shoreline, the decrease in wave height due to persistence dominates and the total radiation stress is smaller for the case with breaking wave persistence.

Roller lag method

The apparent lag between the modeled and measured roller component of the radiation stress for both test stages of the Delta Flume experiment emphasizes the necessity of implementing a lag to the roller momentum, i.e. the roller component of the radiation stresses in the numerical model. The roller lag method implemented in this study was described in Chapter 2. Figure 32 shows the cross-shore variation of newly breaking waves, $Q_{b,new}$, the fraction of breaking waves used in the roller lag method, $Q_{b,lag}$ given by Equation 55 and the modified total fraction of breaking waves, $Q_{b,tot}^{mod}$ given by Equation 54. It may be observed that as a larger roller lag length calibration coefficient (C_r) is used, $Q_{b,lag}$ increases since a larger contribution is made by $Q_{b,new}$. $Q_{b,tot}^{mod}$ goes negative and almost zero for C_r values of 4 and 6, respectively. This indicates that the roller lag length exceeds the persistence length with those C_r values and are therefore not feasible.

Figure 33(a) shows the cross-shore variation of roller component of radiation stress for test stage 1B using a surface shape parameter, B_o, value of 0.1 and a smaller than default roller front slope angle, σ_r, value of 5. It is observed that when a roller lag length calibration coefficient, $C_r = 1$, is used, a shift in the peak of roller component of the radiation stress, S_{xxr}, towards onshore is observed along with a decrease in magnitude. It may easily be seen that larger C_r values of 2 and 4 flatten out the first peak onshore of the bar crest. For this reason, they are immediately eliminated as the options. $C_r = 1$ results in a shift of the first peak as may also be seen from Figure 33(b) in the gradient of the roller component of radiation stress and improves

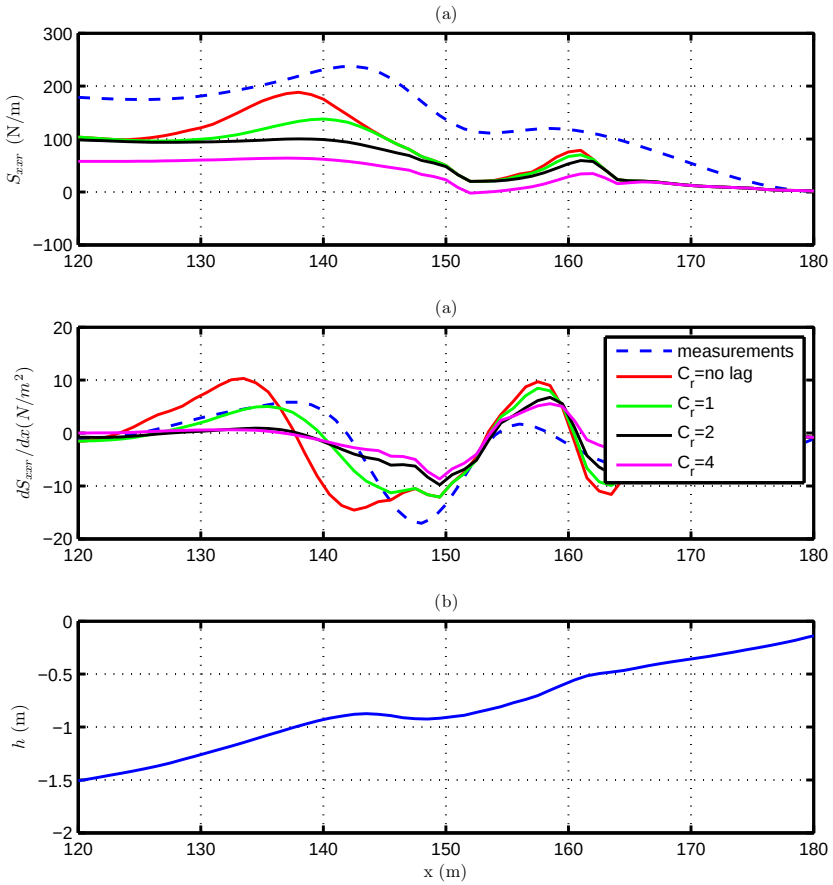

Figure 33: (a) Model results of the cross-shore variation of the roller component of radiation stress, S_{xxr} vs. the estimation from measurements with Equation 137 for test stage 1B with a surface shape parameter, B_o, value of 0.115 and a roller front slope angle, σ_r, of 5, (b) model results of the cross-shore variation of the gradient of the roller component of radiation stress, dS_{xxr}/dx vs. estimations from measurements with Equation 137 for test stage 1B, (c) bathymetry in the bar - trough zone.

the agreement with the measurements. Even though the magnitude of S_{xxr} compare better before the roller lag implementation, the magnitude and peak locations of the gradient of S_{xxr} compares better after the implementation. The gradient of the radiation stress has more importance since it affects not only the mean water level estimations but also the currents.

Figure 34(a) shows the effect of roller lag on the cross-shore variation of roller component of radiation stress for test stage 1C. It is observed that when a roller lag length constant, $C_r = 4$ is used, a shift in the peak of roller component of radiation

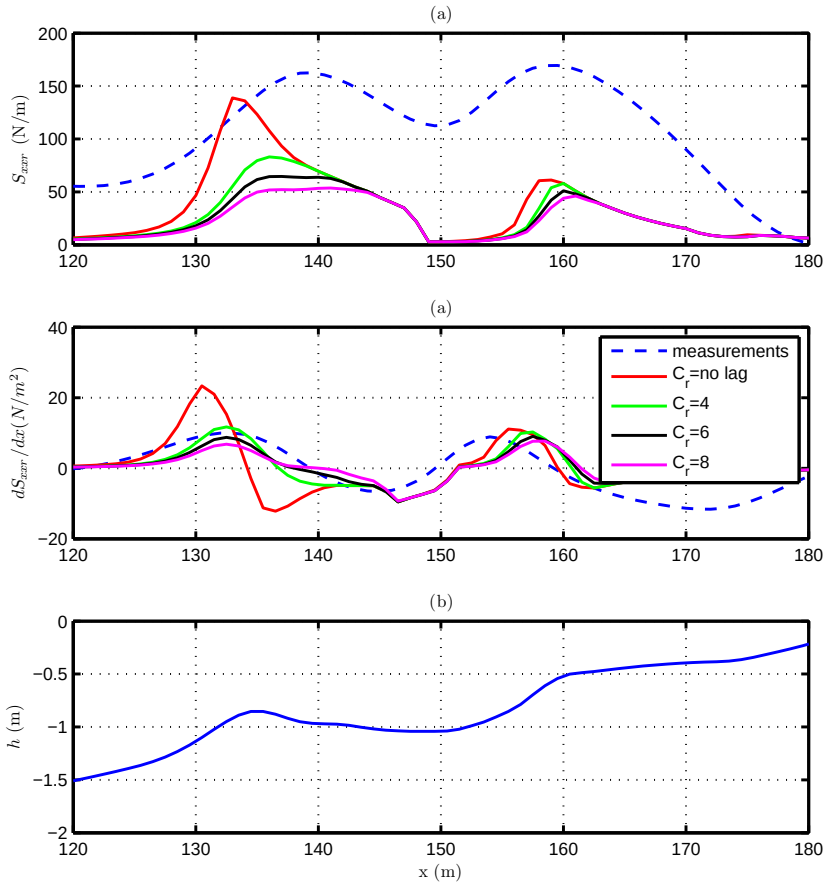

Figure 34: (a) Model results of the cross-shore variation of the roller component of radiation stress, S_{xxr}, vs. the estimation from measurements with Equation 137 for test stage 1C with a surface shape parameter, B_o, value of 0.115 and a roller front slope angle, σ_r, of 5, (b) model results of the cross-shore variation of the gradient of the roller component of radiation stress, dS_{xxr}/dx, vs. estimations from measurements with Equation 137 for test stage 1C, (c) bathymetry in the bar - trough zone.

stress, S_{xxr}, towards onshore is observed along with a decrease in magnitude. It may easily be seen that larger C_r values of 6 and 8 flatten out the first peak onshore of the bar crest. For this reason, they are immediately eliminated as the options. $C_r = 4$ results in a reasonable shift of the first peak to a point onshore of the bar crest, i.e. from x=133 to x=136 m. Similar to test stage 1B, since the fraction of breaking waves used in the roller lag method, $Q_{b,lag}$ reduces the fraction of breaking waves and consequently the dissipation, the magnitude of the roller component of radiation stress gets smaller once the roller lag is used.

The apparent lag between radiation stresses in the model and measurements in Figure 34(a) is improved once the roller lag method is implemented. The lag not only helps the model to get a closer prediction for the peak location with zero gradient but also improves the prediction for the magnitude of the gradient of the roller component of radiation stress.

Even if accurate predictions of radiation stresses are desired, it needs to be emphasized that what matters more for accurate mean water level and current predictions is the gradient of radiation stresses such that locations of peaks are more important than overall magnitudes. Since there are no direct measurements of radiation stresses, the Wilmott skill of the numerical model for radiation stress predictions is not evaluated.

3.2.3 Mean Water Level

The pressure gradient, i.e. the mean water level gradient is a function of the radiation stress gradients, therefore improvements in the radiation stresses mentioned in the previous section should affect the mean water level predictions and consequently improve the undertow predictions leading to better estimations of sediment transport. The predictions by the circulation module, SHORECIRC, of the mean water level are analyzed in this section and the depth-varying currents in the next. The focus of this section is to understand the variation of the mean water level on barred beaches and

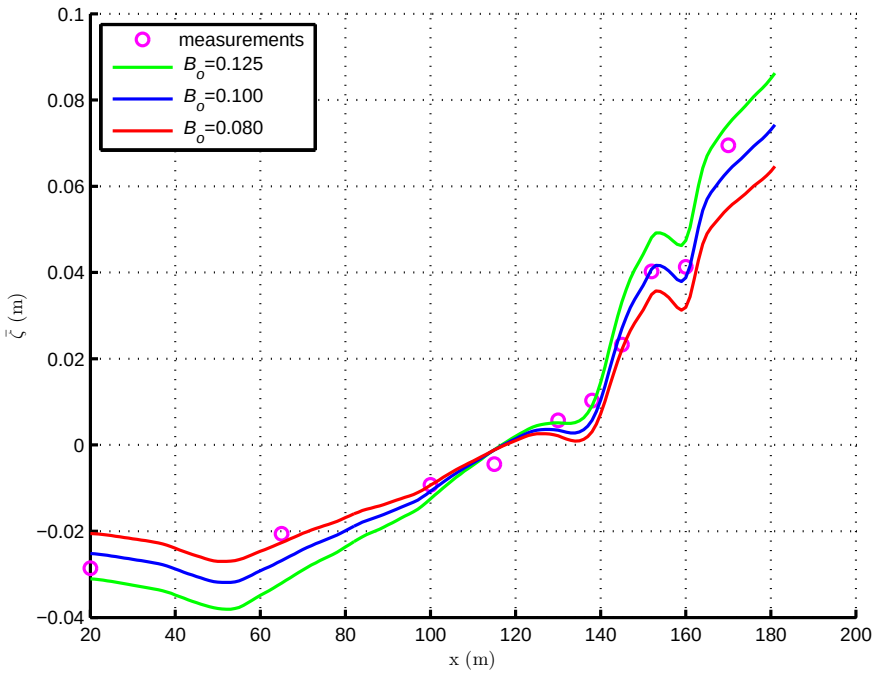

Figure 35: Cross-shore variation of the mean water level for test stage 1B; measurements (circles) vs model predictions (solid lines) for different surface shape parameter, B_o, values with a roller front slope angle, σ_r, value of 5.

the role of the roller enhancements and radiation stresses to the mean water level predictions.

The model results are compared to the pressure gage measurements for both test stages. It has been mentioned in the radiation stress analysis that the surface shape parameter, B_o, and the roller front slope angle, σ_r, are the two parameters that affect the radiation stress variations evaluated within the wave module. As a result, those parameters will affect the model computations of the mean water level variations.

Figure 35 shows the cross-shore variation of the mean water level for test stage 1B predicted by the numerical model using different surface shape parameter, B_o values with a roller front slope angle, σ_r value of 5. Unlike the effect of σ_r, which is a local effect due to the breaking initiated roller, B_o has a general effect of changing the magnitude of the radiation stress and hence changing the gradient accordingly. Due to the primary cross-shore momentum balance between the radiation stress gradient

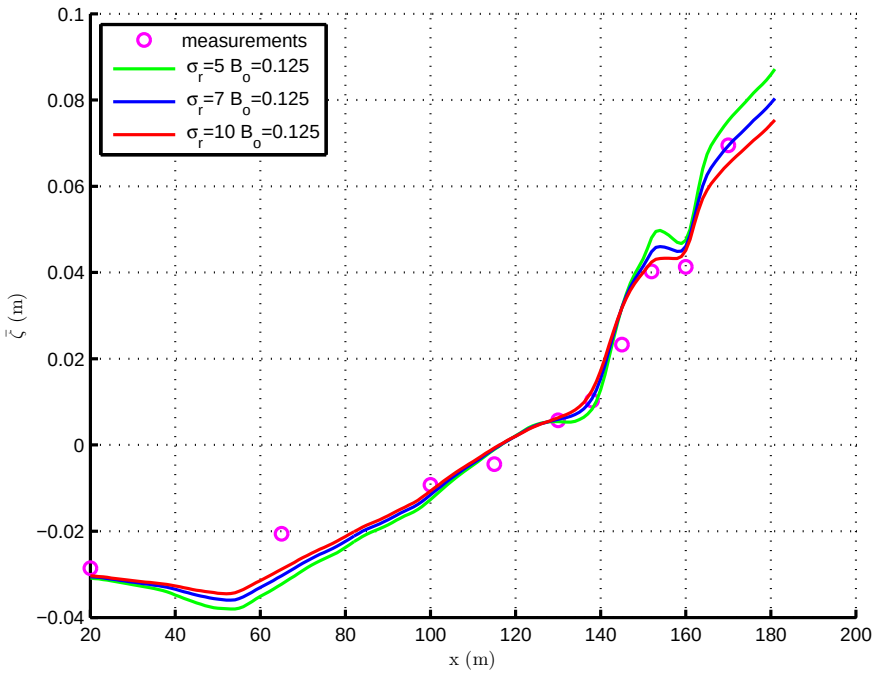

Figure 36: Cross-shore variation of the mean water level for test stage 1B; measurements (circles) vs model predictions (solid lines) for different roller front slope angle, σ_r, values with a surface shape parameter, B_o, value of 0.125 .

and the pressure gradient, changes in B_o will directly change the mean water level everywhere. As B_o gets smaller, the mean water level gradient gets smaller in the entire domain with less set-down prior to breaking and less set-up after breaking. It is realized from Figure 35 that the magnitude of the set-down and set-up for the model results with the default B_o value of 0.125 is close to but generally slightly larger than the measurements. This is an implication of a large value of B_o and actually the default value of 0.125 is the maximum possible value of it. A smaller B_o value of 0.100 was observed to give a more realistic variation of measured radiation stresses compared to the default value of 0.125 in the previous section as shown in Figure 26. It may be seen in Figure 35 that a B_o value of 0.100, in fact, results in a better agreement of the model predictions of the mean water level to the measurements.

The mean water level variations for various values of roller front slope angle, σ_r, are shown in Figure 36 for the model runs with the default surface shape parameter,

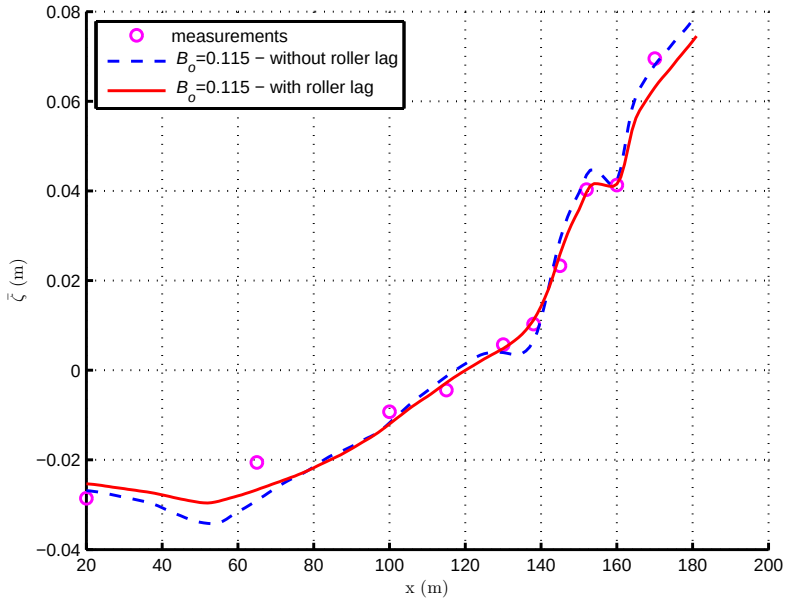

Figure 37: Cross-shore variation of the mean water level for test stage 1B; measurements (circles) vs model predictions with the roller lag (solid line); without the roller lag (dash line) with a surface shape parameter, B_o, value of 0.115 and a roller front slope angle, σ_r, value of 5.

B_o value of 0.125 without the roller lag implementation. It may be observed that even if the mean water level magnitudes are similar for any σ_r value used, the gradients are different at locations where the roller starts contributing. The mean water level gradient even changes sign at the end of the trough (x=155 m) as the σ_r value decreases resulting in a small region of set-down. It is not possible to tell whether such a set-down occurs in experiments since the measurements are sparse. However, the pressure gradient, i.e. the gradient of the mean water level is a dominant forcing for the currents, and it will be shown in the next section that the current predictions are highly sensitive to these variations in pressure gradient.

Figure 37 shows the mean water level variations from the model with and without the roller lag implementation using a roller lag length calibration coefficient, C_r of 1 and using a surface shape parameter, $B_o = 0.115$. It may now be seen that once the

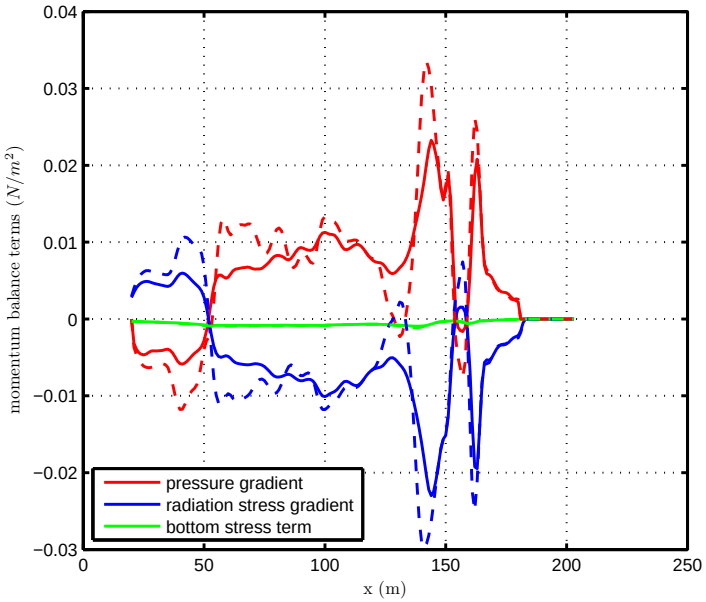

Figure 38: Modeled cross-shore variation of depth integrated momentum balance for test stage 1B with the roller lag method (solid lines) and without the roller lag method (dash lines).

roller lag is implemented, the model predictions improve at the gage locations in the zones with strong breaking, i.e. x=132 and x=138 right offshore of the bar crest and x=160 at the end of bar trough.

The roller lag method affects the roller component of radiation stresses and wave volume fluxes. In order to understand the effect of roller lag on the mean water level variations, the cross-shore variation of the dominant cross-shore momentum balance is shown in Figure 38 with and without the roller lag method. The variations in the pressure gradient are balanced by the variations in radiation stress gradient for both cases almost like a mirror image. The roller lag decreases the roller contribution to the radiation stress as shown in Figure 33 which reduces the magnitude of the peaks in the cross-shore variation of the radiation stress. As a result, the gradient of radiation stress decreases as well as the mean water level gradient. This effect is most pronounced right offshore of the bar crest (x=140 m) and at the inshore end

of bar trough (x=160 m) where the majority of new breaking is occuring and the roller makes a significant contribution to the flow momentum. Without the roller lag, the new breaking occuring between x=120 and 140 m (see Figure 32) leads to an increase in radiation stress due to the immediate addition of the roller. This results in a positive radiation stress gradient as seen in Figure 38 which must be balanced by a negative pressure gradient thereby creating the small set-down prior to x=140 seen in Figure 37. Once the roller lag is included, the sudden increase in radiation stress does not happen and radiation stress gradient remains negative and therefore the pressure gradient is always positive.

The Wilmott skill of the numerical model in predicting the mean water level increases from 0.98 for the case with default values of surface shape parameter, B_o = 0.125 and roller front slope angle, σ_r = 10 and with no roller lag to 0.996 for test stage 1B for $B_o = 0.115$ and $\sigma_r = 5$, and the roller lag method implementation with $C_r = 1$.

Test Stage 1C

Figure 39 shows the cross-shore variation of the mean water level predicted by the numerical model using different surface shape parameter, B_o values and with the roller front slope angle, σ_r value of 5. The peak at x=152 m before shoaling starts at the end of the trough is observed to be captured when B_o values of 0.125 and 0.100 are used. Both B_o values result in a strong dip at x=131 m at the end of the set-down region before the set-up zone starts. Even though there are no measurements between x=130 and x=138 m, the measured value at x=130 m is higher. It may be observed that both B_o values of 0.125 and 0.100 results in a very strong gradient in the set-up region between x=131 and x=152 while the measurements show a smaller gradient. This discrepancy is one of the main reasons for inaccurate predictions of the currents as will be shown in the following section. Figure 40 shows the cross-shore variation of the mean water level predicted by the numerical model using different roller front slope

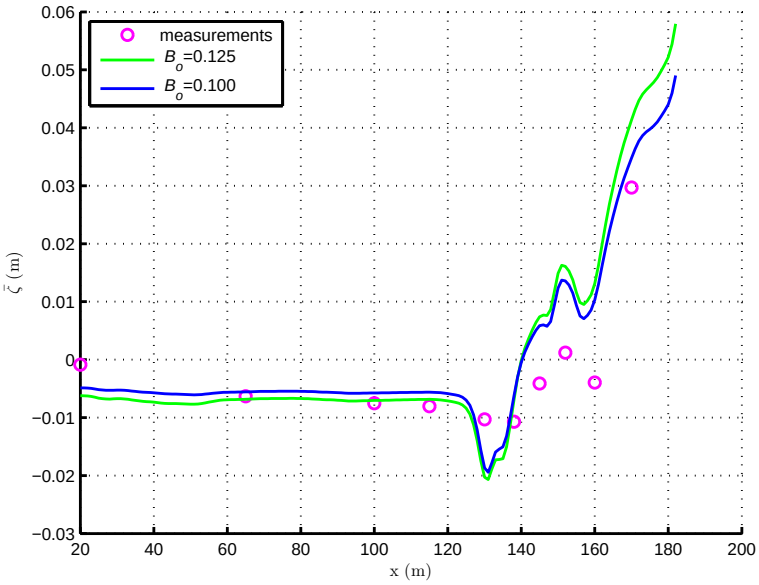

Figure 39: Cross-shore variation of the mean water level for test stage 1C; measurements (circles) vs model predictions (solid lines) for different surface shape parameter, B_o, values with a roller front slope angle, σ_r, value of 5.

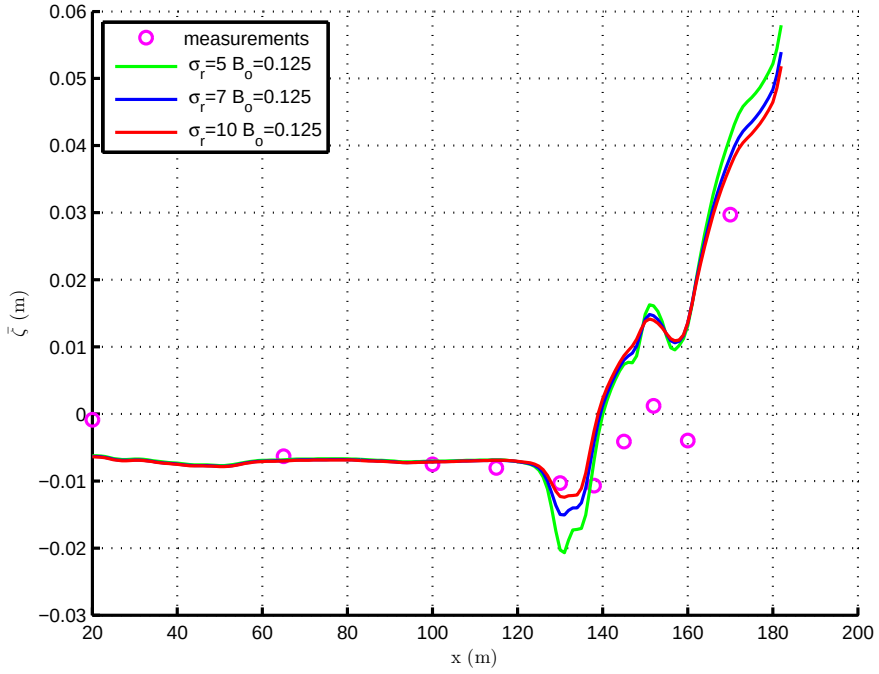

Figure 40: Cross-shore variation of the mean water level for test stage 1C; measurements (circles) vs model predictions using different roller front slope angle, σ_r, values with the default surface shape parameter, B_o, value of 0.125 (solid lines).

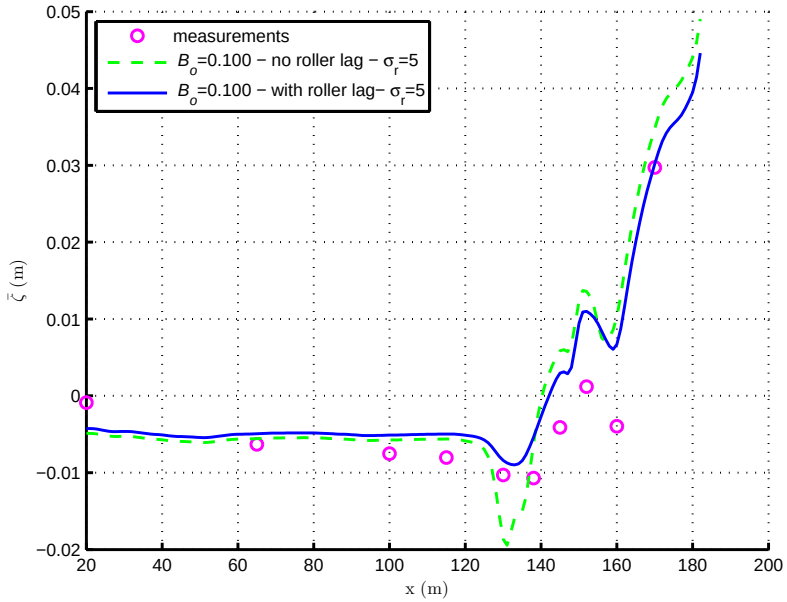

Figure 41: Cross-shore variation of the mean water level for test stage 1C; measurements (circles) vs model predictions with the roller lag (solid line); without the roller lag (dash line) with a surface shape parameter, B_o, value of 0.100 and a roller front slope angle, σ_r, value of 5

angle, σ_r values, a surface shape parameter, B_o value of 0.125 and without the roller lag method implementation. Similar to test stage 1B, the results are most different in the transition zones between set-down and set-up where the roller contribution is changing most rapidly. The set-down is strongly affected prior to the bar crest due to the rapid addition of the roller contribution indicating the need for the roller lag. Figure 41 shows the cross-shore variation of the mean water level predicted by the numerical model with and without the roller lag method. It is clear that without the roller lag method implemented, the strong gradients in radiation stress, as shown in Figure 34, cause a dip in the mean water level right offshore of the bar crest and also in the bar trough right onshore of the bar crest. The resultant strong gradients in the mean water level has a significant effect on the current variations. Once the roller lag method is implemented, these strong gradients at the break zones are eliminated

and the variation of modeled mean water level and its gradients for test stage 1C are closer to the measurements.

The roller lag implementation and the calibration of surface shape parameter, B_o, and roller front slope angle, σ_r, resulted in model predictions very close to the measurements for test stage 1B. The same changes and parameter calibrations in the model also improved the predictions for test stage 1C. As found in test stage 1B, the results with the B_o value of 0.115, and in accordance with earlier findings for test stage 1C with the B_o value of 0.100 are both better in the set-up region. Similarly, a σ_r value of 5 is again shown to be superior to the default model value of 10. But as may be seen in Figure 41, there are still some discrepancies between model results and measurements. The model still overpredicts the set-up in the bar - trough zone leading to stronger pressure gradients after wave breaking as compared to those extracted from measurements. Despite of those discrepancies, the Wilmott skill of the model for the mean water level predictions of test stage 1C is observed to increase from 0.76 with default values of $B_o = 0.125$ and $\sigma_r = 10$ and with no roller lag to 0.96 for $B_o = 0.115$ and $\sigma_r = 5$ and the roller lag method implementation with a roller lag length constant of $C_r = 4$.

3.2.4 Wave Volume Fluxes and Currents

The final element of hydrodynamics predictions is the calculation of the currents. Accurate predictions of the currents are very important for the calculation of sediment transport and predictions for the morphological evolution on barred beaches. For this reason, a comprehensive analysis is done on the parameters affecting the cross-shore distribution and the depth structure of currents. Accurate predictions of the bottom currents in the bar - trough zone is especially important for LIP test stage 1B since the sandbar moves offshore mainly due to the sediment transport governed by the current. The focus here is to understand how the currents vary on a barred beach and

their connections to the enhancements in the dissipation and the radiation stresses.

Wave Volume Fluxes

As described by Equation 75 in the previous chapter, the modeled currents have a depth-averaged component and a depth-varying component. The former is calculated based on the total and wave volume fluxes given by Equation 76. Since the experiments are conducted in a closed basin, the total volume fluxes are equal to zero. Therefore the depth-averaged component of the mean currents is only a function of wave volume fluxes and equal to the depth integral of the total mean current. Similar to the radiation stresses, the wave volume fluxes have a non-broken wave component and a roller component. Since the wave volume fluxes are computed on a component-by-component basis, accurate predictions of the complex amplitudes have a great importance. Therefore, all the calibrations made during wave height estimations apply for the volume fluxes and are expected to improve predictions. The roller component to the wave volume fluxes, given by Equation 50 and Equation 51, is inversely proportional to the front slope angle of the roller at the surface, σ_r as in the case of the radiation stresses. For this reason, the calibrations made to the free parameter σ_r are also expected to apply for the volume fluxes. Like the radiation stresses, the wave volume fluxes may be estimated from the measurements. The currents measurements by the electromagnetic current meters mounted on the moving carriage are used to derive depth-averaged currents by integrating the measurements at each cross-shore location over depth. With zero total fluxes, the wave volume fluxes are directly proportional to the depth-averaged currents and they may be calculated from the measured depth-averaged currents. The model results for the depth-averaged currents as well as the wave volume fluxes for test stage 1B are compared to the results extracted from the current measurements in Figure 42 and Figure 43. As it may be seen from Figure 42, the depth-averaged current inside the bar trough locations x=145 and x=152 m are underpredicted for test stage 1B when

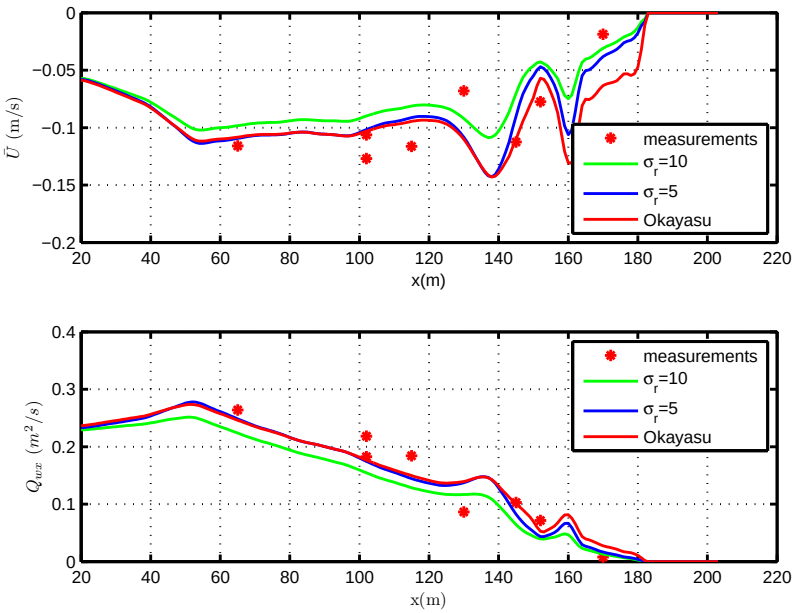

Figure 42: Cross-shore variations of (Top panel) depth-averaged currents, $\overline{U}$, and (Bottom panel) wave volume fluxes, Q_{wx}, for measurements (red stars) and model results (solid lines) for different roller front slope angle, σ_r, values with the default surface shape parameter, B_o value of 0.125 for test stage 1B.

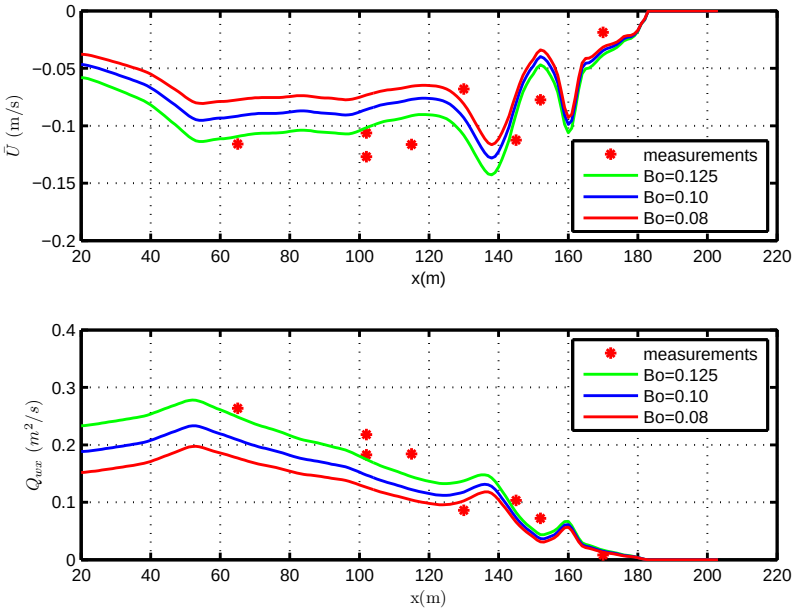

Figure 43: Cross-shore variations of (Top panel) depth-averaged currents, $\overline{U}$, and (Bottom panel) wave volume fluxes, Q_{wx}, for measurements, Q_{wx}, (red stars) and model results (solid lines) for different surface shape parameter, B_o values with the roller front slope angle, σ_r value of 5 for test stage 1B.

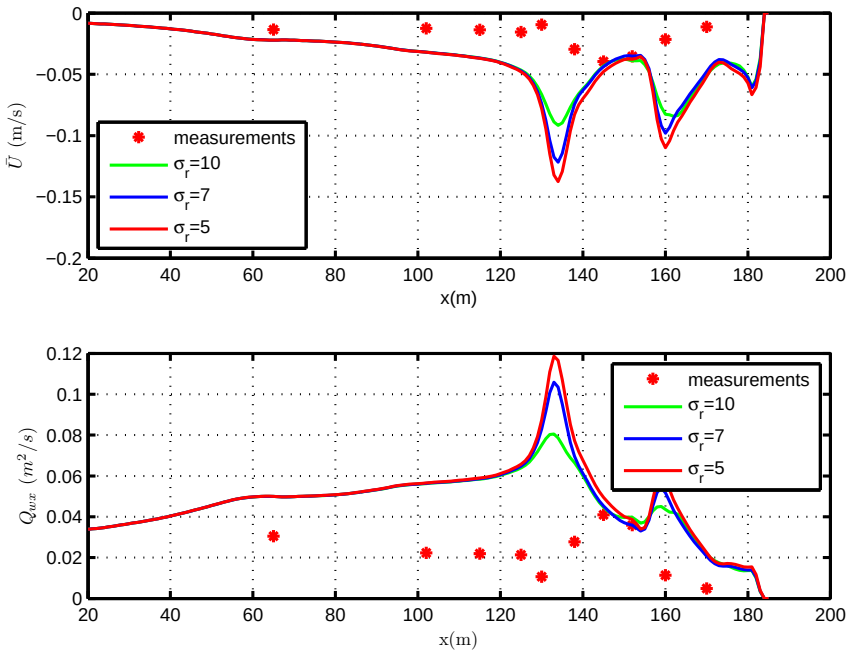

Figure 44: Cross-shore variations of (Top panel) depth-averaged currents, $\overline{U}$, and (Bottom panel) wave volume fluxes, Q_{wx}, for measurements (red stars) and model results (solid lines) for different roller front slope angle, σ_r values with the default surface shape parameter, B_o value of 0.125 for test stage 1C.

the default σ_r value of 10 is used in Lippman's roller model. The model results are improved at x=145 m as the smaller σ_r value of 5 is used in the roller model.

Okayasu *et al.* (1986)'s wave model results are also included in Figure 42 for comparison. It is observed that Okayasu's roller model gives better results for the depth-averaged currents and wave volume fluxes inside the trough. However, Okayasu's model does not give good results for the case with longer waves in test stage 1C and overestimates the roller contribution by almost an order of magnitude since the breakers are saturated in that case. Therefore, the use of Okayasu's roller model instead of the default roller model of Lippman's is not pursued.

Figure 44 shows the cross-shore variation of the wave volume flux and the depth-averaged current for test stage 1C. The model overpredicts the depth-averaged current for test stage 1C even for the default roller front slope angle, σ_r value of 10 and for

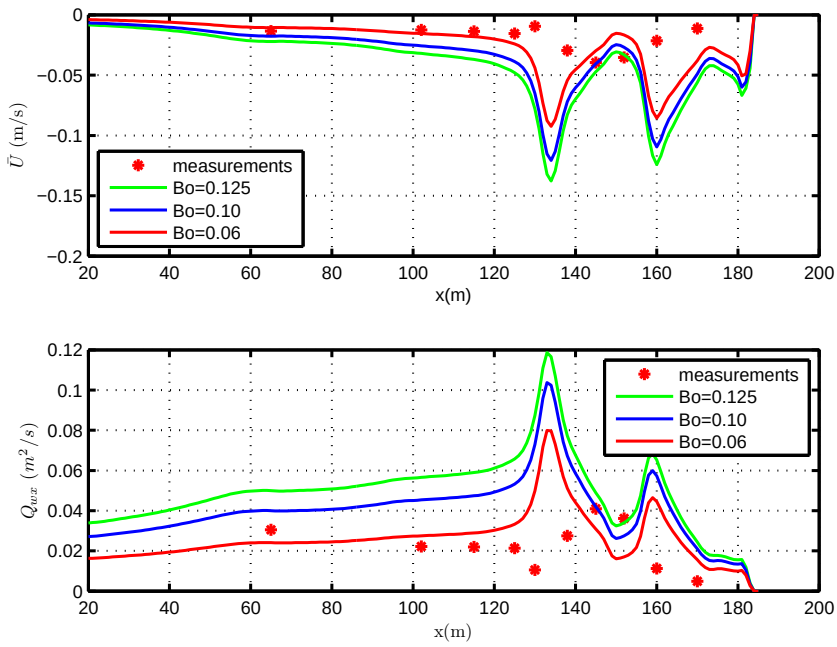

Figure 45: Cross-shore variations of (Top panel) depth-averaged currents, $\overline{U}$, and (Bottom panel) wave volume fluxes, Q_{wx}, for measurements (red stars) and model results (solid lines) for different surface shape parameter, B_o values with the roller front slope angle, σ_r value of 5 for test stage 1C.

smaller σ_r values, the model predicted even larger volume fluxes and depth-averaged currents. Figure 45 shows the depth-averaged current, $\overline{U}$, and the cross-shore wave volume flux, Q_{wx}, for various B_o values. Once again it may be observed that the model overpredicts Q_{wx} and $\overline{U}$ for all values of B_o.

The peak of the measured depth-averaged current is observed in the bar trough, at x=145 m, during both test stages as shown in Figure 42 and Figure 44. The model results show one peak right offshore of the bar crest where the majority of wave breaking occurs and a second peak at the end of the bar trough where secondary breaking occurs for both test stages. The model results are close to the measurements in magnitude for test stage 1B including the first measurement location in bar trough at x=145 m. Unfortunately, there are no measurements at x=138 m or at x=160 m to see if the peaks also exist at those locations in the measurements and to validate the

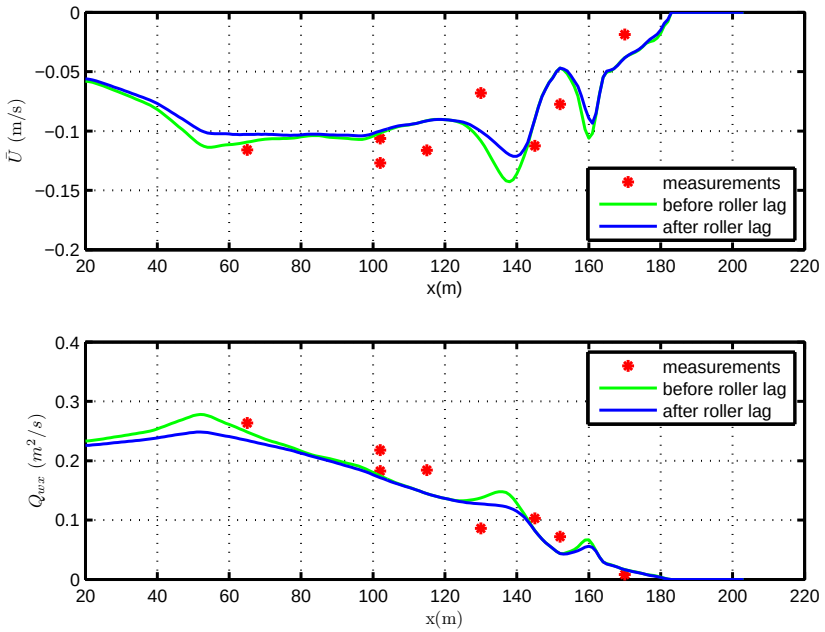

Figure 46: Cross-shore variations of (Top panel) depth-averaged currents, $\overline{U}$, and (Bottom panel) wave volume fluxes, Q_{wx}, for measurements (red stars) and model results (solid lines) before and after the roller lag method is implemented for a surface shape parameter, B_o value of 0.125 and with a roller front slope angle, σ_r value of 5 for test stage 1B.

model for the cross-shore variation of depth-averaged currents. On the other hand, there are measurements at those locations for test stage 1C showing that those are not the peak locations for the depth-averaged currents. As a result, for test stage 1C, not only the magnitude but also the variation of the depth-averaged current is predicted poorly by the model.

Figure 46 shows the wave volume flux and the depth-averaged current predictions with and without the roller lag for test stage 1B. The main effect of roller lag method is to shift the location of the peak of the depth-averaged current onshore near the bar crest. Figure 47 shows the wave volume flux and the depth-averaged current predictions with and without the roller lag method for test stage 1C. The model still overpredicts the depth-averaged current and wave volume fluxes. Since we know that the model does fairly well for the wave height predictions for test stage 1C as shown

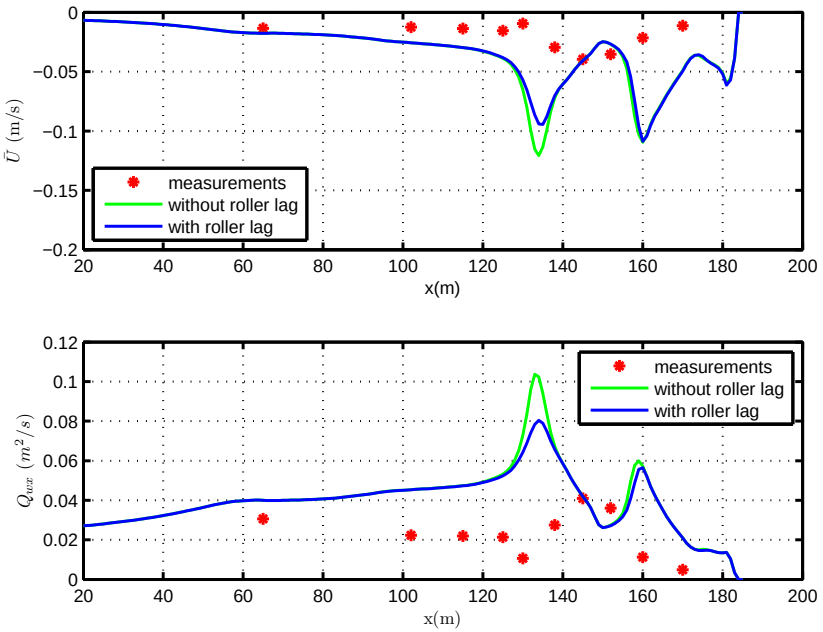

Figure 47: Cross-shore variations of (Top panel) depth-averaged currents, $\overline{U}$, and (Bottom panel) wave volume fluxes, Q_{wx}, for measurements (red stars) and model results (solid lines) before and after the roller lag method is implemented for a surface shape parameter, B_o value of 0.125 and with a roller front slope angle, σ_r value of 5 for test stage 1C.

in Figure 22, we may assume that the dissipation is predicted at a sufficient level. Besides, the roller component of the radiation stress is underpredicted by the model as shown in Figure 30. Therefore, it is not expected to have such a big difference between the model results and measurements for the wave volume flux and the depth-averaged current as shown in Figure 44 and it is not certain if this may be attributed to an error in the interpretation of the measurements.

Depth-varying currents

As explained in the previous chapter, SHORECIRC is not a fully-3D but is a quasi-3D circulation model in which the depth-varying currents are solved semi-analytically. The vertical variation of mean currents is found by using Equation 81 which may be rewritten by using an eddy viscosity formulation and assuming quasi-steady currents

as

$$\frac{\partial}{\partial z}\left((\nu_t+\nu_s)\frac{\partial V_{d\alpha}}{\partial z}\right)=g\frac{\partial\overline{\zeta}}{\partial x_\alpha}+V_\beta\frac{\partial V_\alpha}{\partial x_\beta}+W\frac{\partial V_\alpha}{\partial z}+f_\alpha \tag{138}$$

where the term on the left hand side is the vertical viscosity term, denoted as *vvisc*, the first term on the right hand side is the pressure gradient, denoted as *prsgrd*, f_α is the local contribution to the radiation stress, and the remaining two terms on the right hand side are horizontal and vertical advection terms, denoted as *hadv* and *vadv*, respectively. The cross-shore momentum balance inside and outside the surfzone is dominated by the local balance between the wave forcing, the pressure gradient and the vertical viscosity term (Haas and Warner, 2009). In this study, we have also included the roller contribution to the short wave forcing given by Equation 95.

In SHORECIRC, the short wave forcing f_α and the pressure gradient are depth uniform. However, the resulting solution of the depth-varying currents from the second integral of the vertical viscosity term in Equation 138 is quadratic in nature. The vertical viscosity term responds to the changes in the pressure gradient term affecting the curvature of the depth variation of the undertow current. Set-up has a positive pressure gradient term leading to a quadratic depth variation of the current with onshore flow at the surface and maximum offshore current at the bottom. The pressure gradient term for set-down during wave shoaling is negative, creating a quadratic term in the offshore direction along the water column which is larger at the surface.

The wave forcing term, f_α, given by Equation 82 is negative in the wave breaking region in the surf zone and causes an offshore directed current at the surface and an onshore directed current at the bottom. When wave breaking is stronger, the curvature due to the wave forcing term becomes larger. When wave breaking is weaker, the curvature created by the short wave forcing becomes smaller and the onshore transport at the bottom becomes smaller.

Because of the boundary condition at the bottom given by Equation 88, the vertical variation of the undertow current also depends on the bottom shear stress,

τ_B. The bottom shear stress contributes to the linear variation of the current in the vertical with onshore flow at the bottom and offshore flow at the surface in the cross-shore.

Test Stage 1B

The depth-varying undertow current and components as predicted by the numerical model and the measurements where available are shown along the cross-shore transect in Figure 48. The results in Figure 48 are with the default values for B_o, σ_r and f_{cw}, and include the persistence length method implementation but not the roller lag method. The bottom shear stress component is always a linear term contributing to the negative curvature with onshore directed values at the bottom and offshore directed values at the surface. The roller forcing addition also contributes to the negative curvature and it is even larger than the bottom shear stress component for the trough locations. It is observed in Figure 48 that the pressure gradient term is the dominant term of all across the domain. The magnitude of the near-bed total current is observed to depend heavily on the bottom value of the pressure gradient term while the other terms have a stronger effect on the curvature of the depth-varying currents. Since all the measurement locations are in set-up zones, the pressure gradient term has a positive curvature at all locations.

The model predictions are in agreement with the measurements for the first four measurement locations. However, starting from the bar trough ($x > 143$), the model results underestimate the undertow current in both magnitude and curvature.

The roller contribution to the short wave forcing is applied as uniform over depth. In reality, this is not expected to be the case since the roller is generated at the surface and its effect is expected to be reduced over the water column towards the bottom. It is very apparent that the results, especially within the bar-trough zone, need to be improved.

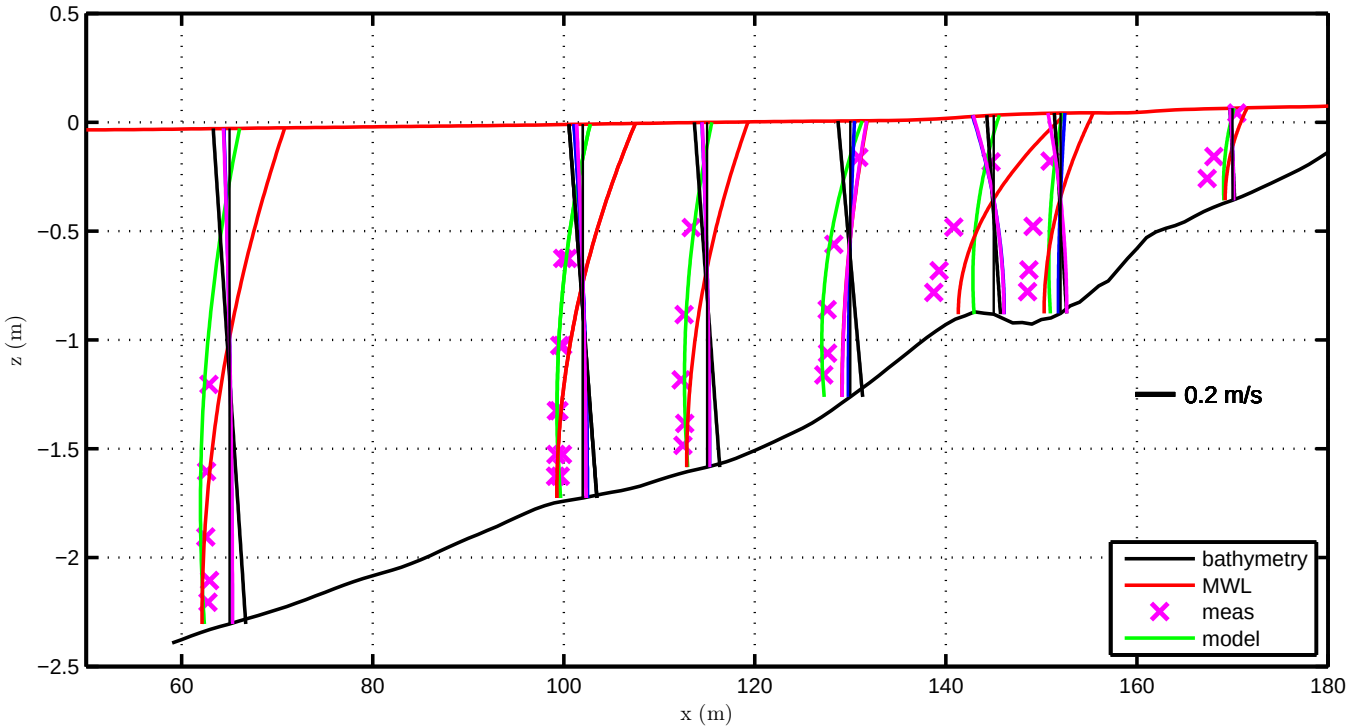

Figure 48: Depth-varying current profiles for test stage 1B at different locations along the cross-shore for the measurements (crosses) vs. the model results (solid lines) with current components due to pressure gradient term (red), short wave forcing term (blue), bottom shear stress term (black), roller contribution to the short wave forcing term (magenta) and total current (green) using a surface shape parameter, $B_o = 0.125$, roller front slope angle, $\sigma_r = 10$, combined wave-current friction factor, $f_{cw} = 0.024$, $nr = 0$ in Equation 95 and persistence length method with a persistence length constant $C_p = 800$.

Figure 49 shows the model results for the components of the vertical momentum balance across the domain matching the locations for the measurement devices: x=130 offshore of the bar, x=138 right offshore of the bar crest, x=145 right onshore of the bar crest, x=152 in the middle of trough and x=160 at the end of the trough. The model parameters match those used in Figure 48. Even if all the terms look depth uniform, the horizontal and vertical advection terms and the vertical viscosity term have depth variations that are not visible in the figure. The undertow current is solved through a double integration of the vertical viscosity term as described in chapter two with Equations 91 and 92. Therefore, the curvature of the depth-varying current depends on the magnitude of the vertical viscosity term. The magnitude of the vertical viscosity term depends mainly on the local imbalance of pressure gradient and wave forcing. Since the wave forcing term is smaller in magnitude than the pressure gradient term, the vertical viscosity term generally has the opposite sign of the pressure gradient as observed in Figure 48.

Two of the parameters impacting the magnitude and depth structure of the current are the eddy viscosity and the combined wave-current friction factor. As can be seen from Equation 138 and Equation 92, the eddy viscosity is an important parameter which is inversely proportional to the magnitude of curvature of the depth-varying structure of the current. The friction factor is not only used in the calculations of the bottom shear stress value used in the bottom boundary condition but also used in the calculations of the eddy viscosity term. Therefore, these parameters need to be estimated reasonably well. The default values of 0.024 for the friction factor, f_{cw} and the eddy viscosity coefficients, $M = 0.06$ and $C_{1v} = 0.06$ are used for the estimation of current profiles presented in Figure 48. The eddy viscosity was calculated using Equation 98 given in the previous chapter.

As discussed in Chapter 2, the water depth h in the second term represents the turbulent length scale and H_{rms} was also used as suggested by Battjes (1975) to be

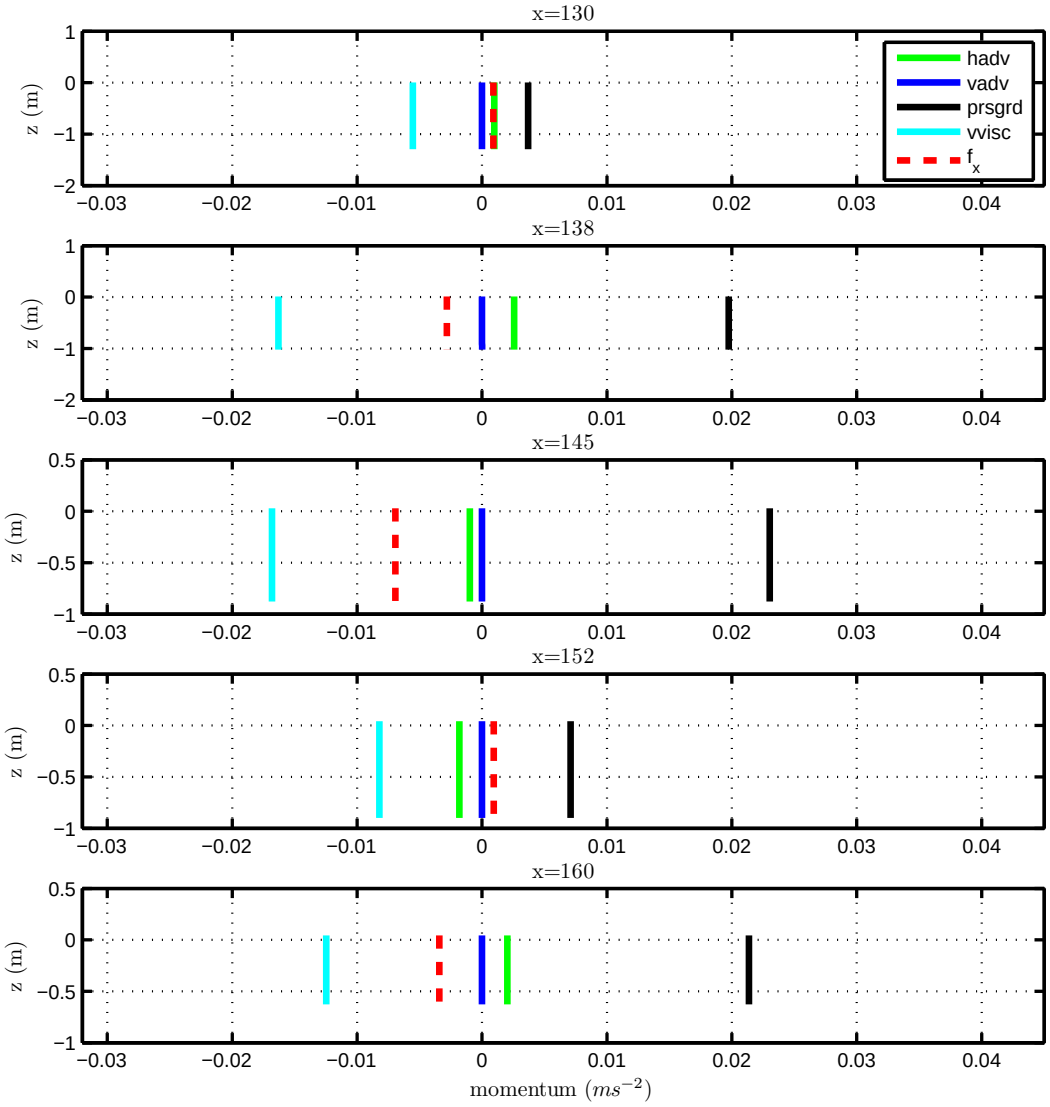

Figure 49: Vertical variation of the cross-shore momentum balance from SHORECIRC using a surface shape parameter, $B_o = 0.125$, roller front slope angle, $\sigma_r = 10$, combined wave-current friction factor, $f_{cw} = 0.024$, $nr = 0$ in Equation 95 and persistence length method with a persistence length constant of $C_p = 800$ (without the roller lag method).

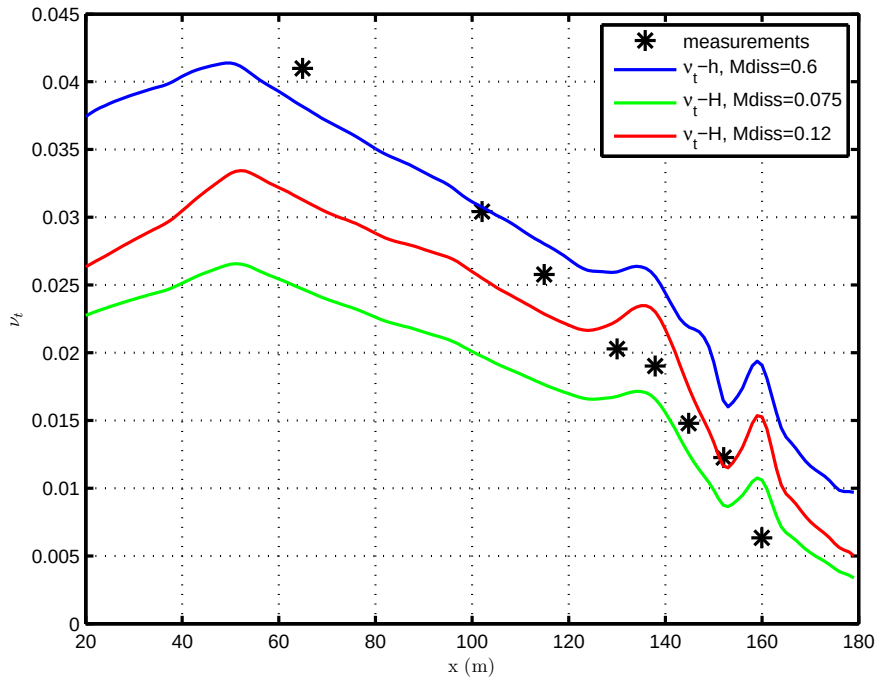

Figure 50: Cross-shore variation of eddy-viscosity for test stage 1B extracted from the measurements (black stars) by Boers (1995) and predicted by Equation 96 and Equation 98.

the turbulent length scale due to wave breaking instead of the water depth. If a constant wave height to water depth ratio of 0.8 is assumed, the change in turbulent length scale would require a change in the value of M from 0.06 to 0.075 to maintain the magnitude of the eddy viscosity. Figure 50 shows the cross-shore variation of the eddy viscosity term as predicted by Equation 96 as well as Equation 98. The model results are also compared to the values extracted from the measurements via an inverse modeling technique and reported by Boers (1995).

It is observed that the model result from the default definition (blue line) is close to the reported values only at the measurement locations offshore of x=115 m. After that location, the predictions by the default model are larger than the reported values. This overprediction in eddy viscosity eventually leads to the underprediction of the curvature of depth-varying currents especially in the bar-trough zone since the undertow velocity is inversely proportional to the eddy viscosity. Once the wave height

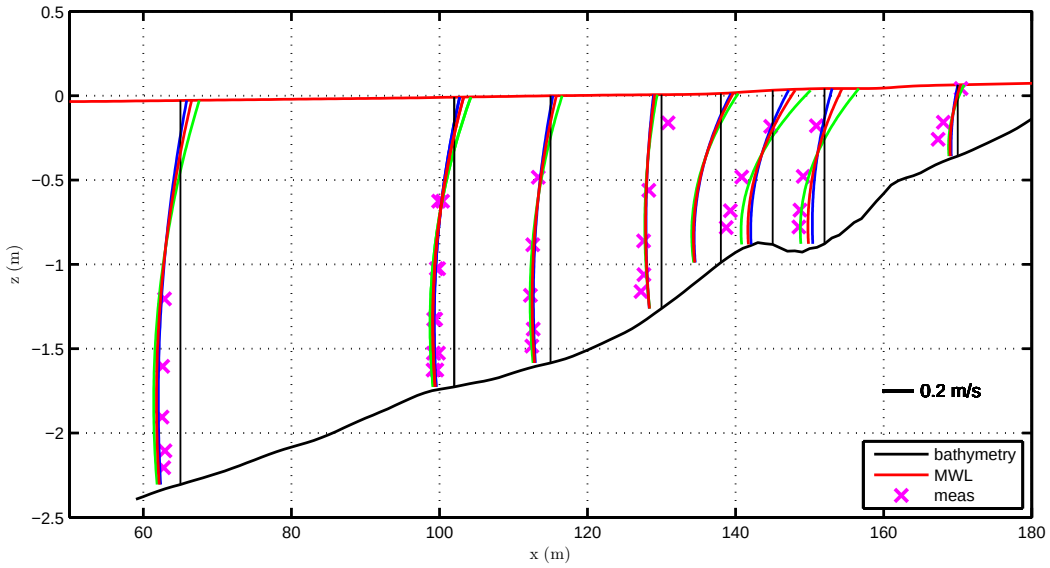

Figure 51: Depth-varying current profiles for test stage 1B at different locations along the cross-shore for different eddy viscosity descriptions: Equation 96 with $M = 0.06$ (blue line), Equation 98 with $M = 0.075$ (green line), Equation 98 with $M = 0.12$ (red line).

is used as the turbulent length scale instead of the water depth, the predictions of eddy viscosity onshore of x=115 m show better agreement compared to the reported values. However, the eddy viscosity is underpredicted over the entire domain. For that reason, a larger eddy viscosity coefficient, M value of 0.12 is used instead of the default value of 0.075 with H_{rms} as the turbulent length scale value. As can be seen from the figure, as M increases, the eddy viscosity increases and the agreement is better in the vicinity of the bar.

The total current variations are shown in Figure 51 in order to compare the effect of using a different eddy viscosity formulation with a different turbulent length scale. Changing the eddy viscosity formulation slightly enhances the current predictions particularly in the trough where the decreased eddy viscosity increases the vertical variation. The value of M is observed to have a very small effect on current profiles before strong breaking occurs at the bar crest ($x < 143$). However, the depth variation

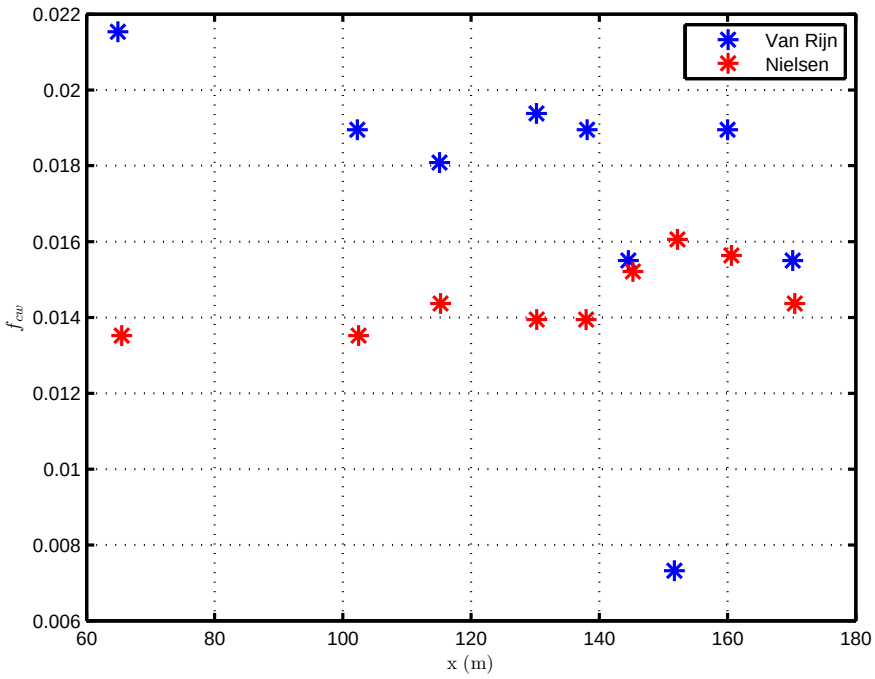

Figure 52: Cross-shore variation of friction factor for test stage 1B extracted from the measurements by Boers (1995) for different friction factor formulations.

of current profiles and the bottom current value is observed to be more sensitive to the value of M in the bar trough.

As mentioned before, it is also necessary to examine the effect of friction factor. Boers (1995) used Van Rijn (1990)'s formula which specifies the roughness as a function of the mobility number and Nielsen (1992)'s formula which finds the roughness based on the Shield's parameter, also accounting for the bedforms. After the roughness is found, Swart's formula [Equation 7] was used in order to estimate a friction factor. The default value of 0.024 for the friction factor is larger than the values for the measurements reported by Boers (1995) as shown in Figure 52. Therefore, a smaller friction factor value of 0.015 is chosen as the new constant friction factor value conforming well to the predictions by Nielsen's formula.

Since changing the friction factor not only modifies the bottom current but also changes the eddy viscosity, it is necessary to see the effect of changing the friction

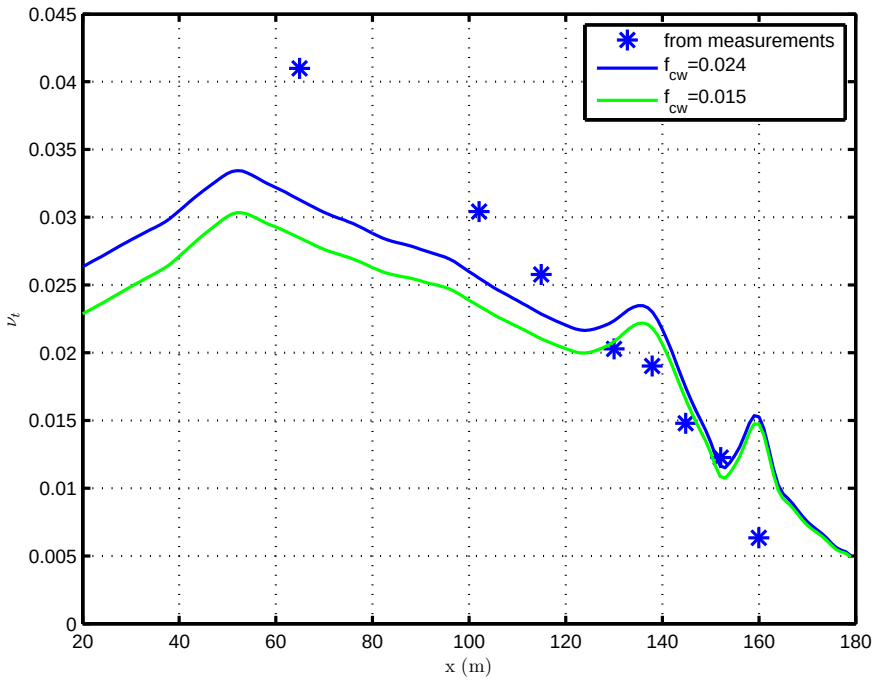

Figure 53: Cross-shore variation of eddy-viscosity for test stage 1B extracted from the measurements (blue stars) and predicted by the model with different friction factors (solid lines).

factor on the eddy viscosity. As can be seen from Figure 53, a smaller friction factor leads to smaller eddy viscosity predictions. The effect is more pronounced offshore of x=140 m where the turbulence created by the bottom friction has a proportionally stronger effect and less pronounced after that location where the breaking wave induced energy dissipation dominates over the dissipation due to the bottom friction.

Figure 54 shows the depth-varying current profiles for the different friction factors. The smaller friction factor leads to slightly stronger currents at the bottom due to smaller bottom shear stress along with more curvature due to smaller eddy viscosity. It is observed that the effect is not significant.

As can be seen by comparing the modeled profiles with the measurements in Figure 54, the changes for the eddy viscosity and the friction factor do not produce the improvement required particularly in the bar trough measurement locations. Since

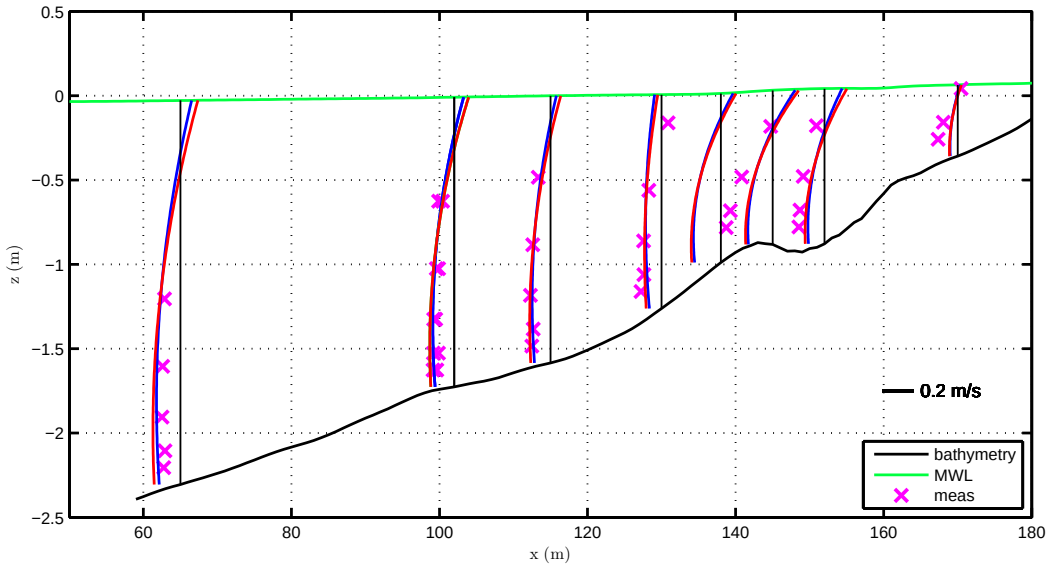

Figure 54: Depth-varying current profiles during test stage 1B for different friction factor values of 0.024 (blue line) and 0.015 (red line) with $M = 0.12$ in Equation 98, roller front slope angle, $\sigma_r = 10$ and surface shape parameter, $B_o = 0.125$.

the pressure gradient of the component is observed to dominate at those locations (See Figure 48), it may be hypothesized that the pressure gradient term needs to be larger in this vicinity to get more accurate results. It may also be suggested that the depth uniform roller term which adds to the negative curvature may be too large.

It was mentioned in section 3.2.2 and shown in Figure 27 that decreasing the σ_r value enhances the roller contribution to the radiation stresses at certain locations inside the domain and improves the model predictions of radiation stress compared to the measurements. A smaller σ_r value was also observed to enhance the mean water level variation, i.e. the pressure gradient, as discussed in the previous section and shown by Figure 36. It may be observed from Figure 55 that a value of $\sigma_r = 5$ instead of the default value of $\sigma_r = 10$ produces current profiles that do not change much for the points offshore of the bar. On the other hand, it causes a big change at both trough locations, x=145 and x=152 m. In addition, at x=130 the curvature is reversed once a smaller σ_r value is used.

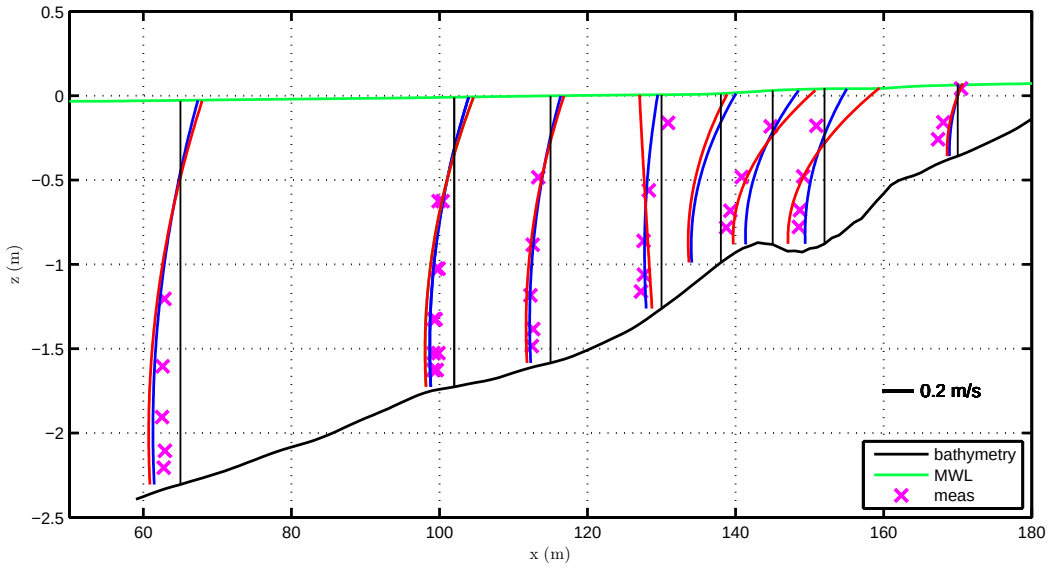

Figure 55: Depth-varying current profiles during test stage 1B for different roller front slope angles of 10 (blue line) and 5 (green line) with friction factor, $f_{cw} = 0.015$ and M=0.12 in Equation 98.

Figure 56 shows the model results for the above described components of vertical momentum balance across the domain matching the locations for the measurement devices for different σ_r values of 10 and 5. There is almost no affect of σ_r value offshore of the bar crest since the breaking of random waves is negligible there. A smaller σ_r value is observed to increase the pressure gradient in the trough at x=145 and 152 m which leads to enhanced curvature through an increased vertical viscosity term and also a larger bottom value of the undertow current at both trough locations as shown in Figure 55. Offshore of the bar (x=130 m) where the profile curvature is reversed, the pressure gradient is reduced nearly to zero due to smaller σ_r enhancing the roller contribution to the radiation stress as shown in Figure 27. Essentially, changing σ_r affects the roller contribution to the radiation stress which in turn changes the pressure gradient, thereby altering the vertical profile of the undertow current.

The individual effects of f_{cw}, σ_r, turbulent length scale definition with h or H_{rms} in ν_t, and M value on currents have been shown so far. All the results were using the

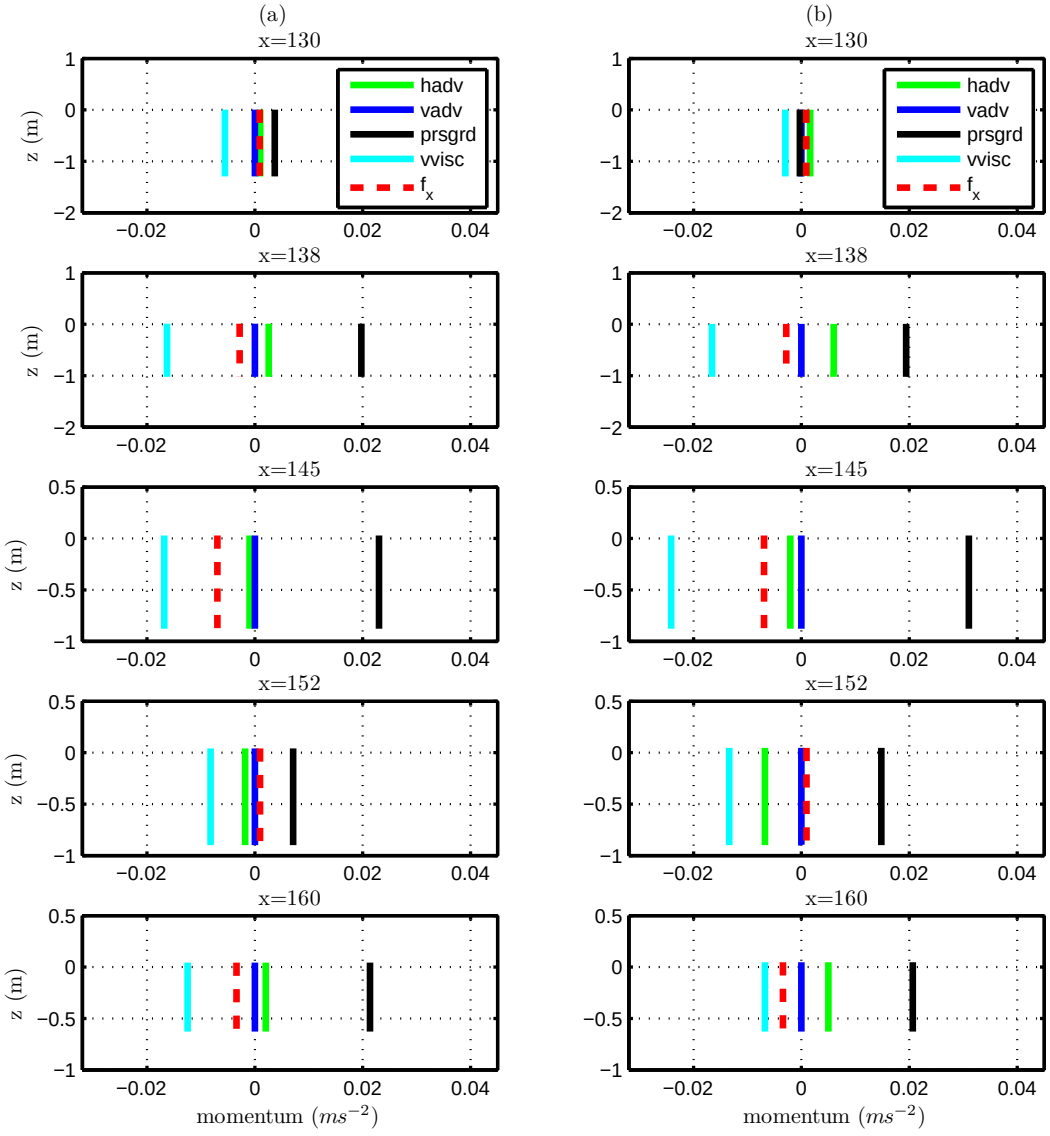

Figure 56: Vertical variation of the cross-shore momentum balance from SHORE-CIRC with different roller front slope angles, (a) $\sigma_r = 10$ (b) $\sigma_r = 5$, and with the persistence length method in the numerical model for test stage 1B (without the roller lag method).

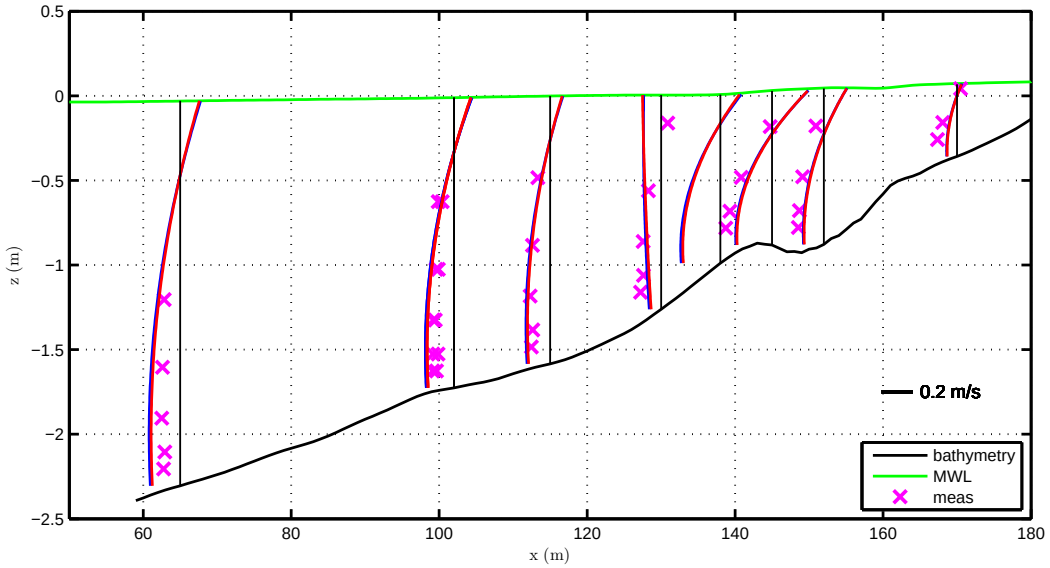

Figure 57: Depth-varying current profiles during test stage 1B for different surface shape parameters of 0.125 (blue line) and 0.115 (red line) with friction factor, $f_{cw} = 0.015$ and $M = 0.12$ in Equation 98.

default B_o value of 0.125. However, we have already shown in the previous section that a smaller B_o value of 0.115 gives better agreement with the measurements for the mean water level predictions. Figure 57 shows profiles for two different values of B_o. As seen from Figure 35, a smaller B_o value results in a smaller pressure gradient thereby reducing the curvature in the depth-varying currents as seen in Figure 57, producing a lower bottom current value. The effect is actually observed to be weak for a change of the B_o value from 0.125 to 0.115.

All the undertow results presented so far included the persistence length method which was earlier shown to play an important role for hydrodynamics in the bar-trough for the wave module. Figure 58 shows the depth-varying current profiles with and without the persistence length method. The roller lag method is not included in order to isolate the effect of the persistence length method. The current structure is observed to have wrong curvature with maximum value at the surface and minimum at the bottom in the bar-trough at x=152 m before the persistence length method

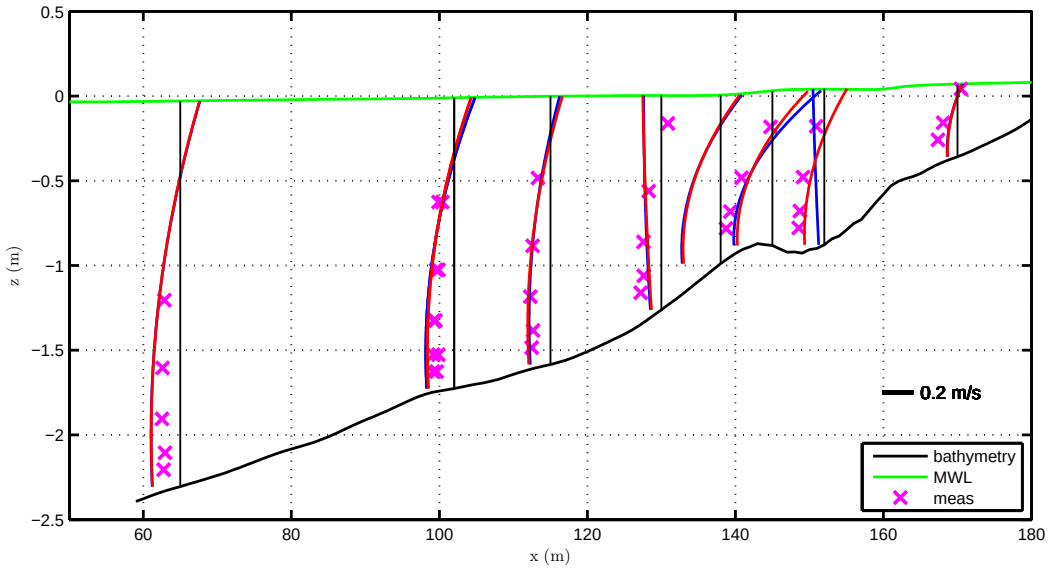

Figure 58: Depth-varying current profiles during test stage 1B with (red line) and without (blue line) the persistence length method implementation with roller front slope angle, $\sigma_r = 5$, surface shape parameter, $B_o = 0.115$, friction factor, $f_{cw} = 0.015$, $M = 0.12$ Equation 98 and persistence length constant, $C_p = 800$.

is implemented. The depth variation of the current at x=130 m is wrong both with and without the persistence length method.

Figure 59 shows the components of vertical momentum balance across the domain matching the locations for the measurement devices with and without the persistence length method. As shown earlier in Figure 16, the breaking wave persistence has an effect after the major breaking occurs near the bar crest. In fact, the vertical momentum balance does not change due to persistence offshore of the bar crest, x=142, as shown in Figure 59. Before the breaking wave persistence is included, all the momentum balance terms are observed to be weak at x=130 and x=152 which due to the bottom shear stress leads to an almost linear depth structure for the depth-varying current with a larger and offshore directed value at the surface. After the persistence length method is used, the pressure gradient increases due to the increasing radiation stresses at x=152 as shown in Figure 28, balanced by the vertical

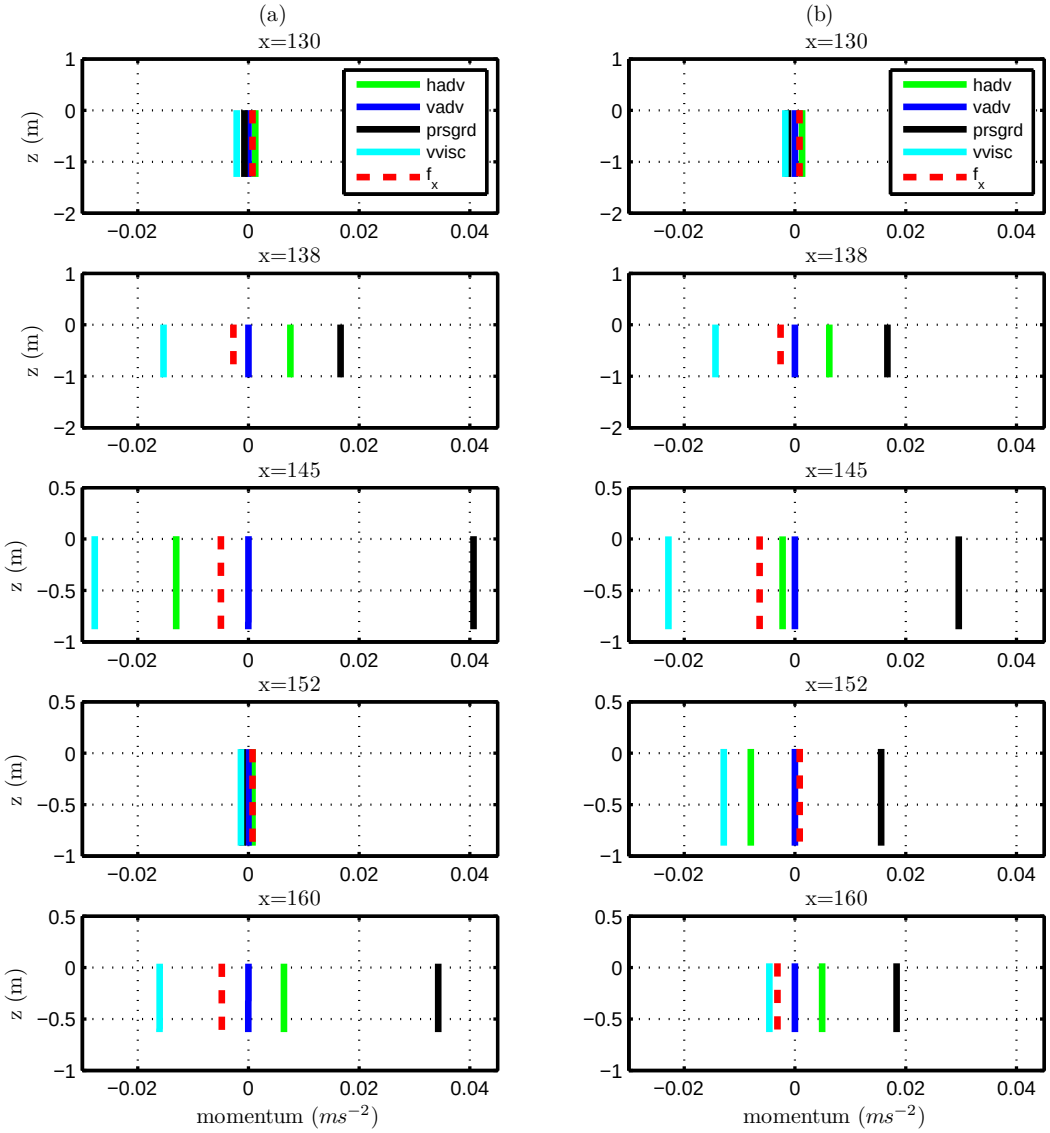

Figure 59: Vertical variation of the cross-shore momentum balance from SHORECIRC (a) without the persistence length method (b) with the persistence length method in the numerical model for test stage 1B (without the roller lag method)

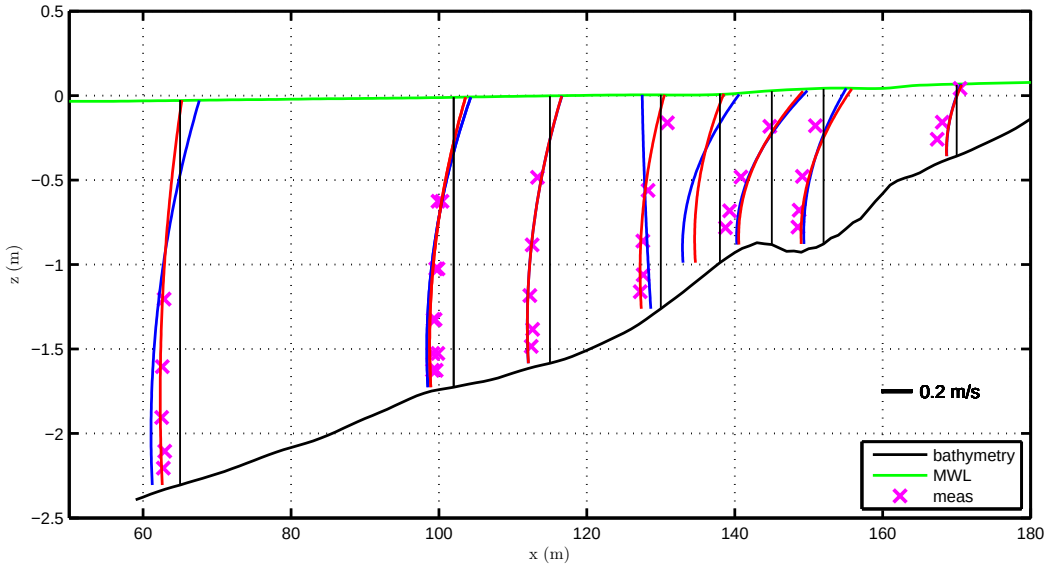

Figure 60: Depth-varying current profiles during test stage 1B without (blue line) and with (red line) the roller lag method with roller front slope angle, $\sigma_r = 5$, surface shape parameter, $B_o = 0.115$, friction factor, $f_{cw} = 0.015$, $M = 0.12$ in Equation 98, persistence length constant, $C_p = 800$, and roller lag length coefficient, $C_r = 1$.

viscosity and the horizontal radiation terms. At x=145 and 160 m, the breaking wave persistence causes a decrease in the pressure gradient and in the wave forcing leading to a decrease in the *vvisc* term resulting in less curvature.

Another important method implemented in the numerical model to improve the model predictions for the radiation stresses and the mean water level was the roller lag method. In fact, it may be realized in Figure 58 that offshore of the bar crest, at x=130 m, the model predicted current has a depth variation with a negative curvature increasing over depth towards the surface. This does not concur with the observations of the currents. The reason for the reversed curvature is a negative pressure gradient predicted by the model at that location as seen in Figure 37. Without the roller lag, the mean water level gradient changes sign at x=130 m. Figure 60 shows the depth-varying undertow currents with and without the roller lag method. The roller lag method improves the mean water level prediction and therefore alters the curvature

of the depth variation of the undertow current at x=130 m. In a similar manner, the roller lag method is also expected to improve the undertow predictions at the end of the trough where the pressure gradient reverses without its implementation in Figure 37. A negative effect of roller lag method is observed to give a slight increase in the underprediction of the current at the first trough location, x=145 m. This is due to the decreased dissipation (Figure 32) as a result of the roller lag method.

Figure 61 shows the vertical momentum balance with and without the roller lag. It is observed that the roller lag method causes an increase in the pressure gradient term which is balanced by the vertical viscosity term at x=130 m. Before the roller lag method is implemented the immediate roller addition to the radiation stress leads to a positive radiation stress gradient which is balanced by a negative pressure gradient which causes the reversed curvature of undertow current at that location as shown in Figure 60. Due to the roller lag, the mean water level gradient at x=138 m reduces as shown in Figure 38 . On the other hand, there are only slight changes at the other locations since they are out of the region mainly affected by the roller lag in the model.

After both the persistence length and the roller lag methods are implemented, it is observed in Figure 61 that the pressure gradient term, $prsgrd$, is the dominant term in the vertical momentum balance while the wave forcing term, f_α, is much smaller and even zero at several locations. The horizontal advection term is stronger than the wave forcing term at several location. This vertical imbalance is countered by the vertical viscosity term yielding to increasing depth structure of the undertow current as the pressure gradient gets larger.

Figure 62 shows the component of the depth-varying current due to the roller contribution to the short wave forcing only. The effect of changing the depth structure of the roller forcing from depth uniform, i.e. $nr = 0$, to a cubic, i.e. $nr = 3$, on the depth-varying currents is observed. It may be observed especially at both trough

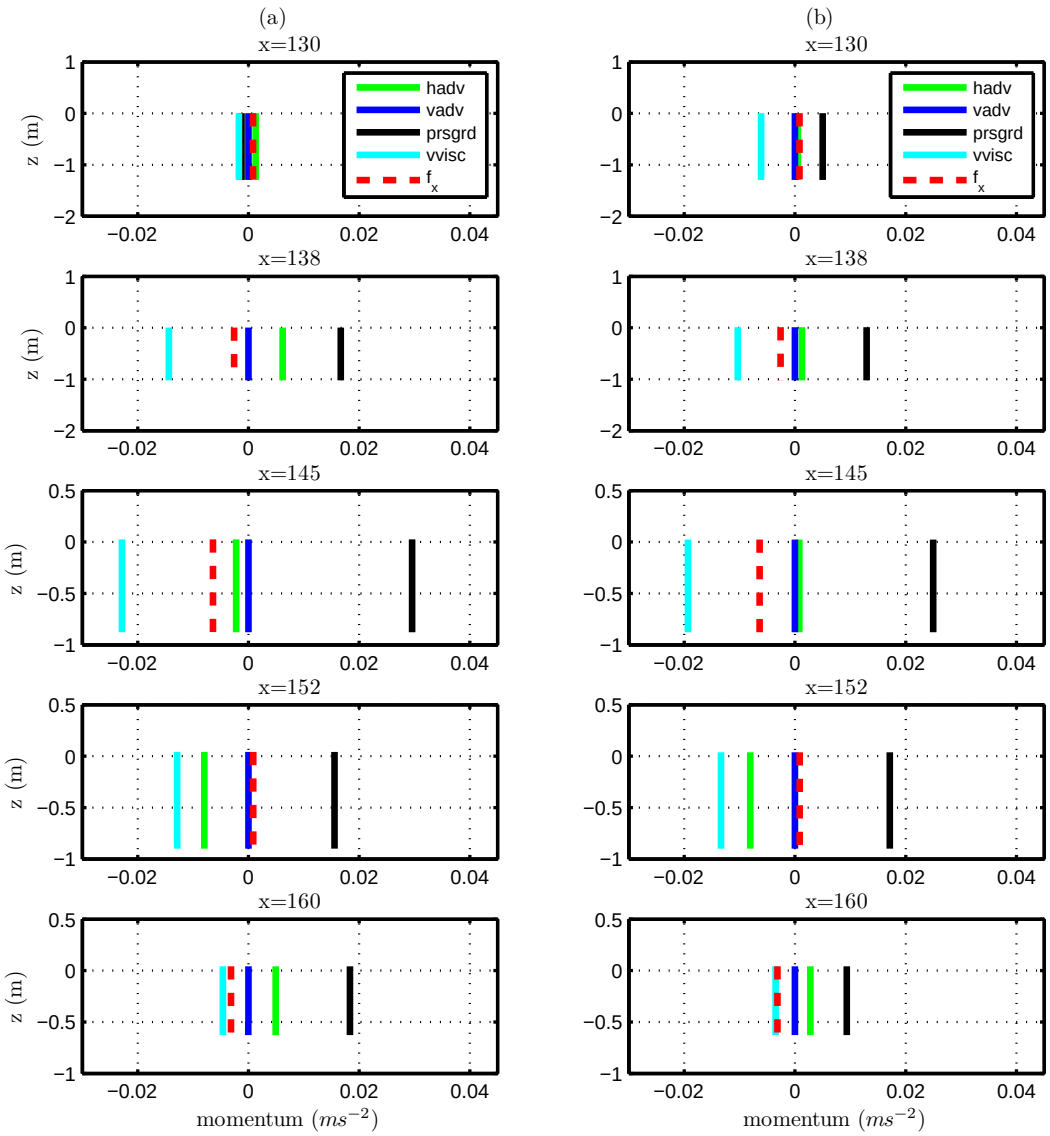

Figure 61: Vertical variation of the cross-shore momentum balance from SHORECIRC (a) without the roller lag method (b) with the roller lag method in the numerical model for test stage 1B (with the persistence length method in both cases)

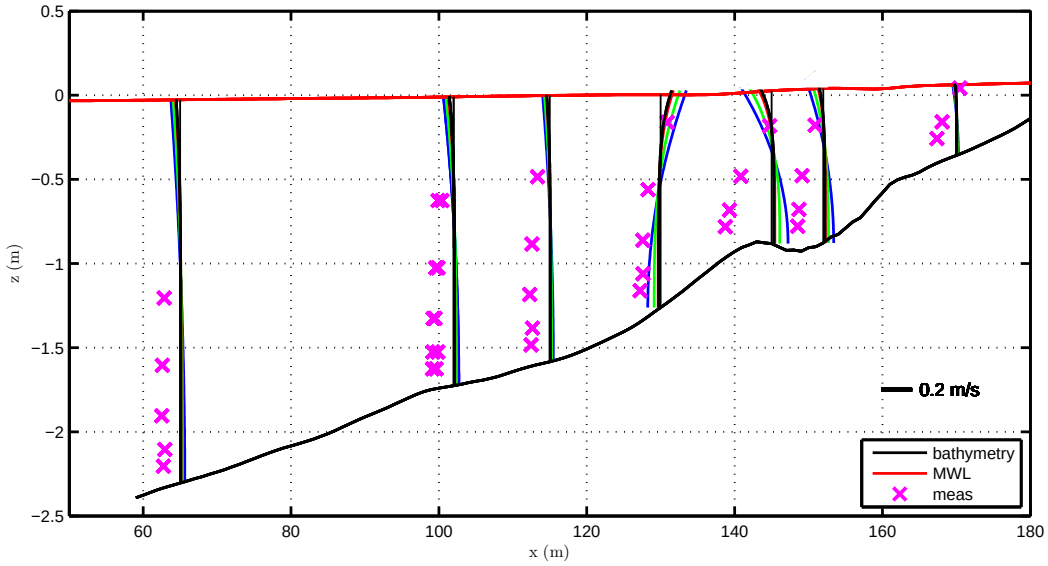

Figure 62: The component of the depth-varying current profiles due to the roller contribution during test stage 1B for different depth structures of the roller contribution to the short wave forcing, $nr = 0$ (blue line), $nr = 1$ (green line), $nr = 2$ (red line), $nr = 4$ (black line), with roller front slope angle, $\sigma_r = 5$, surface shape parameter, $B_o = 0.115$, friction factor, $f_{cw} = 0.015$, $M = 0.12$ in Equation 98 and persistence length constant, $C_p = 800$.

locations that the contribution of the roller term to the negative curvature is reduced with increasing nr. Everything else being the same, this simply improves the current predictions compared to those with the default model values especially offshore of the bar crest. The quadratic and cubic depth variation of the roller contribution to the short wave forcing results in very similar values for the current component.

As a summary, Figure 63 shows the cross shore variation of the magnitude of the undertow current at x=10 cm above the bed for test stage 1B since the measurements were taken at that location. The effect of using the persistence length and roller lag methods on the bottom current is shown in the figure. Without both methods, the value of the bottom current is observed to be underpredicted after x=145 m. The persistence length method brings the values closer to measurement in the bar-trough, but it produces a secondary peak inside the bar trough. Once the roller lag method

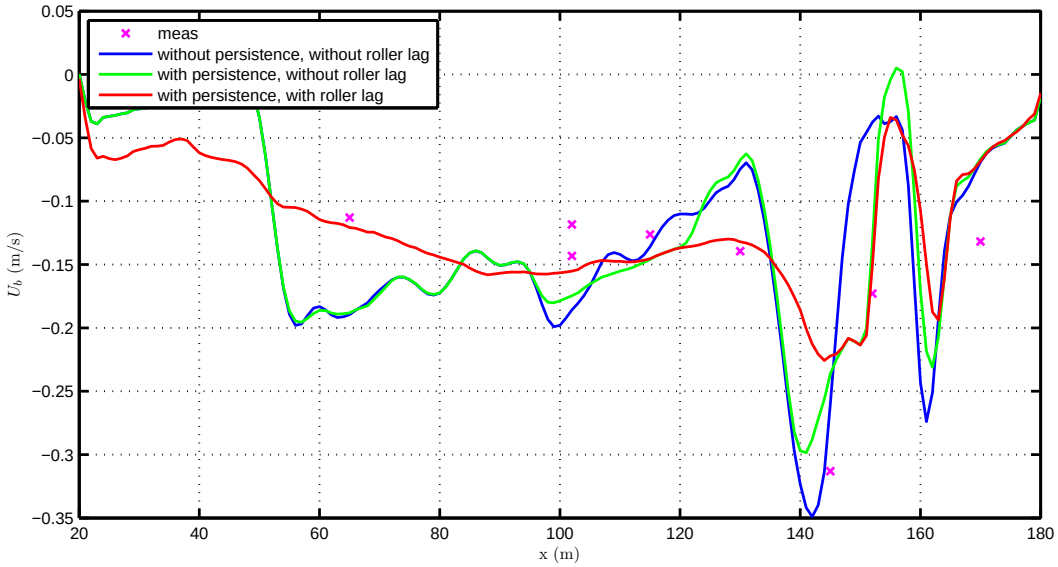

Figure 63: The cross-shore variation of the bottom value of the undertow current for test stage 1B with roller front slope angle, $\sigma_r = 5$, surface shape parameter, $B_o = 0.115$, friction factor, $f_{cw} = 0.015$, $M = 0.12$ in Equation 98.

is added to the wave module, the model can predict the location of the peak of the undertow current but underpredicts the maximum bottom current value right onshore of the bar crest at x=145 m.

Table 4 shows the model skill for the undertow profiles at the profile locations as well as the overall model skill considering all measurement points from all profiles for test stage 1B. Once the persistence length method is used, i.e. $C_p = 800$ is used instead of $C_p = 0$, the model skill at the trough location, x=152 m, increases from 0.35 to 0.80. As stated earlier, the persistence length method improves the model skill for undertow current profiles at both trough locations by enhancing the dissipation, thereby improving the radiation stress as well as mean water level predictions and their gradients. Once the roller lag method is used, i.e. $C_r = 1$ is used instead of $C_r = 0$, the model skill at the measurement location just onshore of the bar crest, x=145 m, increases from 0.09 to 0.89. The roller lag method improves the model skill at those locations by reducing the immediate roller contribution to the radiation

Table 4: The model skill calculated by Equation 135 for undertow profiles at each instrument location and the overall model skill considering all undertow measurement points for test stage 1B with surface shape parameter, B_o=0.115, roller front slope angle σ_r=5 and different values for the model parameters for the persistence length method, C_p, and the roller lag method, C_r.

		model skill at x=							overall
C_p	C_r	65	102	115	130	145	152	170	skill
0	0	0.17	0.59	0.87	0.09	0.94	0.35	0.87	0.78
800	0	0.17	0.66	0.81	0.04	0.93	0.80	0.86	0.81
0	1	0.52	0.72	0.87	0.89	0.93	0.53	0.88	0.88
800	1	0.53	0.81	0.81	0.91	0.91	0.83	0.87	0.90

stresses and applying it over a transition zone within a roller lag length, thereby improving radiation stress and consequently the mean water level predictions in that set-down region. The overall model skill increases from 0.78 before the persistence length and roller lag methods are used to 0.90 after both methods are introduced to the numerical model.

Test Stage 1C

In the previous part of this section, the depth-varying currents for test stage 1B have been discussed including analysis of the effects of different parameters on the depth-varying current profiles. The analysis for several of these parameters will not be presented again for test stage 1C since the overall physical effects are very similar. The parameter values of σ_r and B_o determined during the radiation stress and the mean water level analysis for test stage 1C are used in the current analysis as well but will not be evaluated further. The effects of the friction factor and the new mechanisms, persistence length and roller lag are presented and the applicability of those new methods for the currents in low-energetic wave conditions are systematically tested.

Figure 64 shows the friction factor calculated using Van Rijn (1990)'s formula and Nielsen (1992)'s formula (Boers, 1995). Similar to test stage 1B, the default friction factor value of 0.024 is larger than the values for the measurements reported. It may

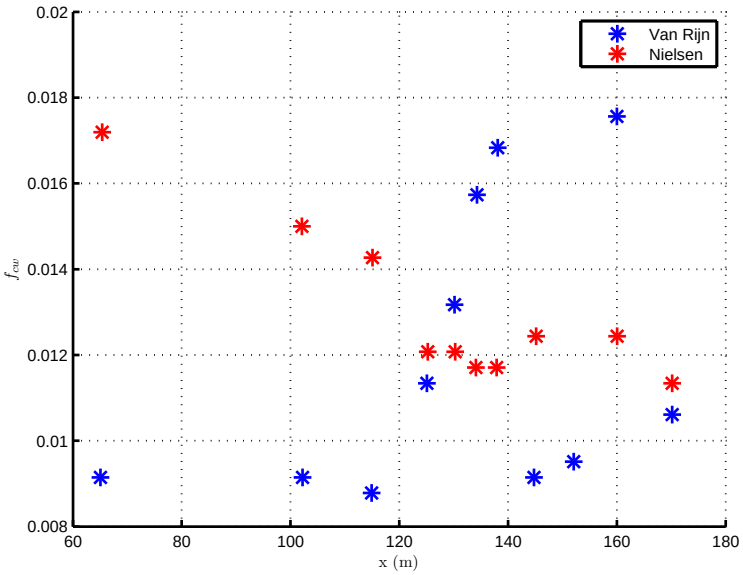

Figure 64: Cross-shore variation of friction factor for test stage 1C extracted from the measurements for different friction factor formulations used by Boers (1995).

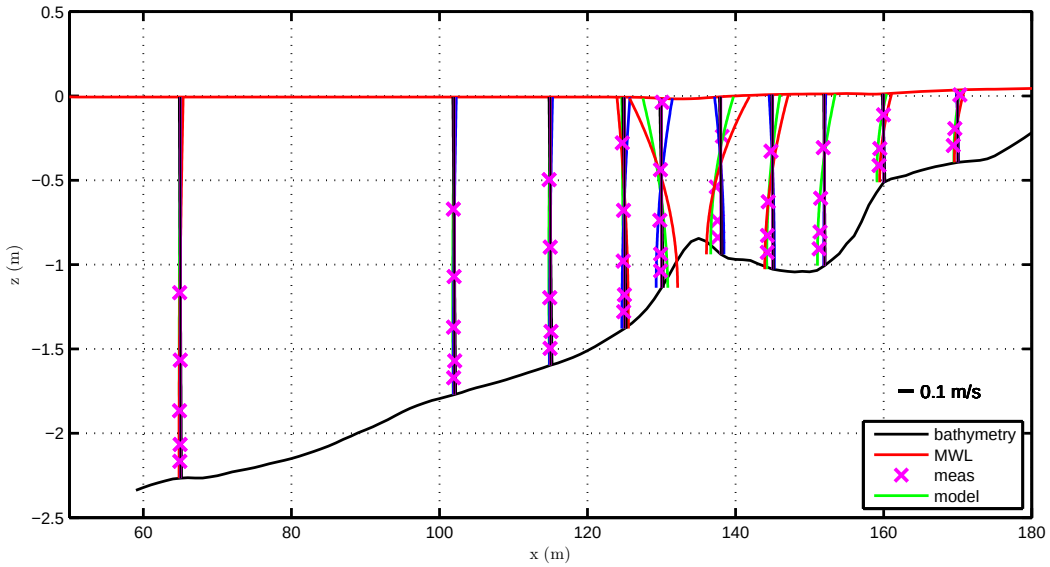

Figure 65: Depth-varying current profiles for test stage 1C at different locations along the cross-shore for the measurements (crosses) vs. the model results (solid lines) with current components due to pressure gradient term (red), short wave forcing term (blue), bottom shear stress term (black), roller contribution to the short wave forcing term (magenta) and total current (green) using surface shape parameter, $B_o = 0.115$, roller front slope angle, $\sigma_r = 5$, friction factor, $f_{cw} = 0.012$, $nr = 3$ in Equation 95 and persistence length method with $C_p = 4800$.

be seen that a smaller friction factor value of 0.012 may be used compared to the 0.015 used for test stage 1B. Since test stage 1C simulated a lower energetic season, it is reasonable to use a smaller friction factor in the numerical model. The M value for Equation 98 of 0.075 is used for the calculation of the eddy viscosity.

The depth-varying undertow current and components as predicted by the numerical model and the measurements where available are shown along the cross-shore transect in Figure 65. The results in Figure 65 are with the calibrated values for B_o, σ_r and f_{cw}, and include the persistence length method implementation but not the roller lag method and H_{rms} in eddy viscosity given by Equation 98. The roller contribution to the short wave forcing is applied as cubic over depth due to the observations made for test stage 1B. Similar to test stage 1B, it is observed in Figure 65 that the pressure gradient term is the dominant term of all across the domain.

The model predictions are in agreement with the measurements for the first four measurement locations. However, starting from the bar trough, the model results are overestimating the undertow current in both magnitude and curvature. This result is in contrast with the test stage 1B results.

Figure 66 shows the model results for the components of vertical momentum balance for the same case in Figure 65 matching the locations for the measurement devices: x=130 offshore of the bar, x=138 right onshore of the bar crest, x=145 onshore of the bar crest in the trough, x=152 in the middle of trough and x=160 at the end of the trough. Even if all the terms look depth uniform, the horizontal and vertical advection terms and as a result the vertical viscosity term have weak depth variations. Similar to test stage 1B, the vertical viscosity term counteracts the pressure gradient term across the domain except at the middle of the trough, x=152 m. Offshore of the bar crest, at x=130 m, the pressure gradient is negative leading to the opposite curvature for the depth variation of the undertow current at that location as shown in Figure 65.

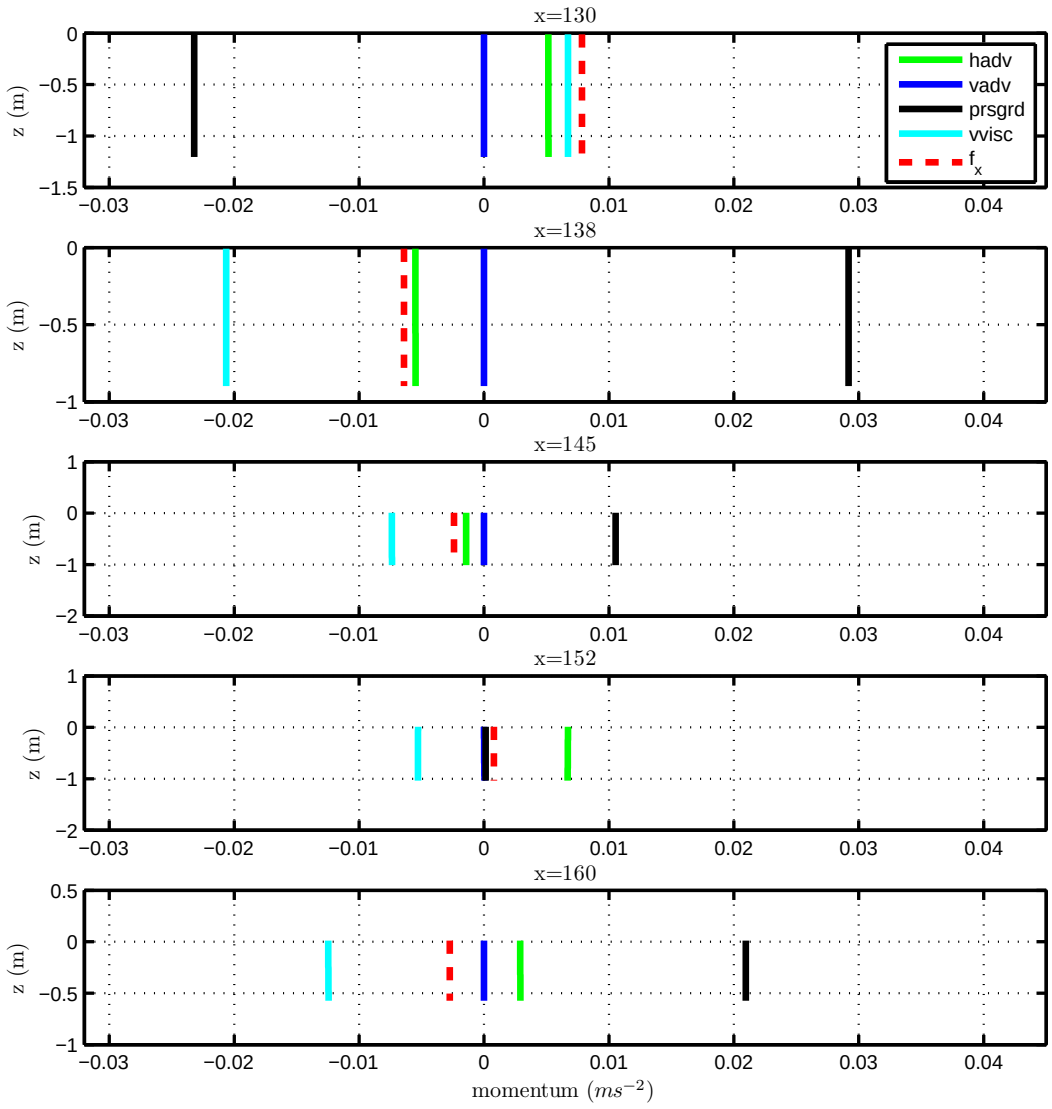

Figure 66: Vertical variation of the cross-shore momentum balance from SHORE-CIRC for test stage 1C using surface shape parameter, $B_o = 0.115$, roller front slope angle, $\sigma_r = 5$, friction factor, $f_{cw} = 0.012$, $nr = 3$ in Equation 95 and persistence length method with $C_p = 4800$ (without the roller lag method).

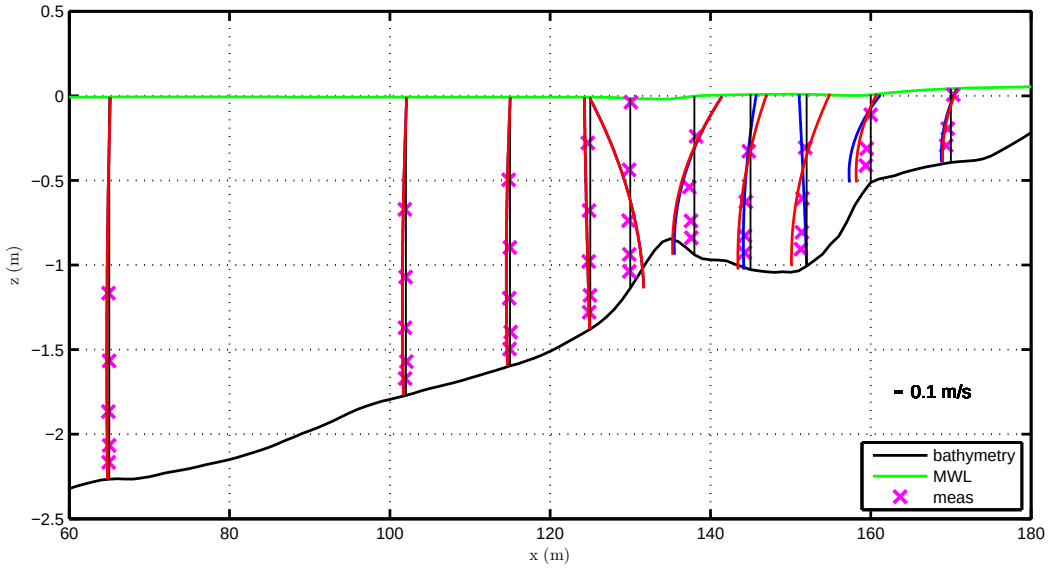

Figure 67: Depth-varying current profiles during test stage 1C with (red line) and without (blue line) the persistence length method implementation with roller front slope angle, $\sigma_r = 5$, surface shape parameter, $B_o = 0.115$, friction factor, $f_{cw} = 0.012$, $M = 0.12$ in Equation 98 and persistence length constant, $C_p = 4800$.

Figure 67 shows the measured and modeled depth-varying currents at measurement locations with and without the persistence length method implemented. Since there is minimal wave breaking at offshore locations, the persistence length method has no effect at those points offshore of x=135 m. After x=135 where the waves start to break on the bar crest, the persistence length method is observed to positively affect the current predictions. The model predicts the wrong curvature in the bar-trough at x=145 and x=152 m before the persistence length method is implemented. Once the persistence length method is included, the correct depth variation of the current is predicted.

Figure 68 shows the variation of vertical momentum balance terms across the domain with and without the breaking wave persistence. As shown earlier in Figure 21, the breaking wave persistence has an effect after the major breaking occurs around the bar crest. The vertical momentum balance does not change due to persistence

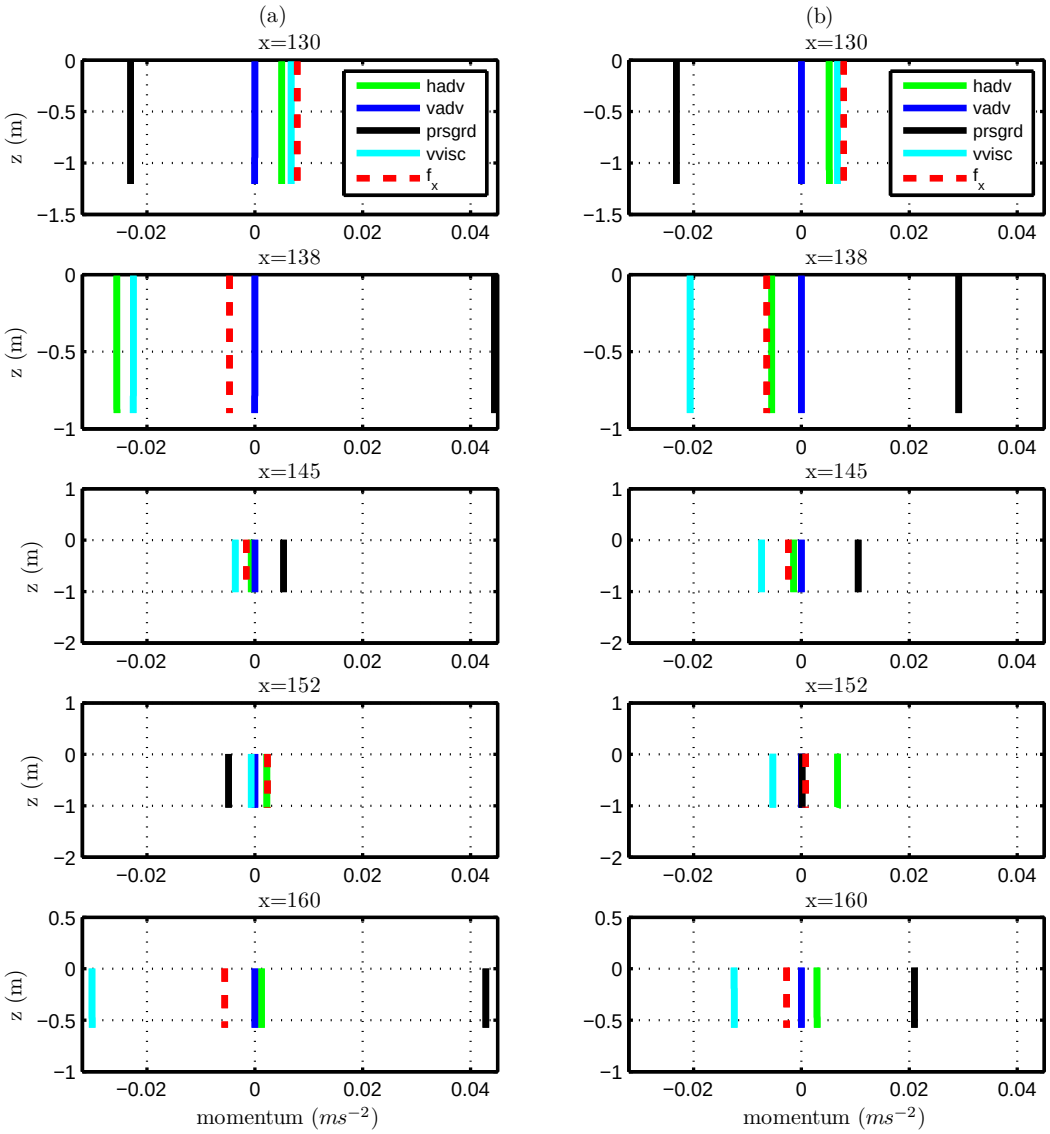

Figure 68: Vertical variation of the cross-shore momentum balance from SHORECIRC for test stage 1C .

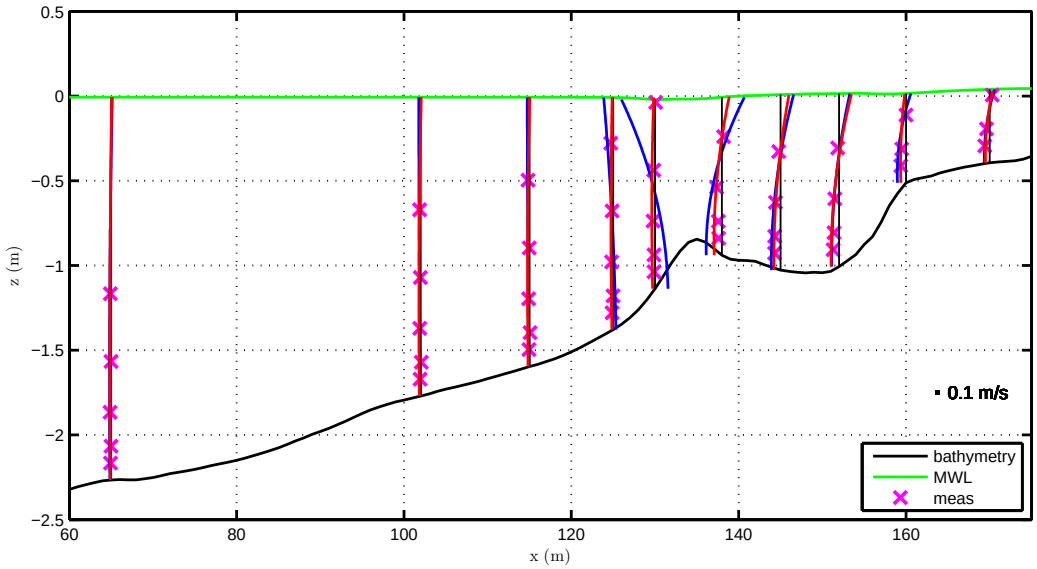

Figure 69: Depth-varying current profiles during test stage 1C without (blue line) and with (red line) the roller lag method with roller front slope angle, $\sigma_r = 5$, surface shape parameter, $B_o = 0.115$, friction factor, $f_{cw} = 0.012$, $M = 0.075$ in Equation 98, persistence length constant, $C_p = 4800$ and roller lag length coefficient, $C_r = 4$.

offshore of the bar crest (x=135) as shown in Figure 68. The negative pressure gradient at that location due to wave set-down as shown in Figure 40 dominates the vertical momentum balance. Inside the trough at x=152 m, due to the negative pressure gradient term, the vertical viscosity term is almost zero without the persistence leading to a linear depth structure of the undertow current. With the persistence the pressure gradient drops to zero leading to a nonzero *vvisc* term. However, it is not balanced by the pressure gradient but the horizontal advection term. At x=138, 145 and 160, the breaking wave persistence causes a decrease in all the components of vertical momentum balance due to a decrease in wave properties and consequently the mean water level gradients.

After both the persistence length and the roller lag methods are implemented, the pressure gradient term, $prsgrd$, is the dominant term in the vertical momentum balance as shown in Figure 70, similar to test stage 1B. This vertical imbalance between

the pressure gradient and the wave forcing is countered by the vertical viscosity. Figure 69 shows the depth variations of undertow currents at the measurement locations for test stage 1C before and after the roller lag method is implemented together with the persistence length method. It is observed that the roller lag method improves the model predictions at locations offshore of the bar crest at x=125 and x=130 as well as in the bar trough at x=138 m. The improvement in current predictions at those locations offshore of the bar crest is due to the improvements in the mean water level after the roller lag method is implemented as shown in Figure 41. The model does a good job in predicting the depth-varying undertow currents in the surf zone under low-energetic random waves. Before the roller lag method is implemented the model is observed to overpredict the currents and the roller lag method reduces this overprediction resulting in a better agreement with the measurements.

Figure 70 shows the vertical momentum balance with and without the roller lag. It is observed that the roller lag method causes a decrease in the pressure gradient term at all locations. At x=130 m, the reduction in the pressure gradient is now balanced by the wave forcing and the vertical viscosity becomes negative, changing the vertical profile curvature. On the other hand, there are almost no changes at the trough locations, x=145 and 152 m since they are out of the region affected by the roller lag in the model shown in Figure 34(b). At the locations where strong breaking occurs, i.e. right onshore of the bar crest, x=138 and at the end of the trough, x=160 m, the roller lag method causes a reduction in the pressure gradient since it decreases the radiation stress gradients changing the vertical momentum balance.

The bottom current is one of the main processes driving sediment transport. Therefore, accurate predictions of the current after all the enhancements to the wave and circulation models is important. Figure 71 shows the cross-shore variation of bottom value of the undertow current and the effect of persistence length and roller

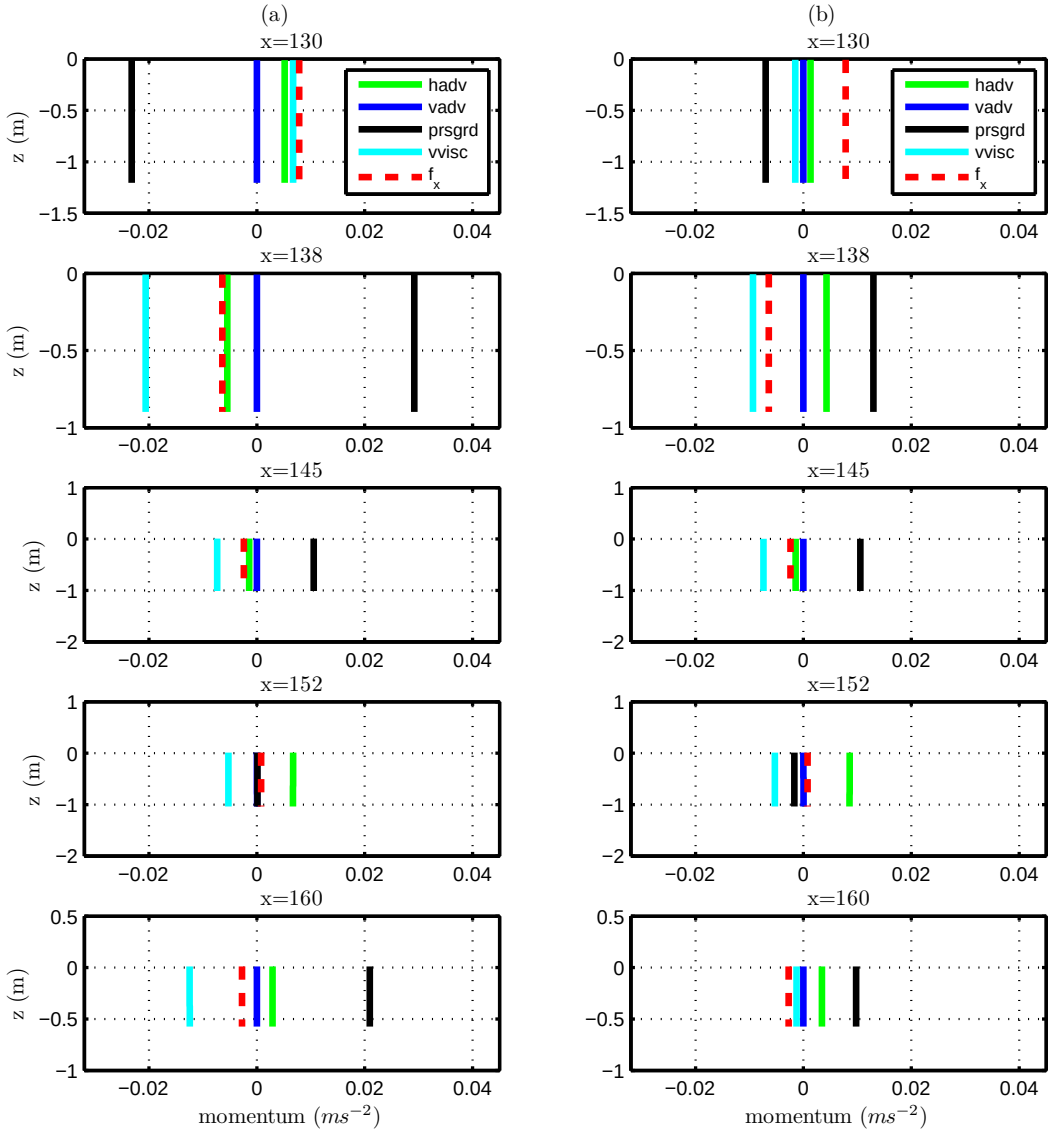

Figure 70: Vertical variation of the cross-shore momentum balance from SHORECIRC (a) without the roller lag method (b) with the roller lag method in the numerical model for test stage 1C (with the persistence length method in both cases).

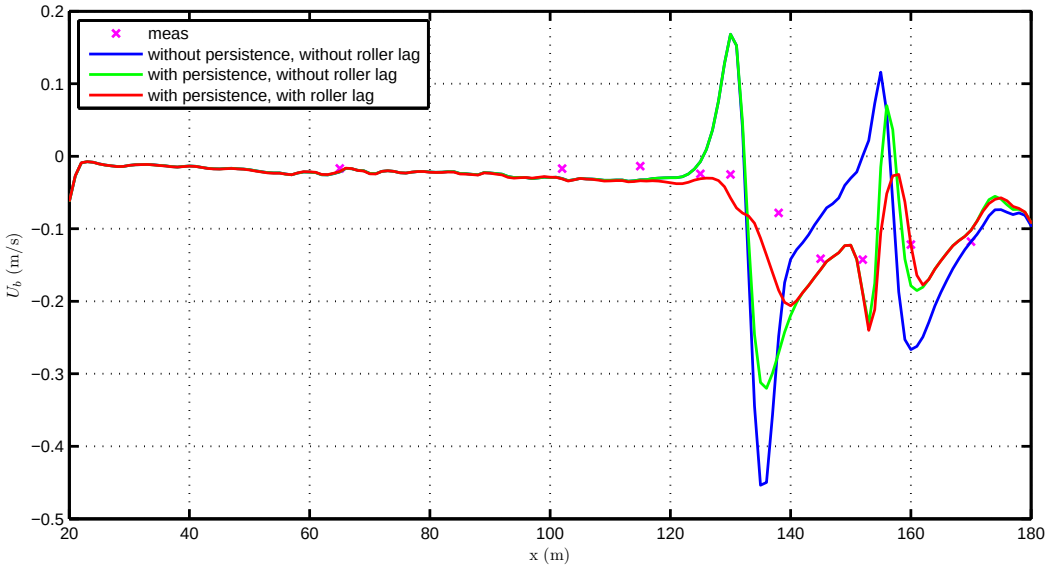

Figure 71: The cross-shore variation of the bottom value of the undertow current for test stage 1C with roller front slope angle, $\sigma_r = 5$, surface shape parameter, $B_o = 0.115$, friction factor, $f_{cw} = 0.015$, $M = 0.12$ in Equation 98 and persistence length constant, $C_p = 800$.

lag methods are shown. It is observed that before the roller lag method is implemented the model is unable to predict the variation of the current with unrealistic peaks around the bar crest. With the roller lag method, the model makes a more reasonable prediction regarding the cross-shore variation up to x=152 m even if it overpredicts the current value and estimates the peak to be at an earlier location (x=140 m) compared to the measurements. The persistence length method causes a secondary peak at x=153 m because of a secondary peak at the mean water level gradient as shown in Figure 41.

Table 5 shows the model skill for the undertow profiles at the profile locations as well as the overall model skill considering all measurement points from all profiles for test stage 1C. Once the persistence length method is used, i.e. $C_p = 4800$ is used instead of $C_p = 0$, the model skill at both trough locations, x=145 and x=152 m, increases from 0.56 and 0.12 to 0.97 and 0.89, respectively. Once the roller lag method

Table 5: The model skill calculated by Equation 135 for undertow profiles at each instrument location and the overall model skill considering all undertow measurement points for test stage 1C with surface shape parameter, B_o=0.115, roller front slope angle, σ_r=5 and different values for the model parameters for the persistence length method, C_p, and the roller lag method, C_r.

		model skill at x=										overall
C_p	C_r	65	102	115	125	130	138	145	152	160	170	skill
0	0	0.45	0.62	0.66	0.73	0.01	0.72	0.56	0.12	0.58	0.97	0.42
4800	0	0.45	0.62	0.66	0.73	0.01	0.66	0.97	0.89	0.79	0.97	0.53
0	4	0.45	0.61	0.64	0.83	0.33	0.85	0.56	0.29	0.58	0.97	0.74
4800	4	0.45	0.61	0.64	0.83	0.33	0.78	0.97	0.89	0.52	0.97	0.89

is used, i.e. $C_r = 4$ is used instead of $C_r = 0$, the model skill at the measurement locations offshore of the bar, x=125, 130 and 138 m, increases from 0.73, 0.01 and 0.72 to 0.83, 0.33 and 0.85, respectively. The overall model skill increases from 0.42 before the persistence length and roller lag methods are used to 0.89 after both methods are introduced to the numerical model.

3.2.5 Velocity Skewness

It has been mentioned in Chapter 1 that the near-bed orbital velocity skewness is an important mechanism for onshore bar migration events. Positive velocity skewness contributes to net onshore movement of the sediment and during low-energetic seasons, this onshore movement may be larger than the offshore movement induced by the undertow current, leading to the onshore movement of a sandbar. In Chapter 2, we have described the method developed by Elfrink *et al.* (2006) to estimate the near-bed orbital velocities. As described, this allows us to introduce nonlinearities in wave orbital velocities while using the REF/DIF-S linear wave model.

Elfrink *et al.* (2006) states that the method's performance for velocity skewness ($r^2 = 0.52$) is not as high as its performance for near-bed orbital velocities ($r^2 = 0.92$). One reason for the reduced performance in velocity skewness predictions is that

Elfrink's method was specifically developed for near-bed orbital velocity estimations without considering skewness as a dependent parameter. Another reason is that Elfrink's method is derived with local parameters while velocity skewness may be affected by the history of the waves.

The closest measurements of the orbital velocities to the bed during Delta Flume experiments may be extracted from the electro-magnetic current meter measurements taken 10 cm above the bed. Figure 72 shows the cross-shore variation of those values extracted from the measurements along with the predictions by Elfrink's method. For comparative purposes, the predictions using Isobe and Horikawa's (1982) method are also included on the same figure. Elfrink's method captures the cross-shore variation of near-bed orbital velocity skewness indicated by the measurements despite an overprediction at offshore locations and the most onshore measurement location. The predictions by Isobe and Horikawa are observed to overpredict the velocity skewness over the entire domain. Due to its strong dependence on local bottom slope values, Isobe and Horikawa shows a dip at the bar - trough zone which is not observed in measurements or predicted by Elfrink's method. Figure 73 shows the cross-shore variation of velocity skewness values extracted from the measurements for test stage 1C along with the predictions by Elfrink's method and Isobe and Horikawa's method. Elfrink's method underestimates the velocity skewness throughout the domain although it does predict similar cross-shore gradients. Such an underestimation will be shown to be crucial in sediment transport predictions. The variability of Isobe and Horikawa is much smaller and it does not capture the cross-shore variation, showing a gradual increase from 0.52 at the offshore boundary to 0.62 at the shoreline.

A comparison of Figure 72 and Figure 73 reveals the differences between test stages 1B and 1C. The measurements show that the waves are more skewed for the low-energetic test stage 1C than the high-energetic test stage 1B. This is because the waves become skewed in the shoaling zone before wave breaking which exists

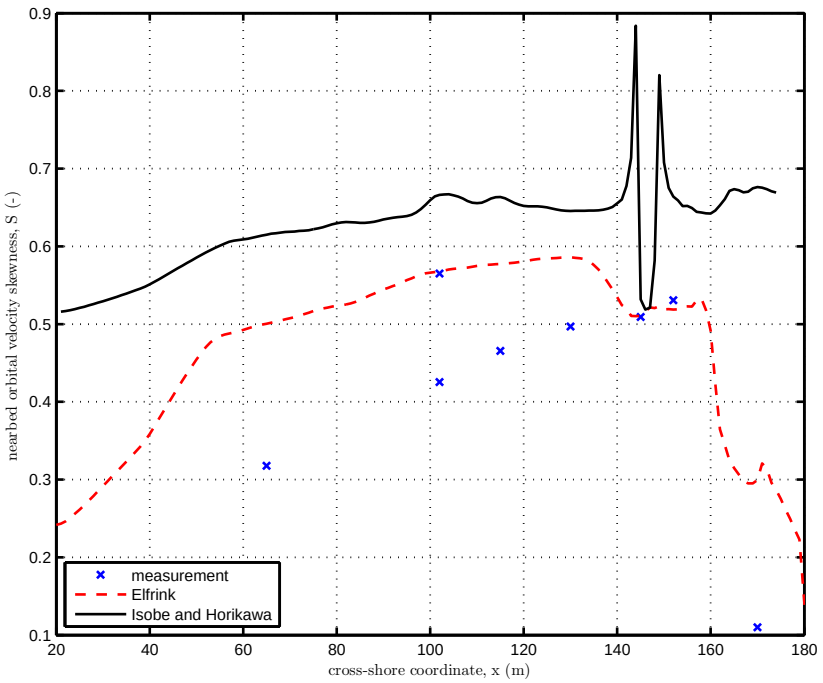

Figure 72: The cross-shore variation of near-bed orbital velocity skewness during test stage 1B.

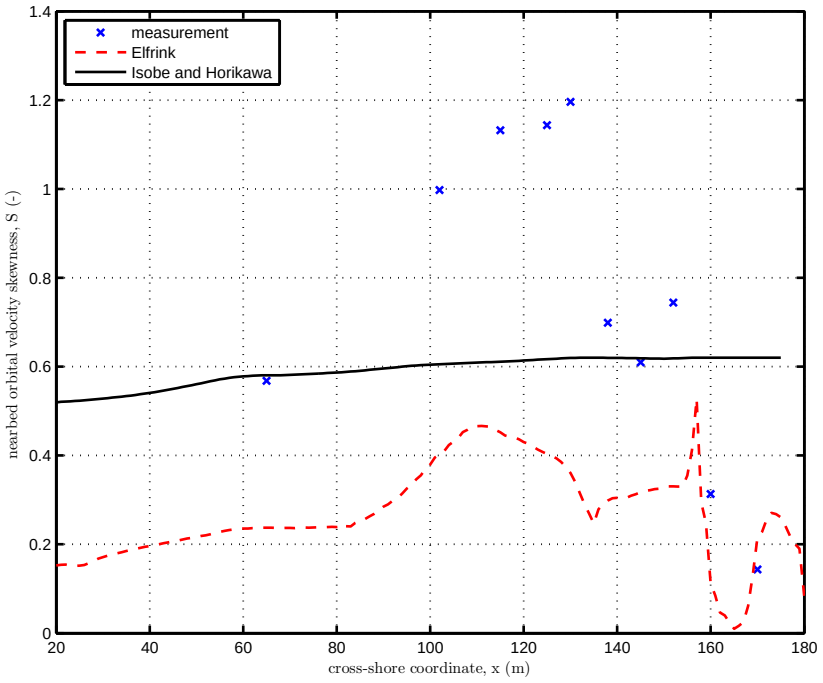

Figure 73: The cross-shore variation of near-bed orbital velocity skewness during test stage 1C.

in test stage 1C but not in test stage 1B as shown in Figure 8. On the other hand, since the waves are already breaking starting from the offshore boundary in test stage 1B, there is a less significant increase in velocity skewness up to the bar crest. The model predictions by Elfrink's method are better for test stage 1B than test stage 1C considering both the magnitude and the variation. The model is unable to produce the large skewness values shown by the measurements of test stage 1C. Furthermore, it cannot predict the location of the peak value right offshore of the bar crest but predicts it at a point further offshore.

The deficiencies in velocity skewness predictions are important for sediment transport and bathymetric changes, especially during low-energetic conditions. Elfrink's method has a range of applicability since it was developed empirically using a large sample set of wave measurements. The less the amount of similar data used in developing it, the larger the errors will be for near-bed orbital velocity estimations.

Figure 74 shows the wave height and wave period distribution for the waves used in developing Elfrink's method. The mean period for test stage 1B is 5 seconds and wave height decreases from a maximum of 1.3 m at the offshore towards the shore. As may be seen in Figure 74, for those mean values, more than 1000-5000 waves were used in deriving Elfrink's formulas. For test stage 1C, the wave height value of 0.6 m at the offshore increases up to 0.65 m before breaking starts over the bar crest and the mean wave period of 8 s corresponds from 1000-5000 up to 10000-50000 waves in Figure 74.

Bottom topography is another important factor for Elfrink's method and data coverage changes for normalized wave height and normalized wave length values. Figure 75 shows the distribution of the wave height to water depth ratio and wave length to water depth ratio for the wave events used.

Figure 76(a) shows the data range of H/h and L/h values of all cross-shore points for test stage 1B. The color of each point denotes the number of waves with similar

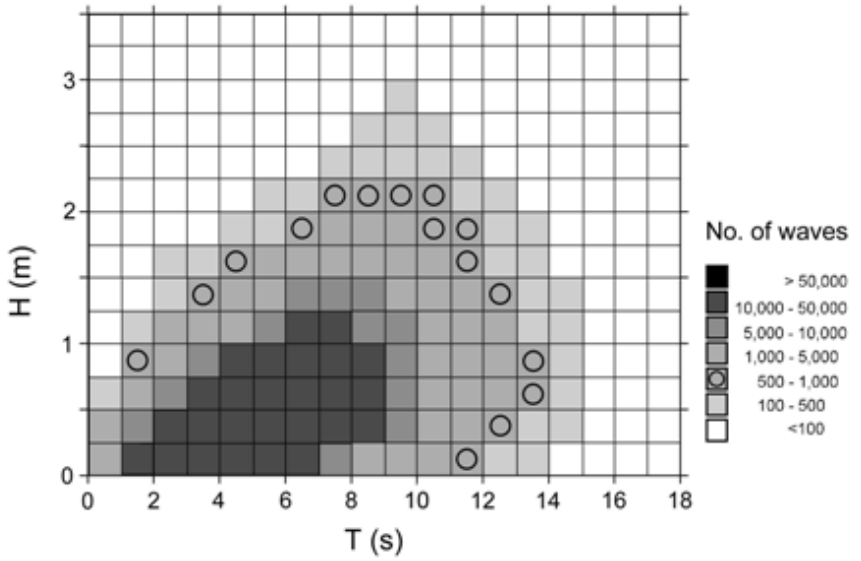

Figure 74: Data coverage of Elfrink's method in terms of wave height H and wave period T (Elfrink *et al.*, 2006).

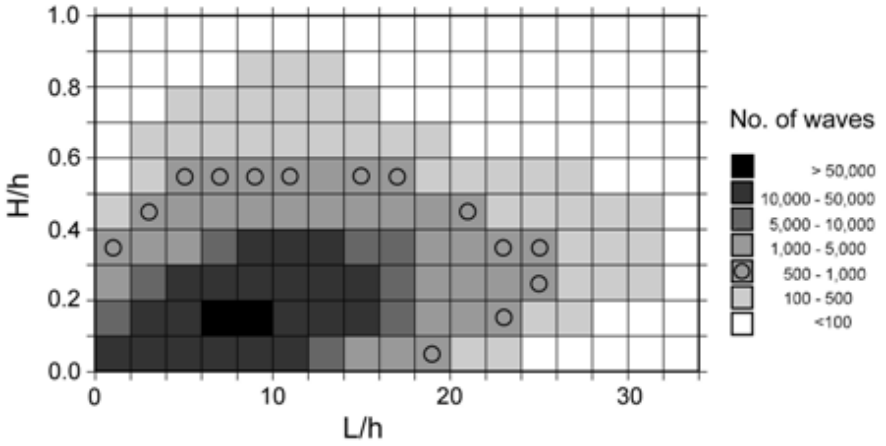

Figure 75: Data coverage of Elfrink's method in terms of H/h and L/h (Elfrink *et al.*, 2006).

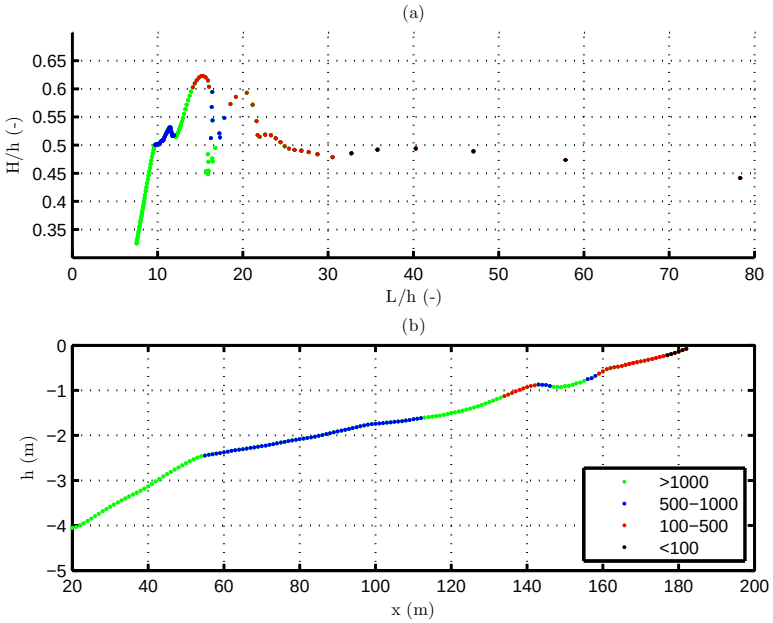

Figure 76: The variation of H/h and L/h values for all cross-shore points in the domain during test stage 1B.

properties used in developing Elfrink's method. Figure 76(b) shows the variation of those number of waves used over the bottom. It may be observed that right offshore of the bar crest and right offshore of the end of trough towards the shoreline, the wave properties for test stage 1B falls into the '100-500' category used during the development of Elfrink's method. More than 500 of the waves used in Elfrink's method development match the wave properties of test stage 1B inside the bar trough and seaward of the bar before x=134 m.

Figure 77(a) shows the variation of H/h and L/h values for all cross-shore points of test stage 1C. Figure 77(b) shows the variation of those number of waves used over the bottom. Those values indicate that less than 100 out of 55000 waves used in Elfrink's formulas matches the characteristics of the breaking waves at the bar crest and at the end of the bar trough. While in the rest of the domain, more than 500 waves matching the characteristics of waves of test stage 1C were used in the development of Elfrink's method. Only at offshore locations offshore of x=120 m,

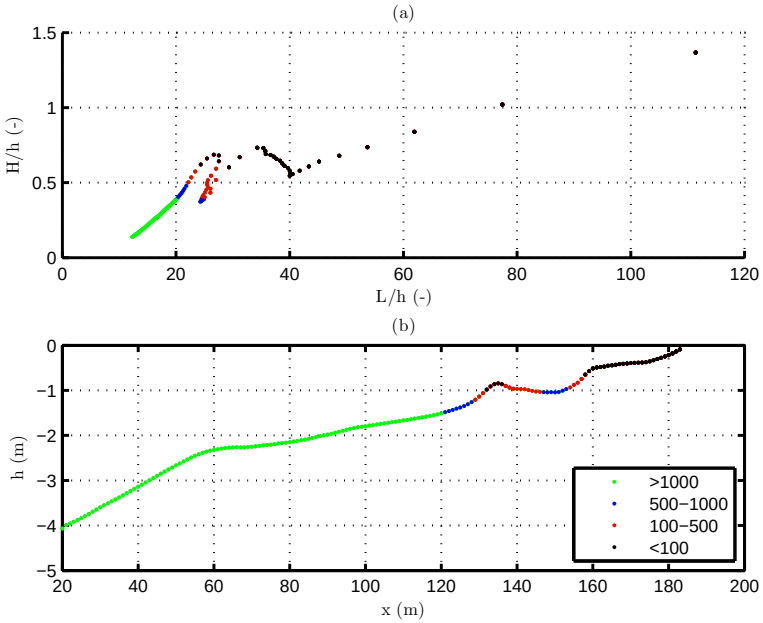

Figure 77: The variation of H/h and L/h values for all cross-shore points in the domain during test stage 1C.

more than 1000 waves matching those of test stage 1C waves were used in developing Elfrink's parametrization method to predict near-bed orbital wave velocities.

When only the mean period and offshore wave height is considered, it was thought that more than 10000 waves were used in developing Elfrink's method matching the wave characteristics of test stage 1C. However, once the bathymetry is considered and H/h and L/h values are calculated, it is observed that less than 500 out of a total of 55000 waves with the same properties of test stage 1C is used in developing Elfrink's method. Therefore, the poor prediction of velocity skewness, particularly for test stage 1C may be attributed to the lack of similar wave data used for creating the algorithm.

CHAPTER IV

NUMERICAL MODELING OF MORPHODYNAMICS ON A BARRED BEACH

This chapter describes the cross-shore movements of alongshore uniform sandbars in the surf zone with non-cohesive sediment particles during storm time-scales. The previous chapter helped us to understand the nearshore hydrodynamics on barred beaches focusing primarily on the waves and currents. The sediment transport is driven by those waves and currents leading to morphological changes. Since we have made enhancements to the numerical model improving the predictions of the hydrodynamics on a barred beach, the effects of the enhancements on sediment transport and morphodynamics will be discussed in this chapter. This chapter will also focus on the transport mechanisms for onshore and offshore bar migration.

As explained in Chapter 3, Delta Flume tests are intended to mimic the behaviour of a sandy barred beach before, during and after a storm. The last two stages are used in our study simulating an erosive stage with offshore bar migration followed by an accretive stage with onshore bar migration, i.e. test stages 1B and 1C, respectively.

The first section presents the model results for the erosive storm case. The capability of the numerical model to estimate the offshore bar movements observed in the large-scale laboratory flume is discussed. The second section presents the model results for the accretive case on a barred beach. The capability of the numerical model to estimate the onshore bar movements observed in a large-scale laboratory flume is discussed.

4.1 Test Stage 1B: An Erosive Case

The morphodynamics includes the calculation of the sediment fluxes and the associated bathymetric changes. After the hydrodynamics calculations are completed by the wave and circulation modules, the sediment transport fluxes are calculated in the circulation module and passed to the morphology module where bathymetric changes are calculated using the sediment conservation equation given by Equation 118. The sediment transport formula developed by Haas and Hanes (2004), [*HH*], given by Equation 109, and the sediment transport formula of Bailard (1981) - Bagnold (1966) - Bowen (1980), [BBB], given by Equation 117 are used in this study to estimate the sediment transport fluxes. A single grain size of $d_{50} = 0.002$ m is used throughout the domain along with a fall velocity of $W_o = 0.022$ m/s, a porosity of 0.35, an angle of repose, $tan\phi = 0.6$, a specific gravity of 2.65 and a seawater density of 1015 kg/m^3. Uniform sand was used for the experiments with a $d_{50} = 220\mu m$ (Roelvink and Reniers, 1995).

The hourly measurements of the bottom are used to extract a temporal variation of the bed, $\partial h/\partial t = \Delta h/\Delta t$, along the domain in the cross-shore. Δh is the difference between two measured bathymetric profiles recorded as separated by an interval of Δt. The cross-shore gradient of total sediment flux, $\partial q/\partial x$, is then found from the extracted $\partial h/\partial t$ according to the sediment conservation equation, Equation 118. The sediment fluxes from the measurements, q_{meas} are then found from taking the cumulative sum of $\partial q/\partial x$ as a function of $\Delta h/\Delta t$

$$q_{meas}(i) = \sum_{x=0}^{x=i}(1 - n_p)\frac{\Delta h}{\Delta t}(x) \tag{139}$$

where x is the cross-shore coordinate and n_p is the porosity.

The measurements are available from 6 of the first 8 wave hours and therefore the model is run for the first 8 hours of the experiment duration. The average sediment fluxes, estimated using the bathymetric differences between the first and eighth hour

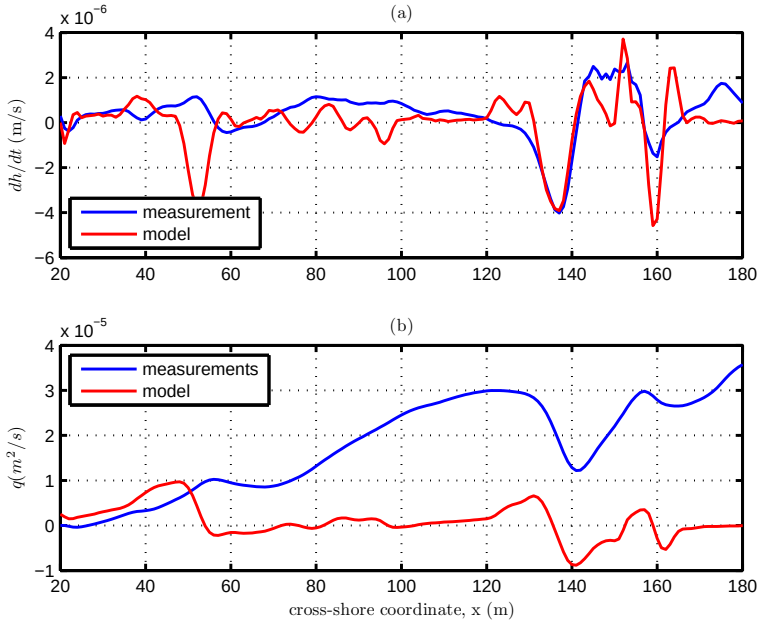

Figure 78: 8 hour averages for test stage 1B of (a) the time rate of change of bed level extracted from the measurements and the model results, (b) sediment fluxes extracted from the measurements and estimated by the model.

and the last hourly difference between hours 7 and 8 are used for comparisons to the model results.

Figure 78 shows the average bathymetric change, $\partial h/\partial t$, and the average sediment fluxes, q, extracted from the measurements and predicted by the model for the 8 hour model run of test stage 1B. The model run includes the persistence length method but not the roller lag method. The parameter values are those determined in the hydrodynamic analysis given in the previous chapter. The results are with C_1 adjusted to a value of 0.02 to acquire magnitudes of sediment transport similar to the measurements. This is much smaller than the value of 1.3 proposed by Haas and Hanes (2004) for longshore sediment transport. The positive regions in Figure 78(a) corresponds to an increase in depth over time indicating areas of erosion while the negative regions indicate areas of accretion with a decrease in depth over time. It may be observed from panel (a) that in the vicinity of the bar especially at the seaward

face of the bar, i.e. at x=140 m, both the model results and the measurements show accretion and the change in depth is observed to be at the same rate. However, the measurements show the accretion over a broader region than the model results, up to x=120 m offshore. The erosion zone observed in the trough ($143 < x(m) < 155$) measurements is also predicted by the model. However, the amount of erosion in the model is observed to be smaller than the amount of erosion observed in the measurements. The reason is a smaller cross-shore gradient of the of sediment flux in the model right onshore of the bar crest between x=144 m and x=152 m. This causes a reduction in the bathymetric change to zero around x=149 m. This is related to the underestimation of the nearbed undertow current along the trough region as shown in the previous chapter. The measurements show a broad erosion zone offshore of the shoreline and the deposition of the eroded sediment over a broad region at the end of the trough. The model predicts a narrow erosion section earlier at x=162 m and that eroded sediment is accreted further offshore in a narrow region around x=160 m at the end of bar trough. This pattern leads to the formation of a secondary berm-like sandbar at the end of trough (which is shown in Figure 82). Because the model does not resolve the swash zone, it is not capable of predicting the erosion in and right offshore of the swash zone. For that reason, the discrepancies in the swash zone are not going to be discussed in this study.

The variation of $\partial h/\partial t$ from the measurements and predicted by the model along with the gradients of sediment flux values are similar. However, the magnitude of the sediment flux is different in the model compared to those extracted from bathymetric measurements. It is not the magnitude but the gradient of sediment fluxes which causes bathymetric changes. Therefore, even if the sediment fluxes predicted by the model are smaller than those estimated from the measurements, the model results in similar bathymetric changes due to similar sediment flux gradients. Meanwhile, the integration constant is set to zero when $\partial h/\partial t$ of measurements is integrated to find

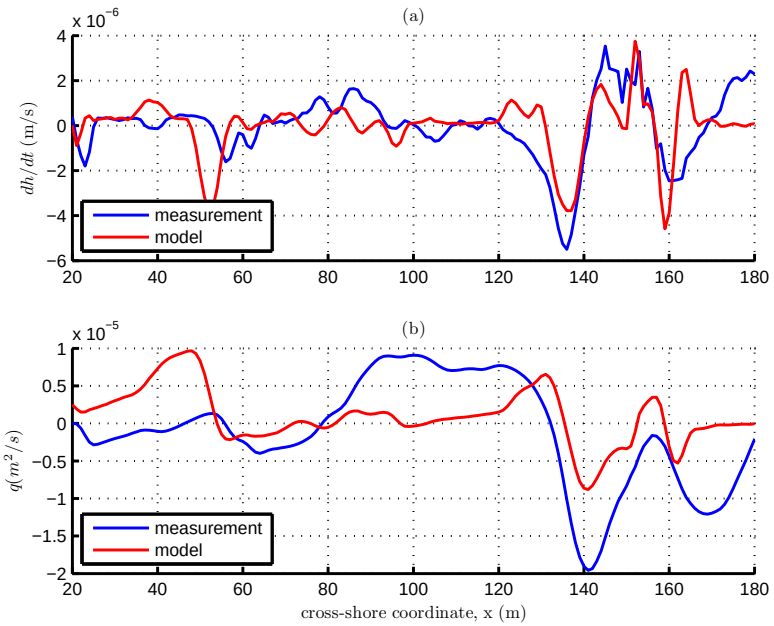

Figure 79: The results from wave hour 8 of test stage 1B. (a) the time rate of change of bed level extracted from the measurements and the model results, (b) sediment fluxes extracted from the measurements and estimated by the model.

q_{meas}. Hence, the offshore value of $\partial q/\partial x$ is assumed to be zero as shown in Figure 78 (b).

In addition to looking at the average results over 8 hours, hourly model results are also compared to the measurements between hours 7 and 8. Figure 79 shows the results from this interval of test stage 1B. The $\partial h/\partial t$ results extracted from the measurements are similar in variation to those for the average of all 8 hours but are slightly higher in magnitude. This is assumed to be due to the increase in significant wave height from 1.32 m to 1.38 m at wave hour 7 of the experiments during test stage 1B. It may clearly be seen that the accretion erosion pattern starting right offshore of the end of trough at x=160 m till the shoreline is not predicted well by the model. The variation and magnitude of $\partial h/\partial t$ of model results and extracted from the measurements is once again similar around the bar. This demonstrates that the coefficient, C_1, chosen for the sediment transport formula is on the correct order of

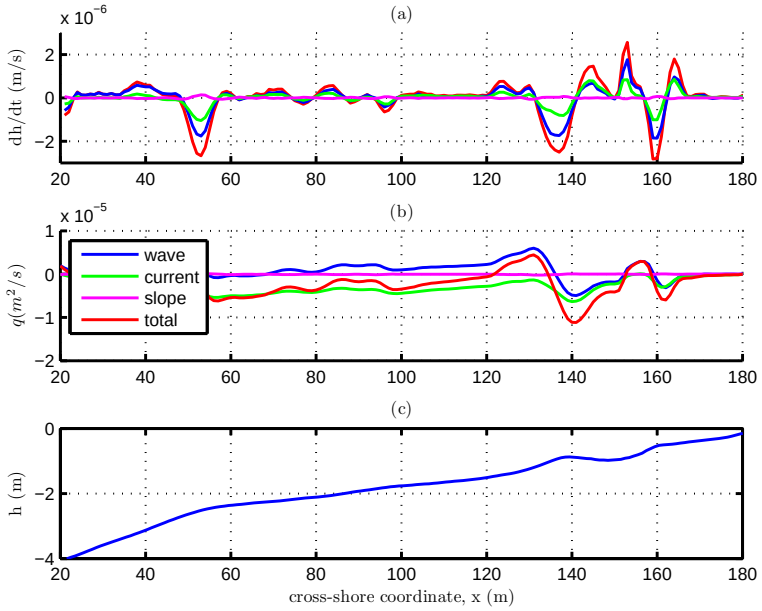

Figure 80: 8 hour averages for test stage 1B of (a) the bathymetric time rate of change due to waves, currents, and the slope term, (b) wave, current and slope components of the sediment transport fluxes; (c) the bathymetry of the domain.

magnitude. The variation of the sediment fluxes of model results are also close to those estimated from the measurements. Similar to the comparison shown in Figure 78, even though the model predicts the magnitude of the gradient of total sediment flux right as reflected by the $\partial h/\partial t$ estimates, it once again shows narrower accretion zones both around the bar crest and around the end of trough. The similarities between the 8-hour average results and the hourly results is because the wave field in the model and the waves generated during measurements are kept almost constant.

To illustrate the reason for discrepancies between the model and the measurements, it is possible to breakdown the total sediment transport into a wave and a current component to understand the physics of sediment transport on barred beaches. This split of *HH* formula for sediment fluxes was explained in Chapter 2 in Equation 113. Figure 80 shows the cross-shore variation of total average sediment flux along with the wave component (Equation 115), current component (Equation 114)

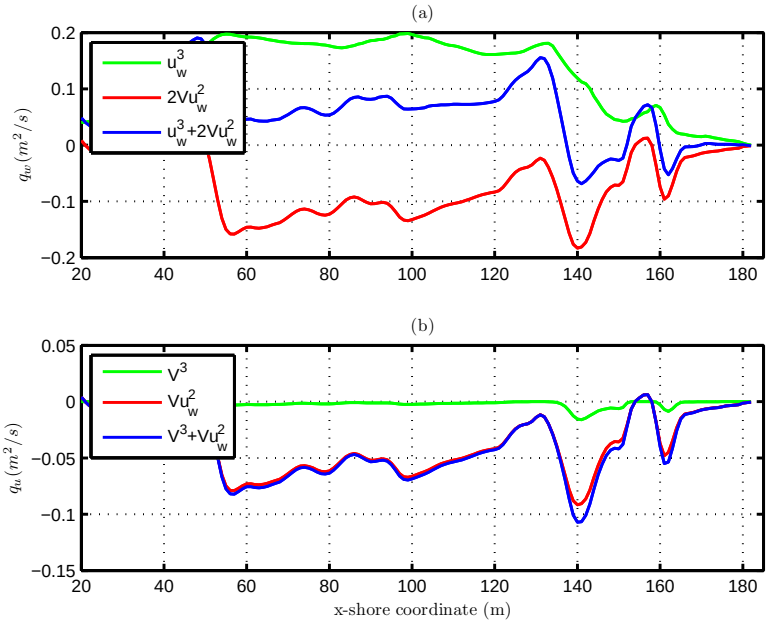

Figure 81: Sediment transport fluxes at wave hour 8 of test stage 1B: (a) wave component of sediment transport rate and its terms given by Equation 115, (b) current component of sediment transport rate and its terms given by Equation 114.

and the slope term (Equation 116). The cross-shore variation of $\partial h/\partial t$ at the top panel of the figure shows that the wave and current components show the same accretion-erosion pattern across the domain. It is observed that at offshore locations the transport due to waves and currents balance each other leading to minimal total sediment transport. Close to the sandbar, the wave component is observed to dominate and the magnitude of total sediment transport flux is close to magnitude of the wave component sediment flux. Inside the bar trough, the situation is reversed and the current component is larger than the wave component. Right offshore of the end of trough where secondary breaking occurs, the wave component dominates again. The slope term is observed to be orders of magnitude smaller than the wave and current components of the sediment transport fluxes as expected.

The *HH* sediment transport formula can be broken down further. Another look at the sediment transport equations reveal that the first term in Equation 114 and

the second term in Equation 115 are basically the same (differing only by a factor of two) and demonstrates the combined action by waves and currents. It needs to be mentioned here that even if those two terms are mathematically the same, they are physically different. The combined term in the wave component comes from the shear stress term (Vu_w) multiplied by the nearbed orbital wave velocity indicating the sediment mobilized by the combined action of wave and current and advected by the wave. The combined term in the current component comes from the the shear stress term (u_w^2) multiplied by the current velocity indicating the sediment mobilized by the waves and advected by the current. Figure 81 shows a breakdown of the wave and current components of sediment transport. The combined term, Vu_w^2, and the current term, V^3, is offshore-directed (negative) across the domain as shown in Figure 81(b) while the wave term is onshore-directed (positive) as shown in Figure 81(a). It is observed that the combined wave-current action term (Vu_w^2) dominates for the current component of sediment transport, q_V. It also has a strong effect on the cross-shore variation of the wave component of total sediment transport, q_w. This explains why the transport due to waves is offshore in the trough. As a result, the variations for the current and wave components of sediment transport are similar to each other for test stage 1B and the overall accretion-erosion pattern due to waves and currents are almost the same inside the surf zone.

Figure 82 shows the initial and final bathymetry from the model results and the measurements for test stage 1B. It is observed that the model can predict the offshore movement of the main sand bar while slightly underpredicting the bar crest height. The model cannot predict the full erosion in the first half of the trough between x=145 and x=152 m where the undertow current is underpredicted as shown previously in Figure 60 and Figure 63. The model results in the formation of a secondary sandbar at the end of the trough where major breaking occurs. An accretion-erosion pattern between x=157 m and x=167 m, shown previously in Figure 79, leads to the formation

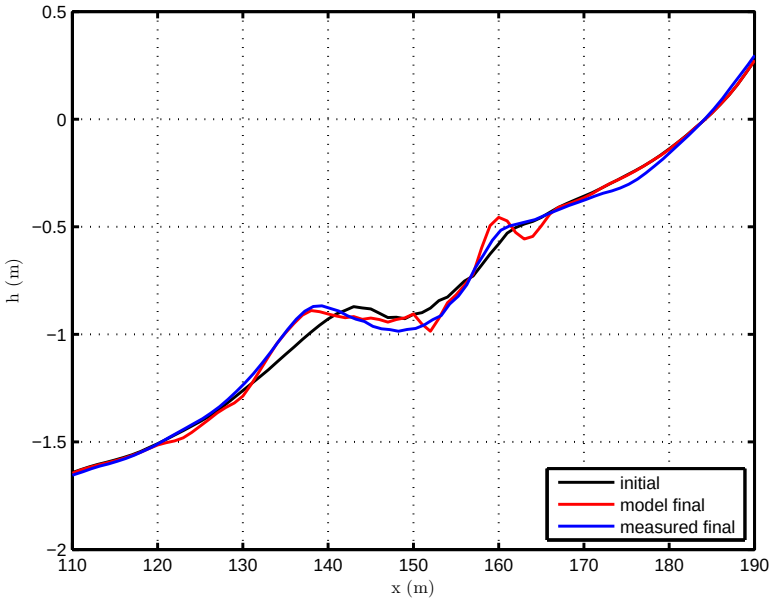

Figure 82: Morphological evolution after the first 8 wave hours of test stage 1B for measurements and model results.

of that bar. On the other hand, the measurements show an accretion-erosion pattern over a much broader region between x=157 m and the shoreline as shown in Figure 80. That is why there is a more gradual offshore movement of the bed at the end of the trough rather than the formation of a bar as shown in model results. The exclusion of the dynamics in the swash zone may contribute to the differences in the erosion along the last 10 m of the beach offshore of the shoreline. The infragravity waves, which have been filtered in this study, are very important for swash zone dynamics which would produce movement of the shoreline thereby smoothing the bathymetry.

4.1.1 Effect of Roller Contribution to Short Wave Forcing

As mentioned in the previous chapter, the roller contribution to the short wave forcing, f_x^r given by Equation 95 is also included in the model and the depth variation of this forcing is controlled via a power coefficient nr. The variation is depth uniform for $nr = 0$, linear for $nr = 1$, quadratic for $nr = 2$ and so on. As the nr value gets larger,

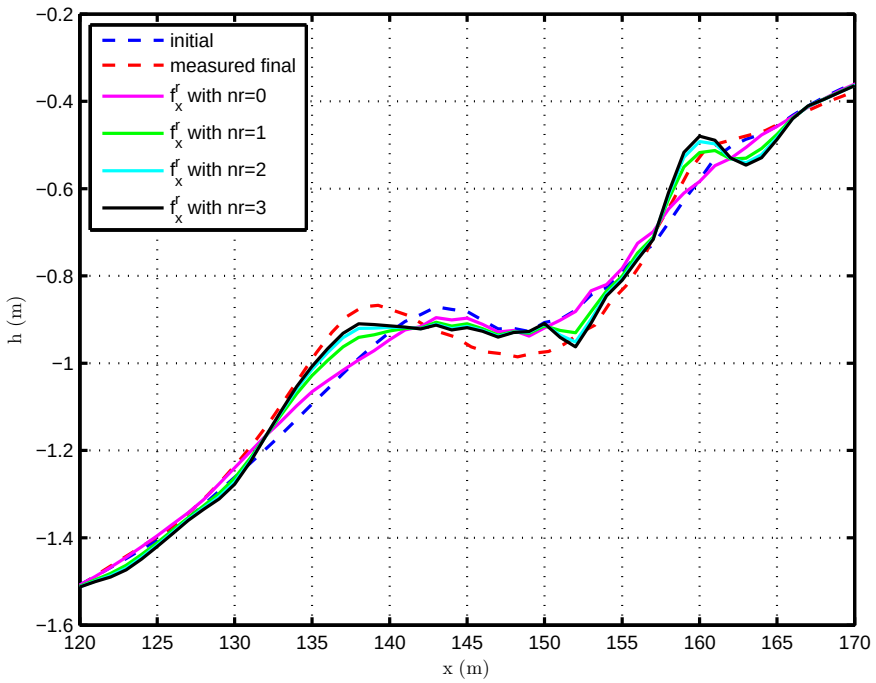

Figure 83: Morphological evolution after the first 8 hours of test stage 1B with measurements and the model results with the roller forcing with different nr values and depth variations.

the roller contribution to the forcing is contained in an area closer to the surface and the effect at the bottom reduces. An f_x^r with a larger nr value was shown to have a smaller effect on the magnitude of the near bed undertow in the previous chapter in Figure 62.

Figure 83 shows the bathymetry for test stage 1B from the measurements together with the model prediction with various roller contributions to the short wave forcing. Previously in Figure 82, it was shown that the bathymetric profile without the roller contribution to the radiation stress is close to the final measured profile in the vicinity of the bar crest, at the seaward face of the bar and the second half of the bar trough. Once the roller term is included the offshore accretion of the bar is diminished particularly for smaller values of nr. For all the roller cases, the shoreward half of the trough is predicted well, but once again, a secondary bar is observed to occur in the

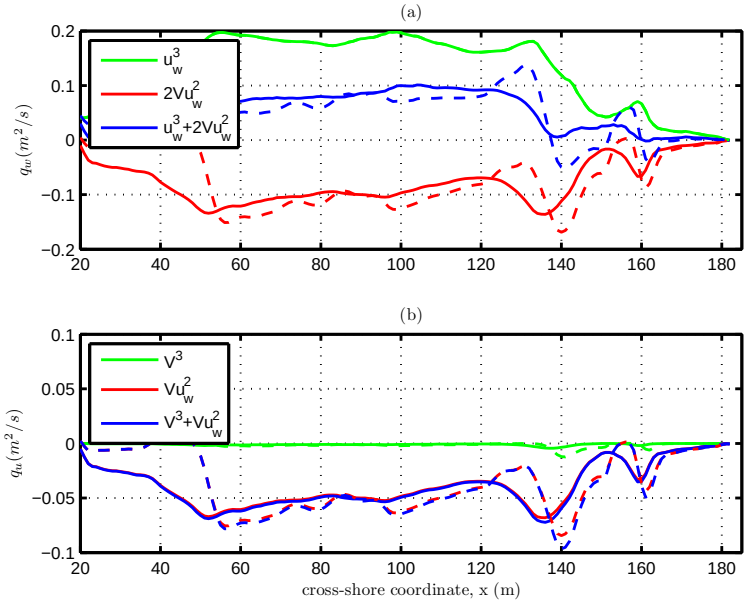

Figure 84: Sediment transport fluxes at wave hour 8 of test stage 1B: (a) wave component of sediment transport rate and its terms given by Equation 115, (b) current component of sediment transport rate and its terms given by Equation 114 for $nr = 0$ (solid lines) and $nr = 3$ (dash lines) in the model.

model at the end of the trough particularly for large values of nr. In fact, the model result with $nr = 3$ is very similar with the case with no f_x^r.

It was shown in the previous chapter that the roller contribution to short wave forcing, f_x^r, decreases the curvature of the depth variation of the undertow and decreases the offshore directed bottom current. A stronger f_x^r at the bottom, i.e. with $nr = 0$ and equal to the surface value leads to a weaker current which changes the sediment transport fluxes and morphological evolution. Physically, this would not be a realistic case since the roller contribution is maximum at the surface and roller momentum is reduced towards the bottom in reality. So, as can be seen from Figure 83, the morphological evolution including a depth uniform roller contribution to short wave forcing, i.e. f_x^r with $nr = 0$, leads to a completely wrong bathymetric evolution with almost no erosion in the trough and the spread of the bar to a wider area instead of a definitive movement.

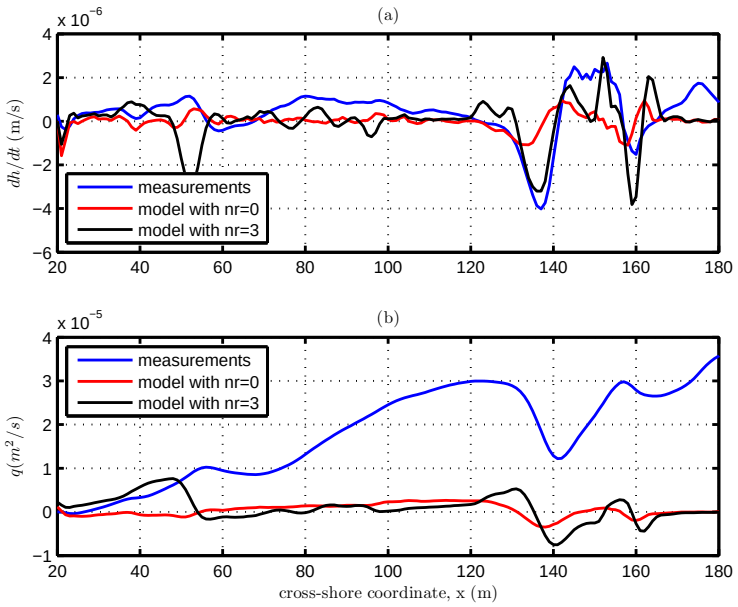

Figure 85: Average results of test stage 1B for 8 hours. (a) the time rate of change of bed level, (b) sediment fluxes extracted from the measurements and the model results, for depth uniform ($nr = 0$) and depth varying ($nr = 3$) roller contribution to the short wave forcing.

To illustrate why there is such a difference between $nr = 0$ and 3, Figure 84 shows a breakdown of the wave and current components of total sediment fluxes for depth uniform and depth varying roller contribution to the short wave forcing in the model. The skewness term u_w^3 does not change, but all the other terms change due to the differences in the cross-shore variation of the bottom value of the current as shown in Figure 63. Due to a shift of the offshore peaks of the bottom current variation in the bar-trough zone, both offshore transport peaks of the combined term, Vu_w^2, offshore of the bar crest and offshore of the end of trough are shifted offshore for the depth uniform roller contribution to the short wave forcing case. This shows that the undertow current is a major driver for the offshore sediment transport and bar migration event; therefore, accurate predictions of the undertow current are important for predictions of sediment transport and morphodynamics by the numerical model.

Figure 85 shows the cross-shore variation of $\partial h/\partial t$ and q, for the measurements

and the model results with the roller contribution to the short wave forcing, i.e. depth uniform and cubic. Panel (a) shows that the model prediction of $\partial h/\partial t$ for $nr = 3$ is close to the measurements while there is an offshore shift in the cross-shore profile of $\partial h/\partial t$ for the case with $nr = 0$ in the model. The cut-off point between the accretion over the bar and erosion in seaward half of the trough is at x=140 m with $nr = 3$. This cut-off point gets shifted up to x=135 m for $nr = 0$ leading to the erosion of the bar crest instead of an offshore migration. This offshore shift of the erosion-accretion pattern results in a poor prediction of the bar migration as shown in Figure 83. The reason for the shift is the changes in the direction of sediment transport as shown in panel (b). When $nr = 3$ is used, the total transport is onshore due to waves before x=135 m and offshore between x=135 and x=152 m. On the other hand, when $nr = 0$ is used, the onshore transport offshore of the bar crest is only up to x=131 and the offshore transport is from that location to right onshore of the bar crest at x=145 m.

4.1.2 Effect of Friction Factor

Initial model runs for sediment transport on bed changes were done with a C_1 value of 0.02 in sediment transport formula which was adjusted for the default friction factor of 0.024. It was shown in Figure 52 that a combined wave-current friction factor, f_{cw}, of 0.015 would be more appropriate than the default value of 0.024 used in the numerical model. Figure 54 also showed that the effect of f_{cw} on the undertow current is minimal with only a slight improvement. However, as shown in Equation 112, the bed shear stress is directly proportional to f_{cw} and an increase from 0.015 to 0.024 means a 60 percent increase in the sediment transport fluxes. Therefore, the effect of f_{cw} on sediment transport is much stronger than its effect on undertow current.

Figure 86 shows the bathymetry from model runs with different f_{cw} values. The model results in a better agreement for the offshore movement of the bar with the higher f_{cw} value. However, because of the decrease in sediment transport, the use

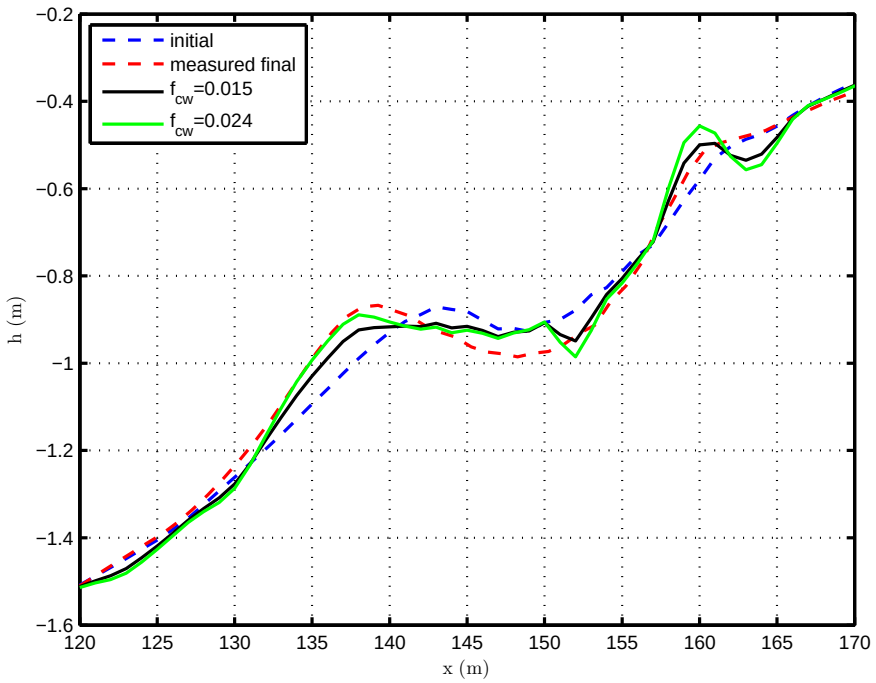

Figure 86: Morphological evolution in the first 8 hours of test stage 1B for model results with different f_{cw} values and the measurements.

of the smaller f_{cw} value of 0.015 would require an increase in C_1 value in q_{HH} from 0.02 to 0.032. Figure 87 shows the morphological evolution for the different C_1 values during the first 8 wave hours of test stage 1B using a f_{cw} value of 0.015 for both cases. Clearly, the offshore transport of the bar is increased with the larger C_1 value.

Figure 88 shows the cross-shore variation of $\partial h/\partial t$ and total sediment transport fluxes with different C_1 values of 0.02 and 0.032 with $f_{cw} = 0.015$ used in the model. It may be seen in panel (b) that an increase in the C_1 value changes the magnitude of the sediment fluxes at the same proportion. Panel (a) shows that the amount of changes in depth are in better agreement with the measurements with the larger C_1 value of 0.032 except at the end of the trough where $\partial h/\partial t$ was already overestimated even with the smaller C_1 value of 0.02. The reason for the better agreement around the bar crest is the change in the gradient of sediment fluxes. There is a very good agreement at the seaward face of the bar around x=135 m. However, there is not

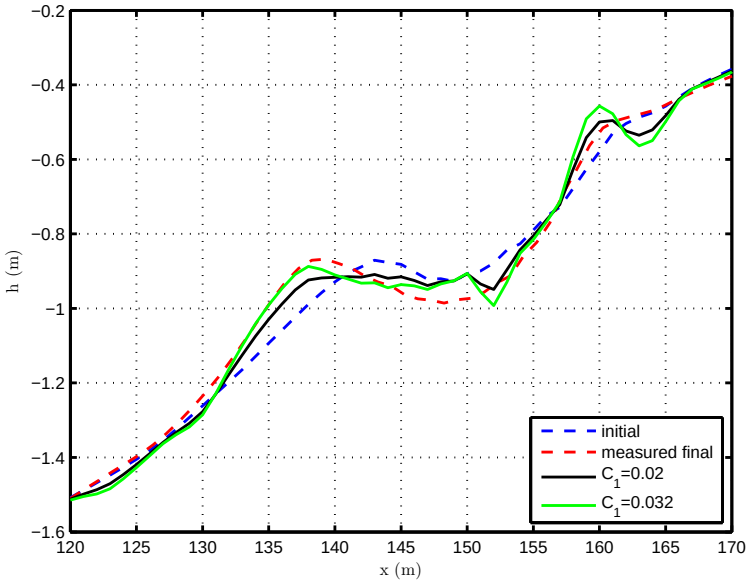

Figure 87: Morphological evolution in the first 8 hours of test stage 1B for model results with different C_1 values and the measurements.

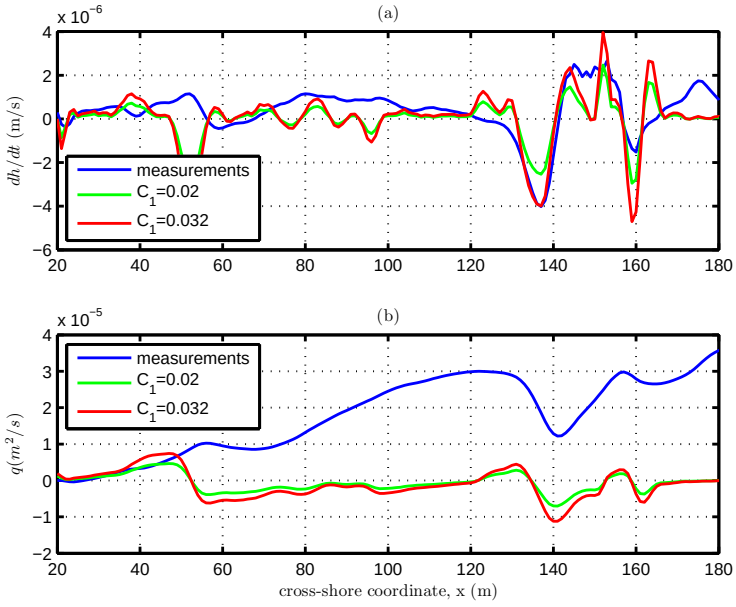

Figure 88: Average results of test stage 1B for 8 hours. (a) the time rate of change of bed level, (b) sediment fluxes extracted from the measurements and the model results, for different C_1 values of 0.02 and 0.032.

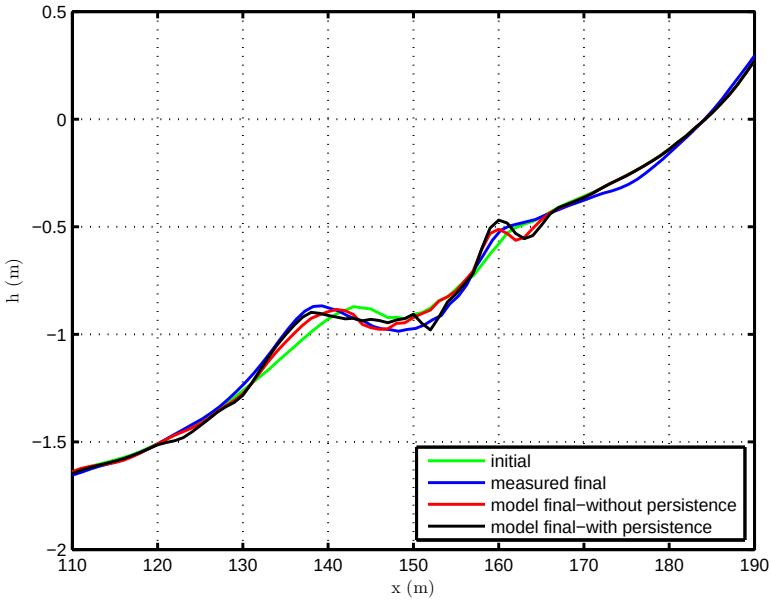

Figure 89: Morphological evolution in the first 8 hours of test stage 1B for model results with and without the persistence length method compared to the measurements.

enough accretion directly offshore of the bar crest to result in the increase of the bar height accompanied with the offshore migration.

4.1.3 Effect of Breaking Wave Persistence

Figure 89 shows the morphological evolution predicted by the model before and after the persistence length method is implemented. Without the persistence length method implemented, the model does not show any erosion in the shoreward half of the trough. The sediment eroded from the shoreward face of the bar between x=141 and 150 m is deposited on the seaward face of the bar causing an offshore movement of the bar at a rate smaller than the measurements. The reason for no erosion predicted by the model in the shoreward half of the trough is an underprediction of the undertow current at that location as shown in Figure 58. The model skill in predicting the bed level change is calculated by Equation 135 using the elevation change in the bathymetric measurements and model predictions for the elevation change for the

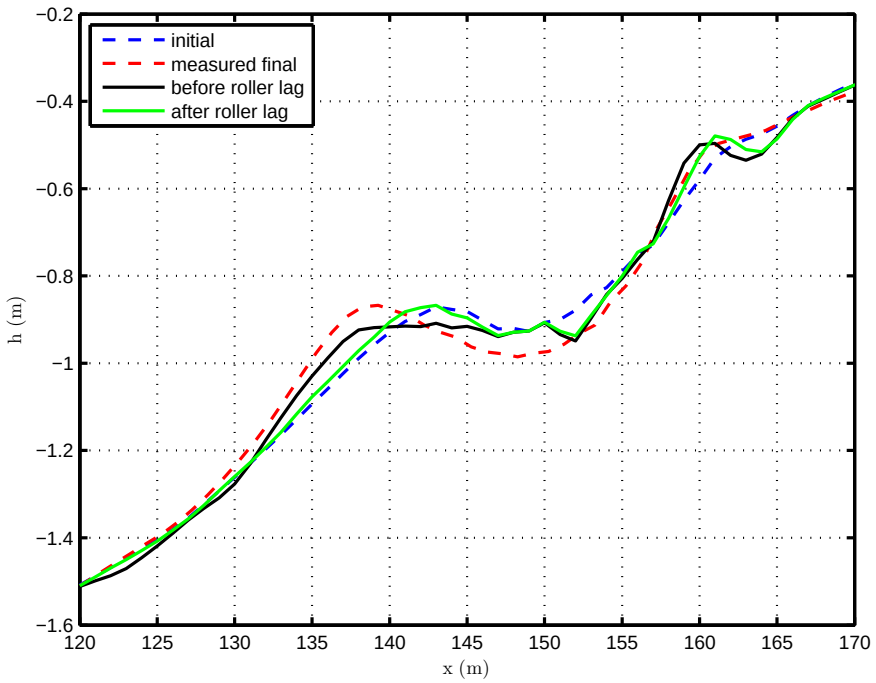

Figure 90: Morphological evolution in the first 8 hours of test stage 1B for model results with and without the roller lag method implementation and the measurements.

first 8 wave hours. The model skill in the shoreward half of the trough, i.e. x=149 to 161 m, increases from 0.75 to 0.86 once the persistence length method is implemented.

At the seaward half of the trough, the model underpredicts the erosion after the persistence length method is implemented while it is in good agreement with the measured profile between x=141 and 147 m before persistence is considered. The former result is because of an underprediction of the undertow current and the latter is due to an overprediction of the undertow current as shown in Figure 58. Hence, a slight overprediction of the nearbed orbital velocity skewness as shown in Figure 72 may be balancing the overprediction in the undertow current and resulting in a $\partial h/\partial t$ value and profile closer to the measurements for the case with no persistence.

4.1.4 Effect of Roller Lag

Figure 90 shows the morphological evolution predicted by the model with and without the roller lag method, including the persistence length method. It may be observed

that without the roller lag method, the offshore movement of the bar is predicted by the model but the height of the bar does not increase during the migration as observed by the measurements. Because the erosion in the trough continues up to x=140 m well beyond the bar crest at x=143 m as shown in Figure 80 in the model results, the erosion of the bar crest leads to a decrease of the bar height as the bar moves offshore. With the roller lag method, the bar again is predicted to move offshore but now along with an increase in the height of the bar. The distance between the initial and final locations of the bar crest is smaller than those observed in the measurements. The measurements show that the bar crest is 4 m seaward of the initial location after 8 hours during test stage 1B while the model predicts only less than a meter movement of the bar in the offshore direction. The model skill for bed level predictions around the bar crest, i.e. x=130 to 148 m, reduces from 0.95 to 0.6 if the roller lag method is used. Without the roller lag method the sandbar moves offshore from x=124 to 119 m but the bar height decreases 20.7 mm in the model, while in the measurements it moves from x=124 to x=120 m but the bar crest height increases 3 mm. After the roller lag method is implemented, the bar crest remains at the same location but the bar crest height increases 5 mm in the model.

Because of the differences in the morphological evolution predictions before and after the implementation of roller lag method, it is necessary to look at the differences between the sediment fluxes to understand the reason for these differences. Figure 91 shows a breakdown of the total sediment flux into wave and current components. It is observed that without the roller lag, the combined term Vu_w^2 has a stronger effect on the variation of both wave and current terms over the entire domain. However, when the roller lag method is implemented, the combined term is smaller in both magnitude and gradient up to x=142 m due to a reduction in the magnitude of the undertow current as shown in Figure 63. Because of this reduction in the magnitude of the combined term in the wave component, the skewness term dominates offshore

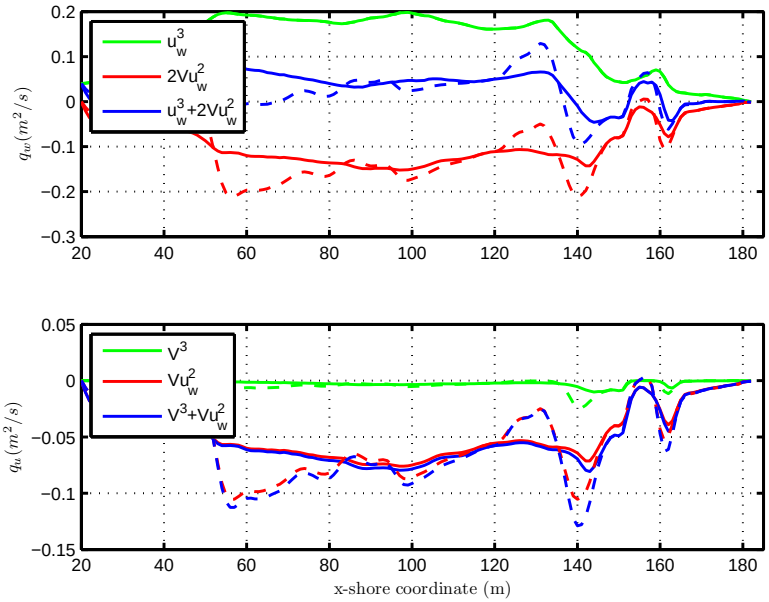

Figure 91: Sediment transport fluxes at wave hour 8 of test stage 1B: (a) wave component of sediment transport rate and its terms given by Equation 115, (b) current component of sediment transport rate and its terms given by Equation 114 without the roller lag (dash lines) and with the roller lag (solid lines) in the model.

of the bar crest up to x=142 m leading to a smaller gradient of the sediment fluxes. After x=142 m where the roller lag ends, the combined term dominates and the sediment fluxes with and without the roller lag are almost the same in the trough. At the end of the trough where breaking occurs, the roller lag once again reduces the magnitude and gradient of the undertow current leading to a reduction in both terms of the current component of sediment flux. The wave component is also reduced in magnitude due to the decrease in the magnitude and gradient of the combined term.

Figure 92 shows the cross-shore variation of $\partial h/\partial t$ and total sediment transport fluxes with and without the roller lag method. Even if the cross-shore variation of total sediment flux, q_{HH}, is similar for both cases, the gradient of q_{HH} is smaller, especially near the bar crest for the case with the roller lag, due to the reduction in magnitude and gradient of both wave and current components of sediment flux

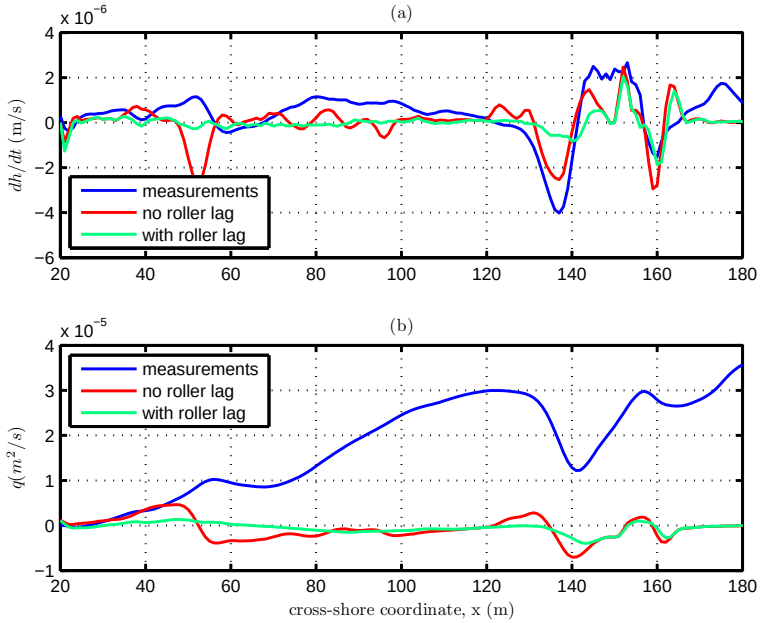

Figure 92: Average results of test stage 1B for 8 hours. (a) the time rate of change of bed level, (b) sediment fluxes extracted from the measurements and the model results, with and without the roller lag.

as shown in Figure 91. The deposition of the sediment eroded from the shoreward face of the bar starts over the bar crest at x=143 m, over the seaward face of the bar, after the roller lag method is implemented. Therefore, the bar height increases over time while it moves offshore. This is not the case before the roller lag method is implemented since the bar crest is also eroded up to x=141 m.

BBB

The second sediment transport formula used in the numerical model is the *BBB* model attributed to Bagnold (1966); Bailard (1981); Bowen (1980). The *HH* model has never been used in the literature for cross-shore sediment transport, however the *BBB* model has been used for bar migration simulations (Gallagher *et al.*, 1998). For that reason, it is important to compare the performance of each model. Figure 93 compares the morphological evolution results of *BBB* sediment transport formula with the *HH* sediment transport formula results with all the same hydrodynamic model

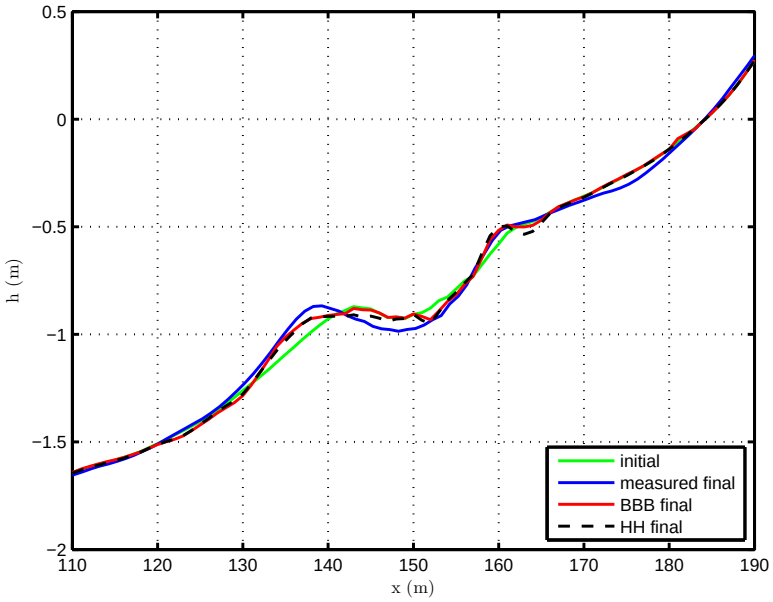

Figure 93: Morphological evolution in the first 8 hours of test stage 1B for model results with *HH* and *BBB* sediment transport formulas and the measurements.

parameters. The results for the *HH* sediment transport formula in Figure 93 are with the initially adjusted C_1 value of 0.02. Also, for *BBB* results the suspended load and bed load efficiencies were $\epsilon_s = .003$ and $\epsilon_b = .042$, respectively. It is observed that the results are very similar to each other especially right offshore of the bar, which is a good indication that the *HH* model performs similarly. Although the formulations are different, both models are energetic-type sediment transport models, therefore the similar performance is expected.

BBB sediment transport formula is written as a function of total velocity given by Equation 117. The total velocity may be split into a nearbed orbital wave velocity and a near bottom current velocity given by Equation 110. Therefore, the *BBB* formula can be broken down into a wave component and a current component, each of which does have a suspended load component and a bed load component. Figure 94 shows the cross-shore variation of $\partial h/\partial t$ and sediment transport fluxes with the wave and current components. It is seen in panel (a) that the wave component dominates

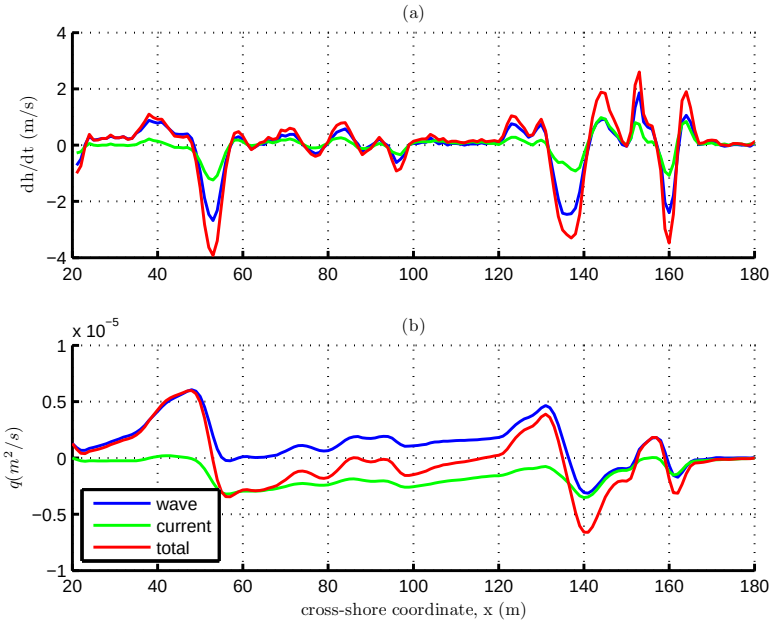

Figure 94: Average results of test stage 1B for 8 hours. (a) the time rate of change of bed level, (b) sediment fluxes extracted from the measurements and the model results, for the total load due to waves and currents estimated by *BBB* sediment transport formula.

across the domain except for the erosion in the seaward half of the trough. Panel (b) shows that the sediment transport attributed to the waves and currents separately by the *BBB* formula is very similar to those estimated by the *HH* formula shown in Figure 80. Once again, the erosion in the middle of the trough reduces up to zero due to a decrease in the gradient of the undertow current in the middle of the trough.

With the *BBB* sediment transport formula it is possible to further breakdown the wave and current components of sediment transport into suspended and bed load components. Figure 95 shows the cross-shore variation of $\partial h/\partial t$ and sediment transport fluxes for all the components of *BBB* sediment transport formula. The suspended wave transport is dominant in shoaling zones offshore of the bar crest and at the end of the trough as shown in panel (b), and is the dominant term for the erosion and accretion of material across the domain as shown in panel (a). In general,

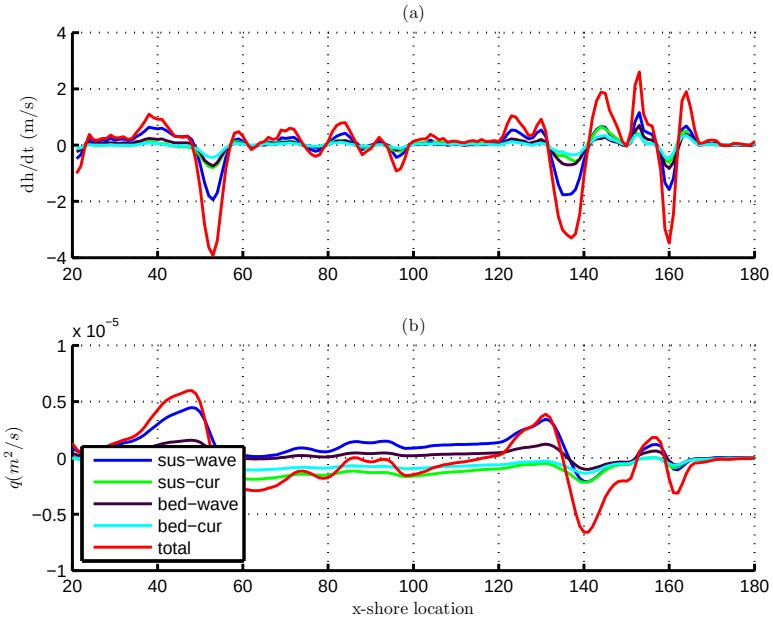

Figure 95: Average results of test stage 1B for 8 hours. (a) the time rate of change of bed level, (b) sediment fluxes extracted from the measurements and the model results, for the suspended and bed load components of *BBB* sediment transport formula.

the total suspended load is larger than the total bed load component for sediment transport due to both waves and currents.

4.2 Test Stage 1C: An Accretive Case

The high-energy erosive test stage 1B is followed by the low-energy accretive test stage of 1C in Delta Flume experiments. Figure 10(b) shows that the sandbar moves onshore during the 13 hour test stage 1C.

A closer look at the *HH* transport formulation shows that both terms in the mean current component (Equation 114) contribute to the offshore sediment transport along with the second term in the wave transport equation (Equation 115) because of the near bed current velocity which is directed offshore for all wave conditions. The skewness term in the wave transport component (Equation 115) is the time averaged third moment of orbital wave velocity and represents the velocity skewness of waves

defined in Equation 1, and it is the only term contributing to the onshore sediment transport. Therefore the net transport direction in the cross-shore is determined by the balance between the skewness term and the other terms.

Even if a linear wave model is used, Elfrink's parametrization method introduces the velocity skewness in near-bottom orbital wave velocities which is one of the major mechanisms responsible for onshore sandbar migration. The infragravity waves have been eliminated from the wave spectrum provided to the wave module as shown in Figure 19 to isolate and analyse the effect of nearbed orbital velocity skewness. Therefore, the only mechanism that could enable the numerical model to produce onshore sandbar migration is the nearbed orbital velocity skewness. It was shown for test stage 1B in the previous section that the undertow velocity is the main mechanism responsible for offshore sediment transport. In this section, the main balance between the offshore transport by the undertow and the onshore transport by the nearbed orbital velocity skewness is analysed for test stage 1C.

Figure 96 shows the morphological evolution over 8 wave hours for test stage 1C when the persistence length and roller lag methods are implemented with a C_1 value of 0.02. It is observed from the figure that the measurements show an onshore evolution of the bar with little change in depth after x=150 m. The model is unable to predict the strong onshore migration of the bar observed in the measurements. The bar slightly grows and tends to move onshore, but not with a definitive migration.

Although the model results in a slight onshore movement of the bar, it cannot result in the bed changes similar to those observed from the measurements. Therefore, it is necessary to look at the details of sediment transport to understand the discrepancies caused by the model leading to those differences. Figure 97 shows the cross-shore variation of $\partial h/\partial t$ and sediment transport fluxes. As can be seen in panel (b), the measurements show a strong peak in onshore sediment transport right offshore of the bar crest at x=135 m followed by a peak of offshore transport in the

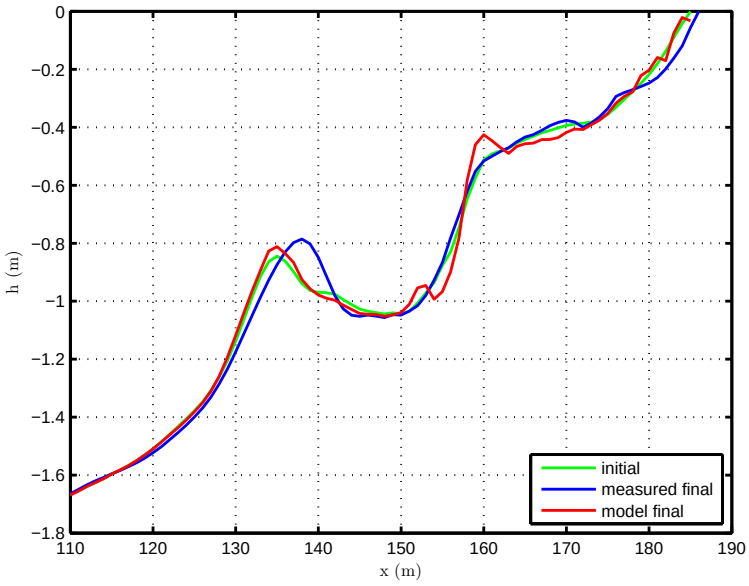

Figure 96: Morphological evolution in the first 8 hours of test stage 1C for model results with the roller lag method and the persistence length method implementation compared to the measurements.

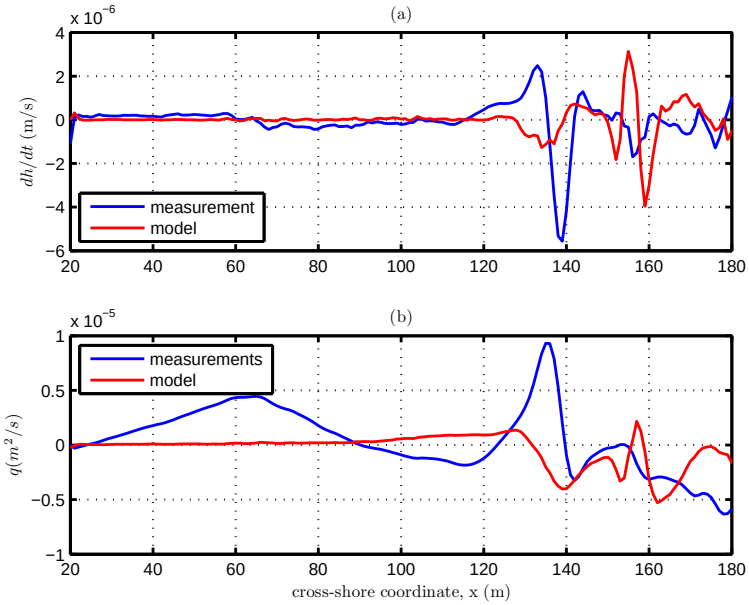

Figure 97: Average results of test stage 1C for 8 hours. (a) the time rate of change of bed level, (b) sediment fluxes extracted from the measurements and the model results, with the roller lag and the persistence length methods.

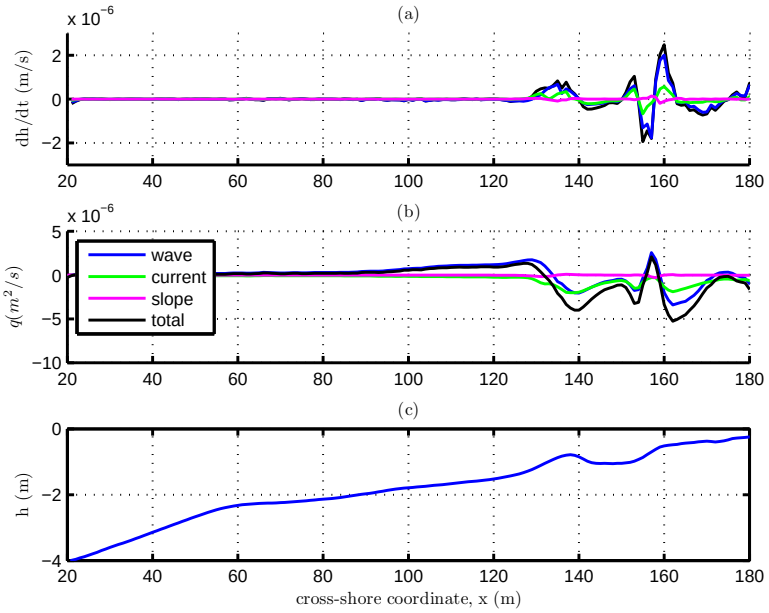

Figure 98: 8 hour averages of test stage 1C of (a) the bathymetric time rate of change due to waves, currents, and the slope term, (b) wave, current and slope components of the sediment transport fluxes; (c) the bathymetry of the domain.

trough at x=142 m. The model shows only a slight increase in the magnitude of onshore transport only up to x=128 m. The model predicts the magnitude of the peak of offshore transport close to the measurements, but further offshore at x=140 m.

The differences in sediment transport fluxes lead to the discrepancies observed in panel (a). The erosion offshore of the bar is observed to be minimal in the model results while measurements show a significant erosion zone seaward of the bar up to the bar crest at x=135 m. While a narrow and strong accretion zone between x=135 and 142 m is observed in the measurements resulting in the onshore movement of the bar, the model results in a much weaker accretion over a wider zone between x=128 and 139 m. Overall, the erosion-accretion pattern predicted by the model is weaker and shifted offshore compared to the measurements over the entire domain.

In order to understand the role of the different mechanisms for the sediment transport from the model, a breakdown of the total sediment flux into wave and current components and the resulting erosion-accretion pattern due to each component is shown in Figure 98. First of all as seen in panel (a), it is observed that both the wave and current components results in the same erosion-accretion pattern across the domain even though the magnitudes are different. This is because the variation of sediment fluxes are similar across the domain with different magnitudes as shown in panel (b). Overall, the wave component is observed to be larger offshore the bar but the magnitude and variation of both components are almost exactly the same in the trough between x=139 and x=154 m.

Figure 99 shows a breakdown of the wave and current components of total sediment flux into their individual components. Similar to the results from test stage 1B, the combined term, Vu_w^2 dominates the current component and it also strongly affects the variation of the wave component. Offshore of the bar crest, the wave component of sediment flux increases up to x=129 m. Even though the skewness term actually increases up to x=131 m, the offshore transport from the combined term starts increasing at x=127 m causing the decrease in the peak of onshore transport due to waves at that location at x=129 m. The skewness term dominates the wave component at the end of the bar trough where the current component goes to zero. This onshore transport due to waves leads to the development of the secondary bar at the end of the trough as shown in Figure 96.

It was discussed in Chapter 3 that the model results in better undertow current profiles when both the persistence length and the roller lag methods are implemented as shown in Figure 69 for test stage 1C. However, the undertow current is still overpredicted by the model in the surfzone starting from the seaward face of the bar at x=130 m. Besides, it was also shown that the nearbed orbital velocity skewness is

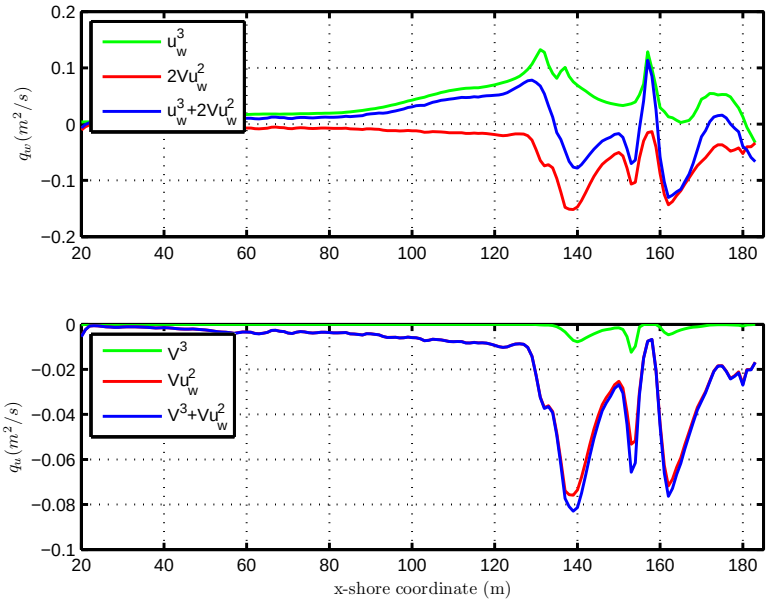

Figure 99: Sediment transport fluxes at wave hour 8 of test stage 1C: (a) wave component of sediment transport rate and its terms given by Equation 115, (b) current component of sediment transport rate and its terms given by Equation 114.

underpredicted by the model for test stage 1C as shown in Figure 73. The combination of these are the primary reason for the underprediction of the onshore transport which cannot overcome the offshore transport due to the undertow current. As a result, the model predicts a less pronounced onshore transport of the bar.

Since we have discussed the effect of friction factor, f_{cw}, the coefficient C_1 of *HH* sediment transport formula and the roller contribution to the wave forcing, f_{xr} for test stage 1B and the effects on sediment transport are similar, they are not going to be discussed for test stage 1C. However, it is important to observe the effect of persistence length and roller lag method on the sediment transport and bar migration.

4.2.1 Effect of Breaking Wave Persistence

Figure 100 shows the morphological evolution with and without the persistence length method for the case without the roller lag. The sandbar moves offshore for both cases

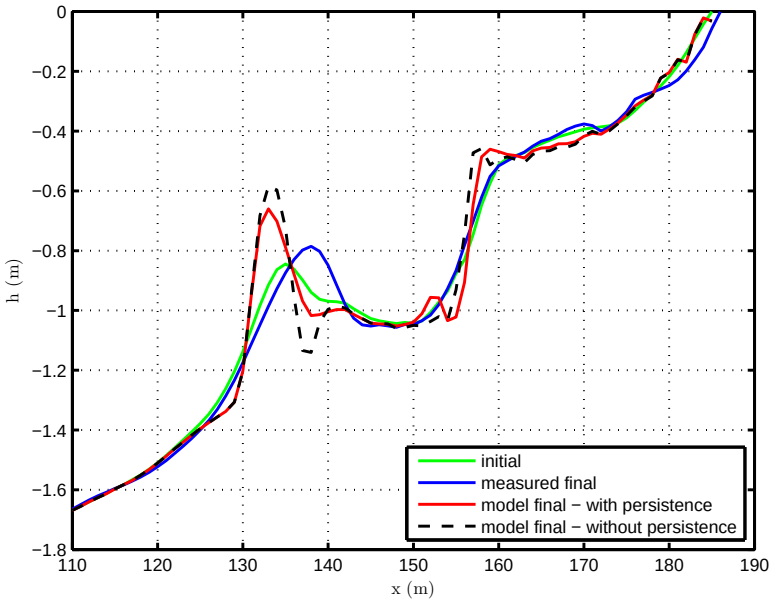

Figure 100: Morphological evolution in the first 8 hours of test stage 1C for model results with and without the persistence length method implementation and the measurements (without the roller lag method).

with similar erosion-accretion patterns around the bar crest; however, the erosion on the shoreward half of the bar is stronger with no persistence. The offshore sediment transport both at the bar crest and at the end of trough is stronger for the case without the persistence length method. The model skill for bed level prediction raises from 0.06 to 0.11 once the persistence length method is used. The measurements show a 3 m onshore movement of the bar crest along with a 6 cm increase in bar height. However, the model shows a 1 m offshore movement with a 16 cm and 24 cm increase in bar height with and without the persistence length method, respectively . The similarities and differences arise from the cross-shore variation of the undertow current shown in Figure 71. The offshore-directed undertow current is stronger at the bar crest, x=135 m, and at the end of the trough, x=160 m, before the persistence length method is implemented. The variation of the undertow current dominates the sediment transport.

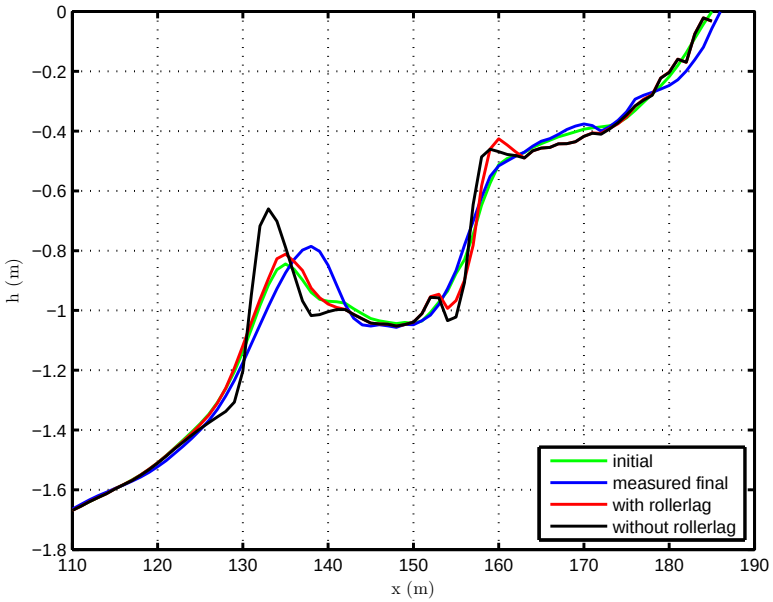

Figure 101: Morphological evolution in the first 8 hours of test stage 1C for model results with and without the roller lag method and the measurements.

4.2.2 Effect of Roller Lag

It may be seen in Figure 101 that if the roller lag method is not implemented, the sandbar moves offshore while the bar crest is eroded and that sediment is deposited on the seaward face of the bar causing an offshore movement. Since the roller lag method does not change the wave properties used in calculating the nearbed orbital velocities by Elfrink's parametrization method, the only reason for this change in sediment transport and morphological evolution is the change in the magnitude and variation of the bottom value of the undertow current. The peak of the undertow current without the roller lag method is shifted offshore right on top of the bar crest and the magnitude also increases as shown in Figure 71.

Figure 102 shows the cross-shore variation of $\partial h/\partial t$ and total sediment transport fluxes with and without the roller lag method. Without the roller lag, the model

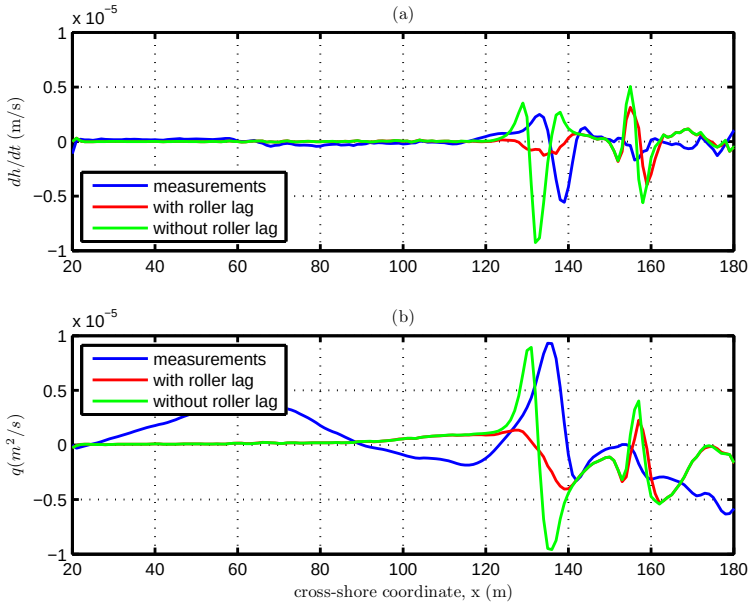

Figure 102: Average results of test stage 1C for 8 hours. (a) the time rate of change of bed level, (b) sediment fluxes extracted from the measurements and the model results, with and without the roller lag.

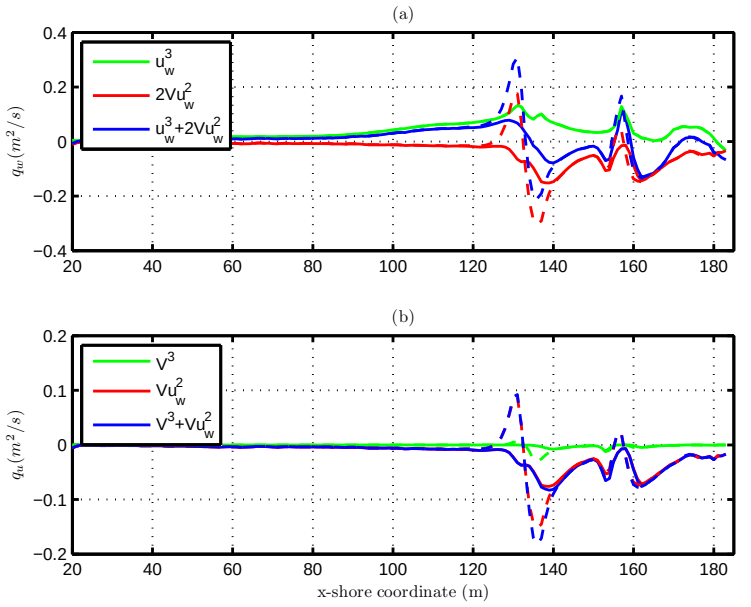

Figure 103: Sediment transport fluxes at wave hour 8 of test stage 1C: (a) wave component of sediment transport rate and its terms given by Equation 115, (b) current component of sediment transport rate and its terms given by Equation 114 without the roller lag (dash lines) and with the roller lag (solid lines) in the model.

results in a cross-shore variation of $\partial h/\partial t$ shifted offshore compared to the measurements in panel (a). As a result, the sandbar moves offshore rather than onshore since the bar crest is eroded and the sediment deposited is accreted on the seaward slope of the bar, as in test stage 1B. The gradient of q_{HH} is smaller especially near the bar crest for the case with the roller lag due to the reduction in magnitude and gradient of both wave and current components of sediment flux as shown in Figure 103. This improves the accretion-erosion pattern with less transport after the roller lag method is implemented. However, there are still important discrepancies compared to the measurements. The deposition of the sediment, eroded from offshore of the bar, starts and ends earlier in the model even if the results are better after the roller lag method is implemented. Therefore, the bar height increases over time while it moves slightly onshore.

Figure 103 shows a breakdown of the total sediment flux into wave and current components. Without the roller lag, the combined term Vu_w^2 has a stronger affect on the variation of both wave and current terms over the entire domain. The combined term contributes to the onshore sediment transport offshore of the bar crest, since the undertow current is onshore directed as shown in Figure 71. This is because the immediate contribution of the roller to the radiation stress causes a strong setdown in the mean water level as shown in Figure 41, thereby causing a negative pressure gradient as seen in Figure 70. After the roller lag method is implemented, the combined term is smaller in both magnitude and gradient offshore of the bar crest up to x=140 m due to a reduction in the magnitude of the undertow current as shown in Figure 71. Because of this reduction in the magnitude of the combined term in wave component, the skewness term dominates offshore of the bar crest up to x=128 m resulting in a smaller gradient of the sediment fluxes. Onshore of the bar crest, i.e. after x=140 m where the roller lag ends, the combined term dominates and the sediment fluxes with or without the roller lag are almost the same in the

trough. At the end of the trough where breaking occurs, the roller lag once again reduces the magnitude and gradient of the undertow current leading to a reduction in both terms of the current component of sediment flux. The wave component of sediment transport is also reduced in magnitude due to the decrease in the magnitude and gradient of the combined term.

The model skill for bed level predictions around the bar crest increases from 0.06 to 0.32 once both the persistence length and the roller lag methods are implemented. The model skill for bed level predictions in the entire domain increases from 0.13 to 0.26 once the roller lag method is implemented. The sandbar moves 2 m offshore if the roller lag method is not implemented, while it remains at the same location once the roller lag method is used. The height of bar crest increases 33 cm during the offshore movement without the roller lag method, while it increases 5 cm with the roller lag method. The measurements show a 2 m onshore movement of the bar along with a 7 cm increase in bar crest height.

BBB

Figure 104 compares the morphological evolution results of *BBB* sediment transport formula with the *HH* sediment transport formula results with all the same hydrodynamic model parameters. A C_1 value of 0.02 is used in *HH* and the suspended load and bed load efficiencies of *BBB* are $\epsilon_s = 0.003$ and $\epsilon_b = 0.042$, respectively. Similar to test stage 1B, the results are similar to each other only with small differences which is a good indication that both energetic based sediment transport models perform similarly in spite of the differences in formulation. This is another indication of the strong dependence of sediment transport on nearshore hydrodynamics for energetic-based sediment transport models.

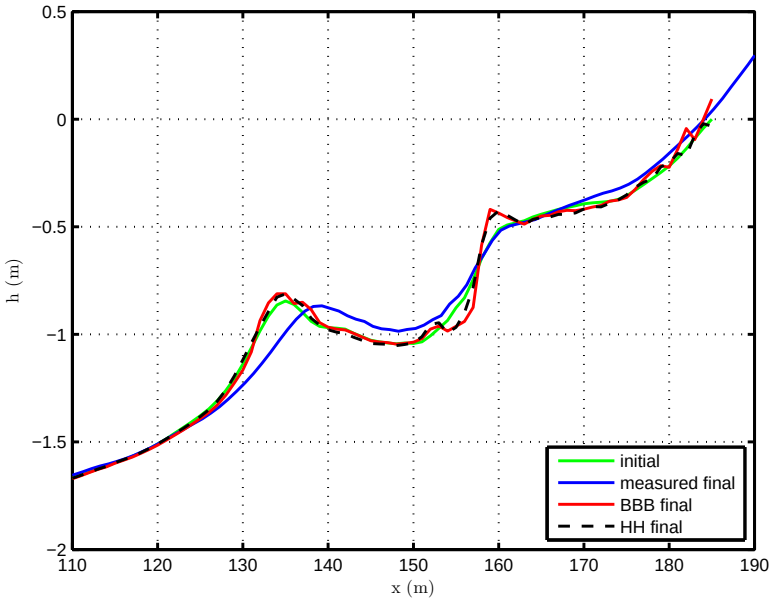

Figure 104: Morphological evolution in the first 8 hours of test stage 1C for model results with *HH* and *BBB* sediment transport formulas and the measurements.

4.2.3 Effect of Slope Term

A slope term is developed and added to the *HH* sediment transport formula as described in Chapter 2. Figure 105 shows the effect of slope term at the end of trough for a model simulation of test stage 1C. It may be seen that without the inclusion of the slope term, irregularities arise in the bed. The effect of the slope term is to reduce these irregularities by diffusing the unrealistic peaks formed at the bottom resulting in a smoother bed profile as shown in the figure.

4.2.4 Effect of Velocity Skewness

Figure 106 shows the morphological evolution predicted by the model with and without parametrization method for velocity skewness by Elfrink *et al.* (2006) with both the persistence length and the roller lag methods. A C_1 value of 0.06 is used in the sediment transport formula. With the Elfrink's method, the sandbar grows in height as also shown by the measurements with accretion on the bar crest. Even if it is

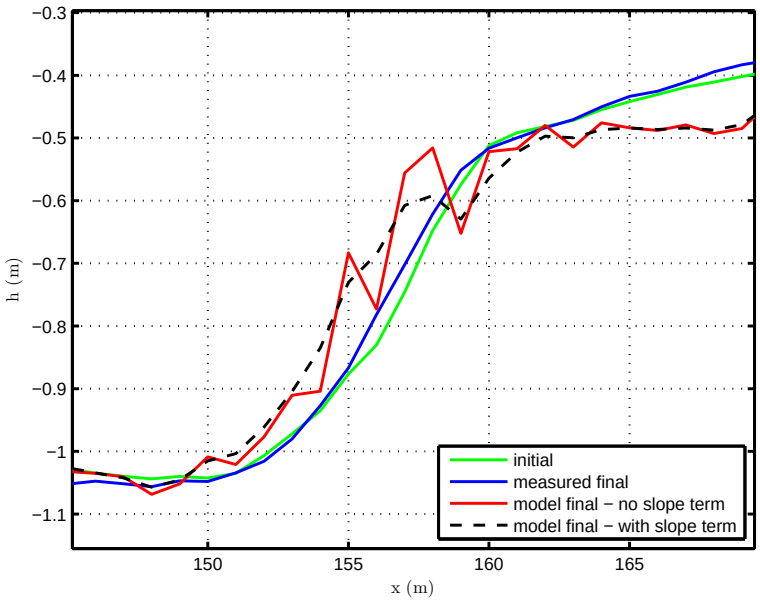

Figure 105: Morphological evolution in the first 8 hours of test stage 1C for model results with *HH* sediment transport formula with and without the slope term and the measurements.

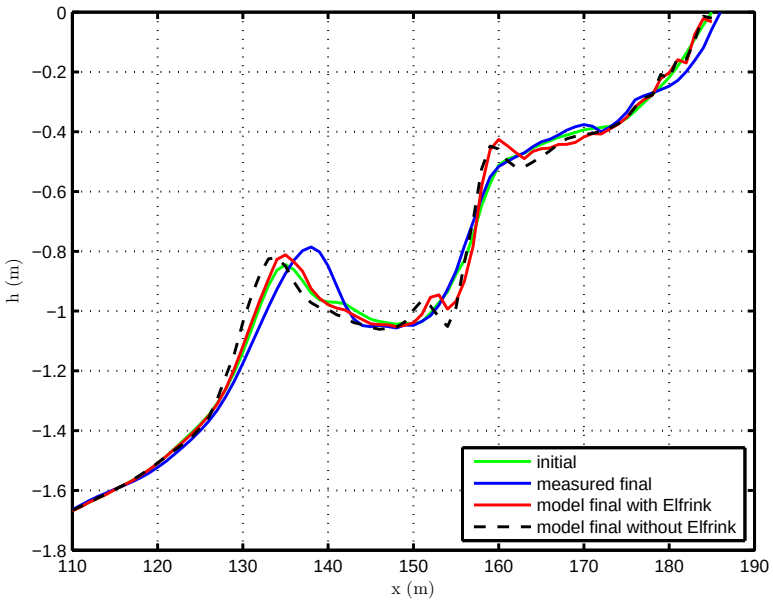

Figure 106: Morphological evolution in the first 8 hours test stage 1C for model results with and without the Elfrink method and the measurements.

not significant, the larger amount of accretion on the shoreward face of the bar is an indication of onshore bar movement. The model generates a secondary bar at the end of trough which is not shown in the measurements. A smaller bar is also shown to be created in the shoreward half of the trough while no change in bed is measured in this section indicating a near perfect balance between the offshore transport due to the current and the onshore transport due to waves during the measurements. When Elfrink's method is not used and the nearbed orbital wave velocities are sinusoidal, more erosion is observed in the trough right onshore of the bar crest and more accretion is observed in the seaward slope of the bar leading to the offshore bar movement. The fact that a bar in the middle and at the end of the trough is created with the case with no onshore transport shows that they are created due to the action of offshore directed undertow current. The bar at the end of the trough is located more onshore with skewed waves and the bar created in the middle of the trough is smaller showing the contribution to onshore transport due to velocity skewness at both locations.

Figure 107 shows the cross-shore variation of $\partial h/\partial t$ and total sediment transport fluxes with and without the Elfrink method. Panel (b) shows that the total transport with the linear waves is offshore across the domain. With skewed waves, it is onshore offshore of the bar crest and at the end of trough where the skewness of waves is maximum just before they break. Without Elfrink's method, the sediment eroded shoreward of the trough is deposited at the end of the trough causing the formation of a secondary bar there as shown in Figure 106; the sediment eroded between x=153 and 157 m is accreted between x=150 and 153 m forming a sandbar in the middle of the trough; the sediment eroded from the shoreward face of the main sandbar is deposited on the bar crest and seaward face of the bar. With Elfrink's method, the sediment is eroded from the offshore boundary to the point where onshore transport peaks (x=128 m) and gets deposited slightly on the seaward face of the bar and mainly on the shoreward face of the bar. The location for the peak onshore transport

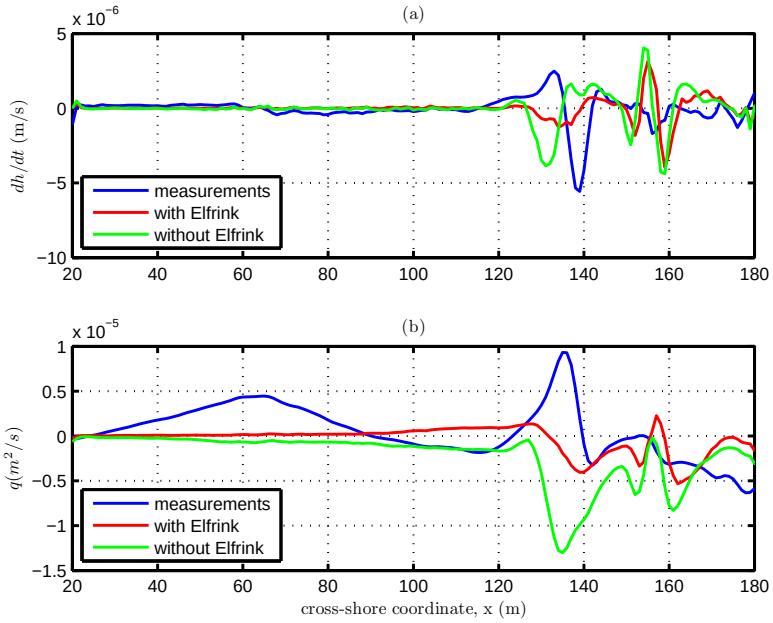

Figure 107: Average results of test stage 1C for 8 hours. (a) the time rate of change of bed level, (b) sediment fluxes extracted from the measurements and the model results, with and without Elfrink's method.

is important since it determines the location where the accretion of the sand begins towards the shore. The onshore transport due to waves is observed to peak at the bar crest (x=135 m) in the measurements. That is why the sediment eroded from offshore is deposited on the shoreward face of the bar causing an onshore movement. However, the peak is predicted well offshore of the bar crest by the model at x=128 m. This causes the accretion zone to be shifted offshore and the bar only slightly moves onshore. There are two reasons for this discrepancy in the peak of onshore transport offshore of the bar crest. One is the early and strong increase in the magnitude of the undertow current, as shown in Figure 71 that reduces the onshore wave transport earlier than expected. The second one is that the location for the peak of the skewness term is not predicted at the bar crest but offshore of the bar crest at x=131 m as shown in Figure 108.

Figure 108 shows a breakdown of the total sediment flux into wave and current

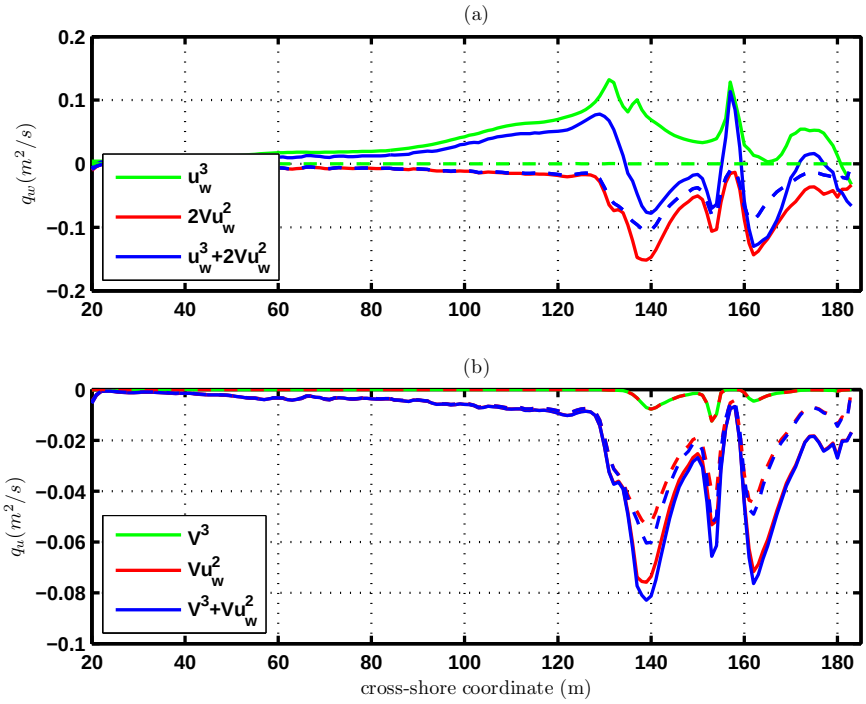

Figure 108: Sediment transport fluxes at wave hour 8 of test stage 1C: (a) wave component of sediment transport rate and its terms given by Equation 115, (b) current component of sediment transport rate and its terms given by Equation 114 without (dash lines) and with Elfrink's method (solid lines) in the model.

components. Since the skewness term causes onshore transport throughout the domain and is larger than the combined term offshore of the bar crest and at the end of the trough, the wave component causes onshore sediment transport with the Elfrink's method. When Elfrink's method is not used, the waves are linear and the skewness term is zero, therefore the sediment transport due to both waves and currents is offshore. Since the second moment of the nearbed orbital velocity is smaller for linear waves, the combined term is smaller without Elfrink's method.

The model does not produce a significant onshore movement with Elfrink's method but shows an offshore movement without it showing the importance of velocity skewness as also shown in Cambazoglu *et al.* (2006). The skewness term is zero in the absence of Elfrink's method and the sediment transport throughout the domain is offshore resulting in an erosion accretion pattern with offshore bar migration for test

stage 1C without Elfrink's method. The undertow current is weaker but overpredicted for the low-energy test stage 1C than the high-energy test stage 1B. Therefore, the reason for the weak onshore movement of the bar with Elfrink's method is either the underprediction of the nearbed orbital velocity skewness or the lack of another mechanism, i.e. acceleration skewness, that will enhance onshore bar migration in the numerical model.

The model skill for bed level change around the bar crest increases from 0.18 to 0.31 once Elfrink's method is used. Without Elfrink's method, the sandbar moves 2 m offshore, while with Elfrink's method it remains at the same location. The bar height increases 2 cm during the offshore movement without the Elfrink's method, while it increases 3 cm in place with the Elfrink's method.

CHAPTER V

CONCLUSION

Sandbars are one of the most common and important features in the nearshore environment. They offer natural protection to sandy beaches causing the initiation of wave energy dissipation away from the shoreline. The reduction in wave height, wave energy and wave forces due to wave breaking around a sandbar reduces the damage of storm events not only to the sandy beaches but also to the the developed areas near the coast. Strong cross-shore and longshore currents are generated between a sandbar and the shoreline. These currents cause sediment transport and the erosion of sandy beaches. The erosion of a beach causes the decrease of recreational area and activities and increases the vulnerability of coastal towns. There is an important feedback between the hydrodynamics and morphodynamics in the nearshore environment. Therefore, accurate predictions of currents are important for coastal engineers in order to be able to predict erosion rates and decide when and if a nourishment may be required for a beach. Strong offshore directed rip currents are also generated on barred beaches and they may become a threat to swimmers.

The nearshore processes are sensitive to the location and height of a sandbar. As the sandbar moves onshore or as the bar height decreases, the beach becomes more prone to wave attack as well as to storm damage and erosion. As the sandbar builds up and the height of the bar increases or as the bar moves offshore, most of the waves break on the bar away from the shoreline protecting the beach. As a result, it is important for coastal engineers to be able to predict sandbar movements for recreational, environmental, economical purposes as well as storm damage reduction.

A process-based numerical model has been used to study nearshore hydrodynamics and morphodynamics on barred beaches. The intent was to expand the body of knowledge of the physics of cross-shore sediment transport and sandbar migration in the nearshore environment.

A quasi-3D numerical model with three main modules, i.e., wave, circulation and morphology modules, is used to simulate the nearshore hydrodynamics and morphodynamics of barred beaches with alongshore uniformities to study bar migration events. Hydrodynamic and morphodynamic measurements of an alongshore uniform barred beach from a large-scale laboratory experiment is used to validate the model results. A high-energetic storm case of erosive conditions with offshore bar migration and a low-energetic post-storm case of accretive conditions with onshore bar migration are the two test stages used in this study.

A number of enhancements are made to the wave and circulation modules of the numerical model system specifically for simulations on barred beaches. The model modifications and enhancements are:

- a combined breaking wave parameter with a spatial variation in the wave model;
- a method accounting for breaking wave persistence in the wave model;
- a method accounting for the new breaker roller lag in the wave model;
- the dynamic pressure component in the radiation stress forcing;
- a roller contribution with different depth variation options for the short wave forcing in the circulation model;
- wave height instead of water depth as the turbulent length scale in the eddy viscosity calculations in the circulation model;
- a slope term for the default sediment transport formula.

The linear spectral wave model, REF/DIF-S, models the wave heights successfully after careful calibration of the empirical breaking parameters of the standard dissipation model. The overall skill of the model is high for wave height predictions, 0.91 for the high-energetic storm case and 0.89 for the low-energetic post-storm case, However, the skill is lower in the bar trough where the wave heights are overestimated, i.e. 0.51 for the high-energetic storm case and 0.37 for the low-energetic post-storm case.

The standard parametric dissipation model used in the linear spectral wave module has two free parameters which are combined into one and a spatial variation is introduced to this single parameter in terms of local parameters, increasing the model skill in the bar trough to 0.77 and 0.55 for the high-energetic storm case and the low-energetic post-storm case, respectively. The dissipation mechanism was developed for monotonic beaches and is directly proportional to wave height, inversely proportional to the local depth. Since most of the waves break over the bar crest, the wave height decreases in the trough while the water depth increases on the shoreward face of the bar. Therefore, the dissipation model predicts a strong decrease in wave energy and does not perform as well over a non-monotonic barred beach. A method accounting for the breaking wave persistence in the surf zone is developed and incorporated in the numerical model to improve model performance and reduce the deficiencies in the wave-related parameters. The effect of the persistence length method is to extend the dissipation into the trough, thereby resulting in decreasing wave heights within the trough, thus improving agreement with the measurements. The model skill for wave height predictions in the trough increases from 0.77 to 0.99 for the high-energetic storm case and from 0.55 to 0.95 for the low-energetic post-storm case once the persistence length method is used. The persistence length method increases the radiation stress gradients due to the increase in dissipation which results in an increase in the mean water level in the bar trough.

A roller model is incorporated in the wave module to account for the contribution of the surface roller to the mass and momentum flux of waves. The roller contribution to the radiation stress and wave volume fluxes are shown to be significant, especially right offshore of the bar crest and at the end of the trough where the majority of new breaking occurs. Comparisons between the model-predicted radiation stresses and those extracted from the measurements show discrepancies due to the immediate contribution of the roller. Therefore, a roller lag mechanism is introduced in the numerical model to improve the predictions for the roller component of radiation stresses. The effect of the roller lag method is to account for the development of the roller by delaying the amount of immediate roller contribution to the radiation stresses, thereby reducing the mean water level and pressure gradient.

The model is also shown to be sensitive to the roller front slope angle, σ_r. The σ_r value is calibrated within the range of values observed in literature and a value smaller than the default value of the model is shown to improve model predictions of mean water level by increasing the amount of roller contribution to the radiation stresses. The surface shape parameter, B_o is also shown to be important for accurate predictions of the mean water level by changing the magnitude of mean water level across the domain.

The undertow current is one of the major driving forces for the cross-shore sediment transport. The vertical momentum balance across the domain is studied to understand the physics affecting the undertow current. In general, the balance between the pressure gradient and the wave forcing determines the magnitude of the vertical viscosity term which denotes the curvature of the undertow current. The pressure gradient is shown to be the most important forcing term for the magnitude and the depth structure of the undertow current. Therefore, accurate predictions of the mean water level variations are crucial. The persistence length method increases the mean water level in the bar trough resulting in a change in the sign of pressure

gradient from negative to positive. Therefore, the negative curvature of the undertow, i.e. a decreasing undertow current from surface to bottom, at the bar trough becomes positive resulting in a correct depth variation for the undertow current as shown in the measurements. After the persistence length method is implemented, the model skill at the trough location increases from 0.35 to 0.80 for the high-energetic storm case and from 0.12 to 0.89 for the low-energetic post-storm case. The roller lag method decreases the mean water level where strong breaking occurs, causing the negative pressure gradient to become positive. Therefore, the negative curvature of the undertow current right offshore of the bar crest, and at the inshore end of the trough becomes positive resulting in a depth variation and bottom value of the undertow current in better agreement with the measurements. The model skill for undertow current predictions directly offshore of the bar crest increases from 0.04 to 0.91 for the high-energetic storm case and from 0.01 to 0.33 for the low-energetic post-storm case once the roller lag method is implemented.

A roller contribution is added to the short wave forcing changing the undertow current predictions. If the depth variation of this roller contribution is uniform, the effect of this term is shown to be significant with increased onshore flow at the bottom of the undertow current. A cubic or quadratic depth variation is suggested since this concentrates the roller contribution near the surface where the roller is located.

The friction factor, f_{cw}, is calibrated using bed roughness. The effect of the decrease from the default model value of the friction factor on the undertow current, by an increase in bottom shear through the boundary condition or by an increase in eddy viscosity, is shown to be insignificant. The eddy viscosity term is modified to use the local wave height instead of local depth in turbulent length scale and calibrated to match the reported eddy viscosity value for the measurements to slightly improve the undertow predictions by decreasing the magnitude of eddy viscosity in the bar trough where the undertow current is generally underpredicted by the model.

The orbital wave velocity skewness is introduced to the linear wave model by means of a parametrization method estimating the nearbed orbital wave velocities in terms of local parameter values. The velocity skewness is shown to be the only mechanism causing onshore sediment transport throughout the domain. A finite number of measured waves were used during the development of the parameterization method for velocity skewness and it is found that the wave conditions for our test stages, especially near the bar and the shoreline for the onshore bar migration case, were not well represented during the development of the parameterization method. This contributed to inaccuracies of the skewness predictions and makes the method questionable for cross-shore profile evolution.

The cross-shore sediment transport and bar migration events are studied using energetics-based sediment transport formulations. The offshore bar migration case has been predicted reasonably well by the numerical model after all the model enhancements. The friction factor is shown to have a stronger effect on sediment transport than on the undertow current, since the effective bed shear stress is directly proportional to the magnitude of the friction factor. The roller lag method is shown to be a key mechanism for the prediction of the offshore bar migration event. The model is observed to predict the offshore movement of the bar without the roller lag method but with a decrease in the height of the bar. On the other hand, with the roller lag method, the bar height increases with reduced offshore movement of the bar causing a reduction of the model skill from 0.95 to 0.6.

The sediment transport formula is broken down to analyze the effect of wave and current components of sediment transport. The term for the sediment transport due to the combined action of waves and currents is observed to dominate the current component and strongly affects the variation of the wave component for the offshore migration case. As a result, the erosion-accretion pattern of the domain is affected by the magnitude and variation of this combined term. The onshore transport due to

waves is driven by the skewness term in the wave component of sediment transport rate and the wave component of sediment transport leads to onshore transport before the bar crest. However, since the erosion-accretion pattern is determined by the gradient of the sediment transport rate, the combined term is observed to have a stronger effect on the prediction of bar migration.

For the onshore migration case, the skewness term is predicted to be smaller in magnitude during the low-energetic conditions contradicting the measurements which show a higher skewness value. Because of the underprediction of the onshore transport due to waves, the undertow current dominated once again and only a slight onshore migration of the bar is predicted by the numerical model. For those cases without the persistence length or roller lag methods, the model can only predict offshore migration of the bar since the undertow current is overestimated. Since the combined term depends on the undertow current, the undertow current is observed to have a major effect on sediment transport and bar migration for both cases. The model skill increases from 0.06 to 0.33 after the persistence length and roller lag methods are implemented.

Overall, the numerical model is used to study the dynamics of waves, currents and sediment transport on barred beaches. Therefore, the hydrodynamics is studied in detail first, rather than calibrating the free parameters to acquire results that are close to the measurements. New mechanisms are introduced in the wave, circulation and sediment transport modules to improve the predictions of hydrodynamics. The new mechanisms are shown to be not only crucial for accurate predictions of the nearshore hydrodynamics and morphodynamics on barred beaches but also effective in improving the model performance. In the end, the numerical model is shown to simulate the offshore bar migration case reasonably well. The onshore bar migration case could not be predicted accurately but the results show that the incorporated improvements to the model are important for both the hydrodynamics and migration

of the bar.

Future studies should focus on improving the predictions for the velocity skewness since it is an important agent for onshore sediment transport. A nonlinear wave model may be used instead of a linear one to have more accurate predictions for the nearbed orbital velocities as well as other wave properties. The effect of infragravity waves on bar formation and migration needs to be studied in order to better understand its role on cross-shore sediment transport and bed evolution. The new mechanisms developed and introduced to the numerical model in this study need to be applied to other data sets for validation and to determine the range of applicability. The model should be coupled with other sediment transport formulas to see the effect of model improvements.

REFERENCES

Aagaard, T. (1988). A study on nearshore bar dynamics in a low-energy environment; Northern Zealand, Denmark. *Journal of Coastal Research*, **4**(1), 115–128.

Alsina, J. and Baldock, T. (2007). Improved representation of breaking wave energy dissipation in parametric wave transformation models. *Coastal Engineering*, **54**(10), 765 – 769.

Amoudry, L., Hsu, T.-J., and Liu, P. L.-F. (2008). Two-phase model for sand transport in sheet flow regime. *Journal of Geophysical Research - Part C - Oceans*, **113**(C3), C03011 (15 pp.).

Apotsos, A., Raubenheimer, B., Elgar, S., and Guza, R. T. (2008). Testing and calibrating parametric wave transformation models on natural beaches. *Coastal Engineering*, **55**(3), 224–235.

Asano, T. (1991). Two-phase flow model on oscillatory sheet-flow. In *Proceedings of the 22nd International Conference on Coastal Engineering*, volume 3, pages 2372 – 2384, ASCE, Delft, Netherlands.

Bagnold, R. A. (1966). Approach to sediment transport problem from general physics. *United States Geological Survey – Professional Papers, 422-I*, pages 1 – 37.

Bailard, J. A. (1981). An energetics total load sediment transport model for a plane sloping beach. *Journal of Geophysical Research-Oceans and Atmospheres*, **86**(NC11), 938–954.

Bailard, J. A. and Inman, D. L. (1981). An energetics bedload model for a plane sloping beach - local transport. *Journal of Geophysical Research-Oceans and Atmospheres*, **86**(NC3), 2035–2043.

Bakker, W. T. (1974). Sand concentration in an oscillatory flow. In *Proceedings of the 14th International Conference on Coastal Engineering*, volume 1, pages 58–76, ASCE, Copenhagen, Denmark.

Baldock, T. E., Holmes, P., Bunker, S., and Van Weert, P. (1998). Cross-shore hydrodynamics within an unsaturated surf zone. *Coastal Engineering*, **34**(3-4), 173 – 196.

Battjes, J. A. (1975). Modelling of turbulence in the surfzone. In *Symposium on Modelling Techniques*, pages 58 – 81, ASCE, Reston,VA.

Battjes, J. A. and Janssen, J. P. F. M. (1978). Energy loss and set-up due to breaking of random waves. In *Proceedings of the 16th International Conference on Coastal Engineering*, volume 1, pages 569 – 587, ASCE, Hamburg, Germany.

Battjes, J. A. and Stive, M. J. F. (1985). Calibration and verification of a dissipation model for random breaking waves. *Journal of Geophysical Research*, **90**(C5), 9159 – 9167.

Berkhoff, J. C. W. (1972). Computation of combined refraction-diffraction. In *Proceedings of the 13th International Conference on Coastal Engineering*, pages 471–490, ASCE, Vancouver, Canada.

Boczar-Karakiewicz, B. and Davidson-Arnott, R. G. D. (1987). Nearshore bar formation by nonlinear-wave processes - a comparison of model results and field data. *Marine Geology*, **77**(3-4), 287–304.

Boers, M. (1995). Bedforms and undertow in the surf zone: an analysis of the LIP 11D-data. Res. Report No. 95-01, Delft University of Technology, Dept. of Civil Eng., Div. of Hydraulic and Geotechnical Eng., Netherlands.

Bosboom, J., Aarninkhof, S. G. J., Reniers, A. J. H. M., Roelvink, J. A., and Walstra, D. J. R. (1997). UNIBEST-TC 2.0, Overview of model formulations. Report H2305, Delft Hydraulics, Delft, The Netherlands.

Bowen, A. J. (1980). Simple models of nearshore sedimentation: Beach profiles and longshore bars. In *The Coastline of Canada; littoral processes and shore morphology*, number 80-10, pages 1–11, Geological Survey of Canada, Nova Scotia, Canada.

Cambazoglu, M. K., Haas, K. A., and Hanes, D. M. (2006). Numerical investigations on the effect of wave skewness on sandbar migration. In *Proceedings of 30th International Conference on Coastal Engineering*, volume 1, pages 58–76, ASCE, San Diego, USA.

Coffey, F. C. and Nielsen, P. (1985). Aspects of wave current boundary layer flows. In *Proceedings of the 19th International Conference on Coastal Engineering*, volume 3, pages 2232 – 2245, ASCE, Houston, TX, USA.

Cornish, V. (1898). On sea beaches and sand banks. *Geography Journal*, **11**, 528–647.

Dally, W. R. (1987). Longshore bar formation - surf beat or undertow? In *Proceedings of Coastal Sediments '87*, volume 1, pages 71 – 86, ASCE, New Orleans, LA, USA.

Dally, W. R. and Dean, R. G. (1984). Suspended sediment transport and beach profile evolution. *Journal of Waterway, Port, Coastal and Ocean Engineering*, **110**(1), 15 – 33.

Dally, W. R., Dean, R. G., and Dalrymple, R. A. (1985). Wave height variation across beaches of arbitrary profile. *Journal of Geophysical Research*, **90**(C6), 11917 – 11927.

De Vriend, H. J. and Stive, M. J. F. (1987). Quasi-3D modelling of nearshore currents. In *Coastal Engineering*, volume 11, pages 565 – 601, Delft, Neth.

Demir, H. (2007). *A Process Based Model for Beach Profile Evolution*. Ph.D. thesis, Georgia Institute of Technology, Savannah, GA.

Doering, J. C. and Bowen, A. J. (1995). Parametrization of orbital velocity asymmetries of shoaling and breaking waves using bispectral analysis. *Coastal Engineering*, **26**, 15 – 33.

Doering, J. C., Elfrink, B., Hanes, D. M., and Ruessink, G. (2000). Parametrization of velocity skewness under waves and its effect on cross-shore sediment transport. In *Proceedings of the 27th International Conference on Coastal Engineering*, volume 1, pages 3263–3276, ASCE, Sydney, Australia.

Dong, P. and Zhang, K. (1999). Two-phase flow modelling of sediment motions in oscillatory sheet flow. *Coastal Engineering*, **36**(2), 87 – 109.

Dulou, C., Belzons, M., and Rey, V. (2000). Laboratory study of wave bottom interaction in the bar formation on an erodible sloping bed. *Journal of Geophysical Research*, **105**(C8), 19745 – 19762.

Dulou, C., Belzons, M., and Rey, V. (2002). Bar formation under breaking wave conditions: A laboratory study. *Journal of Coastal Research*, **18**(4), 802–809.

Dyhr-Nielsen, M. and Sørensen, T. (1970). Some sand transport phenomena on coasts with bars. *Proceedings of the 12th International Conference on Coastal Engineering*, **2**, 855–866.

Eldeberky, Y. and Battjes, J. A. (1996). Spectral modeling of wave breaking: application to Boussinesq equations. *Journal of Geophysical Research*, **101**(C1), 1253 – 1264.

Elfrink, B., Rakha, K. A., Deigaard, R., and Brøker, I. (1999). Effect of near-bed velocity skewness on cross shore sediment transport. In *Proceedings Coastal Sediments '99*, pages 33–47, Long Island, NY, USA.

Elfrink, B., Hanes, D. M., and Ruessink, B. G. (2006). Parameterization and simulation of near bed orbital velocities under irregular waves in shallow water. *Coastal Engineering*, **53**(11), 915 – 927.

Elgar, S., Gallagher, E. L., and Guza, R. T. (2001). Nearshore sandbar migration. *Journal of Geophysical Research*, **106**(C6), 11623 – 11627.

Faria, A. F. G., Thornton, E. B., Lippmann, T. C., and Stanton, T. P. (2000). Undertow over a barred beach. *Journal of Geophysical Research*, **105**(C7), 16999 – 17010.

Gallagher, E. L., Elgar, S., and Guza, R. T. (1998). Observations of sand bar evolution on a natural beach. *Journal of Geophysical Research*, **103**(C2), 3203 – 3215.

Gotoh, H. and Sakai, T. (1997). Numerical simulation of sheetflow as granular material. *Journal of Waterway Port Coastal and Ocean Engineering*, **123**(6), 329–336.

Greenwood, B. and Osborne, P. D. (1990). Vertical and horizontal structure in cross-shore flows: An example of undertow and wave set-up on a barred beach. *Coastal Engineering*, **14**, 543–580.

Guza, R. T. and Thornton, E. B. (1985). Velocity moments in the nearshore. *Journal of Waterway, Port, Coastal and Ocean Engineering*, **111**(2), 235–256.

Haas, K. A. and Hanes, D. M. (2004). Process based modeling of total longshore sediment transport. *Journal of Coastal Research*, **20**(3), 853–861.

Haas, K. A. and Svendsen, I. A. (2000). Three-dimensional modeling of rip current systems. (Ph. D. Dissertation), Res. Report CACR-00-06, Center for Applied Coastal Research, Univ. of Delaware.

Haas, K. A. and Warner, J. C. (2009). Comparing a quasi-3D to a full 3D nearshore circulation model: SHORECIRC and ROMS. *Ocean Modelling*, **26**(1-2), 91–103.

Henderson, S. M., Allen, J. S., and Newberger, P. A. (2004). Nearshore sandbar migration predicted by an eddy-diffusive boundary layer model. *Journal of Geophysical Research-Oceans*, **109**(C6,C06024), 1–15.

Hoefel, F. and Elgar, S. (2003). Wave-induced sediment transport and sandbar migration. *Science*, **299**(5614), 1885–1887.

Houston, S. H. and Dean, R. G. (1991). Method for prediction of bar formation and migration. In *Proceedings of the 22nd International Conference on Coastal Engineering*, volume 2, pages 2145 – 2158, ASCE, Delft, Netherlands.

Howd, P., Bowen, T., Holman, R., and Oltman-Shay, J. (1991). Infragravity waves, longshore currents, and linear sand bar formation. In *Coastal Sediments '91*, pages 72 – 84, ASCE, Seattle, WA, USA.

Howd, P., Bowen, A. J., and Holman, R. (1992). Edge waves in the presence of strong longshore currents. *Journal of Geophysical Research*, **97**(C7), 11357 – 11371.

Hsu, T.-J., Jenkins, J., and Liu, P. L.-F. (2003). On two-phase sediment transport: dilute flow. *Journal of Geophysical Research*, **108**(C3), 3057.

Hsu, T.-J., Jenkins, J. T., and Liu, P. L.-F. (2004). On two-phase sediment transport: sheet flow of massive particles. *Proceedings of the Royal Society of London, Series A (Mathematical, Physical and Engineering Sciences)*, **460**(2048), 2223 – 2250.

Hsu, T.-J., Elgar, S., and Guza, R. T. (2006). Wave-induced sediment transport and onshore sandbar migration. *Coastal Engineering*, **53**(10), 817–824.

Isobe, M. and Horikawa, K. (1982). Study on water particle velocities of shoaling and breaking waves. *Coastal Engineering in Japan*, **25**, 109–123.

Janssen, T. T. and Battjes, J. A. (2007). A note on wave energy dissipation over steep beaches. *Coastal Engineering*, **54**(9), 711 – 716.

Kaihatu, J. M. and Kirby, J. T. (1995). Nonlinear transformation of waves in finite water depth. *Physics of Fluids*, **7**(8), 1903 – 1914.

Kennedy, A. B., Chen, Q., Kirby, J. T., and Dalrymple, R. A. (2000). Boussinesq modeling of wave transformation, breaking and runup:1D. *Journal of Waterway, Port, Coastal and Ocean Engineering*, **126**(1), 39 – 47.

Kirby, J. T. and Kaihatu, J. M. (1997). Structure of frequency domain models for random wave breaking. In *Proceedings of the 25th International Conference on Coastal Engineering*, volume 1, pages 1144 – 1155, ASCE, Orlando, FL, USA.

Kirby, J. T., Dalrymple, R. A., and Shi, F. (2004). Refraction-Diffraction model REF/DIF-S version 1.3, documentation and user's manual. Res. Report CACR-04-01, Center for Applied Coastal Research, Univ. of Delaware.

Kuriyama, Y. and Nakatsukasa, T. (2000). A one-dimensional model for undertow and longshore current on a barred beach. *Coastal Engineering*, **40**, 39–58.

Li, L. and Sawamoto, M. (1995). Multi-phase model on sediment transport in sheet-flow regime under oscillatory flow. *Coastal Engineering Journal*, **38**(2), 157 – 178.

Lippmann, T. C., Brookins, A. H., and Thornton, E. B. (1996). Wave energy transformation on natural profiles. *Coastal Engineering*, **27**(1-2), 1 – 20.

Long, W., Kirby, J. T., and Shao, Z. (2006). Numerical schemes for bed level updating in sediment transport. Res. Report CACR-06-01, Center for Applied Coastal Research, Univ. of Delaware.

Madsen, P. A., Søresen, O. R., and Schäffer, H. A. (1997). Surf zone dynamics simulated by a Boussinesq type model. Part I. Model description and cross-shore motion of regular waves. *Coastal Engineering*, **32**, 255–287.

Mase, H. and Kirby, J. T. (1993). Hybrid frequency-domain KdV equation for random wave transformation. In *Proceedings of the 23rd International Conference on Coastal Engineering*, volume 1, pages 474 – 487, ASCE, Venice, Italy.

Meyer-Peter, E. and Mueller, R. (1948). Formulas for bed-load transport. Report on the second meeting, International Association for Hydraulic Structures Research, Stockholm, Denmark.

Miche, R. (1944). Mouvements ondulatoires de la mer en profondeur constante ou decroissante. *Annales des Ponts et Chaussées*, **114**.

Nairn, R. B. and Southgate, H. N. (1993). Deterministic profile modelling to nearshore processes. Part 2. Sediment transport and beach profile development. *Coastal Engineering*, **19**(1-2), 57 – 96.

Nairn, R. S., Roelvink, J. A., and Southgate, H. N. (1990). Transition zone width and implications for modeling surfzone hydrodynamics. In *Proceedings of the 22nd International Conference on Coastal Engineering*, pages 58 – 81, ASCE, Barcelona, Spain.

Nielsen, P. (1992). *Coastal Bottom Boundary Layers and Sediment Transport*. World Scientific, Singapore.

O'Connor, B. A., Pan, S., Nicholson, J., MacDonald, N., and Huntley, D. A. (1998). A 2D model of waves and undertow in the surf zone. In *Proceedings of the 26th International Conference on Coastal Engineering*, pages 286–296, ASCE, Copenhagen, Denmark.

O'Hare, T. J. and Davies, A. G. (1990). A laboratory study of sand bar evolution. *Journal of Coastal Research*, **6**(3), 531 – 544.

O'Hare, T. J. and Davies, A. G. (1993). Sand-bar evolution beneath partially-standing waves - laboratory experiments and model simulations. *Continental Shelf Research*, **13**(11), 1149–1181.

O'Hare, T. J. and Huntley, D. A. (1994). Bar formation due to wave groups and associated long waves. *Marine Geology*, **116**(3-4), 313–325.

Okayasu, A., Shibayama, T., and Mimura, N. (1986). Velocity field under plunging waves. In *Proceedings of the 20th International Conference on Coastal Engineering*, pages 660–674, ASCE, Taipei, Taiwan.

Okayasu, A., Shibayama, T., and Horikawa, K. (1988). Vertical variation of undertow in the surf zone. In *Proceedings of the 21st International Conference on Coastal Engineering*, pages 478–491, ASCE, Málaga, Spain.

O'Shea, K. F., Nicholson, J., and O'Connor, B. A. (1991). Analysis of existing laboratory data to find expressions for the transition zone length. Res. Report MCE/1, Dept. Civil Eng., University of Liverpool, UK.

Paola, C. and Seal, R. (1995). Grain size patchiness as a cause of selective deposition and downstream fining. *Water Resources Research*, **31**(5), 1395–1407.

Putrevu, U. and Svendsen, I. A. (1993). Vertical structure of the undertow outside the surf zone. *Journal of Geophysical Research*, **98**(C12), 22707–22716.

Putrevu, U. and Svendsen, I. A. (1999). Three-dimensional dispersion of momentum in wave-induced nearshore currents. *European Journal of Mechanics, B/Fluids*, **18**(3), 409 – 427.

Rattanapitikon, W. (2007). Calibration and modification of energy dissipation models for irregular wave breaking. *Ocean Engineering*, **34**, 1592 – 1601.

Rattanapitikon, W. and Shibayama, T. (2000). Simple model for undertow profile. *Coastal Engineering Journal*, **42**(1), 1 – 30.

Rattanapitikon, W., Karunchintadit, R., and Shibayama, T. (2003). Irregular wave height transformation using representative wave approach. *Coastal Engineering Journal*, **45**(3), 489 – 510.

Reniers, A. J. H. M. and Battjes, J. A. (1997). Cross-shore momentum flux due to shear instabilities. In *Proceedings of the 25th International Conference on Coastal Engineering*, volume 1, pages 175 – 185, ASCE, Orlando, FL, USA.

Ribberink, J. S. (1998). Bed-load transport for steady flows and unsteady oscillatory flows. *Coastal Engineering*, **34**(1-2), 59 – 82.

Rivero, F. J., Sánchez-Arcilla, A., and Beyer, D. (1994). Comparison of a wave transformation model with LIP-11D data. In *Coastal Dynamics - Proceedings of the International Conference*, pages 518 – 532, Barcelona, Spain.

Roelvink, J. A. and Reniers, A. J. H. M. (1995). LIP 11D Delta Flume experiments; a dataset for profile validation. Data Report H2130, Delft Hydraulics.

Roelvink, J. A. and Stive, M. J. F. (1989). Bar-generating cross-shore flow mechanisms on a beach. *Journal of Geophysical Research*, **94**(C4), 4785 – 4800.

Rouse, H. (1937). Modern conceptions of the mechanics of fluid turbulence. *Trans. Am. Soc. Civ. Eng.*, **102**(1965), 463–543.

Ruessink, B., Walstra, D., and Southgate, H. (2003). Calibration and verification of a parametric wave model on barred beaches. *Coastal Engineering*, **48**(3), 139 – 149.

S.-Arcilla, A., Roelvink, J. A., O'Connor, B. A., Reniers, A., and Jiménez, J. A. (1994). The Delta Flume'93 experiment. In *Coastal Dynamics - Proceedings of the International Conference*, pages 488–502, ASCE, Barcelona, Spain.

Sallenger, A. H. J. and Holman, R. A. (1987). Infragravity waves over a natural barred profile. *Journal of Geophysical Research*, **92**(C9), 9531 – 9540.

Sallenger, A. H. J., Asbury, H., and Howd, P. A. (1989). Nearshore bars and the break-point hypothesis. *Coastal Engineering*, **12**(4), 301 – 313.

Sancho, F. E. and Svendsen, I. A. (2000). Unsteady nearshore currents on longshore varying topographies. Res. Report CACR-97-10, Center for Applied Coastal Research, Univ. of Delaware.

Shand, R. D., Bailey, D. G., and Shepherd, M. J. (1999). An inter-site comparison of net offshore bar migration characteristics and environmental conditions. *Journal of Geophysical Research*, **15**(3), 750 – 765.

Short, A. D. (1975). Multiple offshore bars and standing waves. *Journal of Geophysical Research*, **80**(27), 3838 – 3840.

Sierra, J. P., Azuz, I., Rivero, F. J., and Sánchez-Arcilla, A., R. (1997). Morphodynamic modelling in the nearshore area. In *Proceedings of International Conference on Computer Modelling of Seas and Coastal Regions*, pages 433–442, La Coruña, Spain.

Singer, M. B. and Dunne, T. (2004). Modeling decadal bed material sediment flux based on stochastic hydrology. *Water Resources Research*, **40**(3), W033021–W0330214.

Southgate, H. N. and Nairn, R. B. (1993). Deterministic profile modelling of nearshore processes. Part 1. Waves and currents. *Coastal Engineering*, **19**(1-2), 27 – 56.

Southgate, H. N. and Wallace, H. M. (1994). Breaking wave persistence in parametric surf zone models. In *Coastal Dynamics - Proceedings of the International Conference*, pages 543 – 555, Barcelona, Spain.

Stive, M. J. F. (1987). Model for cross-shore sediment transport. In *Proceedings of the 20th International Conference on Coastal Engineering*, volume 2, pages 1550 – 1564, ASCE, Taipei, Taiwan.

Stive, M. J. F. and Battjes, J. A. (1985). Model for offshore sediment transport. volume 2, pages 1420–1436.

Sunamura, T. and Maruyama, K. (1987). Wave-induced geomorphic response of eroding beaches with special reference to seaward migrating bars. In *Coastal Sediments '87*, volume 1, pages 788–801, ASCE, New Orleans, LA, USA.

Svendsen, I. A. (1984a). Mass flux and undertow in a surf zone. *Coastal Engineering*, **8**(4), 347 – 365.

Svendsen, I. A. (1984b). Wave heights and set-up in a surf zone. *Coastal Engineering*, **8**(4), 303 – 329.

Svendsen, I. A. (2005). *Introduction to Nearshore Hydrodynamics*. World Scientific, Singapore.

Svendsen, I. A. and Hansen, J. B. (1988). Cross-shore currents in surf-zone modelling. *Coastal Engineering*, **12**, 23–42.

Svendsen, I. A., Schäffer, H. A., and Hansen, J. B. (1987). The interaction between the undertow and the boundary layer flow on a beach. *Journal of Geophysical Research*, **92**(C11), 11845 – 11856.

Svendsen, I. A., Haas, K. A., and Zhao, Q. (2002). Quasi-3D nearshore circulation model SHORECIRC, version 2.0 . Res. Report CACR-02-01, Center for Applied Coastal Research, Univ. of Delaware.

Swart, D. H. and Loubster, C. C. (1978). Vocoidal water wave theory for all non-breaking waves. In *Proceedings of the 16th International Conference on Coastal Engineering*, pages 467 – 486, ASCE, Hamburg, Germany.

Thornton, E. B. and Guza, R. T. (1983). Transformation of wave height distribution. *Journal of Geophysical Research*, **88**(C10), 5925 – 5938.

Thornton, E. B., Humiston, R. T., and Birkemeier, W. (1996). Bar/trough generation on a natural beach. *Journal of Geophysical Research*, **101**(C5), 12097 – 12110.

Trowbridge, J. and Young, D. (1989). Sand transport by unbroken water waves under sheet flow conditions. *Journal of Geophysical Research*, **94**(C8), 10971 – 10991.

Van Dongeren, A. R. and Svendsen, I. A. (1997). Quasi-3D modeling of nearshore hydrodynamics. Res. Report CACR-97-04, Center for Applied Coastal Research, Univ. of Delaware.

Van Rijn, L. C. (1990). Handbook of sediment transport by currents and waves. Report H 461, 2nd edition., Delft Hydraulics, Netherlands.

Van Rijn, L. C. (1998). Effect of sediment composition on cross-shore bed profiles. *Proceedings of the 26th International Conference on Coastal Engineering*, **3**, 2495 – 2508.

Van Rijn, L. C. (2000). General view on sand transport by currents and waves; data analysis and engineering modelling for uniform and graded sand (TRANSPORT2000 and CROSMOR2000 models). Report Z2899.20, Z2099.30, Z2824.30, WL Delft Hydraulics, The Netherlands.

Van Rijn, L. C., Wasltra, D. J. R., Grasmeijer, B., Sutherland, J., Pan, D., and Sierra, J. P. (2003). The predictability of cross-shore bed evolution of sandy beahes at the time scale of storms and seasons using process-based profile models. *Coastal Engineering*, **47**(3), 295 – 327.

Van Rijn, L. C., Ruessink, G., Grasmeijer, B., Van Der Werf, J., and Ribberink, J. (2007). Wave-related transport and nearshore morphology. In *Coastal Sediments '07*, ASCE, New Orleans, LA, United States.

Watanabe, A. (1993). Total rate and distribution of longshore sand transport. In *Proceedings of the 23rd International Conference on Coastal Engineering*, volume 3, pages 2528 – 2451, ASCE, Venice, Italy.

Wilcock, P. R. (1992). Flow competence: a criticism of a classic concept. *Earth Surface Processes and Landforms*, **17**(3), 289 – 298.

Willmott, C. J. (1981). On the validation of models. *Physical Geography*, **2**(2), 184 – 194.

Wright, L. D., Guza, R. T., and Short, A. D. (1982). Dynamics of a high energy dissipative surf zone. *Journal of Marine Geology*, **45**, 41–62.

Zai-Jin, Y. (1994). Simple model for current velocity profiles in combined wave-current flows. *Coastal Engineering*, **23**(3-4), 289 – 304.

VITA

Mustafa Kemal Cambazoglu was born in Ankara, Turkey. He received his B.Sc. in Civil Engineering from Middle East Technical University, Ankara, Turkey in 1999 and his M.Sc. in Civil Engineering with a focus on Hydromechanics from Middle East Technical University, Ankara, Turkey in 2002. He worked as a graduate research assistant at the Hydraulics Laboratory of Middle East Technical University between 1999 and 2004. He came to the United States in August 2004 to pursue a doctorate in Civil Engineering with a focus on Coastal Engineering at Georgia Institute of Technology. He worked with Dr. Kevin A. Haas at Georgia Tech Savannah as a graduate research assistant between 2004 and 2009. He currently is a research scientist at University of Southern Mississippi and works at the Naval Research Laboratory in Stennis Space Center, MS.